PhD Thesis

Applications of L-band missions for environmental research

David Chaparro Danon

CommSensLab/Remote Sensing Laboratory – Departament de Teoria del Senyal i Comunicacions, Universitat Politècnica de Catalunya

UNIVERSITAT POLITÈCNICA
DE CATALUNYA
BARCELONATECH

Thesis Advisors:

Dr. Mercè Vall-llossera and Dr. Maria Piles

Barcelona, July 2018

Applications of L-band missions for environmental research. David Chaparro Danon, PhD Thesis. Universitat Politècnica de Catalunya.

This work has been funded by the Spanish government through grants BES-2013-066240 and EEBB-I-17-12200, projects ESP2015-67549-C3-1-R and ESP2017-89463-C3-2-R, and the award MDM-2016-0600. The work has also been supported by the European Regional Development Fund (ERDF).

Binding design: Clara Muñoz Danon

Binding images: Vince Fleming (wildfire); David Becker (crop); Chris Petersom (forest decline); Tieu Moi (tropical forest); ESA (SMOS); NASA (SMAP).

A la Blanca, als meus pares i a la meva germana.

En record dels Avis.

Abstract

Present environmental changing conditions have large impacts on ecosystems in general and on vegetation conditions in particular. These changes are mainly induced by human activity, either directly or indirectly: global warming trends due to higher greenhouse gas atmospheric concentrations, deforestation and land cover changes due to agricultural expansion, or modified land, ocean and ice surface properties altering the Earth's surface albedo, are some examples of these environmental changes. Additionally, natural hazards such as droughts and wildfires may increase their frequency and intensity in some regions of the globe due to climate shifts.

In this context, remote sensing missions are needed to further our knowledge of the Earth's system, monitor global ecosystems, and ultimately quantify changes in vegetation, carbon stocks and water resources. In particular, satellite passive microwave sensors provide a unique means to regularly obtain global maps of the Earth's surface soil moisture (SM) and of the attenuation of the soil microwave emission through the vegetation canopy (represented by the vegetation optical depth parameter; VOD). VOD is linked to the vegetation water content (VWC) and can also be related to the above-ground carbon density. Importantly, low microwave frequencies (L-band) are more sensitive to high densities of vegetation canopy and to soil moisture than higher frequencies (e.g., C- or X-band). The first two space missions carrying an L-band radiometer on-board for measuring the Earth's SM have been launched in the last decade: the European Space Agency's (ESA) Soil Moisture and Ocean Salinity (SMOS, in 2009) and the National Aeronautics and Space Administration's (NASA) Soil Moisture Active Passive (SMAP, in 2015).

The main goal of this Thesis is to assess the applicability of L-band satellite retrievals of SM and VOD on vegetation studies. The first part of this Thesis applies SM information – complementarily to other data sources- to assess and prevent drought-derived impacts on vegetation in the Iberian Peninsula:

- Soil moisture and land surface temperature (LST) data are applied to study the soil conditions before fire ignitions in the region. A fire risk index is developed to predict the potential extent of fires under particular SM-LST conditions. Results show that SM explains >30% of the predicted potential burned area.
- The forest decline in Catalonia after a severe drought in summer 2012 is modelled as a function of species, climate variables and SM. The contribution of SM to the forest affectation is coherent with what is reported by other variables, and is shown to explain about 5% of the model variance.

The second part of this Thesis presents the capacity to infer vegetation conditions and carbon density from VOD with two dedicated research studies:

- The sensitivity of L-band VOD to carbon stocks in tropical regions is compared with VOD at higher frequency bands and with optical-infrared vegetation indices. The L-band VOD shows enhanced sensitivity to carbon density in most regions, regardless of

altitude and vegetation types. The complementary use of VOD at different frequencies and optical-infrared vegetation indices should improve carbon estimates.

- Seasonal metrics of VOD have been proposed for crop yield assessment. Results over the US Corn Belt show that VOD explains up to 78% of yield variance and can potentially be used to enhance crop yield forecasts.

The results presented in this Thesis contribute to improve present capabilities of predicting wildfires, forest decline and crop yield, as well as of monitoring forest carbon stocks, using new global information from L-band Earth observation sensors. SM and VOD are very valuable indicators to support food security and ecosystem preservation decision making, as well as to enhance present capabilities of mapping carbon stocks.

Contents

List of tables

List of figures

1

Introduction

Abstract

Present environmental changes induced by different factors, including human activity, land-use pressure and climate change, have large impacts on vegetation conditions with inmediate consequences for forest health, vegetation carbon stocks, or crop productivity. In this context, new measurements at low frequency microwaves (L-band) from the SMOS and SMAP satellites provide a unique means to obtain global estimates of SM, as well as to infer vegetation hydric conditions and biomass from the VOD parameter, a variable linked to the vegetation canopy density. This PhD Thesis takes leverage of the first global datasets of L-band SM and VOD to assess whether recent episodes of wildfires and forest mortality are linked to droughts, to explore the capacity of L-band VOD to estimate carbon stocks, and to produce satellite-derived metrics for crop yield assessment. This chapter starts presenting the motivation of this work and describing the environmental risks and challenges under study. It then provides a review of the fundamentals of microwave remote sensing needed for a deeper understanding of SM and VOD retrievals. The chapter concludes providing an overview of scientific and societal applications that benefit from L-band measurements.

1.1. Motivation: a changing world

Human activity, including fuel fossils use and land-use pressure, leads to higher atmospheric concentrations of greenhouse gases, modifies vegetation types, and changes land, ice and ocean surface properties altering the surface albedo. These variations have large impacts on the Earth's radiation budget, increasing the irradiance retained in the Earth (Forster et al., 2007; Hartmann et al., 2013). As a consequence, the average global surface temperature has increased during the last 100 years and heat waves have become more frequent in some regions (e.g., in Europe and in the Mediterranean; Hartmann et al., 2013). The rise of temperatures is expected to continue in present and future times and, in close relation with this trend, precipitation extremes could increase. Most predictions agree on the fact that the precipitation change would not be spatially uniform: while the tropics and Polar Regions could receive up to 50% more precipitation, major reductions of rainfall (between -10% and -30%) are forecasted in the Mediterranean, Central America, northern South America, and in west and south of Africa. Although these predictions are still uncertain, the severity of droughts is likely to increase in some regions (Hartmann et al., 2013; IPCC, 2013), as is the case of Southern Europe (EEA, 2008; IPCC, 2012).

Drier and warmer conditions, degradation of ecosystems (including continued deforestation), and natural hazards (e.g., wildfires), are among the main factors inducing environmental changes on Earth. They may threaten forest health and reduce areas of natural vegetation, affecting ecosystem services, and leading to biomass losses and carbon releases to the atmosphere, with the ultimate consequence of possible climate change reinforcing. Also, changing environmental conditions may have negative impacts on croplands and food security worldwide.

In this context, Earth Observation (EO) satellites permit to exhaustively study the environment and to monitor vegetation and water resources. In particular, environmental monitoring for the threats and challenges addressed in this PhD Thesis requires to (i) accurately monitor the water content in soils and vegetation, in order to assess and prevent drought impacts; (ii) map carbon stocks in forests, which is essential to the global carbon assessment and to evaluate the actions oriented to the reduction of forest degradation; and (iii) enhance present cropland monitoring and yield assessment capabilities, in order to increase future capacity to forecast insecure food situations.

To achieve these purposes, passive microwave EO satellites can prove very useful as their measurements are sensitive to the water content in soils and vegetation. On one hand, microwave measurements allow retrieving information on surface soil moisture. On the other hand, the attenuation of the soil microwave emission through the vegetation canopies is expressed as the VOD, which is an ecological indicator related to vegetation water content and vegetation biomass. The first two space missions dedicated to soil moisture monitoring have passive L-band microwave radiometers on-board, and have been launched in the last decade: these are the Soil Moisture and Ocean Salinity (SMOS; launched in November 2009), and the Soil Moisture Active Passive (SMAP; launched in January 2015). In comparison with recent L-band sensors, microwave sensors operating at higher frequency bands with longer heritage (e.g., C- and X-bands, operating since 1978) have a shallower soil sensing depth (top 1 cm at C-band vs. 5 cm at L-band) and have a larger attenuation in presence of vegetation (Ulaby et al., 1986, pp. 1551–1596). At present, there is an increasing interest of the scientific community on L-band satellite information to monitor the Earth's water and carbon cycles (e.g., Vittucci et al, 2016a and b; Konings and Gentine, 2017; Brandt et al., 2018).

This PhD Thesis is focused on the applicability of the SMOS and SMAP L-band microwave satellite measurements to (i) understand and prevent specific environmental risks which may increase due to warming trends, in particular wildland fires and forest decline; (ii) assess the feasibility of L-band VOD to improve present carbon stock estimates in tropical forests, which is crucial for monitoring forest degradation and for global carbon assessment; and (iii) provide VOD-based crop yield assessment in order to enhance our ability to monitor and forecast food resources to reduce food insecurity.

This PhD Thesis has been mainly developed at the Universitat Politècnica de Catalunya (UPC) Remote Sensing Laboratory, in close collaboration with the Barcelona Expert Centre (BEC). Both institutions are specialized on research activities involving the SMOS instrument and its scientific applications. The study on the capacity of L-band VOD to derive carbon estimates was conducted during a 3-month stay at the Joint Research Centre of the European Commission, sited in Ispra (Italy), under the supervision of Drs. Grégory Duveiller and Alessandro Cescatti.

1.2. Environmental changes and risks

Present environmental changes impact human safety and livelihood conditions, increase economic losses, and threaten human health in many regions of the world. Such impacts are frequently associated to changes in ocean, cryosphere, and land systems of the Earth. Over land, hydrological systems have changed due to glaciers shrinking and permafrost thawing, water resources have been altered, and significant trends towards drier soils are observed in some regions (Jung et al., 2010; IPCC, 2013). Threatens on agricultural systems are increased by climate impacts on vegetation phenology and productivity, and by the loss of ecosystem services that permit to preserve the quality of water and soils, recycle nutrients, and pollinate crops, among other functions. Furthermore, ecosystem disturbances may become more frequent and/or intense in a near future, including droughts and floods, wind storms, fires, and pest outbreaks (Seidl et al., 2017). As previously mentioned, the focus of this PhD Thesis is the applicability of L-band observations to deal with particular threats: forest fires, forest degradation and loss of carbon stocks, and crop insecurity. The relationship of these threats with environmental changes is detailed hereafter.

1.2.1. Wildfires

Drying conditions as well as the rising number of extreme temperature events have the potential to increase the risk of wildfires during this century (Settele et al., 2014).

Nevertheless, recent global fire patterns are dominated by human-driven shifts rather than by the climate context. This has led to a decrease of 24% of burned area worldwide during the period 1998-2015, which has been driven mainly by the expansion and intensification of agricultural activity. The global decline of burned area is mainly explained by a reduction on the number of fires rather than by a decrease on their average extent, and is mostly concentrated in tropical savannas of Africa and South America, in Asian steppes, in Australia and in the Sahel (Andela et al., 2017, and Figure 1.1).

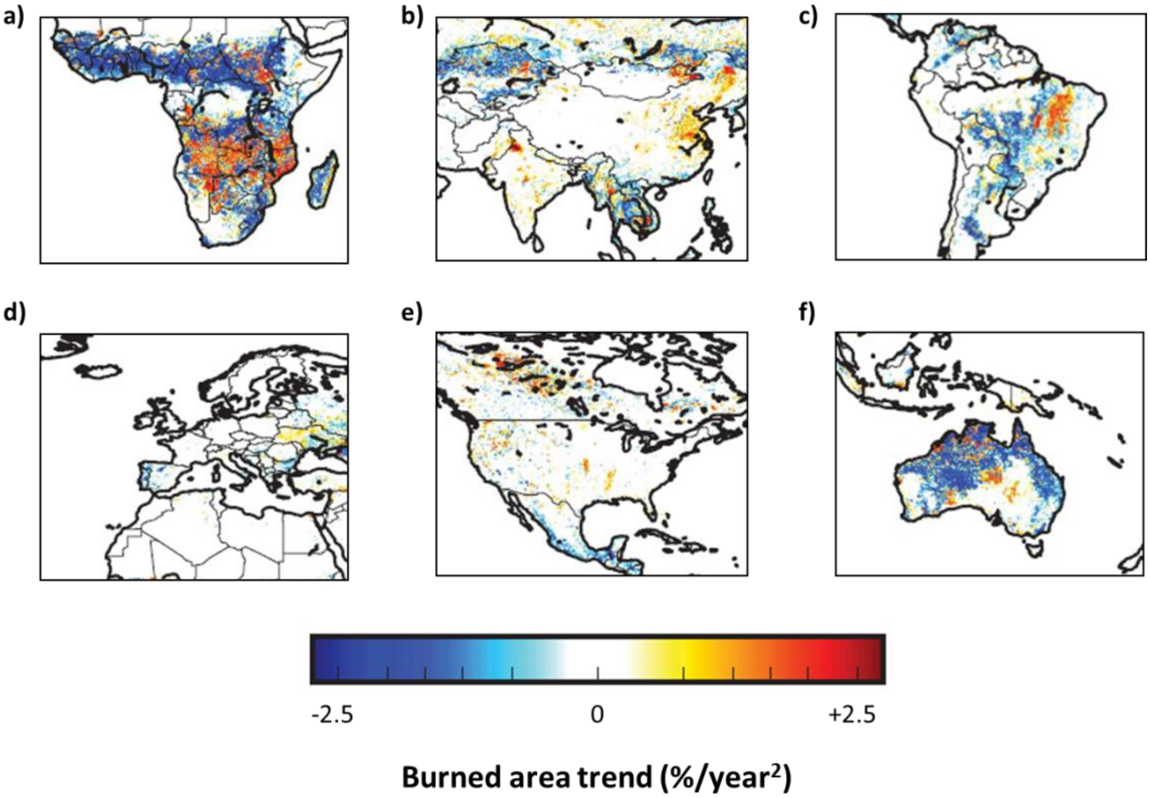

Figure 1.1. Examples of burned area trends (period 1998-2015) in all continents: (a) Africa, (b) Asia, (c) South America, (d) Europe and northern Africa, (e) North America, and (f) Oceania. Adapted from Andela et al. (2017).

Despite this trend, in several regions the yearly burned area has increased or maintained. Some remarkable increases have been found in large areas in southern Africa, in eastern China, in central Canada, in eastern Brazil, and in some regions with high forest dominance. No remarkable changes have been detected mainly in most of the Mediterranean coasts, in most tropical forests, in most central and western Europe, and in the eastern United States (Andela et al., 2017, and Figure 1.1). For this reason, the expected increase on fire risk associated to the changing climate may become particularly concerning in these regions, where no human-driven declines in burned area are found. For instance, a raise in fire risk is expected in areas with extensive forest cover in the European Mediterranean countries, such as the Balkans, the Pyrenees, and the Alps (Moriondo et al., 2006). In addition, the fire weather season has enlarged in most continents and biomes during the last four decades (Jolly et al., 2015). Hence, it is needed to improve our capacity to monitor drought and heat conditions leading to fire-prone situations.

1.2.2. Forest decline

Changes in climate conditions and land use are putting forests under pressure (Bonan, 2008; Cohen et al., 2016). Droughts and high temperatures reduce soil water availability and increase evaporative demand, and have been associated with widespread events of drought-induced mortality in forests even in environments not considered to be water limited (Allen et al., 2010; McDowell et al., 2011; Martínez-Vilalta et al., 2012a; Greenwood et al., 2017). Climatic changes, together with disturbances directly related to human activities, are putting many forests outside the ranges of conditions under which they developed, and may be too fast for evolutionary adaptation processes to keep pace (Trumbore et al., 2015). Forest decline events are generally defined as episodes with increased mortality and crown defoliation rates, which can have dramatic effects on forest ecosystem services and have the potential to modify the climate regulation and biogeochemical cycles at local and regional scales (Anderegg et al., 2013a). Forest decline is predicted to increase as a result of climate change, especially in areas where the climate is expected to become hotter and drier, such as the Mediterranean basin (EEA, 2008).

A growing number of forest decline events are being documented worldwide (Allen et al., 2010; Cramer et al., 2014; Settele et al., 2014). However, the number of studies showing consistent increases in leaf loss or mortality over substantial (e.g., decadal) time scales (e.g., Carnicer et al., 2011; Cohen et al., 2016; Neumann et al., 2017) is still scarce. In addition, most studies have focused on relatively small spatial scales, showing that mortality frequently affects preferentially larger trees (Bennett et al., 2015) and tends to be associated with high tree density, and thus competition (Linares et al., 2010), and with shallow soils (e.g., Vilà-Cabrera et al., 2013). Still, there is high uncertainty on the determinants of the spatial variability in forest mortality and further research is needed to assess the impact of droughts at regional scales.

1.2.3. Forest degradation and carbon losses

Terrestrial ecosystems act as global and significant carbon sinks, although the sink strengths' show large variability among years and its future dynamic is uncertain (Le Quéré et al., 2009 and 2016). In that sense, the forest's carbon sink could increase due to enhanced plant growth, which may be caused by future warming conditions, by longer growing seasons, and by the rising CO_2 concentration (Settele et al., 2014). However, this can be counterbalanced by land use changes converting forests to farmlands, which are particularly severe in tropical regions, where forests can turn into a net carbon source (Pan et al., 2011; Liu et al., 2015; Baccini et al., 2017). In addition, severe regional droughts and heatwaves could lead to reductions on Gross Primary Productivity (GPP) throughout all major biomes of the Earth, having negative impact on carbon sequestration (Reichstein et al., 2013; Sippel et al., 2018). This was found, for instance, during the unprecedented droughts and heatwaves occurring in Europe in 2003 (Ciais et al., 2005) and in Russia in 2010 (Barriopedro et al., 2011).

Importantly, coupling among deforestation, drought episodes, and forest fires, diminish the amount of carbon uptake in forested areas. For instance, the Amazon rainforest may become gradually a drought and fire-adapted ecosystem with less vegetation density, leading to a decrease on carbon uptake in this region (Saatchi et al., 2013). Additionally, the global impact of tree mortality, fires, and pest attacks could cancel out the enhanced forest carbon sequestration. Consequently, the carbon stored in forests is vulnerable, and the atmosphere-land CO_2 flux is expected to weaken during this century. In this context, monitoring the land carbon stocks at global scale is essential to close the carbon budget, reduce uncertainties, gain precision on modelling future climate change scenarios, and contribute to appropriate strategies against forest degradation.

1.2.4. Crop yields and food security

During the last fifty years, concurrently to the doubling of human population, the global crop production has increased substantially due to improvement of techniques (e.g., mechanization, irrigation, fertilizers and pesticides) and to the expansion of croplands (Foley et al., 2011). In particular, most main crop grain stocks have tripled (e.g., wheat and rice) or quadrupled (e.g., corn) (Godfray et al., 2010; FAO 2017). Nevertheless, total consumption can exceed production when adverse weather conditions occur (Becker-Reshef et al., 2010a), leading to insecure food situations. The expected increase of adverse weather for crop production due to climate change has a negative impact on crops and may ultimately result in a future decline of most grain yields (Deryng et al., 2014; Asseng et al., 2015; Zhao et al., 2017).

Furthermore, as the population is growing, a need for increased food supply in the coming decades is anticipated, at least until the middle of this century. Additionally, agriculture has important environmental impacts: the loss of biodiversity, the increase of deforestation, or the land and water degradation (Foley et al., 2005). In this context, agriculture faces a remarkable challenge: to fulfil the raising food demands improving food security, while reducing the environmental impacts. Hence, it is needed to rise food production and to do this without increasing impacts on the environment. This requires avoiding agricultural expansion causing deforestation and focus instead on increasing crop yields and reducing insecure crop situations. This will allow closing the so-called 'yield gaps' (i.e., reduce the difference between the potential and the real yield on croplands; Godfray et al., 2010; Foley et al., 2011; Tilman et al., 2011). EO satellites allow monitoring agroecosystems and could contribute to enhance crop yieldassessment as well as to forecast insecure food conditions.

1.3. Microwave radiometry: estimation of water content in soils and vegetation from space

1.3.1. Key concepts of microwave radiometry

The Earth's surface absorbs part of the electromagnetic radiation mainly received from the Sun, transforms it into thermal energy, and also emits radiation to keep the energy balance. This radiation depends on the surface properties and on the wavelength observed. Measuring it in the microwaves region of the spectrum provides mainly two advantages: (i) it allows sensing soil moisture and vegetation hydric conditions, as these parameters are directly linked to the soil microwave emission and to its attenuation; and (ii) these measurements are obtained regardless of weather conditions, as microwaves are almost transparent to clouds.

Microwave soil emission can be measured with high accuracy by radiometers (tower-based or on-board airborne and satellite platforms). Specifically, radiometers are passive sensors that measure the amount of radiation emitted by a source –considering a solid angle- in terms of power by unit surface. This quantity is called radiance or brightness. This and other concepts necessary to understand the measurement of soil emissions are described hereafter:

A. Black body radiation and the Rayleigh-Jeans law

A black body is a theoretical concept which defines an ideal, perfectly opaque material that absorbs all the incident radiation regardless of its frequency and polarization. Consequently, in order to reach the thermodynamic equilibrium, it must be a perfect emitter. A black body radiates the energy omnidirectionally.

To study the emission of a black body at microwave wavelengths, it must be considered that the brightness (B_f) is approximately proportional to the physical temperature of the body (T):

$$B_f \sim \frac{2f^2 k_B T}{c^2} = \frac{2k_B T}{\lambda^2}, \tag{1.1}$$

where f is the frequency in Hz, k_B = 1.38·10^{-23} J/K is the Boltzmann constant, c = 3·10^{8} m/s is the speed of light, and $\lambda = c/f$ is the wavelength. Eq. (1.1) is known as the Rayleigh-Jeans law, an approximation of the Planck's radiation law for low frequencies (see Ulaby et al., 1981, pp. 197-198, for more detail on the relationship between both laws).

According to the Rayleigh-Jeans law, the brightness of a black body (B_{bb}) at a physical temperature (T) and a particular frequency bandwidth (Δ_f) is expressed as:

$$B_{bb} \sim B_f \cdot \Delta_f = \frac{2k_B T}{\lambda^2} \Delta_f\,. \tag{1.2}$$

B. Gray body radiation, brightness temperature, and emissivity

Black bodies are useful for a conceptual description, but real objects or surfaces behave differently: they do not absorb all the energy received and consequently their emission is lower than that of blackbodies. To characterize the brightness emitted by a gray body, it is necessary to define the concept of microwave brightness temperature $T_B(\theta,\phi)$. This is the temperature a blackbody would have to produce the brightness emitted by the gray body under study. The brightness temperature is not a real temperature, but an effective one. Hence, the brightness of a gray body is expressed as follows:

$$B(\theta,\phi) \sim \frac{2k_B}{\lambda^2} T_B(\theta,\phi)\Delta_f. \tag{1.3}$$

Importantly, the ratio between the brightness of gray bodies and that of black bodies is expressed by the emissivity $e(\theta,\phi)$:

$$e(\theta,\phi) = \frac{B(\theta,\phi)}{B_{bb}} = \frac{T_B(\theta,\phi)}{T}. \tag{1.4}$$

The emissivity ranges between 0 (a perfect reflector) and 1 (a black body, which is a perfect absorber). Note that according to Eq. (1.4), the brightness temperature of a body cannot be higher than its physical temperature.

C. Measuring brightness temperatures from space

Similarly to the brightness temperature, the apparent temperature of an antenna $T_{AP}(\theta,\phi)$ is used to characterize the total brightness incident over the antenna of a radiometer $B_i(\theta,\phi)$:

$$B_i(\theta,\phi) \sim \frac{2k_B}{\lambda^2} T_{AP}(\theta,\phi)\Delta_f. \tag{1.5}$$

The apparent temperature is linked to the power received by the antenna (see Ulaby et al., 1981, p. 203) and it is a function of different contributions in the case of an Earth-looking radiometer:

$$T_{AP}(\theta,\phi) = T_{UP} + \frac{1}{L_a}(T_B + T_{SC}), \tag{1.6}$$

where T_{UP} is the atmospheric upwelling radiation, L_a is the attenuation of the atmosphere, T_B is the brightness temperature of the observed scene, and T_{SC} is the downwelling atmospheric radiation scattered by the Earth's surface. Importantly, the atmospheric effects are negligible at the L-band (1-2 GHz) microwave frequency range used in soil moisture remote sensing.

Imaging satellite radiometers transform the radiation collected by an antenna into brightness temperature maps. The performance of this process is determined by (i) the radiometric resolution or sensitivity, which is the smallest difference between brightness temperatures that can be distinguished; (ii) the radiometric accuracy, which is the degree of agreement between the measured antenna temperature and the real one or true value; and (iii) the spatial resolution, which is the closest distance at which the radiometer can obtain different measures coming from two different points.

1.3.2. Soil emission

The emission of natural surfaces depends on their dielectric constant (ε). This term refers to the impedance that a medium exerts to an electromagnetic wave passing through it, divided by the impedance exerted by the vacuum, which is used as a reference value. The dielectric constant of soils is expressed as a complex number ($\varepsilon_S = \varepsilon'_S + j\varepsilon''_S$), where the real part ($\varepsilon'_S$) determines the propagation of the energy through the soil, and the imaginary part ($j\varepsilon''_S$) determines the energy losses. In the case of dry soils the dielectric constant is much lower (ε=4) than that of water (ε=80). This is crucial in soil moisture remote sensing, as the dielectric constant of soil-water mixtures rises with increasing water content: from ε=4 in dry soils to ε~40 in saturated soils. Consequently, at microwave frequencies, the emission of the soil is linked to the soil water content by the dielectric constant. The emissivity of dry soils ($e(\theta, \phi)$~0.95) decreases with increasing water until soil saturates ($e(\theta, \phi)$~0.60; Schmugge et al., 1986). Nevertheless, other factors influence the emissivity of soils and must be considered:

- *Soil texture and density:* water in soils can be bounded to soil particles (bounded water) or allocated in the soil pores (free water). Bound water has little impact on the dielectric constant due to its less free molecular rotation in comparison with free water. Soils with the lowest percentages of bound water (sands; 2-3%) present higher dielectric constants than soils with the highest proportions of bound water (clay soils; 20-40%).

- *Roughness:* the soil roughness increases the soil emissivity, decreases the sensitivity of emissivity to soil moisture variations, and reduces the difference between the vertical (V) and the horizontal (H) polarizations.

- *Temperature:* the dependence of the dielectric constant on temperature is weak for the range of temperatures found in the Earth's surface. However, frozen soils present higher dielectric constants than unfrozen soils due to the different phases of water.

- *Salinity:* at L-band, salinity has a large effect on the imaginary part of the dielectric constant, but the effect of typical field salinity can be ignored as emissivity is not particularly sensitive to ε''_S (Jackson and O'Neill, 1987).

- *Wavelength:* the real part of the dielectric constant increases –and the imaginary part decreases- for longer wavelengths (i.e., lower frequencies).

In addition, note that the penetration depth of microwaves diminishes when the soil moisture increases. At L-band, it is generally considered to be about 4 cm in a wet soil, but it can be deeper (approximately up to 75 cm) in very dry conditions.

1.3.3. Vegetation effects

The vegetation layers attenuate and scatter the soil emission, and also add their own contribution. The most commonly used model to account for the effects of vegetation is the $\tau-\omega$ model:

$$T_{Bp} = e_p T_s \gamma + (1-\omega) T_v (1-\gamma) + (1-e_p)(1-\omega) T_v (1-\gamma)\gamma \,, \qquad (1.7)$$

where T_{Bp} stands for the brightness temperature either at the vertical or horizontal polarizations, e_p is the emissivity, T_s and T_v refer to the effective temperatures of soil and vegetation, respectively, ω is the single scattering albedo, and γ is the vegetation transmissivity. The first term of Eq. (1.7) represents the radiation of the soil when attenuated by the vegetation. The second term defines the upwards radiation directly emitted by the vegetation. The third term expresses the downwards radiation from the vegetation, once it is reflected upward by the soil, and then attenuated by the canopy.

The single scattering albedo (ω) describes the scattering of the soil emission within the vegetation layer, and is a function of the soil geometry. The transmissivity of the vegetation is a function of the VOD and the incident angle (θ):

$$\gamma = \exp(-VOD/\cos(\theta)) \ . \qquad (1.8)$$

The vegetation optical depth is related to the vegetation density through the vegetation water content (see Section 1.3.6), and is also linked to the frequency. Note that in this Thesis the vegetation optical depth is capitalized as VOD, while the term τ is a synonym which is also common in the literature.

Importantly, note that the SMOS and SMAP orbits were designed to pass over the Equator at 6 a.m. and 6 p.m. (see Section 1.4), when temperature gradients between soil and vegetation are minimized. Then, Eq. (1.7) can be simplified because $T_v = T_s$:

$$T_{Bp} = [e_p \gamma + (1-\omega)(1-\gamma)(1+(1-e_p)\gamma)] T_s \,. \qquad (1.9)$$

1.3.4. Retrieval approaches

Soil moisture retrievals need to take into account several of the geophysical variables involved in soil emission and vegetation attenuation. Different approaches have been used for this purpose, including empirical relationships between the variables and the radiative transfer equation (Wigneron et al., 2003), neural networks (Del Frate et al., 2003), and the inversion of geophysical model functions (e.g., Wigneron et al., 2007). The latter is the approach used for the SMOS and SMAP passive soil moisture retrievals. It is based on a geophysical model which considers important variables affecting the soil emission: soil moisture, soil roughness, soil temperature, scattering albedo, and vegetation optical depth. The number of geophysical variables which can be inverted is linked to the independent information provided by the brightness temperature measurements. This can be quantified using the Degrees-of-Information (DOI) metric (Konings et al., 2015), and depends on how many polarizations and/or incidence angles are observed, and on the number of satellite overpasses employed. The more information is used, the more variables of interest can be inferred, with the aim being principally on estimating SM and VOD. A cost function is defined considering the weighted square differences between the modelled and the observed brightness temperatures, and a minimization procedure is set-up to obtain the modelled brightness temperatures (and the parameters to be retrieved) which best match the brightness temperatures observed by the satellites' radiometer. The variables which are not estimated (e.g.,soil roughness, vegetation albedo, soil temperature, soil texture) are derived from ancillary information, in order to be used also in this process.

Main retrieval approaches applied for SMOS and SMAP are summarized here, with particular focus on the algorithms used for retrieving the datasets employed in this Thesis:

- *The SMOS multi-angular retrieval model:* it consists on the inversion of the L-band Microwave Emission of the Biosphere forward model (Wigneron et al., 2007), which is mainly based on the τ–ω function described in Eq. (1.7). The inversion allows obtaining the set of input variables (mainly SM, VOD, T_S, ω and roughness), and is based on the observed and modelled brightness temperatures at different SMOS incidence angles (Camps et al., 2005; SMOS Algorithm Theoretical Basis Document, 2007).

- *SMAP retrieval algorithms and the multi-temporal approach:* the SMAP single-look angle configuration limits the possibility to extract soil moisture and VOD information with just one acquisition using a single-channel approach (i.e., only vertical or horizontal polarization). Consequently, the SMAP single-channel baseline algorithm retrieves only soil moisture at every acquisition and relies on auxiliary information of VOD, albedo, and roughness. In particular, VOD is estimated from the Normalized Difference Vegetation Index (NDVI) climatology, and albedo and roughness are fixed parameters per land-cover (Chan, 2013). In contrast, the SMAP dual-channel baseline algorithm provides simultaneous retrievals of VOD and SM. Nevertheless, Konings et al., (2015) introduced the concept of DOI to argue that the information content on single look-angle polarized brightness temperatures at a single time step does not allow for an accurate retrieval of two variables. Based on DOI analysis, the Multi-Temporal Dual Channel Algorithm (MT-DCA; Konings et al., 2016) is proposed for the retrieval of soil moisture, VOD and effective scattering albedo using two consecutive overpasses of SMAP. The algorithm assumes that the vegetation conditions do not change among the consecutive overpasses. Note that a single, constant value of albedo is obtained for an entire study period. Konings et al. (2017a) show that the SMAP MT-DCA retrievals of VOD have very similar mean and seasonal amplitude in comparison with the SMOS multi-angular retrievals.

- *Land Parameter Retrieval Model (LPRM):* the LPRM (Owe et al., 2008) has been used to retrieve the VOD datasets at C- and X-bands used in Chapter 4 of this Thesis. The LPRM is based on the Microwave Polarization Difference Index (MPDI; Meesters et al., 2005) parameter, which is used to normalize for temperature dependence and is highly related to the dielectric properties of the emitting surfaces. The relationship between MPDI, VOD and ε (Owe and Van de Griend, 2001; Meesters et al., 2005) is the basis for the LPRM, and allows retrieving SM and VOD data.

1.3.5. Soil moisture

Soil moisture was recognized as an Essential Climate Variable (ECV) in 2010 (GCOS, 2010). It influences the exchange of water and heat between the soil surface and the atmosphere and, consequently, it is a key variable in the land-atmosphere interactions, with great relevance in energy, water and carbon cycles. Soil moisture has great importance for vegetation as it determines water availability for plants. Hence, changes in soil moisture can have great impact on forests, agriculture and ecosystems in general.

Global warming conditions may increase evaporation, decreasing soil water content and easing drought-prone conditions to happen. In addition, increase on the water evaporation from soils and oceans leads to a larger concentration of water vapor in the air. This is in turn reinforced by the fact that warmer air can contain more water vapor. As a consequence, the intensity of rainstorms may increase, which may augment the runoff and contribute little to moisten soils. Soil moisture information is essential to understand how precipitation is allocated into runoff, subsurface flows, and infiltration in soils.

At present, there are various microwave-based soil moisture products available. These are mainly obtained from (i) the SMOS and SMAP missions (L-band radiometers; see Section 1.4); (ii) the Advanced SCATterometer (ASCAT; C-band) on board of Metop satellites (Wagner et al., 2013); and (iii) the Advanced Microwave Scanning Radiometer 2 (AMSR2; C- and X-bands) on board of the Global Change Observation Mission 1st - Water (GCOM-W1; Kim et al., 2015). Importantly, longer soil moisture records are available from the ESA Climate Change Initiative (ESA-CCI) soil moisture dataset, which merges different past and present SM products to obtain a temporally and spatially consistent dataset ranging from 1978 to the present (Dorigo et al., 2015 and 2017).

1.3.6. Vegetation optical depth

The VOD accounts for the attenuation that vegetation exerts over the soil microwave emissions (see Section 1.3.4). VOD is proportional to the vegetation water content and can be used as a proxy of above-ground biomass (Ulaby and Long, 2014; Jackson and Schmugge, 1991). Some experimental studies have reported that VWC and VOD are linearly related through an empirical parameter b, which is dependent on frequency and polarization:

$$VOD = b \cdot VWC, \tag{1.10}$$

Also, it is generally assumed that VWC and VOD are tightly linked to the biomass of the life and woody parts of the plant, at least when considering relatively long-term averages of these variables (e.g., years). Consequently, VOD is used as a proxy of the carbon content of vegetation (see Section 1.5). In addition, VOD has been used to derive information on the vegetation hydric conditions and on the response of vegetation to droughts (Konings and Gentine, 2017; Konings et al., 2017b), and for crop yield assessment (e.g., Patton & Hornbuckle, 2013, Chaparro et al., 2018, and Chapter 5).

Nowadays, VOD data has been derived from several sensors at different microwave frequencies (Table 1.1). Also, Liu et al. (2011) have provided a merged long-term VOD dataset for the period 1987-2008. In this Thesis, VOD from SMAP (L-band) and from AMSR2 (C- and X-bands) will be used.

Table 1.1. The main sensors, satellites and frequencies for which VOD products are available.

Sensors	Satellites	Frequency
Scanning Multichannel Microwave Radiometer (SSMR)	Nimbus 7 and Seasat	C, X
Special Sensor Microwave Imager (SSM/I)	Defense Meteorological Satellite Program (DMSP)	Ku
Tropical Rainfall Measuring Mission's (TRMM) Microwave Imager (TMI)	Tropical Rainfall Measuring Mission (TRMM)	X
Advanced Microwave Scanning Radiometer (AMSR-E)	Aqua	C, X
Advanced Microwave Scanning Radiometer 2 (AMSR2)	Global Change Observation Mission 1st - Water (GCOM-W1)	C, X
Microwave Imaging Radiometer using Aperture Synthesis (MIRAS)	Soil Moisture and Ocean Salinity (SMOS)	L
Soil Moisture Active Passive (SMAP)		L

1.4. L-band satellite missions and products

During the last decade, the interest of the scientific community for L-band microwave remote sensing has increased notably. There are two main reasons for this. On one hand, L-band is sensitive to microwave emissions from the top 5 cm of soil (or even deeper for the driest soils). This is an advantage as compared to higher frequencies, which are only sensitive to the soil skin layer. On the other hand, the soil emission is less attenuated by vegetation at L-band than at higher frequency bands, allowing L-band microwaves to penetrate denser vegetation canopies. Theoretical as well as experimental studies support that L-band radiometry is the most appropriate technique for measuring the water content in soil and vegetation.

At the moment of writing, there are two L-band satellite missions in orbit: the SMOS (Kerr et al., 2010), launched by the ESA on November 2009, and the SMAP (Entekhabi et al., 2010), launched by the NASA on January 2015. Also, note that a third mission was operating an L-band radiometer: the Aquarius satellite, a joint effort of the Argentinian Comisión Nacional de Actividades Espaciales (National Comittee for Space Activities) and the NASA (Le Vine et al., 2010). It was launched on June 2010 and ceased its operations on June 2015. As the focus of this work is on SMOS and SMAP, these satellites and their main products are described in section 1.4.1.

The continuity of L-band missions beyond SMOS and SMAP is ensured by the Water Cycle Observation Mission from the Chinese Academy of Sciences, expected to be launched in 2022, and by the Copernicus Imaging Microwave Radiometer, which is a high priority candidate mission to Sentinel Expansion (MET Norway and CIMR Expert Team, 2018).

1.4.1. The SMOS mission and products

A. Characteristics of the mission

The SMOS satellite (Figure 1.2) is the first ever space mission dedicated to measuring surface SM and sea surface salinity (SSS) with an L-band radiometer. This satellite is part of the ESA's Living Planet Program, being its second Earth Explorer Opportunity mission. Although SMOS was initially planned as a 3-year mission, the satellite is still in good health after almost 9 years of operations and unique datasets of global L-band microwave measurements and derived parameters (SM, VOD and SSS) are currently available. SMOS orbits the Earth at a mean altitude of 758 km, following a sun-synchronous orbit. It passes at 6 a.m. and 6 p.m. through the Equator, and has a revisit time of 3 days. The satellite swath is about 1,000 km and its spatial resolution is of ~40 km.

The SMOS payload is the Microwave Imaging Radiometer using Aperture Synthesis (MIRAS). This is an innovative, Y-shaped instrument containing 69 antennas regularly distributed along its three arms. The brightness temperature retrievals are obtained using a 2-D interferometric technique: the cross-correlation among the measurements from all the possible combinations of pairs of antennas is computed, and using a Fourier synthesis process, a brightness temperatures image is obtained. Importantly, MIRAS estimates L-band soil emissions at different incidence angles (from 0 to 65°), and using dual- and full-polarimetric modes. The polarimetric and multi-angular SMOS characteristics allow obtaining multiple T_B measurements per point and retrieve more than one variable at the same time (i.e., SM and VOD can be inverted simultaneously; Kerr et al., 2012).

Figure 1.2. The SMOS satellite in orbit (artist's view). Source: ESA, 2009.

B. SMOS products

The original products of the SMOS mission are classified in different levels (L) as follows:

- L0: it consists of the sensor's raw data.
- L1: it is divided in three steps. First, L1A products are the calibrated visibilities (i.e., cross-correlations) grouped as snapshots. Second, L1B products are snapshots of radiometrically corrected and calibrated brightness temperatures. Third, L1C products are georeferenced swath maps of brightness temperatures. These products are produced separately for sea and land applications. Level 1C data are inputs for the SMOS baseline retrieval algorithm (Kerr et al., 2012).
- L2: SM and SSS maps at ~40 km resolution. The products can be resampled at finer scales. This is the case of the ESA L2 SM product, which is a swath-based product provided in the Icosahedral Snyder Equal Area (ISEA) 4h9 grid with a gridding of 15km. VOD information can also be derived at this step (Kerr et al., 2012).
- L3: L3 datasets filter and merge L2 swath data into global maps of SM and VOD and are provided in a regular grid (e.g., the Equal-Area Scalable Earth Grid 2; EASE2) and in standard format (e.g.,netCDF files; BEC, 2018).

- L4: L2 or L3 datasets with enhanced properties due to the addition of auxiliary variables. This includes downscaled datasets such as those described in Section 1.4.1.C.

Note that the SMOS L2/L3 SM products have been extensively validated (e.g., Albergel et al., 2012; Dente et al., 2012; Kerr et al., 2012; Sánchez et al., 2012; Bircher et al., 2012 and 2013; Petropoulos et al., 2014; Rahmoune et al., 2014; González-Zamora et al., 2015; Polcher et al., 2016). In addition, recently another version of SM and VOD retrievals has become available: the SMOS-IC product. It defines different values of albedo and surface roughness than the L2 and L3 products, and is designed to be more independent of ancillary information. The application of the SMOS-IC VOD dataset to vegetation studies is promising (Fernández-Morán et al., 2017; Brandt et al., 2018).

C. L4 high resolution soil moisture products

SMOS L2/L3 soil moisture maps are provided at spatial scales which are too coarse to serve local or regional applications such as those proposed in this Thesis. In order to fill this gap, pixel downscaling or data disaggregation is a recognized modeling framework to improve the spatial resolution of available surface soil moisture satellite products (Peng et al., 2017). A number of studies to improve L-band SM resolution have emerged using different input ancillary data and different linking models. Several downscaling procedures take profit of optical and infrared information (Merlin et al., 2008, 2010 and 2013; Piles et al., 2011a, 2014 and 2016; Sánchez-Ruiz et al., 2014; Portal et al., 2018). Others merge passive and active (i.e., radar) data, which is the case of algorithms taking leverage of both the active and passive SMAP sensors (Das et al., 2011 and 2014). Nevertheless, since the SMAP radar ceased operations, the combination of SMOS/SMAP L-band data with C-band radar backscatter from Sentinel-1 is envisaged as a feasible solution (Rüdiger et al., 2016). Also, downscaling methods can be based on physical models (e.g., Merlin et al., 2005 and 2013), on semi-empirical models (e.g., Piles et al., 2014), and others (Peng et al., 2017).

The soil moisture datasets used in this Thesis are L4 high-resolution (1 km) SM products (BEC, 2018), which are based on the algorithm described in Piles et al. (2014). This algorithm uses a semi-empirical approach combining SMOS data with LST and NDVI information, both estimated with the Moderate Resolution Imaging Spectroradiometer (MODIS; see NASA, 2018), in order to obtain the finer scale (1 km) SM as follows:

$$SM_{HR} = a_0 + a_1 \cdot LST_N + a_2 \cdot NDVI_N + \frac{a_{3i}}{3}\sum_{i=1}^{3} T_{Bh\theta_i N} + \frac{a_{4i}}{3}\sum_{i=1}^{3} T_{Bv\theta_i N} \tag{1.11}$$

where SM_{HR} is the resulting SM at 1 km resolution, LST_N and $NDVI_N$ are the normalized LST and NDVI, respectively, and $T_{Bh\theta_i N}$ and $T_{Bv\theta_i N}$ are the normalized brightness temperatures for the θ_i incidence angles at horizontal and vertical polarizations, respectively. The incidence angles used are 32.5°, 42.5° and 52.5°. Importantly, the NDVI information is a 16-day averaged product, for which the time window length reduces the probability of working with cloud masked information. In contrast, LST is obtained daily and cloud masking is relatively frequent, impeding the high resolution SM data to be retrieved in some cases. To avoid the presence of clouds masking the L4 retrievals, a so-called “cloud-free” product has been developed in which ERA-Interim modelled LST data from the European Centre for Medium Range Weather Forecasts (ECMWF; ECMWF, 2018) are also used when clouds are masking the MODIS LST information. Recently, new work has improved the downscaling procedure including a spatially adaptive moving window (Portal et al., 2018) and substituting (in the cloud-free product) the ERA-Interim LST for the ERA5 LST (the new LST reanalysis product from ECMWF).

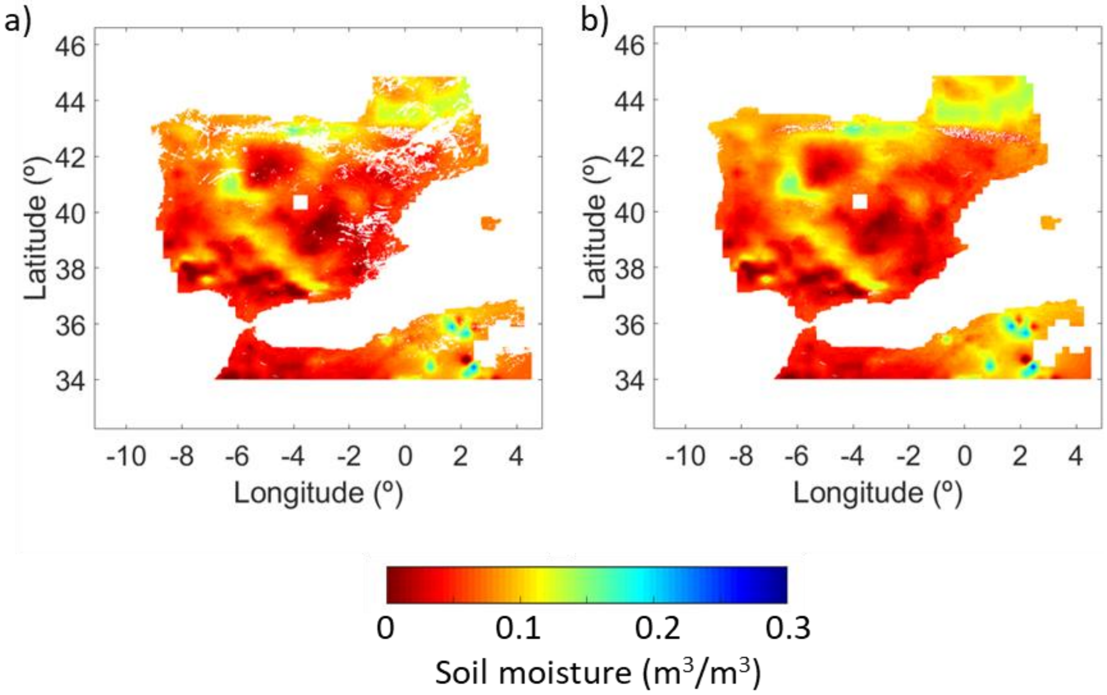

Figure 1.3. High resolution (1 km) soil moisture products used in this PhD Thesis (10th March 2015; Iberian Peninsula). (a) SMOS-MODIS product, (b) SMOS cloud-free product. The empty squared areas in the two images (i.e., in central Spain and in northern Africa) are due to RFI filtering.

The BEC, a joint initiative of the Spanish Research Council (CSIC) and the UPC, provides the SMOS-derived products for scientific applications. At the time of writing, the BEC offers the following L4 high resolution soil moisture products for the Iberian Peninsula (BEC, 2018):

- The high resolution (HR) SMOS-MODIS, described above and applied in Chapter 3 in this thesis (Figure 1.3a).

- The HR near real time (NRT) SMOS-MODIS product (Piles et al., 2013) takes profit of immediate acquisitions of MODIS data, which are obtained and provided by the Remote Sensing Laboratory at the University of Valladolid.

- The HR SMOS cloud-free product which uses ERA-Interim LST data as described above (Figure 1.3b). This product is applied in Chapter 2 of this Thesis.

The enhanced HR SM dataset based on Portal et al. (2018) will be operationally available in the BEC website in a near future. Also, note that BEC offers a fire risk L4 product which is developed in Chapter 2 of this Thesis.

1.4.2. The SMAP mission and products

A. Characteristics of the mission

The SMAP mission (Figure 1.4) was developed in response to the United States National Research Council's Decadal Survey, and is devoted to measure the surface soil moisture and the thaw/freeze soil state (National Research Council, 2007). The SMAP platform carries a radar and a radiometer, with both instruments sharing a conically-scanning reflector antenna, which is designed as a deployable light-weight mesh in order to avoid size and weight problems due to its large diameter (6 m). Although the radar instrument failed five months after launch, the mission continues providing information on soil moisture and soil state conditions using the passive instrument. SMAP orbit is sun-synchronous, at an altitude of 685 km. The satellite has a revisit time of between 2 and 3 days, depending on the latitude, and a swath of 1,000 km. The resolution of its real aperture radiometer is of approximately 40 km. Soil emission measurements are obtained at a constant incidence angle of 40°, using both dual-polarization and full-polarimetric modes.

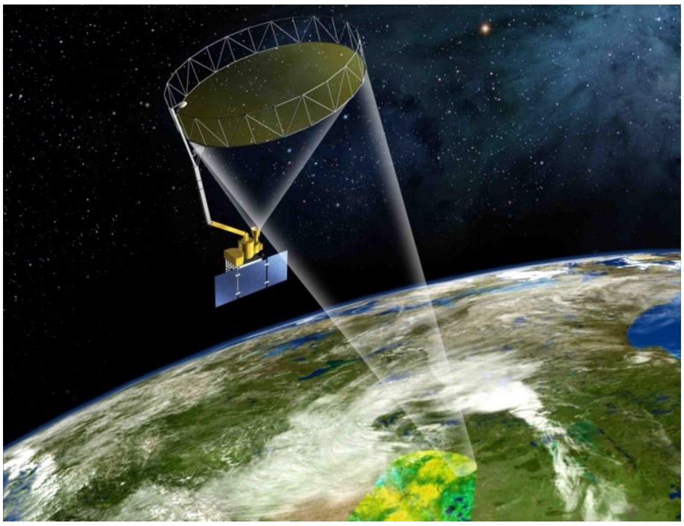

Figure 1.4. The SMAP mission in orbit (artist's view). Source: NASA, 2014.

B. SMAP products

The classification of SMAP radiometer products is similar to that for SMOS and also divided in different levels (L). Here, these products are briefly explained. More detailed information can be found in JPL (2018a):

- L0: it consists of the raw instrument's data.
- L1A_Radiometer: it is the radiometer data for each half orbit in time order and considering vertical and horizontal polarizations.
- L1B_TB: this level provides calibrated estimates of geolocated brightness temperatures in time order.
- L1C_TB: it consists of the half orbit L1B_TB data resampled to a 36 km grid (EASE2).
- L2_SM_P: TBs allow obtaining these half orbit SM products, which are provided in the 36 km EASE2 grid.
- L3_SM_P: this L3 product contains daily composites of global SM data resampled at 9 km and 36 km scales using an EASE2 grid.
- L4_SM: advanced products which include surface and root-zone soil moisture (RZSM) data resampled at 9 km gridding.

VOD information can also be retrieved at levels L2 to L4. In Chapters 4 and 5 of this PhD Thesis, the SMAP VOD datasets used are retrieved using the MT-DCA algorithm, and provided at 9 km sampling. Figure 1.5 shows an example for this product.

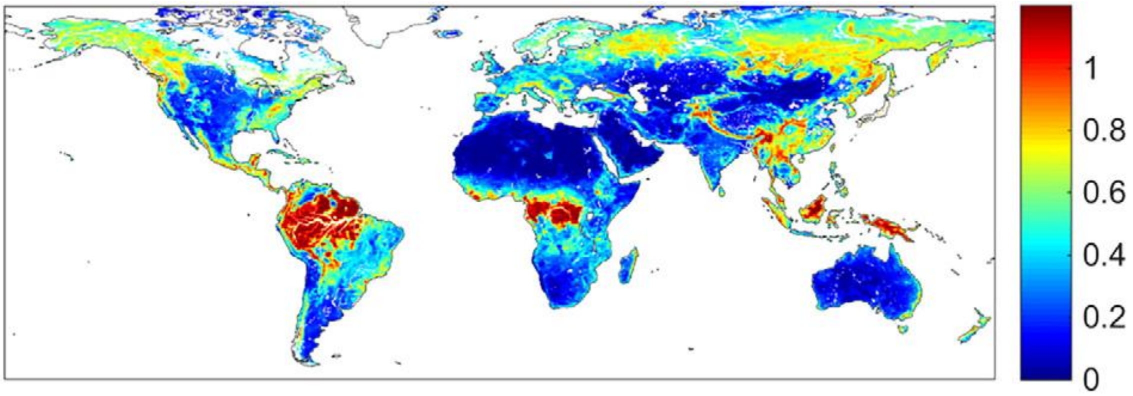

Figure 1.5. Mean SMAP VOD (9 km gridding; period April 2015-March 2016) retrieved using the MT-DCA. From Konings et al. (2017).

1.5. Applications of L-band land products for society

L-band land products can prove useful for a wide range of applications within environmental sciences as well as for monitoring essential resources (Brown et al., 2013; Petropoulos et al., 2018). In the last years, they are becoming of great interest for society, in particular through the development of operational and near real time products. In that sense, the synergy between L-band data and several monitoring and forecasting tools (e.g., meteorological and hydrological models, forest and crop exhaustive databases, or other EO datasets) has great potential for developing such products. This section reviews current and potential L-band applications over land, and their synergies with other datasets.

1.5.1. Weather, hydrology and flood forecasting

Weather forecasts ranging from mesoscale to global scale are addressed using numerical weather predictions (NWP). SMOS and SMAP data fit the spatial resolution requirements to be used as input variables in these models. In these tools, soil moisture information is appropriate to initialize the land component, as it reduces uncertainties occurring when moisture is estimated by auxiliary variables (i.e., temperature and relative humidity; Drusch, 2007). Nevertheless, the spatial resolution of NWP models is expected to improve in the near future. In such case the applicability of downscaled moisture information such as the BEC L4 SM products should be studied. Complementarily to this, microwave SM data has been used to improve or correct precipitation estimates from NWP and EO satellites, which present a limited accuracy if compared with *in situ* measurements (see Brocca et al., 2016 for an example). The enhanced precipitation data should be used, for instance, to estimate river discharge or surface fluxes in large watersheds.

At regional and local scales, the focus has been put mainly in flood forecasting. The availability of SM data from EO satellites provides important information to enhance the current flood prediction systems. In that sense, Wanders et al. (2014) have studied the capacity of microwave SM information from SMOS, ASCAT, and AMSR-E to improve flood predictions of the European Commission’s European Flood Awareness System (EFAS). To this purpose, the authors have integrated the SM datasets within the LISFLOOD hydrological model (which is the core of the EFAS system). Results show that the accuracy of flood forecasts improves and that time errors in flood prediction decrease. In addition, the applicability of SMOS SM data to assess flood risks has been explored in Morocco (Kerr, 2014). Although the results in this field have been satisfactory till now, the spatial and temporal resolution of SM need improvement in order to predict flash-floods often occurring at small scale basins in extremely short time periods. In that sense, SM products with enhanced spatial resolution should be appropriate. In contrast, the 3-days revisit time over small areas remains as a limitation.

1.5.2. Drought and associated hazards

Drought conditions are usually monitored using precipitation-derived indices. Complementarily to this approach, L-band soil moisture data offers the possibility to quantify water depletion in soils, which has a direct impact on vegetation. In that sense, Scaini et al. (2015) have shown good correlation (r >0.6) between SMOS L2 soil moisture anomalies and two common drought indices: the Standard Precipitation Index (SPI) and the Standard Precipitation Evapotranspiration Index (SPEI). These correlation values are found for short time scales (≤1 month), and are smaller than those found between SPEI or SPI and the *in situ* SM values in the region. The study has been carried out in the Soil Moisture Measurement Stations Network (REMEDHUS network; Duero Basin, Spain).

Droughts, as well as record-breaking heat waves, have large impacts on vegetation, particularly affecting vegetation conditions and its biophysichal mechanisms, endangering crop production, and triggering wildfires. Remotely-sensed soil moisture data is a potential tool to detect drought conditions posing a risk of wildfires. Chapter 2 in this Thesis reviews and explores the applicability of microwave-derived SM information for fire risk assessment, taking profit of a large and consistent fire database from the European Forest Fires Information System (EFFIS) to study the soil state before fire occurrences in the Iberian Peninsula. Surface soil moisture is a variable linked to weather conditions in general, and to the dead fuel water content in particular. Concerning to VOD, it is related to the life vegetation water content, which is of great importance in fire propagation. In that sense, Forkel et al. (2017) use C-band VOD as a proxy of biomass (i.e., fuel amount) and vegetation hydric state (i.e., fuel dryness) to improve predictions of burned area and fire activity at a global scale.

Importantly, drought conditions may lead to forest decline episodes. In this Thesis, Chapter 3 takes profit of one of the few forest yearly monitoring programs to explain forest decline as a function of SMOS soil moisture data and regional climate and weather information. Concerning VOD, to author's knowledge, no work has been developed exploring its capacities to detect forest decline. Nevertheless, Konings and Gentine (2017) show an interesting approach to explore vegetation isohydricity (i.e., the amount of stomatal regulation over the leaf water loss) from SMAP VOD data. Isohydricity determines the behavior of vegetation under hydric stress.

Also, droughts and high temperatures reduce the GPP of vegetation thus reducing the carbon sink (Ciais et al., 2005; Barriopedro et al., 2011). Teubner et al. (2018) have shown that absolute values of VOD and changes on VOD (ΔVOD) are correlated with GPP globally, and suggest that VOD at different frequencies (L-, C-, and X-bands) could potentially be used for GPP estimates. In addition, Sánchez-Ruiz et al. (2017) have applied L-band SM data as a water stress factor to track light use efficiency and to assess GPP in water-limited ecosystems.

1.5.3. Monitoring carbon stocks

Long records of VOD information allow monitoring changes in vegetation carbon stocks, providing highly valuable information to estimate the global carbon trends and fluxes. This has been mainly addressed using C-, X- and K-bands VOD (e.g., Liu et al., 2015; Van Marle et al., 2016; Brandt et al., 2017). L-band VOD records are still short and the first study providing carbon trends in vegetation using this microwave frequency is recent: Brandt et al. (2018) report carbon losses in African drylands' vegetation, and explain that L-band VOD shows not saturation at high carbon densities. Chapter 4 in this Thesis and Chaparro et al. (*in review*) provide further analysis on the capacity of L-band VOD to estimate carbon stocks, comparing it with higher frequency bands and with carbon maps derived from airborne LiDAR (Light Detection and Ranging) measurements.

The carbon cycle is tightly coupled to the water cycle (see Sippel et al., 2018 for a detailed review on this topic). For this reason, information on soil moisture is also important to improve our understanding on the carbon cycle. Scholze et al. (2016) analyse the constraint of SMOS L3 SM data on carbon fluxes within the Carbon Cycle Data Assimilation System. The authors demonstrate that the SMOS product contributes to reduce the uncertainties on the net primary production, and changes the carbon flux pattern. Also, including L-band VOD as an additional observation within this model is promising. Hence, L-band SM and VOD data are of great interest to carbon cycle studies.

1.5.4. Agriculture

In croplands, soil water content and vegetation hydric state determine production and are crucial for food security. Agricultural droughts endanger crop yields and must be monitored. In that sense L-band SM data have been applied to compute the Soil Water Deficit Index (SWDI), an agricultural drought index defined by Martínez-Fernández et al. (2015). The SMOS-based SWDI has shown good agreement with other indices monitoring agricultural droughts, the Crop Moisture Index and the Atmospheric Water Deficit index, in the Duero Basin (Spain) and in northeastern Brazil (Martínez-Fernández et al., 2016; Paredes-Trejo and Barbosa, 2017). The same index has shown good capacity to report drought conditions in the United States using SMAP SM data (Mishra et al., 2017; Liu et al., 2017). Also, the applicability of L-band SM to monitor agricultural droughts has been shown by Sánchez et al. (2016) building the remote-sensing based Soil Moisture Agricultural Drought Index. This index takes profit of the inverse relationship between SM, LST, and vegetation conditions (e.g., measured by the NDVI), and has been applied recently at a global scale (Sánchez et al., 2018). Finally, the Agriculture and Agri-Food Canada (AAFC) uses SMOS SM to derive crop-related applications (e.g., drought risk assessment, flood prediction, and food production estimation). AAFC is working to also include SMAP data to this system (Champagne et al., 2015; AAFC, 2016).

Despite satellite surface moisture has proven to be useful to detect drought conditions in croplands, agricultural droughts are generally defined in the root-zone of soils (~1 m depth). RZSM can be modelled from surface retrievals (Ceballos et al., 2005; Albergel et al., 2008; Renzullo et al., 2014; Martens et al., 2017; Pablos et al., 2018) and be used for agricultural applications. For instance, Chakrabarti et al. (2014) have improved yield predictions in a Brazilian agricultural area assimilating 1-km downscaled SMOS SM data into a crop growth model, estimating both surface SM (0 to 5 cm) and RZSM (5 to 120 cm). Also, vegetation information from spectral indices (e.g., NDVI) reports the vegetation vigor, which is linked to the water content of the soil root-zone. However, such indices present a lagged response to soil drought conditions (Schnur et al., 2010; Sánchez et al., 2016).

Microwave EO data could also improve irrigation assessments. Satellite SM has been used to account for irrigation in different studies (e.g., Ines et al., 2013; Qiu et al., 2016; Singh et al., 2016). Although irrigation techniques need higher spatial resolution (at least <100 m) than the currently available from microwave remote sensing, it is feasible to generally approximate crop water requirements at coarse scales. On one hand, monitoring soil moisture deficit (SMD) can be useful for irrigation schedule. In that sense, in the United Kingdom the Met Office provides SMD information at 40 km resolution using meteorological data. The SMD data can be improved using SMOS SM information in combination with a land surface model (Srivastava et al., 2013). On the other hand, estimating the RZSM and evapotranspiration (ET) is another approach to account for the crop water requirements. Estimating ET involves a modelling approach using SM or combining SM and VOD information (Martens et al., 2016).

Importantly, VOD has great applicability to agriculture due to its relationship with water content, which can be used to monitor vegetation hydric state, as well as vegetation phenology and biomass. In that sense, L-band VOD has been applied to study crop phenology in different regions of the world (Hornbuckle et al., 2016; Piles et al., 2017) and to estimate corn and soy yields in Iowa, USA (Patton and Hornbuckle, 2013). Chapter 5 in this Thesis and Chaparro et al. (2018) apply SMAP VOD to derive seasonal metrics for crop yield estimation in north-central United States. Chapter 5 also provides more detailed review on VOD applicability to monitor vegetation phenology and crop yields.

In addition, note that one of the objectives of the SMAP mission is to contribute to the predictions of the Famine Early Warning Systems Network (FEWS-NET, 2018). Right now this is only based on weather forecasts, and the future application of L-band SM and VOD retrievals should be studied.

1.5.5. Other applications

Several applications of L-band satellite data over land have been studied in this Thesis, and a review on the studied fields has been provided above. Nevertheless, the number of potential applications and derived research paths which could benefit and/or arise from the use of microwave remote sensing observations (including L-band) is very large (Brown et al., 2013; Petropoulos et al., 2018). A succinct review on some of these applications/paths that have not been covered by this Thesis is provided hereafter.

Concerning land applications, there is some evidence showing that SM data could be used to anticipate conditions prone to the outbreak of desert locust (*Schistocerca gregaria*) plagues, a species which needs moist soils and vegetation blooms to reproduce (Gómez et al., 2017; Escorihuela et al., 2018). Similarly, the presence of flooded areas and moist conditions may favour the expansion of mosquito-borne diseases (e.g., malaria), and SM information can contribute to detect regions under epidemiological risk. Also, the sensitivity of microwave measurements to water contents can be applied to monitor standing water (e.g., inland surface waters extent), as well as to predict risks after floods (e.g., landslides; Brocca et al., 2012). In addition, SM is also a useful variable to study biodiversity, as it is correlated with species richness in some habitats. This has been demonstrated both for *in situ* soil moisture measurements (Litaor et al., 2008) and for EO SM data from the European Remote Sensing satellites (ERS-1 and 2; Sass et al., 2012).

Finally, other land applications where L-band products could play a significant role include transportation of nutrients and contaminants, runoff simulations, monitoring water reservoirs, improving greenhouse gases' emission assessments, and monitoring habitat conditions for animals and plants, among others (see Tebbs et al., 2016).

1.6. Thesis outline

This PhD Thesis presents a suite of environmental applications in which L-band microwave satellite observations are shown to provide new perspectives to the study of vegetation status and dynamics within a context of threats and challenges associated to present environmental changes. The work is organized in the following chapters:

- **Chapter 1** explains the motivation of this work, presents the main concepts of microwave radiometry, and reviews applications of microwave remote sensing for vegetation, with specific focus on L-band missions and products.

- **Chapter 2** studies the soil conditions prior to fire occurrences in the Iberian Peninsula. It provides a fire risk model for the region using SMOS SM and LST data to estimate the potential extension of wildfires. Also, this chapter reviews the applicability of other EO products for fire risk assessment, to put in context the relevance of satellite SM information in this field.

- **Chapter 3** explains the occurrence of forest decline episodes in Catalonia as a function of climate variables, SMOS SM data, and summer drought conditions. The interaction among the studied variables and the affected species is analyzed to understand the impact of drought on each particular tree species.

- **Chapter 4** presents a comparative analysis of the sensitivity of different VOD products (at L-, C-, and X-bands) and the Enhanced Vegetation Index to the above-ground carbon density (ACD) of vegetation. The study is conducted in Peru, southern Colombia and Panama, and it is mainly focused on tropical forests. It quantifies the relative contribution of ACD and forest cover proportion to the VOD and EVI signals.

- **Chapter 5** provides seasonal SMAP VOD metrics to model crop yields in the United States Corn Belt. The effect of crop heterogeneity on the accuracy of these estimates is studied, and the capacity of VOD to provide yield estimations for particular crops is assessed.

- **Chapter 6** provides the main conclusions of this PhD Thesis, lists the original contributions, and suggests future work to enhance the proposed applications.

1.6. Thesis outline

2

The role of soil moisture and surface temperature on wildfires in the Iberian Peninsula

Abstract

This chapter analyses the applicability of soil moisture data for fire risk assessment over the Iberian Peninsula. Firstly, this work provides a review of the variables needed in fire risk prediction tools, and puts in context the importance of soil moisture in this field. Secondly, it studies the soil conditions prior to fire outbreaks in the Iberian Peninsula for the period 2010-2014. The study uses SMOS soil moisture data and surface temperature information to capture drought episodes that can increase the risk of fires, and to determine thresholds of moisture and temperature that condition the fire spread. Results have been used in operational applications for fire prevention in the province of Barcelona. Finally, this chapter provides a linear regression model estimating the potential propagation of fires as a function of soil surface conditions, land cover, ecoregions, and months when fire outbreaks occur. The model explains 65% of potential burned area variability, and it has an overall accuracy of 83%. This suggests that the proposed methodology is valid for fire risk prediction in the region.

2.1. Introduction

Wildfires are a multifaceted phenomenon involving interactions between human and environmental factors. A comprehensive framework to assess wildfires causes and risk should focus on anthropogenic causes, vegetation characteristics, topography, and weather. First and foremost, humans must be considered as the main component affecting wildfires behaviour. Human activities (e.g., land clearing, agriculture, resettlements, negligence, or arson, among others) are principal causes of fire ignition in most areas of the world. For instance, 95% of fires in the Mediterranean regions are directly or indirectly caused by humans (FAO, 2007, pp. 111-118). Moreover, humans change the availability, continuity, and distribution of fuels as a result of land use changes, sprawl of urban areas, and systematic fire extinction. Consequently, most wildfires burn in patchy landscapes where forest, agricultural, and urban zones intermingle, representing a risk for human lives and beings. In particular, the expansion of wildland–urban interface (WUI) areas and the fuel accumulation due to systematic suppression of fires increase these risks (Cohen, 2008; Syphard et al., 2008). Importantly, vegetation, topography, and weather conditions strongly influence fire behaviour and extent (Syphard et al., 2008; Verdú et al., 2012). The abundance, distribution, and structure of vegetation are critical in wildfire ignition and spread and respond to natural and anthropogenic factors. Locally, topography influences climate and vegetation characteristics, fuel moisture, and wind effects (Whelan, 1995, pp. 29-44). Finally, weather determines the fire environment and the ignition conditions (Padilla and Vega-García, 2011). In particular, wind is the most important driver of fire spread (Whelan, 1995, pp. 29-44). Temperature and rainfall are crucial for fire ignition and propagation, as they condition the water availability for vegetation, and the moisture of dead fuels. In that sense, climate change could lead to more frequent and intense droughts in some regions (e.g., the Mediterranean basin) and to extreme temperature events, which facilitate drying and combustion of vegetation fuels. As a result, fire seasons have lengthened, and the area affected by anomalous long exposure to weather situations posing a risk of fire has increased globally (Oppenheimer et al., 2014; Jolly et al., 2015).

Due to the complexity of fires causality, assessing fire risk needs of timely and regular information on a wide range of variables, at different temporal and spatial scales. Nowadays EO satellites fulfil these requirements, providing large amount and diversity of data applicable to forest fires prevention. Nevertheless, most common fire risk indices are meteorological indices based on estimates of fuel moisture conditions, which, in turn, are derived from modelled and *in situ* information of temperature, precipitation, and wind. Instead, developing new fire risk assessment tools based on satellite data is still a work in progress, especially regarding those variables linked to the fuel moisture content, such as soil moisture.

In this chapter, the potential contribution of remotely sensed soil moisture data to fire risk prediction tools is assessed, and a fire risk model in part based on SMOS-derived soil moisture information is built. The chapter is structured as follows: Section 2.2 provides a review on fire risk assessment from remote sensing derived variables and fire risk meteorological indices. This section is mainly focused on the Copernicus programme, a European Union initiative aiming to monitor the Earth. Section 2.3 reviews previous research applying remotely sensed soil moisture in fire risk assessment. Sections 2.4 to 2.9 report the study of moisture and temperature conditions previous to forest fires occurrences in the Iberian Peninsula, and detail the development of new fire risk indices based on SMOS SM and LST data from the ECMWF, which is the main objective of this work. Conclusions for this chapter are explained in Section 2.10.

2.2. An approach to fire risk assessment from the Copernicus programme

2.2.1. An overview of the Copernicus Programme: monitoring the Earth

The Copernicus Programme aims to monitor the Earth from satellite, airborne, and *in situ* data. It provides a complete range of products from different thematic areas and at different spatial scales. Data are classified into six main services: land, marine, atmosphere, climate change, emergency management, and security. The Copernicus land service permits a multi-scalar approach as it is structured in the local, pan-European, and global components. These components provide key data for fire risk studies, such as land cover and land use changes, topography, vegetation conditions, and soil moisture and surface temperature. The climate change service provides meteorological information through the ECMWF. Finally, concerning to the Copernicus emergency management service, it includes the EFFIS and the Global Wildfire Information System (GWIS), which provide fire risk forecasting and fire monitoring services. Hence, the structure of the Copernicus programme is particularly consistent with the comprehensive approach needed in fire risk assessment. More details on this structure and these products are provided in Figure 2.1, and examples of applications using Copernicus datasets are reviewed in Sections 2.2.2 to 2.2.5.

2.2.2. Mapping land cover and land use from space: understanding fire-human interaction and fire behaviour

Satellite-derived land cover and land use data provide information on fuel types and their coexistence with human activities. This is required to evaluate fire ignition and propagation risks threatening human lives and beings, as well as agricultural and environmental services.

In WUI areas, the anticipation to fire danger situations is crucial to protect human populations and their economic activities. In that sense, the Urban Atlas (Copernicus, 2018a) provides an accurate picture of urban sprawl in the fringe of urban zones. It contains land cover and land use data for ~700 European cities (>50,000 inhabitants) and their surroundings. The Urban Atlas is built from very high-resolution satellite imagery (mainly from the “Satellite Pour l'Observation de la Terre – 5”; SPOT-5), which enhances its applicability in fire prevention. For instance, it has been used to detect urban structures, which could be endangered under extreme fire conditions (Mitsopoulos et al., 2015).

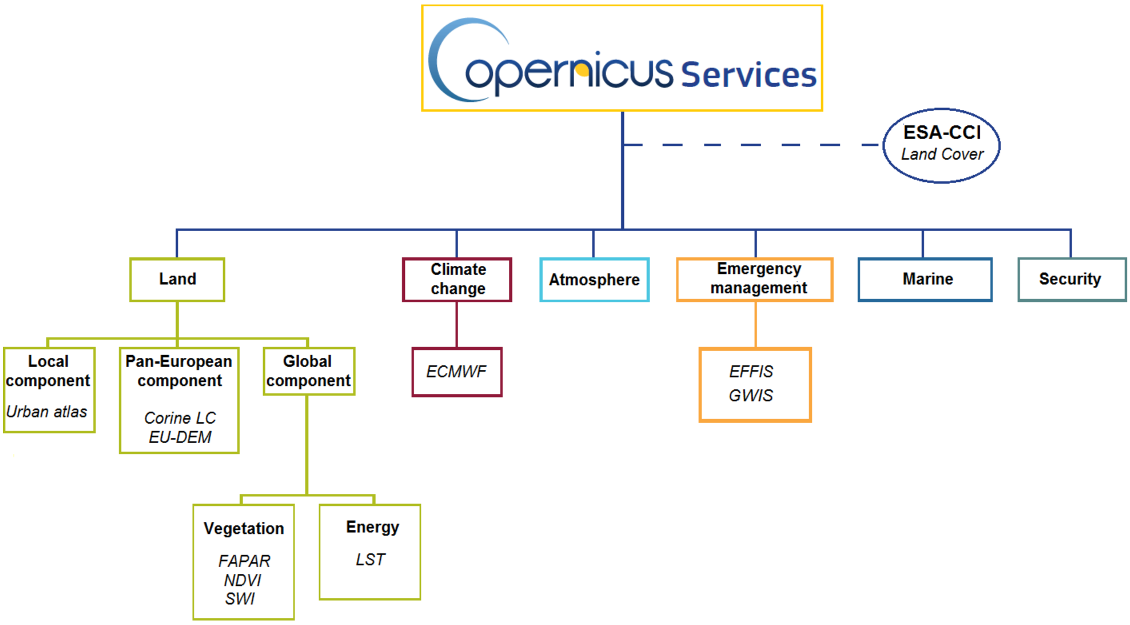

Figure 2.1. Copernicus programme services. Services, datasets and systems which can contribute to fire prediction applications are detailed, and those specifically mentioned in Sections 2.2.2 to 2.2.5 are written in italics. Note that the ESA-CCI is a project linked to Copernicus but not included in any particular service (dashed line). Adapted from Copernicus, 2018b.

Beyond urban zones, the density of human population decreases, and agriculture and natural vegetation lands predominate. Consequently, the number of fire ignitions is lower but, in contrast, fires may propagate throughout large areas. They can affect different vegetation covers and land uses, which can be classified from satellite-derived land cover maps. At a global scale, the ESA–CCI Land Cover supplies land cover data at 300 m resolution, with accuracy between 70.8% and 74.4% (ESA, 2016). In Europe, the Corine Land Cover map contains harmonized data of land cover and its changes since 1990. This information is used to estimate the effect of land covers on fire spread. Particularly, it has been found that larger fires burn coniferous forests and scrublands, whereas smaller ones burn broad-leaved forests, agroforestry areas, crops, and urban zones (Bajocco and Ricotta, 2008; Verdú et al., 2012).

2.2.3. Digital Elevation Models account for topography effects on fire behaviour

Topography influences the local vegetation distribution and climate conditions due to altitudinal gradients, and affects the direction and speed of fire propagation (Whelan, 1995, pp. 29-44). Importantly to the scope of this chapter, topography influences solar radiation, which conditions moisture content of fuels and the vegetation density. Topography is considered in fire risk modelling using digital elevation models (DEM) from national databases (e.g., Verdú et al., 2012). Nevertheless, a European DEM (EU-DEM) is now available (Copernicus, 2018b). It is based on the fusion of different DEM sources, including the Global

Digital Elevation Model from the Advanced Spaceborne Thermal Emission and Reflection Radiometer (JPL, 2018b). The application of EU-DEM in fire risk studies is still a matter of future work.

2.2.4. Spaceborne-derived measurements of fuel and soil conditions

Together with human-related factors, vegetation types, topography, and meteorology, fuel loads and vegetation hydric status are main factors in fire risk assessment. They condition the availability and flammability of fuels, and are usually assessed with optical and near infrared vegetation indices. For instance, Knorr et al. (2011) found that under homogeneous fire-prone meteorological conditions in Greece, large fires occurred majorly in areas with high fuel loads (i.e., vigorous vegetation). In that case, these areas were detected by high values of the fraction of absorbed photosynthetically active radiation (FAPAR), which is related to GPP.

Vegetation indices, such as the NDVI, have also been used as indicators of vegetation water stress in fire risk studies (Wang et al., 2013). Actually, NDVI has been applied to estimate live fuel moisture content (FMC), a crucial variable in fire ignition and propagation (Chuvieco et al., 2014). Initially, the link between NDVI and FMC was established for grasslands (Hardy and Burgan, 1999). However, weak correlations between both variables were obtained in scrublands and forests (Chuvieco et al., 1999). To bridge this gap, the combined use of NDVI and LST was applied to estimate FMC and associated fire risk (Chuvieco et al., 2004). Note that an increase in LST can be interpreted as an increase in vegetation water stress and/or soil surface dryness (Chuvieco et al., 2004; Li et al., 2016).

Consequently, the study of the soil surface state is paramount to detect dry conditions increasing the risk of fire. LST and SM are directly related to live FMC and also to the moisture content of dead fuels (e.g., litter), which is as well a main driver of fire propagation (Chuvieco et al., 2014). SM and LST are variables which can be estimated at global scale using space borne sensors. Satellite-derived LST datasets can be obtained from several platforms (see Tomlinson et al., 2011 for a review, and Copernicus 2018b), but present the disadvantage of cloud masking. In contrast, modelled surface temperatures such as those provided by ECMWF have a continuous coverage, which will be necessary for the development of fire risk estimates presented in this chapter. Concerning SM state, Copernicus provides the Soil Water Index (SWI) as the percentage of water in the soil at different time lengths. This is currently derived from MetOp C-band radar backscatter measurements. MetOp satellites are planned to provide continuous data complementing the quantitative SM estimates from SMOS and SMAP missions (Naeimi et al., 2009).

2.2.5. Meteorological fire risk indices and burned area mapping

The Copernicus emergency management service encompasses the EFFIS and GWIS systems. EFFIS is devoted to support the European Union environmental policies providing a wide range of information related to fire (San-Miguel-Ayanz et al., 2012 and 2013). GWIS is the extension of EFFIS at a global level, and is a joint initiative of Copernicus and the Group on Earth Observations (GEO, 2018). Among the information provided by these systems, the burned area product and the fire risk forecast are within the scope of this chapter.

The burned area mapping is based on the MODIS images at 250 meters resolution. Burned areas larger than 30 ha can be mapped, although smaller fires may be included if they are detected (San-Miguel-Ayanz et al., 2012). The fire risk evaluation is based on the well-known Canadian Fire Weather Index (FWI; Van Wagner, 1987). This index uses meteorological data (temperature, relative humidity, wind, and rain), which are applied to derive the six components of the FWI (Figure 2.2). Three of these components are fuel moisture codes, which correspond to the moisture contents of surface, medium depth, and deep organic matter (Fine Fuel Moisture Code [FFMC], Duff Moisture Code [DMC], and Drought Code [DC], respectively). The combination of the latter two results on the Build Up Index (BUI), and the joining of the FFMC with wind speed data, builds the Initial Spread Index (ISI). Finally, ISI and BUI are grouped to obtain the FWI (Figure 2.2). In the case of EFFIS, the FWI information is derived from the ECMWF, which offers a wide range of weather forecast models and reanalysis products derived from *in situ* meteorological information (ECMWF, 2018).

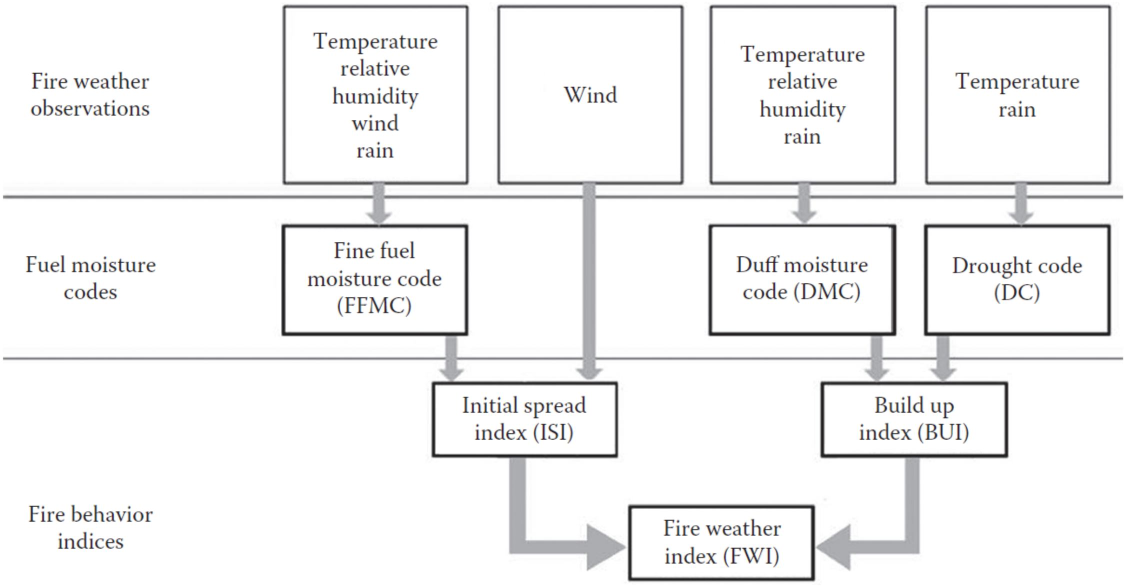

Figure 2.2. Diagram showing the six components of the FWI. Adapted from Government of Canada, 2016.

It is also important to note that, outside the scope of Copernicus, many other fire risk indices are mainly based on dead fuels moisture estimation from *in situ* meteorological data. This is the case of the McArthur Forest Fire Danger Index (FFDI; McArthur, 1967), or the National Fire Danger Rating System (Deeming et al., 1977), which are mainly applied in Australia and the United States, respectively. These indices, as well as the FWI, afford reliable and widely used fire risk predictions, but could potentially be complemented with L-band estimates of soil moisture. These estimates are obtained globally, in contrast to the limited distribution of meteorological stations in some regions of the world. Additionally to this advantage, the retrieved variable (SM) is directly linked to the water content of fuels and organic matter of soils.

2.3. Review of fire risk assessment studies based on microwave remote sensing soil moisture data

Different authors have analysed the relationship between wildfires and satellite soil moisture estimates derived from microwave sensors. For instance, Aubrecht et al. (2012) compared monthly fire products for an especially dry year (2009) in Africa with the SWI from the ASCAT satellite. They reported seasonal spatial correlation patterns between dry soils and burned regions. Another study case was reported by Bartsch et al. (2009), who analysed satellite-derived soil moisture anomalies from ERS-1 and ERS-2 scatterometers, measuring at C-band (ESA, 2018a), and compared these data with forest fires burning in Siberia between 1992 and 2000. The authors reported that 80% of fires occurred under dry soil conditions in summer and that wet soil surface limited the extent of burned area.

Further insight into the relationship among soil moisture and fires was presented by Forkel et al. (2012) in the region of Lake Baikal (Siberia). The authors studied fires for the period 2003–2009, and used the surface moisture product derived from the AMSR-E. The authors mentioned that in 2003 fires occurred mainly in permafrost soils, which presented negative surface moisture anomalies. Interestingly, the authors concluded that lack of precipitation during the previous summer (2002) led to frozen soils storing an unusual low water content during winter 2002/2003. Consequently, the amount of water released by permafrost melting in spring 2003 was low, as detected by remotely sensed soil moisture products. Clearly, this situation favoured the extreme fires that occurred in June 2003.

Research has also been focused on the comparison between meteorological fire weather indices and remotely sensed soil moisture. Shvetsov (2013) compared the FWI with SMOS data in Siberia during 2011 and 2012, and found concordance between increasing soil moisture and decreasing risk (FWI) in some areas. However, a good FWI-SM relationship was difficult to obtain for the whole region under study. Also, Holgate et al. (2017) studied the link between SMOS data and risk indices. In this case, the authors replaced different FFDI components by SMOS-derived soil moisture. The resulting FFDI showed very close results with the original FFDI, when the component replaced was the Drought Factor (DF). The authors suggested that applying this replacement would simplify the FFDI calculation.

Concurrently to part of the above-mentioned research, our group at the UPC started preliminary studies on the applicability of SMOS data to wildfire risk prediction over the Iberian Peninsula. These studies considered the complementarity between SMOS-derived high resolution (1 km) SM data (L4 product) and MODIS LST information (also at 1 km resolution).

This was expected to provide accurate information on the soil state. Firstly, Piles et al. (2011b) compared moisture-temperature conditions prior to the occurrence of 12 fires (>35 ha) burning in 2010, with the same information obtained for randomly selected unburned zones. Soil moisture was found to be lower, and LST to be higher, in burned areas prior to fire occurrences. Using these differences between burned and unburned sites, it was concluded that high fire risk was found for SM < 0.04 m^3/m^3 and LST > 33°C. A validation test with 67 randomly selected fires was done achieving an accuracy of 58%. Using a similar approach, Chaparro et al. (2014) analysed 63 fires occurring in Catalonia (NE Spain) for the period 2010–2013. The methodology was the same as in the previous study, but the comparison between burned and unburned pixels ensured similar conditions in solar radiation and aspect, two variables that condition soil moisture. Results showed significant differences ($p<0.05$) between burned areas (median SM = 0.10 m^3/m^3) and unburned ones (median SM = 0.13 m^3/m^3).

This research demonstrated that the role of satellite-derived soil moisture in fire risk assessment is very promising, and that its operational applicability is feasible. First studies in the Iberian Peninsula were encouraging, and suggested that the combined use of surface moisture and temperature -together with the consideration of complementary variables-, could lead to obtain reliable fire risk indices based on L-band soil moisture data. Hence, focusing on the Iberian Peninsula and the Balearic Islands, this research line has been one of the main topics of this PhD.

2.4. Study area

The Iberian Peninsula and the Balearic Islands are located in the southwest of Europe (−9.9°W – 4.4°E; 43.9°N – 35.9°N), and cover approximately 590,000 km^2. Figure 2.3 shows the temperature and precipitation patterns in the region. In general terms, it can be classified in three main climatic areas: (i) the Mediterranean region, with hot and dry summers, mild winters, and annual precipitation generally below 900 mm; (ii) the central region, with continental climate (cold winters and hot summers) and low annual precipitation (<600 mm out of mountain ranges); and (iii) the Atlantic region, with high annual precipitation in northern Portugal and northern Spain (1,000 to 1,400 mm), but warm and dry conditions in southern Portugal and in the Atlantic coasts of Andalucía (southern Spain). In the Iberian Peninsula, mean annual temperatures are warmer in the south and in the Mediterranean coast (generally >15°C), and colder in the northern half of the region (generally <15°C, except for the Ebro valley).

Due to the contrasting climatic conditions, different vegetation types and fuel loads are found through the Iberian Peninsula. In the north and the northwest, humid broadleaved forests are dominant, and high precipitations lead to the accumulation of large amounts of fuel. In contrast, drier conditions in the Mediterranean region reduce the fuel amounts, and forests coexist with scrublands. The central Iberian Peninsula is dominated by agriculture -in the central plateau- and by mixed woodland-agriculture landscapes. Forests dominate the mountain ranges delimiting the plateau area.

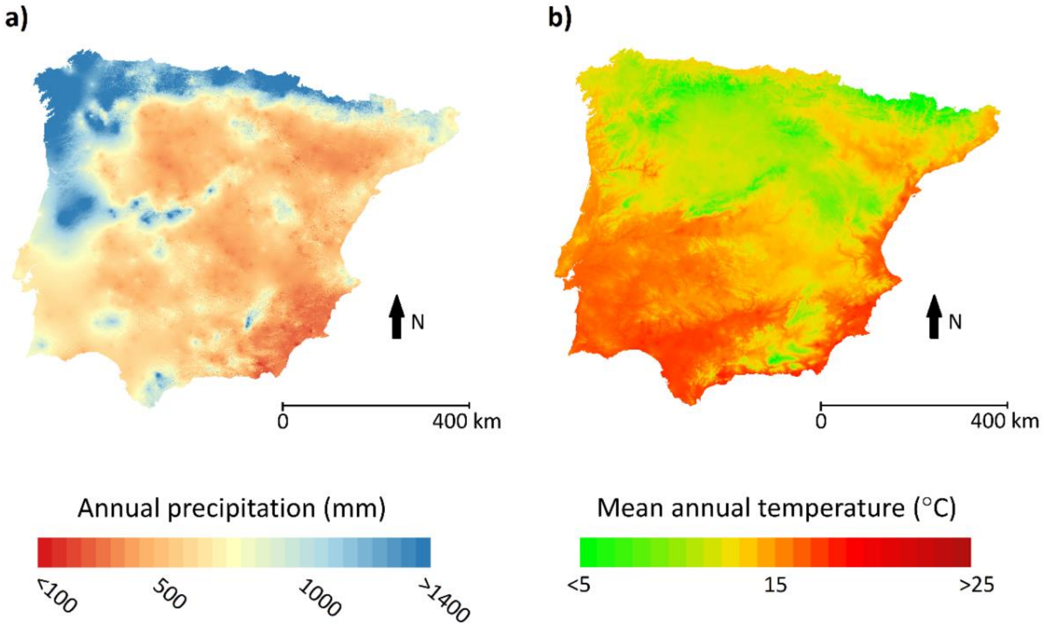

Figure 2.3. (a) Mean annual accumulated precipitation; (b) mean annual temperature. Reference period: 1951-1999. Source: Ninyerola et al., 2005.

The dry and warm summer conditions –especially in the Mediterranean-, the high fuel loads in the northern and northwestern region, and especially the frequent impact of droughts in the entire Iberian Peninsula, propitiate the occurrence and propagation of wildland fires. Consequently, the Iberian Peninsula is a high-fire risk region where extensive areas are burned causing important damage and economic loss (Pereira et al. 2005; Padilla and Vega-García, 2011; San-Miguel-Ayanz et al. 2013). In particular, the countries of the European Union with the largest burned areas per year have been Spain (161,923 ha) and Portugal (107,396 ha), for the period 1980-2016 (San-Miguel-Ayanz et al., 2017, p. 117).

2.5. Data

The following set of variables has been used to describe the conditions before fire occurrences in the Iberian Peninsula: fire burned area, SM and LST conditions before fire both in absolute and relative terms (i.e. anomalies), land cover information, the region where the fire burned, and the month of the fire outbreak. Complementarily, a database for moisture and temperature conditions in unburned pixels has been built in order to compare burned and unburned areas.

2.5.1. Fires dataset

A forest fires dataset containing fires affecting more than 10 ha for the period 2006–2014 has been provided by the European Forest Fires Information System (San-Miguel-Ayanz et al., 2012). The provided GIS layout includes wildfires' perimeters, coordinates, and the date of occurrence. Data for the period 2006–2009 are used as complementary information for unburned cells selection (see Sections 2.2.5, 2.7 and 2.8). The dataset studied here (2010–2014) contains 2,076 wildland fires larger than 10 ha. Approximately the 90% of those fires are smaller than 1,000 ha, while the remaining 10% is larger. Only six fires are larger than 10,000 ha (see Table 2.1).

Table 2.1. Number of fires classified by the size of burned area.

Burned area	Number of fires
10 - 100 ha	968
100 – 1,000 ha	971
1,000 – 10,000 ha	131
>10,000 ha	6
Total	2,076

2.5.2. Moisture and temperature information

The cloud-free SMOS-derived soil moisture product at 1 km resolution (see Section 1.3) has been applied, as it allows robustly computing moisture trends and anomalies for the study period. This dataset is available at the BEC website (BEC, 2018). Only SMOS ascending passes (approximately at 6 a.m., local time) have been used, in order to detect conditions prior to forest fires (most of them burning before the afternoon pass of SMOS). Daily LST at 0.125° has been obtained from ERA-Interim models of the ECMWF (ECMWF, 2018). It is a reanalysis dataset for 12 a.m. (local time), which is interpolated to the SM 1 km grid using the nearest neighbour method.

Moving averages and anomaly time series at 9-day and 30-day time scales are computed for both variables in order to detect drought periods involving risk of fire. To produce the anomalies, firstly monthly means of each variable are calculated. Secondly, in order to obtain continuous time series, a linear interpolation is performed between mean values of each pair of consecutive months. These time series represent the average moisture and temperature conditions. In the third and final step, the difference between the moving means and the corresponding average conditions is calculated from the day of interest to 9 and 30 days backwards.

2.5.3. Land cover information and ecoregions

Land cover data from the CORINE Land Cover Map (Copernicus, 2018b) at 250 m resolution is used to classify the fires depending on the type of vegetation burned. CORINE provides 44 categories of land cover classified in 5 groups: artificial surfaces, agricultural areas, forest and semi-natural areas, wetlands, and water bodies. All the categories are treated separately, except for the group "agricultural areas" which is considered as a single cover category.

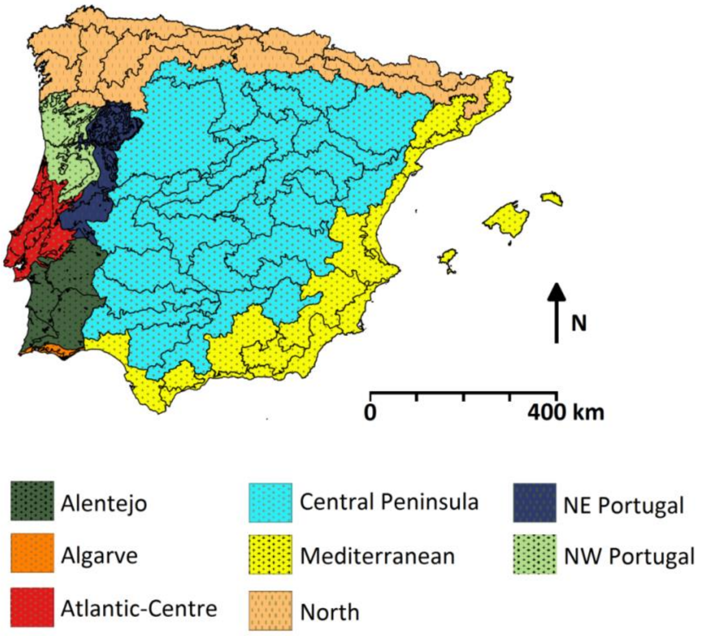

Figure 2.4. Regions defined in the study. Black lines show the borders of the ecoregions and phytoregions used for Spain and Portugal, respectively.

Also, it has been necessary to classify fires as a function of their geographic region and its biogeophysical and climatic characteristics. The 53 ecoregions defined by the Spanish Forest Service have been useful to this purpose, as it has been previously shown in Padilla and Vega-García (2011). In Portugal, the geographical division is based on the map of 24 phytogeographic regions included in the environmental atlas of Portugal (Paes do Amaral, 2000). Regions are grouped as shown in Figure 2.4 in order to simplify the study. Due to different climates and forest fire patterns, ecoregions in the north of Spain (28.9% of fires) and Mediterranean regions (4.8% of fires) are considered separately. A third group is formed with the central Spanish ecoregions (5.7%) located in the inland Peninsula and, in most cases, within the continental climate of the central plateau. In Portugal, the phytogeographic classification assembles the 24 regions in three general groups: North, Centre and South (Paes do Amaral, 2000). However, in order to consider different biogeographic characteristics within the country (Aguiar et al. 2008, Costa et al. 1998), here five regions are finally delimited: northwestern Portugal (43.2% of fires), northeastern Portugal (13.6%), Atlantic-Centre (2.8%), Alentejo (0.8%) and Algarve (0.2%).

2.5.4. Pre-fire conditions database construction

In order to obtain one single datum per variable and burn episode, the GIS layout containing forest fire perimeters has been clipped to the different data layers described above. The median SM and LST data before fire occurrences (as well as the median of the means and anomalies) are calculated using all pixels within a fire, and are assigned to each episode. These data have been considered only when at least one pair of moisture-temperature values is available from the fire date to three days backwards. In this case, the most recent data are included in the database. A 3% of fires have not accounted with moisture and/or temperature data for the day of occurrence to three days backwards, and have been therefore eliminated from the dataset. This leads to a final database containing 2,013 fires out of the 2,076 contained in the EFFIS database (i.e., 97%).

Concerning to land cover, one single category is assigned to each wildfire, corresponding to the modal cover within the fire-affected area. Regions are also assigned to each forest fire. In the few cases in which a fire occurred across more than one region, the region assigned to the episode is the one containing the largest burned area.

2.5.5. Database for unburned areas

A second database is built including SM and LST data in more than 50,000 unburned cells per year. These cells are chosen randomly after excluding (i) pixels without flammable soil uses (based on the CORINE Land Cover Map), and (ii) all the burned cells from 2006 to the study year. The latter criterion has been used as previously burned cells are less probably affected by wildland fires until vegetation recovers some years later.

2.6. Fire distribution and moisture-temperature patterns in the Iberian Peninsula

2.6.1. Spatial and temporal distribution of wildfires during the study period

During the period 2010–2014, approximately a total of 760,000 ha burned in the region (only considering the fires larger than 10 ha registered in EFFIS). Wildfires were irregularly distributed throughout the Iberian Peninsula. Most forest fires burned in Galicia, the Cantabrian coast, and the north of Portugal. In contrast, few fires occurred in other regions such as the Mediterranean area. These fires, however, were extremely large in 2012 (Figure 2.5).

The number of fire occurrences and the burned area broadly varied among different years (Figure 2.5). In 2010, 2011, and 2013, the burned area ranged between 125,000 and 191,000 ha. Rarely, only 33,500 ha burned in 2014. In contrast, in 2012 the burned area was very

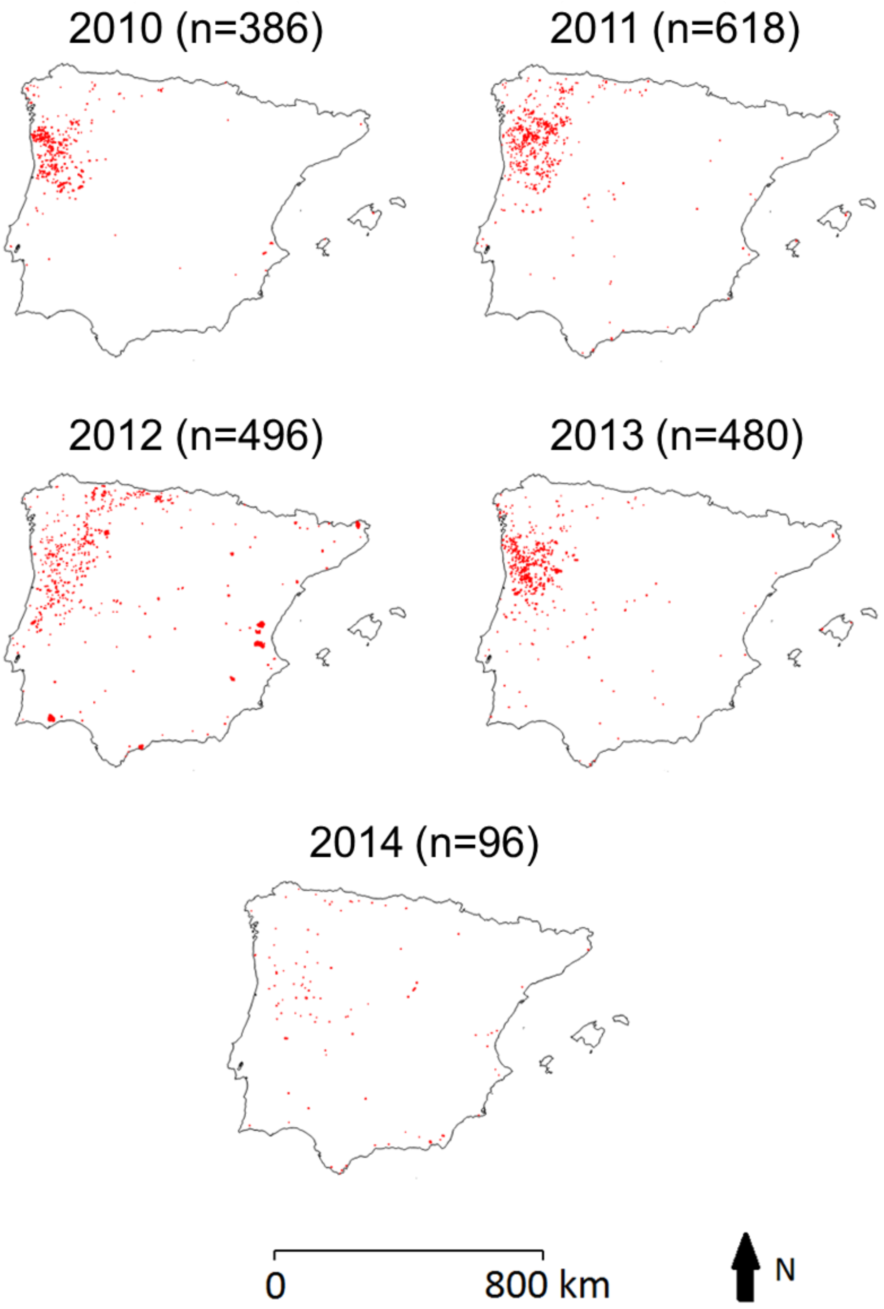

Figure 2.5. Wildland fires in the Iberian Peninsula and Balearic Islands (from EFFIS database) for the period 2010–2014. The number of fires for each year is shown.

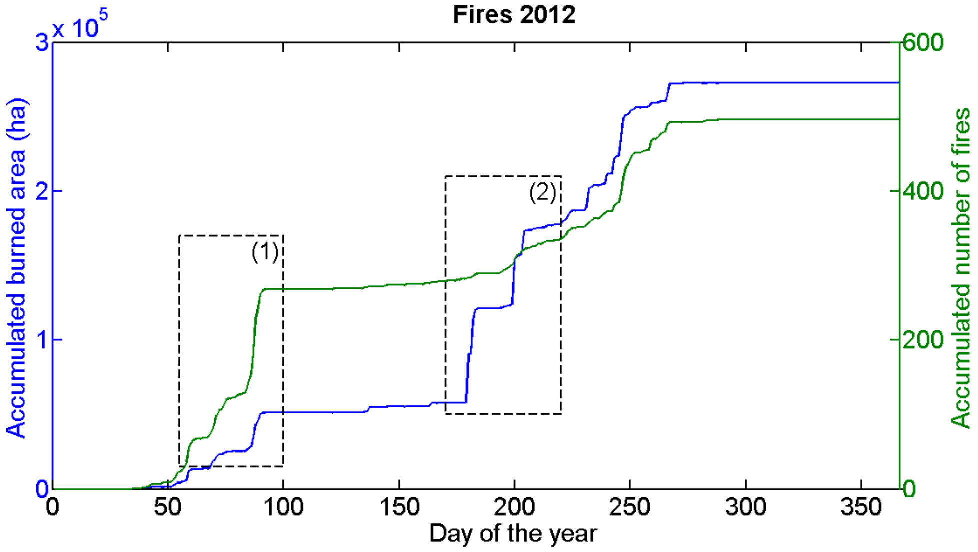

Figure 2.6. Accumulated number of wildfires and accumulated burned area during 2012. Two patterns are observed: (1) numerous small forest fires (mean area = 608 ha) which mainly occurred in the northern Iberian Peninsula and Portugal, and (2) few but large wildland fires (mean area = 2,872 ha) which burned in few days in the Mediterranean region.

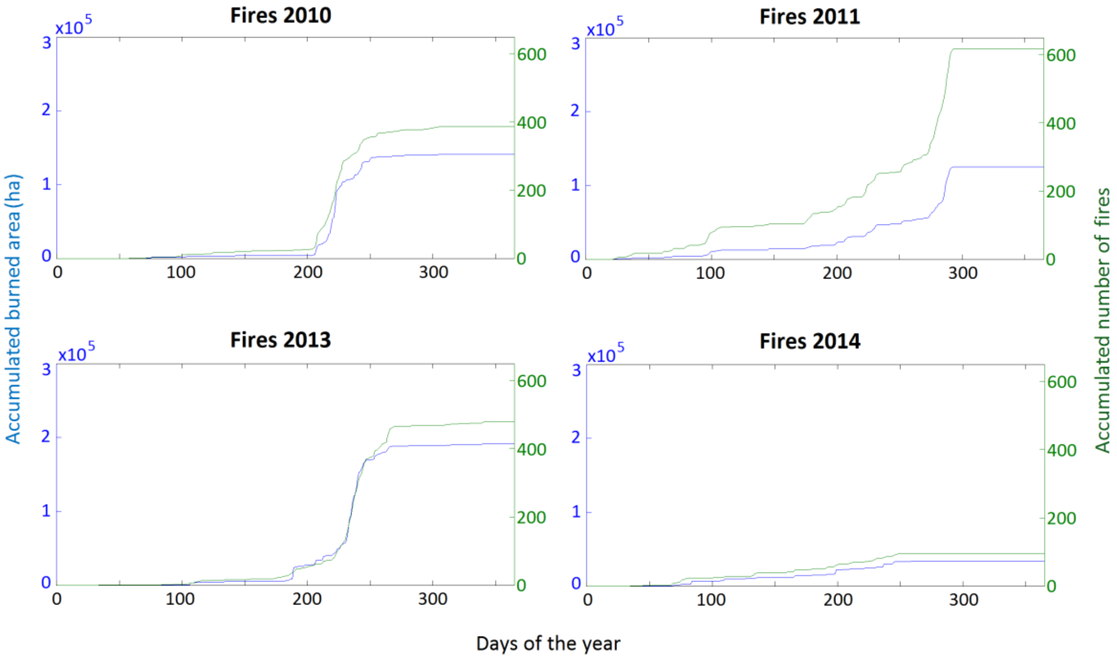

Figure 2.7. Accumulated number of wildfires and accumulated burned area during 2010, 2011, 2013, and 2014.

remarkable (>270,000 ha). This is probably due to the high temperatures (generally 2°C above the mean) and the low precipitations (15% below the average) during that year (AEMET, 2013). Figure 2.6 shows the evolution of burned area and the number of forest fires during the exceptional year of 2012, when the drought situation favoured the occurrence of big forest fires (up to 32,500 ha) especially in the Mediterranean region (see Figure 2.5 and Figure 2.6). During the study period, numerous fire outbreaks occurred in northern Spain and northern Portugal. Two fire periods in this area must be highlighted: October 2011 (see Figure 2.7; fire extensions up to 6,100 ha), and February-March 2012 (see Figure 2.6; fire extensions up to 2,900 ha). Finally, note that fires <10 ha (not studied here) are quantitatively important in the Iberian Peninsula (e.g., in the period 1984–2004, 25% of fires larger than 5 ha in Portugal did not exceed a size of 10 ha; Aguiar et al., 2008).

2.6.2. Fire distribution in the Iberian Peninsula is linked to climate, soil moisture, and temperature patterns

To the scope of this chapter, it is important to stress the climate contrasting conditions between the Mediterranean area and the north-western Atlantic region (see Section 2.4). This led to important differences in moisture and temperature conditions between these two regions during the study period. In that sense, hot and dry soils prevailed in the Mediterranean (Figure 2.8 a and c), and presented little variability in terms of water content (Figure 2.8 b). In contrast, soils were wetter in average in the north-west (Figure 2.8 a).

The distribution and extent of wildfires in the Iberian Peninsula were coherent with these different patterns. On one hand, high moisture facilitates the accumulation of a lot of fuel in the forested landscapes of the northwest. However, this fuel is humid and its low flammability limits the spread of wildfires. Nevertheless, during drought periods large fires may burn in the region (see Figure 2.5). On the other hand, generally, a minor fuel accumulation due to more reduced water availability limits the number of ignitions in the Mediterranean. Still, in particular situations when fuel finally accumulates, the dry summer conditions can lead to the occurrence of very large forest fires, such as during 2012 (Pausas, 2004; Verdú et al., 2012; see Figure 2.5).

Besides the comparison between these two Iberian regions, note that the southwestern Iberian Peninsula was the most humid area in terms of average soil moisture (Figure 2.8a). This shows that fuel accumulation is possibly more dependent on precipitation (higher in the northwest; see Section 2.4). Actually, soil moisture is influenced by different factors and precipitation is not the only important variable conditioning moisture, as shown in recent studies (Polcher et al., 2016). Also, the high variability of moisture in the southwest (Figure 2.8b) and the high temperatures in this area (Figure 2.8c) suggest that dry and hot soils occur in some periods and might restrict the availability of combustible.

Finally, note that the central plateau presented the largest variability in terms of surface temperatures, considering the period 2010-2014 (Figure 2.8d). This is coherent with its continental climate. The high summer temperatures and the lack of precipitation reduce the availability of fuels in the region and the number and extension of fires, except for the mountain ranges which surround this area (Vecín-Arias et al., 2016).

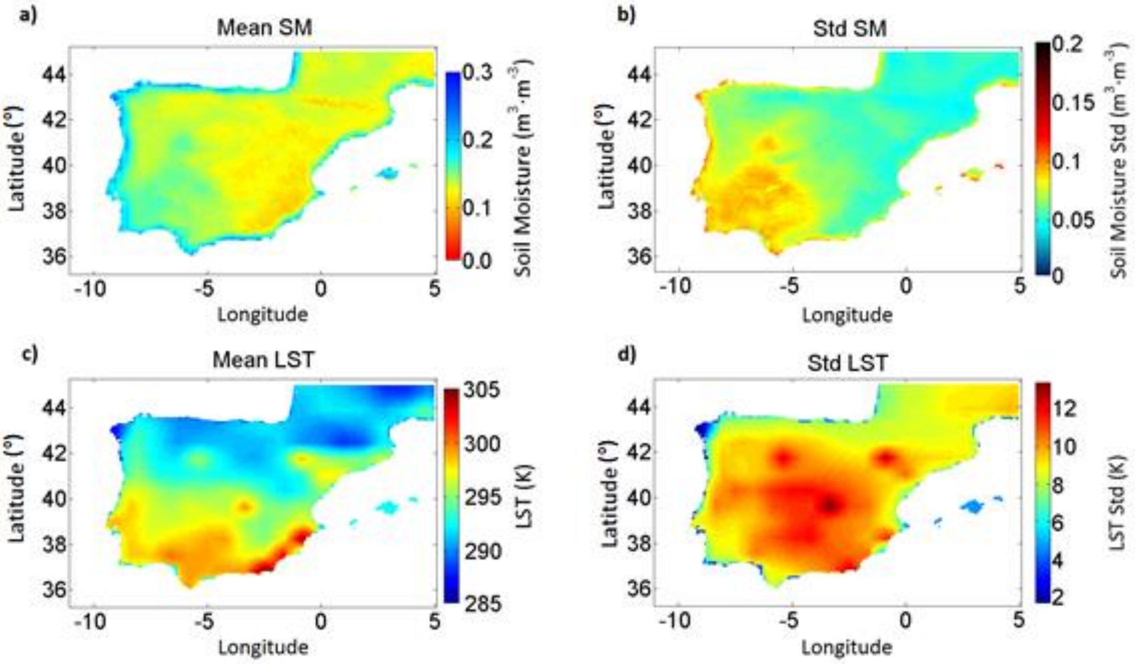

Figure 2.8. (a) Mean soil moisture, (b) standard deviation of soil moisture, (c) mean land surface temperature and (d) standard deviation of land surface temperature. All the variables are computed for the period 2010-2014.

2.7. Pre-fire moisture and temperature conditions in the Iberian Peninsula

To understand the conditions in which fires burned, moisture and temperature data for both burned and unburned cells have been compared. Figure 2.9 shows the results for year 2013 as an example. In order to simplify the interpretation, fires are classified in three groups (<500 ha, 500–3,000 ha, and >3,000 ha). It can be seen that, although the range of conditions for both variables in unburned pixels is wide, generally days with dry and warm soils are frequent in the Iberian Peninsula (Figure 2.9). This facilitates the ignition and spread of wildfires, especially on the warmest and driest days which generally occur in summer. In that sense, the distribution of burned cells shows narrow ranges within the two studied variables. Most fires –and particularly the largest ones- burned in drier and warmer soils than the median of unburned cells (Figure 2.9).

To provide further detail on the fire outbreak conditions, this study has been carried out separately by years and months in order to identify the most important fire episodes and when they occurred. For each fire, moisture-temperature data are coupled to take advantage of the complementarity between both variables, coherently with previous studies (Chaparro et al., 2016a) and with results presented in Figure 2.9. Also, in order to determine which fires burned in dry and warm soils, reference values defining normal moisture-temperature conditions are stablished yearly. Following Figure 2.9, these values are calculated as the overall yearly medians of both variables for the unburned cells in the study region, and are used as an approximation to the general conditions of each year. Considering anomalies, obviously zero is the reference value. Finally, means and anomalies of SM and LST are plotted in Figure 2.10 and Figure 2.11, in combination with the month of occurrence and the burned area, respectively. Figures are plotted only for the 30-day time scale. Similar results have been obtained for 9-day periods (not shown).

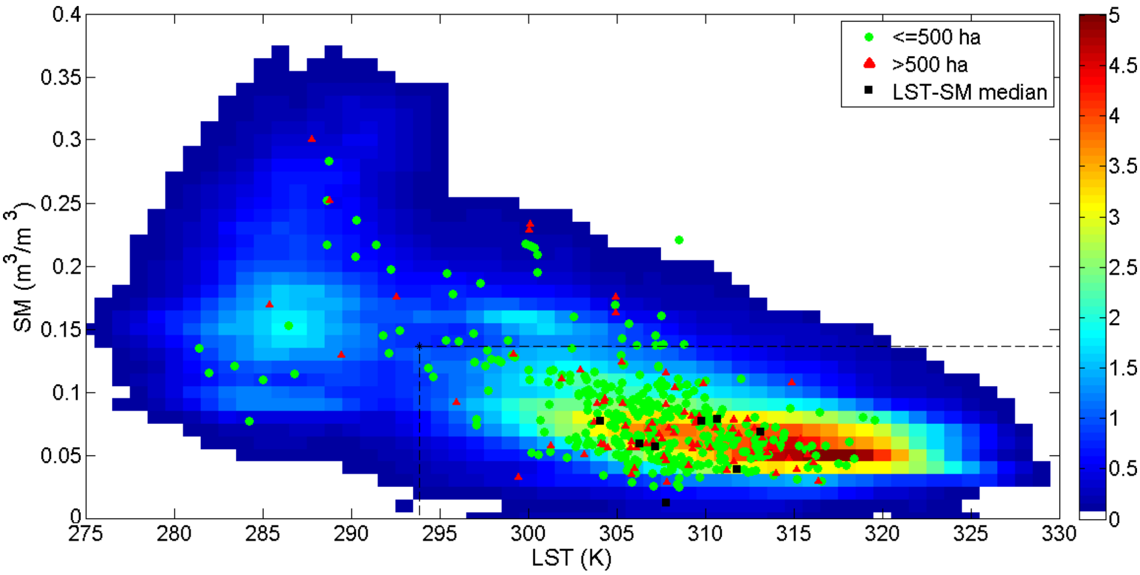

Figure 2.9. Comparison of SM-LST conditions between burned and unburned areas during 2013. Green points, red triangles, and black squares correspond to wildfires <500 ha, between 500 and 3,000 ha, and >3,000 ha, respectively. Black dashed lines show the median SM and LST during 2013 in unburned pixels. The distribution for both variables in not burned areas during 2013 is shown as ‰ of pixels and days presenting each pair of moisture-temperature values. White represents < 0.1‰.

Results show that the warmest (2011) and the driest (2012) years in the study region according to the median soil conditions (see Figure 2.10 and Figure 2.11) were the years with more fire outbreaks (618 and 496, respectively). High soil surface temperatures in 2011 reflect the prevailing high air temperatures in the Iberian Peninsula during that year (AEMET, 2012). In 2012, dry soils are related to the extremely low precipitations in the study area (AEMET, 2013).

In contrast, the number of fire outbreaks in 2014 is unexpectedly low (n=96) regarding the median SM-LST values (similar to 2011 and 2013). Then, an overall yearly value for each variable is not descriptive enough of the real situation in 2014, and a more detailed description is needed: in 2014, winter months were very hot (increasing the average temperature), but rainy, while summer was not markedly abnormal with respect to climatic air temperatures and precipitations (AEMET, 2015). This probably explains the low number of fire occurrences during that year.

Most wildfires burned when temperature was higher and moisture was lower than the reference values (i.e., yearly medians), which hereafter will be simply defined as fires occurring under dry and hot soils (Figure 2.10 and Figure 2.11). In particular, 75% of fires burned in these dry-hot conditions considering 30-day means (79% for 9-day, not shown). Regarding moisture and temperature anomalies, soils drier and hotter than the average preceded the 71% of fire outbreaks (30-day anomalies; 79% for 9-day, not shown), but this proportion changes for different fire sizes (Figure 2.11 and Table 2.2).

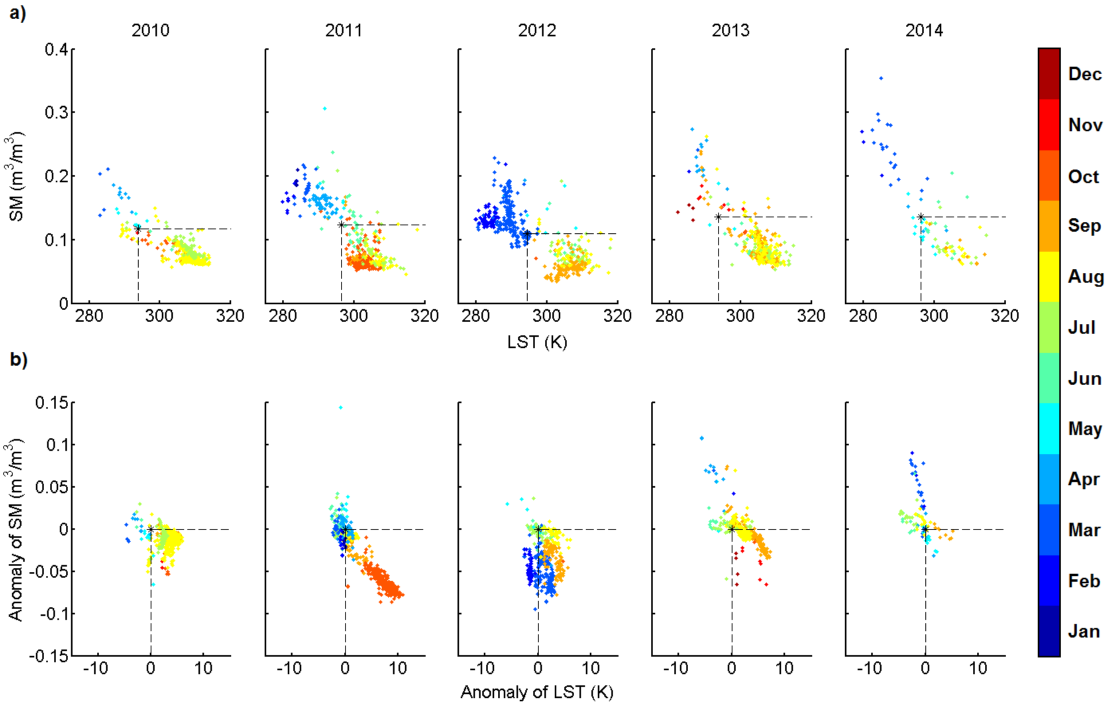

Figure 2.10. (a) Mean SM and mean LST before fires. Dashed lines represent the yearly median of LST and SM in the region; (b) anomalies of SM and anomalies of LST before fires. In (a) and (b), fires are represented per year (columns) and month (colour bar). All the variables have been calculated at 30-day time scale.

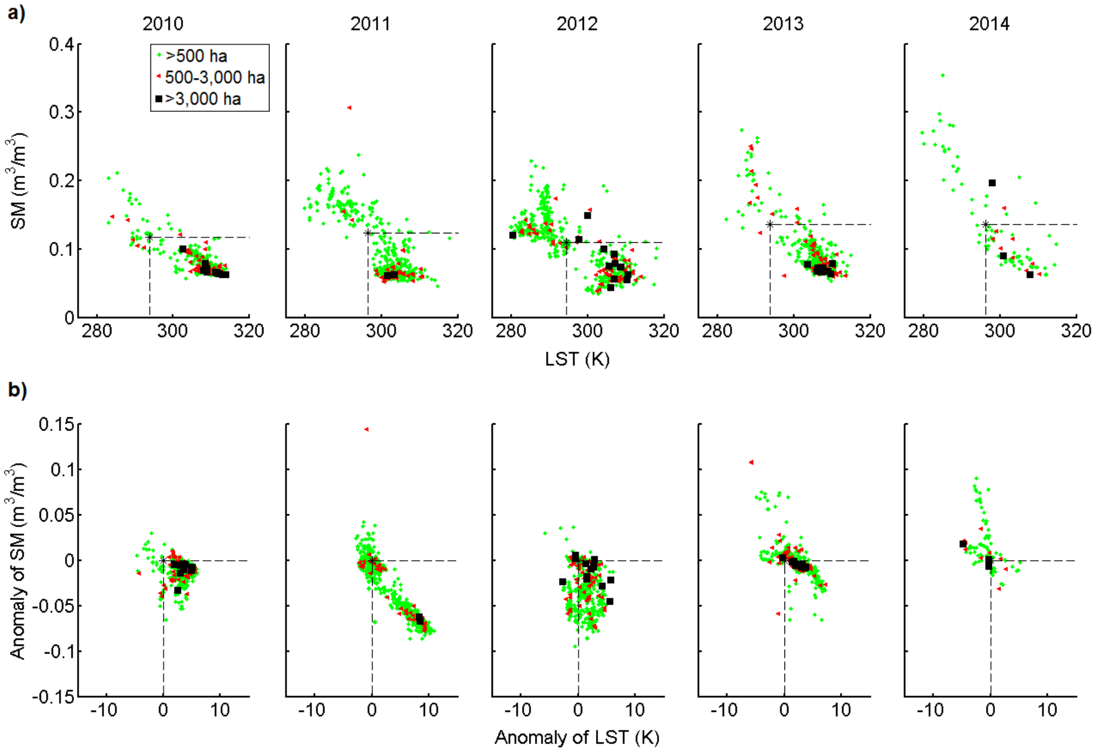

Figure 2.11. (a) Mean SM and mean LST before fires. Dashed lines represent the yearly median of LST and SM in the region; (b) anomalies of SM and anomalies of LST before fires. In (a) and (b), black squares represent fires >3000 ha, red triangles represent fires between 500 and 3000 ha, and green dots represent fires <500 ha.

Table 2.2. Percentage of fires burning in drier and hotter conditions than the median SM-LST (first row) and percentage of fires occurring under drier and hotter than usual conditions in the site (second row). Results are reported at 30-day time scale.

Pre-fire conditions	Burned area (ha)		
	<500	500-3,000	>3,000
SM< annual median & LST > annual median	71%	83%	90%
Anomaly SM< 0 & Anomaly LST > 0	68%	71%	84%

The percentages also vary depending on years and seasons. During 2010, 2011 and 2013, from 77% to 88% of ignitions happened in dry and hot soils. This percentage was lower (58%) in 2014. In 2012, 267 wildfires (54% of the fires studied that year) occurred in February and March, when soils were wet and cold in absolute terms (Figure 2.10a). However, the prone-to-fire situation leading to this remarkable episode is detected by the 30-day moisture anomalies, as 99% of these wildfires occurred in drier than average conditions (Figure 2.10b). This percentage is lower for the 30-day temperature anomalies (66% of fires with positive anomalies). Considering other fire periods occurring in cold and wet soils (e.g.,February-April 2011 and February-March 2014), they did not burn in anomalous conditions. In these particular cases only 89 and 24 fires are registered, respectively (Figure 2.10). Finally, an exceptional situation occurred during October 2011, when 304 fires burned. During the month prior to fires, soil water content was 0.09 m^3/m^3 below the average, and temperatures rose up to 10.9 K above the average conditions (Figure 2.10). This situation got worse in the 9 days before fires (-0.12 m^3/m^3 and +14.3 K).

Hence, results in this section show that surface moisture and temperature information allow detecting situations posing a risk of fire. Especially, dangerous conditions occur for soils drier and warmer than the year and/or the period averages. More specifically, moisture and temperature anomalies detect the conditions which led to the extraordinary fire episodes of October 2011 and February-March 2012 (Figure 2.10). Both episodes burned in the northwestern Iberian Peninsula and are studied specifically in Section 2.8.

2.8. Study of time-series anomalies and wildfires in the north-western Iberian Peninsula

The fire episodes burning in October 2011 and February-March 2012 mainly occurred in the north of Portugal, Galicia, and the western Cantabrian coast. Hence, the study described in this section has been focused on the northwestern Iberian Peninsula. To specifically delimit the extent of the northwestern region, the map of ecoregions of Spain and the map of phytogeographic regions of Portugal are used again. Ecoregions 1 to 7 in Spain (sited in the north-west) and the northern phytogeographic regions of Portugal are grouped. Figure 2.12 shows the study area where the relationship between wildfires and anomalies is studied.

Surface moisture and temperature anomalies trends for the period 2010-2014 have been summarized calculating the median anomalies for the entire region each day, only considering flammable pixels. To that purpose, pixels located in artificial surfaces and water bodies have been excluded using the CORINE Land Cover Map (Copernicus, 2018a). Also, pixels affected by fire in previous years (2006-2009) and during the study period have not been considered. The resulting median anomalies time series at 9-day and 30-day time scales have been compared to the number of fires burning in the region every 9-days and each month, respectively. The sample studied in this region is 1,733 fires (83% of fires of the initial dataset). The number of fires corresponding to the period October 2011 is 304 (15%) and the number of fire outbreaks registered in February and March 2012 is 267 (13%).

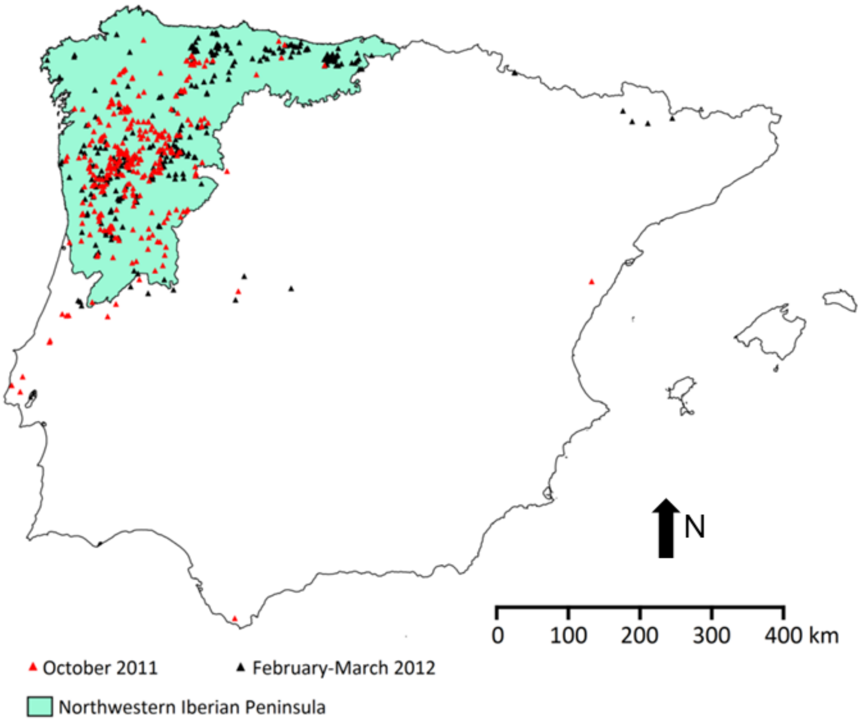

Figure 2.12. Fires burned during the two wildfire episodes studied (October 2011: red; February-March 2012: black). The green shaded area delimits the north-western region.

Figure 2.13 a and b show the median SM and LST anomalies in the region (30-day time scale). Their values are compared to the number of wildfires burning each month (Figure 2.13c). Considering the SM anomalies, five droughts occurred in the region during the study period: (i) August-November 2010, (ii) August-November 2011, (iii) December 2011-April 2012, (iv) August-November 2012 and (v) August 2013-January 2014 (Figure 2.13a). Generally, positive temperature anomalies coincide in time with these periods (Figure 2.13b). Results using 9-day time scale anomalies are coherent with that from 30-day timescale, although with more irregular patterns (Figure 2.14).

The exceptional number of wildfire outbreaks registered in October 2011 and February-March 2012 matches with the droughts detected from August to November 2011, and from December 2011 to April 2012, respectively (Figure 2.13). For October 2011, abnormally high temperature conditions started in July and lasted until November. Driest soils (up to -0.09 m^3/m^3) and highest surface temperature anomalies (up to +8 K) occurred in October, when the most extreme values of both variables matched in time and more than 300 fires burned (Figure 2.13). Also, forest fire outbreaks of February and March 2012 burned in extremely dry conditions, as SM anomalies reached a minimum of -0.10 m^3/m^3 in March 2012 (Figure 2.13b), coinciding with the highest values of temperature anomalies (+1.6 K). While soils were continuously dry for more than three months before this episode, the duration of high temperatures was only limited to the month of March (Figure 2.13).

Interestingly, both fire periods coincided with meteorological anomalous situations. Particularly, abnormal anticyclonic activities in the western and central Iberian Peninsula occurred between 11th and 18th October, 2011 and between 21st February and 2nd March, 2012. These produced above mean air temperatures and low air humidity (Amraoui et al., 2014). In Figure 2.14, dark lines have been plotted on 18th October 2011 and 2nd March 2012, showing the moisture–temperature conditions during the anticyclonic situation. Figure 2.15 shows the maps of the 9-day anomalies of both variables computed before, during, and after the anticyclone. The spatial distribution of high surface temperatures and low SM between

On 11th and 18th October 2011 (Figure 2.15 b and e) the spatial distribution of high air temperatures and low air humidity match. These extended from the central Iberian plateau to the Atlantic coast. The meteorological anomalies were especially intense in the north-western Iberian Peninsula (see Figure 2 in Amraoui et al., 2014). In addition, note that the drought intensity was lower between 2nd and 10th October (i.e., before the anticyclonic interval; Figure 2.15 a and d), increased between 10th and 18th October (Figure 2.15 b and e; i.e. during the anticyclone), and clearly diminished after the anticyclonic period (19th to 27th October 2011; Figure 2.15 c and f). This pattern matches the evolution of the number of wildfires during that month. Particularly, the occurrences of large fires (>500 ha) rose between 2nd and 10th October (8 fires) and between 11th and 18th October (20 fires; Figure 2.15). Hence, the anomaly time series from SM SMOS-derived data and LST ERA-Interim models demonstrate a coherent fitting with the atmospheric conditions and the number of fire occurrences on October 2011 and February–March 2012.

Nevertheless, not all the drought situations led to exceptional wildfire activity. From August to November 2010, the number of fire occurrences was important only in August and September, when summer conditions facilitated the ignition of wildfires (see Figure 2.10 and Figure 2.11). A similar situation was found from August to December 2013. In both cases, minimum moisture conditions (-0.06 m^3/m^3 in October 2010, and -0.09 m^3/m^3 in December 2013) occurred later than maximum anomalies of temperature (Figure 2.13. a and b). Finally, in September 2012, the driest and warmest conditions occurred simultaneously. However, the drought was shorter and milder if compared to the periods August-November 2011 and December 2011-April 2012 (Figure 2.13a) and the number of fires was also smaller (87 wildfires burned in the region in September 2012).

These results suggest that the most dangerous situations in terms of risk of fire ignition occur when moisture-temperature adverse conditions stretch on and when dry and warm peaks match on time. Nevertheless, this is only consistent out of summer season. Considering the studied summers, anomalies of both variables were generally close to 0 (Figure 2.13), while a large number of fires (>200) burned in August 2010 and August 2013. High temperatures and dry soils are frequent in the Iberian Peninsula during summer, and absolute values are better indicators of fire risk (and probably also of drought) during this season.

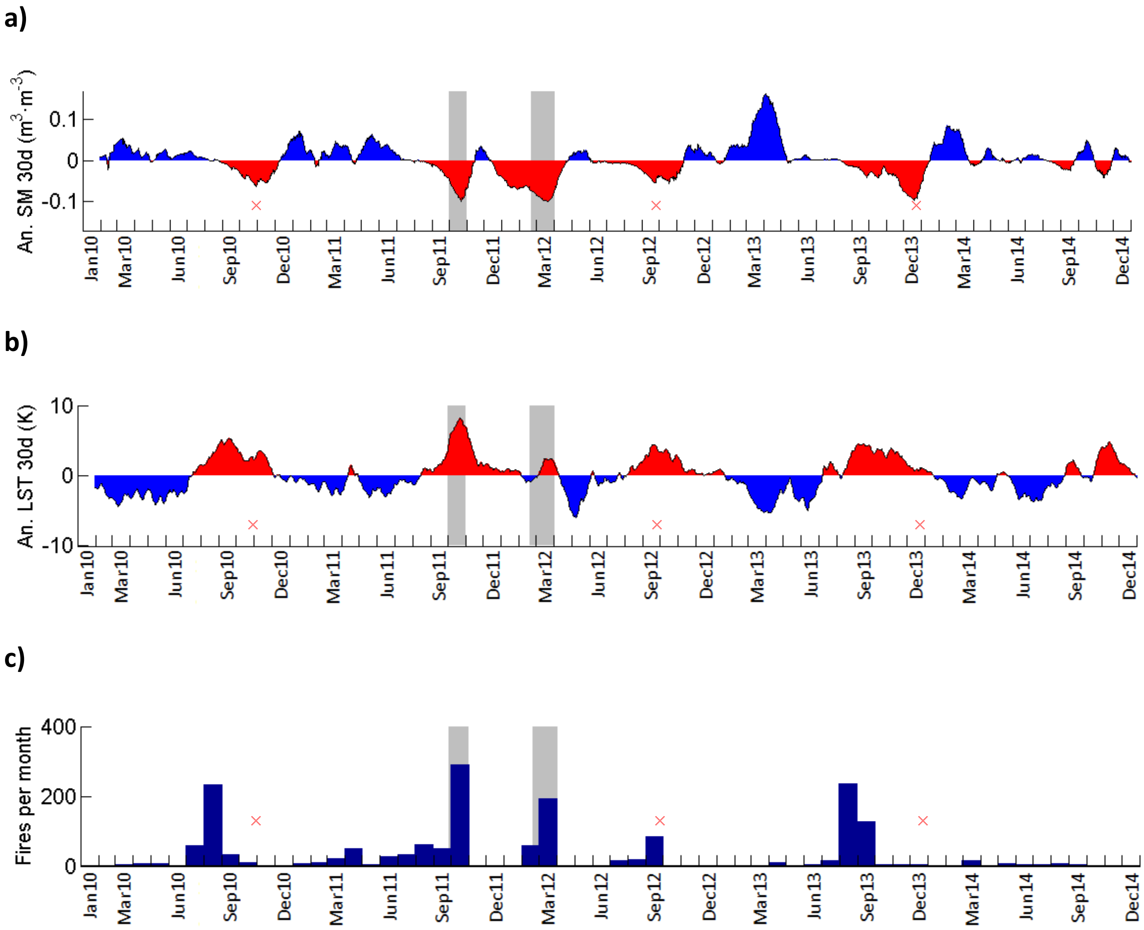

Figure 2.13. Dry and wet intervals compared to fire outbreaks in the north-western Iberian Peninsula during the period 2010-2014. (a) Median anomalies of soil moisture at 30-day time scale, (b) median anomalies of land surface temperature at 30-day time scale and (c) number of fires grouped per month. Grey shaded areas represent the fire episodes of October 2011 and February-March 2012. Red crosses represent periods when dry and warm soils did not lead to the occurrence of important fire episodes.

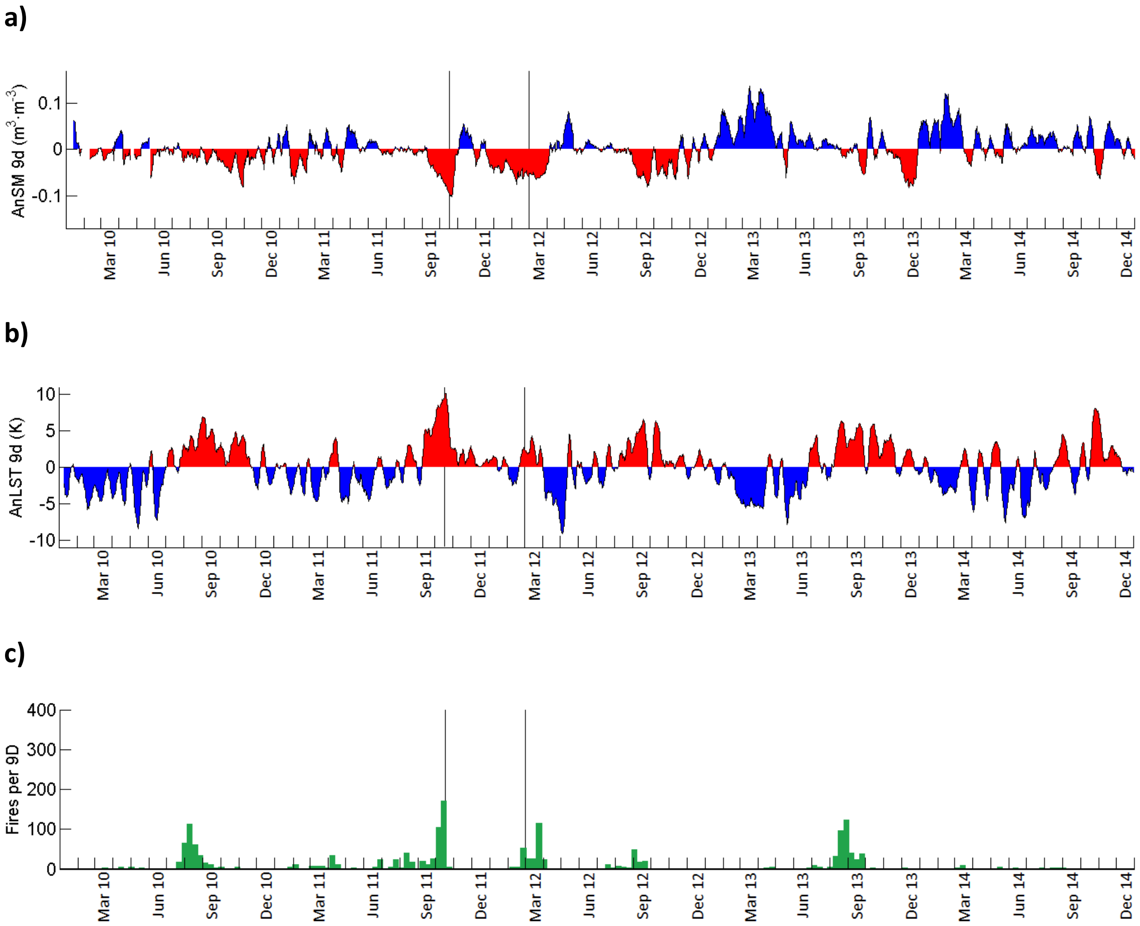

Figure 2.14. Dry and wet periods compared to fire outbreaks in the northwestern Iberian Peninsula during the period 2010-2014. (a) Median anomalies of soil moisture at 9-day time scale, (b) median anomalies of land surface temperature at 9-day time scale and (c) number of fires grouped per each 9-day period. Dark lines in October 2011 and February-March 2012 correspond to the end of the anticyclone periods.

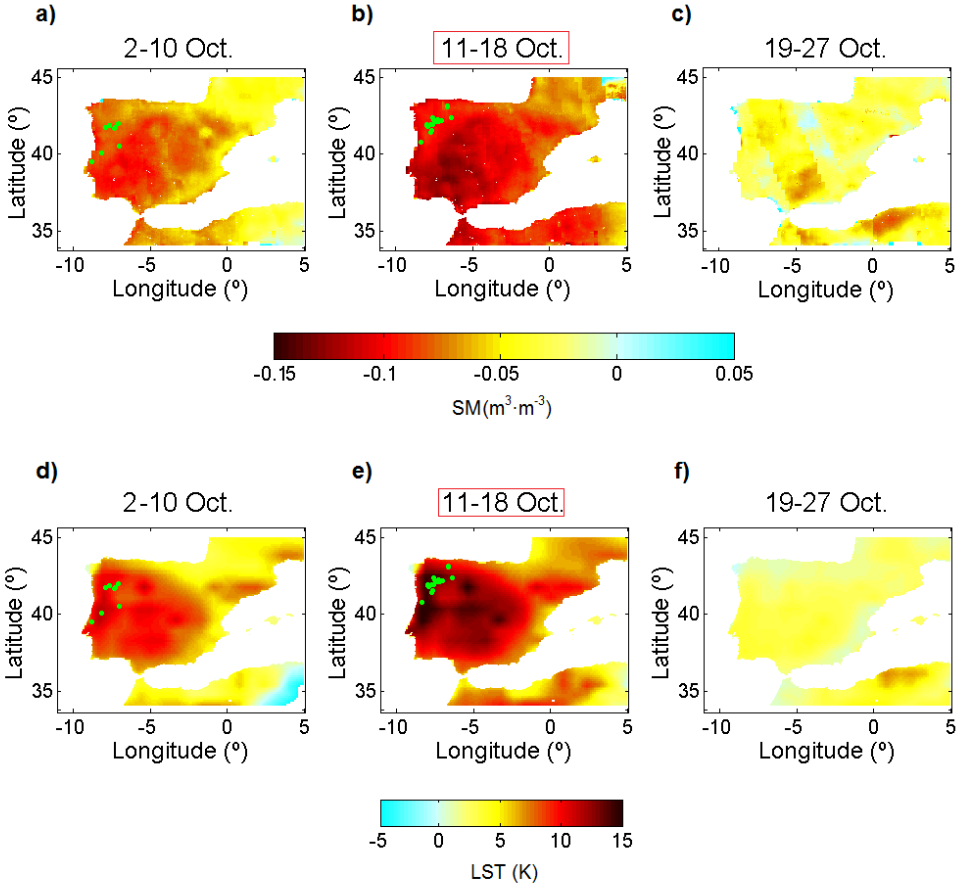

Figure 2.15. 9-day SM anomalies (up row) on (a) 10th October 2011, (b) 18th October 2011 and (c) 27th October 2011. 9-day land surface temperature anomalies (down row) on (d) 10th October 2011, (e) 18th October 2011 and (f) 27th October 2011. The period 11th – 18th October (red rectangle) matches in time with the abnormal synoptic anticyclone activity. Green dots correspond to fires larger than 500 ha in the northwestern Iberian Peninsula.

2.9. Development of a fire risk model

2.9.1. A preliminary model for operational applications

As shown in Section 2.7, the largest fires are associated to very dry and warm soil conditions prior to their ignition. In contrast, fires affecting smaller areas burn in a wider range of conditions, including cold and wet soils in absolute terms (Figure 2.11). These differences permit to configure fire risk thresholds associated with fire propagation, aiming to obtain fire risk maps in near real-time.

To that purpose, the study presented in Section 2.7 has been repeated using the LST at 6 a.m. local time (instead of noon LST). This aims at providing fire risk information during the first hours in the morning. Results are similar to those obtained for noon LST information (Section 2.7), and the same three burned area categories have been used: <500 ha, 500 to 3,000 ha, and >3,000 ha.

To obtain empirical risk thresholds, the first quartile, the median, and the third quartile of SM and LST before fire occurrences are computed for each category of burned area. These statistics are calculated for a random selection of 70% of fires (period 2010-2014). The remaining 30% is allocated for validation. Additionally, SM and LST anomalies are used as complementary information. Then, a fire risk empirical model has been developed using these data in a two-step process:

1. The third quartile of SM (i.e., the wettest) and the first quartile for LST (i.e., the coldest), for each burned area category (<500 ha, 500-3,000 ha, and >3,000 ha), are established as the minimum thresholds for a pixel to be classified in one of the following fire risk categories: risk of very large fire (>3,000 ha), risk of large fire (>500 ha), risk of ignition (<500 ha), and low risk (for pixels with the coldest and wettest soils). Table 2.3 presents the SM-LST thresholds and the corresponding categories.

2. Anomalies of SM and LST are used as complementary variables. Negative anomalies of SM increase risk category even when cold or wet conditions are found. Positive anomalies of LST contribute to determine the highest risk level (see Table 2.3).

Table 2.3. Fire risk categories determined by SM-LST thresholds. Note that anomalies of SM and LST change the risk as follows: (1) low risk pixels are finally classified as ignition risk pixels when the SM anomaly is negative; (2) pixels where the risk of large fires (500–3,000 ha) is predicted are finally considered under risk of very large fire (>3,000 ha) when the LST anomaly is positive.

Risk thresholds	**Low** $^{(1)}$	**Ignition (<500 ha)**	**Large fire (>500 ha)**$^{(2)}$	**Very large fire (>3,000 ha)**
SM (m^3/m^3; 3rd quartile)	>0.11	≤0.11	≤0.09	≤0.08
LST (K; 1st quartile)	<300	≥300	≥304	≥306

An example of a final fire risk map is provided in Figure 2.16. The product has been validated using the remaining, randomly selected, 30% of fires. Results show that 87% of small fires, 59% of fires >500 ha, and 56% of fires >3,000 ha have been correctly predicted. The resulting information can be useful for the fire prevention services. In particular, collaboration with the Diputació de Barcelona (DiBa; the provincial government of Barcelona) has been explored, and soil moisture information and the derived risk index here explained have been provided to the forest rangers of this institution during two summer fire prevention campaigns (2015 and 2016). The resulting fire risk maps are also provided through the Barcelona Expert Centre website (BEC, 2018).

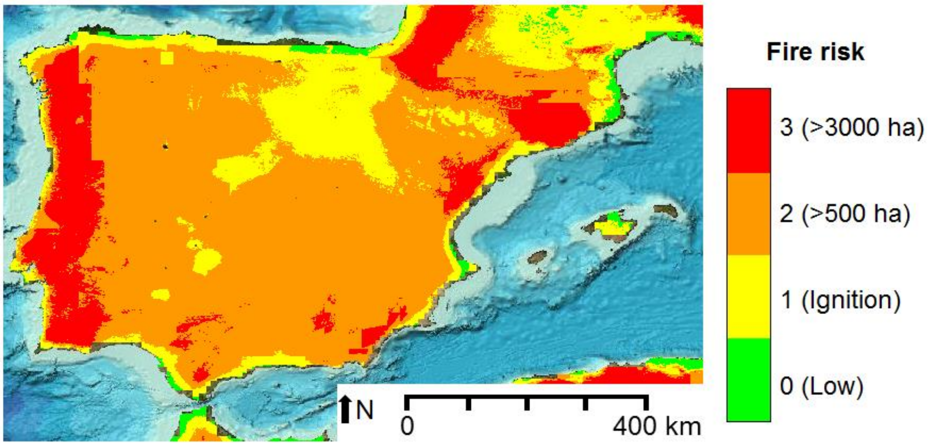

Figure 2.16. Fire risk map for 11th July 2016.

2.9.2. Development of a linear model to predict the potential extension of wildfires

The proposed empirical model is a first approach in the development of a fire risk index partially based in remotely sensed soil moisture. Nevertheless, to improve this preliminary index, a more in deep statistical analysis and the addition of other variables in the methodology are required. To that purpose, soil moisture and temperature are plotted against burned area, which has been logarithmically transformed (decimal logarithm). Figure 2.17 shows that the distribution results in triangle shaped plots where both moisture and temperature limit the fire extent.

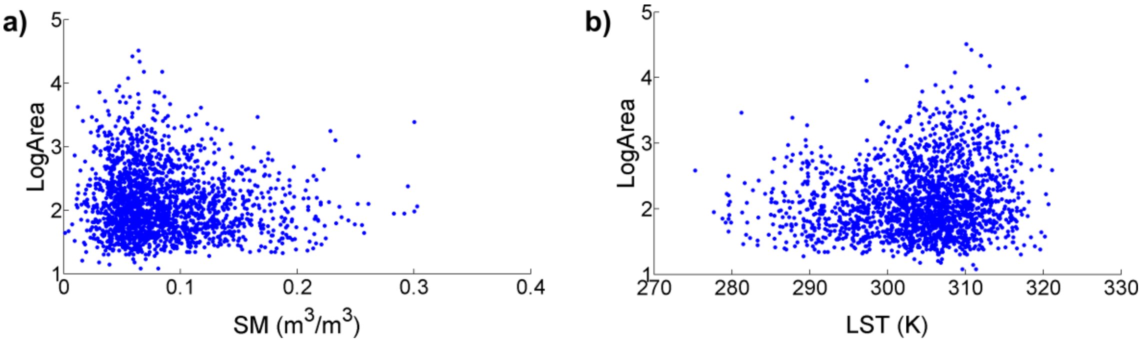

Figure 2.17. Decimal logarithm of the burned area (originally in hectares) for wildfires between 2010 and 2014, plotted as a function of (a) soil moisture and (b) land surface temperature.

From the previous plots, the imaginary hypotenuse of each triangle delimits the maximum burned area at different values of SM or LST. As there is no strong redundancy between moisture and temperature (r = −0.54; Pearson correlation coefficient), the two variables can be combined to estimate the maximum burned area for particular SM-LST conditions. To that purpose, it has been necessary to define bins for SM and LST, and assign a value of maximum burned area to each bin. This approximation is founded on other studies based on triangular-shaped relationships between environmental variables (Moran et al., 1994; Sandholt et al., 2002). Here, in order to increase the sample, it has been decided to include in the regression all wildfires larger than the 90th percentile of burned area for each bin. Forest fires with moisture and temperature at the extremes of the variables' ranges (i.e., beyond percentile 5 for SM, and beyond percentile 95 for LST) are eliminated, as the sample of fires is reduced in these conditions and does not show a representative maximum according to the moisture-temperature data. Model fitting is carried out randomly sampling a 70% of the dataset, while the remaining 30% will be used later for validation. The linear regression explored is:

$$LogArea \approx \alpha \cdot SM_{HR} + \beta \cdot LST, \tag{2.1}$$

where $LogArea$ corresponds to the decimal logarithm of burned area, SM_{HR} stands for high resolution soil moisture, and LST for land surface temperature. Their corresponding coefficients are α and β. Higher order models do not improve the fitting (results not shown). To study the impact of the bin width on the results, several binning possibilities (from [0.005 m^3/m^3 – 0.5 K] to [0.02 m^3/m^3 – 2 K]) are explored. The best regression in terms of R^2 is obtained for the [0.01 m^3/m^3 – 2 K] binning (R^2 = 0.43). For this case, the sample is of 183 wildfires and SM and LST values range from 0.03 to 0.17 m^3/m^3 and from 289.8 to 314.3 K, respectively. The relationship among the studied variables is shown in Figure 2.18, where the complementarity between SM and LST is observed again: the largest fires burn in the driest and the warmest soils. For instance, most of the bins with maximum spread ≥1,000 ha (ie. LogArea ≥ 3) present SM≤0.10 m^3/m^3 and LST≥300 K.

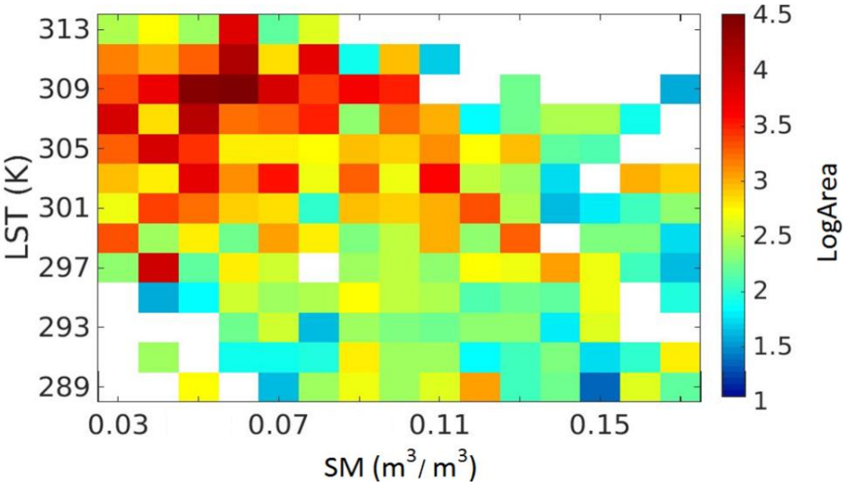

Figure 2.18. Decimal logarithm of maximum burned area (originally in hectares; colorbar) per SM-LST bins. Bins of 2K and 0.01 m^3/m^3 led to the model in Eq. (2.1), with R^2=0.43.

Using the model in Eq. (2.1) as a basis, a linear model predicting the potential extent of forest fires is developed including land cover, the month when the wildfire occurred, and the region of burning as additional variables. The potential extent is defined here as the maximum area that a fire could reach under particular SM-LST conditions. The interactions soil moisture × month, soil moisture × region, and temperature × region are also included in the model as their effects are significant. The interaction soil moisture × land cover and the interactions combining land surface temperature with month and land cover are not significant and are therefore excluded. Eight land cover categories are considered: broadleaved forests, coniferous forests, mixed forests, heathlands and moors, sclerophyllous vegetation, natural grasslands, woodland-shrub transitions, and sparse vegetation areas. Concerning to months, the analyzed forest fires occurred in February, March, April, June, July, August, September, and October. Wildland fires occurring in other months, as well as those burning in agricultural areas do not reach a minimum sample ($n \geq 5$) and are discarded. The same happens for the Portuguese regions of Alentejo, Algarve, and Atlantic-Centre regions (Figure 2.4), where the amount of data is insufficient. As a result, the model only takes into account the northernmost regions of Portugal. The final sample is of 168 forest fires (see Table 2.4). The resulting model can be expressed as:

$$LogArea \approx \delta + M + LC + R + \alpha_{(M,R)} \cdot SM_{HR} + \beta_{(R)} \cdot LST, \tag{2.2}$$

where δ is the intercept corresponding to the logarithm of the potential burned area in the northern Peninsula, on February, for a broadleaved forest land cover. M, LC, and R correspond to the additive terms of month, land cover, and region, respectively. The term $\alpha_{(M,R)}$ is the slope for SM_{HR}, which depends on the month and the region, and $\beta_{(R)}$ is the slope for LST, which depends on the region. The coefficients and terms of the model are reported in Table A.1 in Appendix A.

As some months have been excluded in the proposed model, it is necessary to provide a complementary equation without the variable month, which could be validated and later used in operational applications during January, May, November and December. This model contains the same terms and structure detailed in Eq. (2.2) with the only difference that months are eliminated:

$$LogArea \approx \delta + LC + R + \alpha_{(R)} \cdot SM_{HR} + \beta_{(R)} \cdot LST \tag{2.3}$$

Similarly, agricultural lands are not considered in the main model, so a complementary equation excluding the land cover variable is used for these areas:

$$LogArea \approx \delta + M + R + \alpha_{(M,R)} \cdot SM_{HR} + \beta_{(R)} \cdot LST \tag{2.4}$$

Table 2.4. Sample of the model in Eq. (2.2): number of wildfires studied for each variable and interaction.

Variables		Sample
Soil Moisture		168
Land Surface Temperature		168
Month	February	7
	March	33
	April	7
	June	7
	July	10
	August	58
	September	23
	October	23
Land cover	Broadleaved forests	10
	Coniferous forests	6
	Mixed forests	8
	Natural grasslands	26
	Heathlands and moors	33
	Sclerophyllous vegetation	16
	Wood-shrubland transition	51
	Sparse vegetation	18
Region	Central Peninsula	6
	Mediterranean	12
	North	50
	Northeastern Portugal	25
	Northwestern Portugal	75

2.9.3. Results

The model defined in Eq. (2.2) explains 65.1% of the variance of the potential extension of wildfires. In particular, 33.1% of the variance is explained by soil moisture, 19.8% by land surface temperature, 2.5% by the month when the forest fire occurred, 6.6% by the majorly affected land cover, and 3.1% by the region where the fire took place. The complementary model excluding months (Eq. (2.3)) explains 60% of the variance, while the model without the land cover variable showed in Eq. (2.4) explains 61%.

Dry soils lead to an increased risk of forest fire propagation in most months (Figure 2.19) and regions (Figure 2.20), with the exceptions of northwestern Portugal and the month of September. High temperatures facilitate wildfire spread in the north of the Iberian Peninsula and in northwestern Portugal. Unexpectedly, the effect is opposed in the Mediterranean region (Figure 2.21). No significant effect of temperature is found in the other regions.

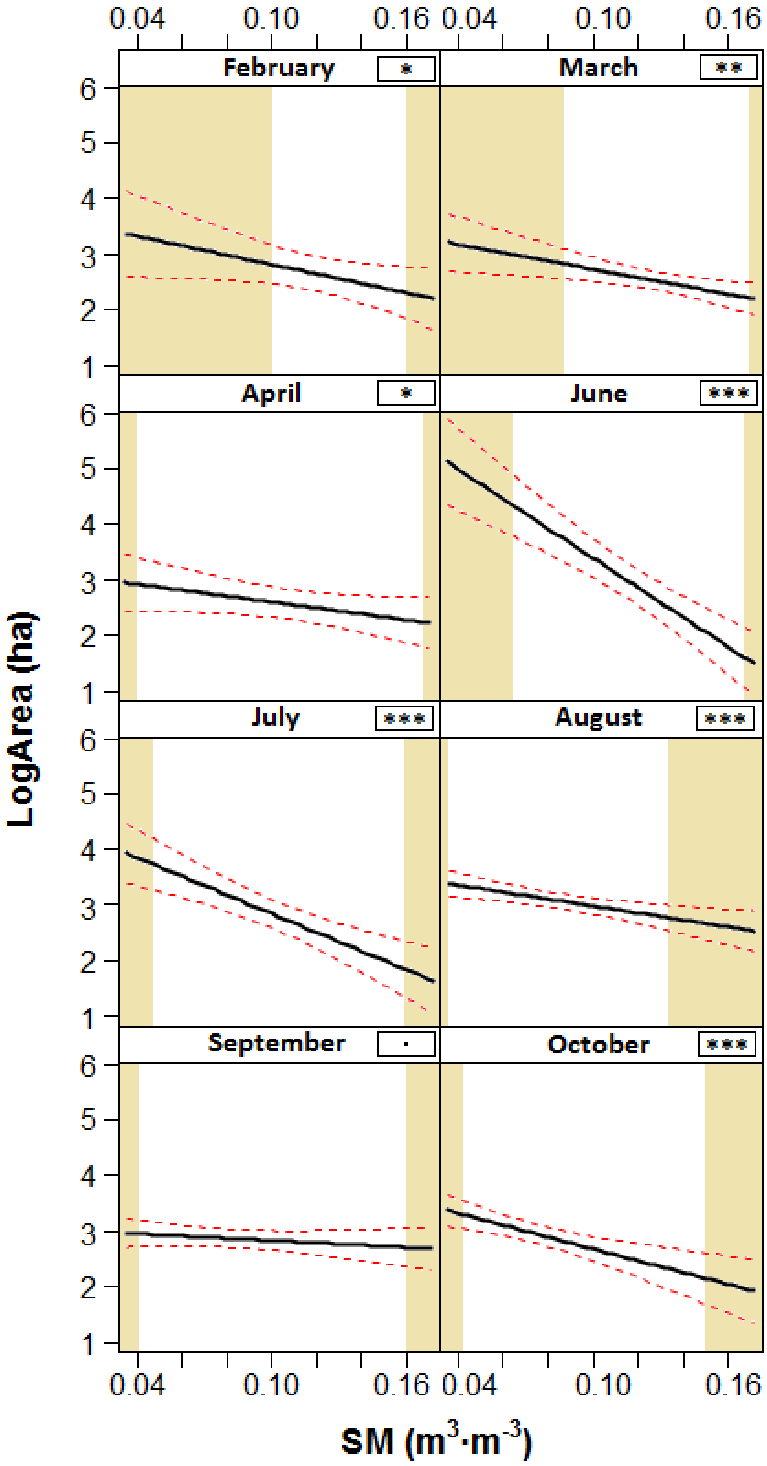

Figure 2.19. Modelled effect of soil moisture on the potential extension of wildfires for each of the significant interactions between soil moisture and month. Black lines show the modelled effects and dashed lines show 95% confidence intervals. Shaded rectangles show moisture values out of the range for each region, where effects are extrapolated. Top-right boxes show the significance of the effects for a given month, as $p < 0.1$ (.), $p < 0.05$ (∗), $p < 0.01$ (∗∗) and $p < 0.001$ (∗∗∗).

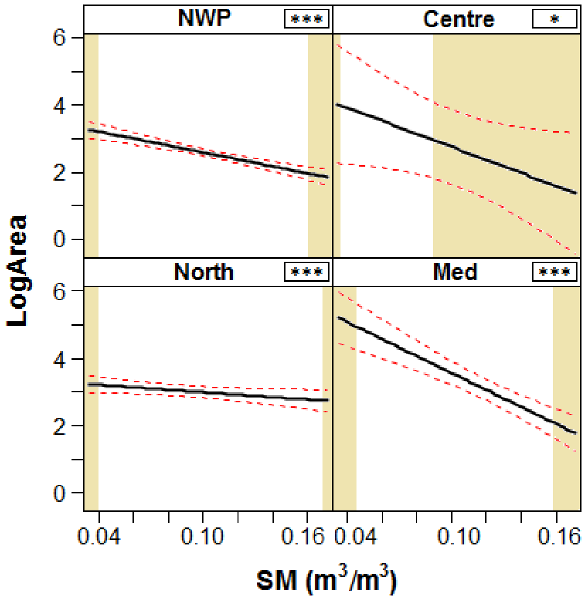

Figure 2.20. Modelled effect of soil moisture on the potential extension of wildfires for each of the significant interactions between soil moisture and regions: northwestern Portugal (NWP), central Peninsula (Centre), northern Iberian Peninsula (North), and Mediterranean (Med). Black lines show the modelled effects and dashed lines show 95% confidence intervals. Shaded rectangles show moisture values out of the range for each region, where effects are extrapolated. Top-right boxes show the significance of the effects for a given region, as $p < 0.1(.)$, $p < 0.05(*)$, $p < 0.01(**)$ and $p < 0.001(***)$.

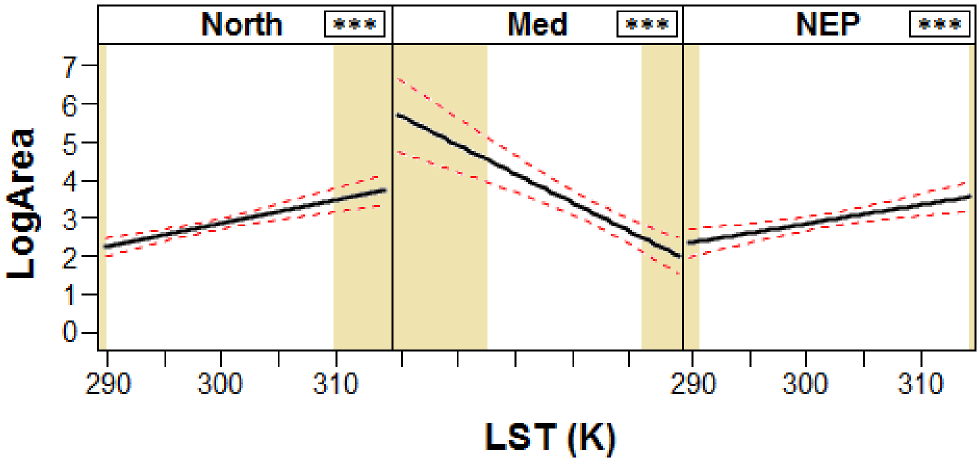

Figure 2.21. Modelled effect of the surface temperature on the potential extension of wildfires for each of the significant interactions between surface temperature and regions: northern Iberian Peninsula (North), Mediterranean (Med) and northeastern Portugal (NEP). Black lines show the modelled effect and dashed lines show 95% confidence intervals. Shaded rectangles show temperature values out of the range for each region, where effects are extrapolated. Top-right boxes show the significance of the effects for a given region, as $p < 0.1(.)$, $p < 0.05(*)$, $p < 0.01(**)$ and $p < 0.001(***)$.

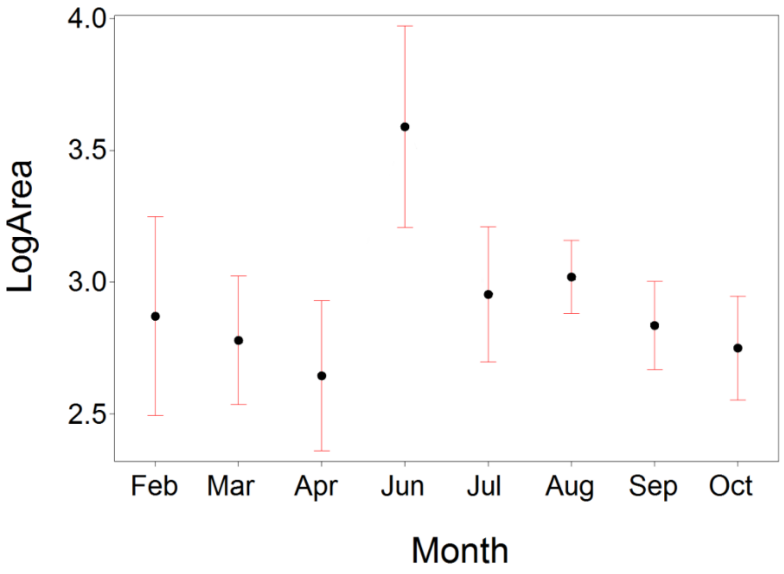

Figure 2.22. Coefficients showing the predicted logarithm of potential burned area (originally in hectares) for each of the studied months in the model. Central black dots indicate the median. Whiskers account for ±1.58 IQR (Inter-Quartile Range).

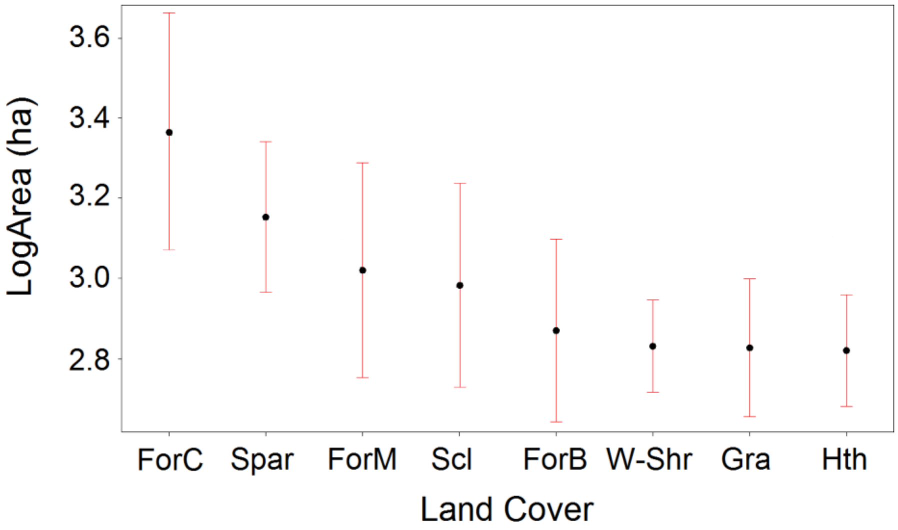

Figure 2.23. Coefficients showing the predicted logarithm of potential burned area (originally in hectares) for each of the studied land covers in the model. Land cover acronyms represent: coniferous forests (ForC), sparse vegetation (Spar), mixed forest (ForM), sclerophyllous vegetation (Scl), broadleaved forests (ForB), wood-shrubland transitions (W-Shr), natural grasslands (Grass), and heathlands and moors (Hth). Central black dots indicate the median. Whiskers account for ±1.58 IQR (Inter-Quartile Range).

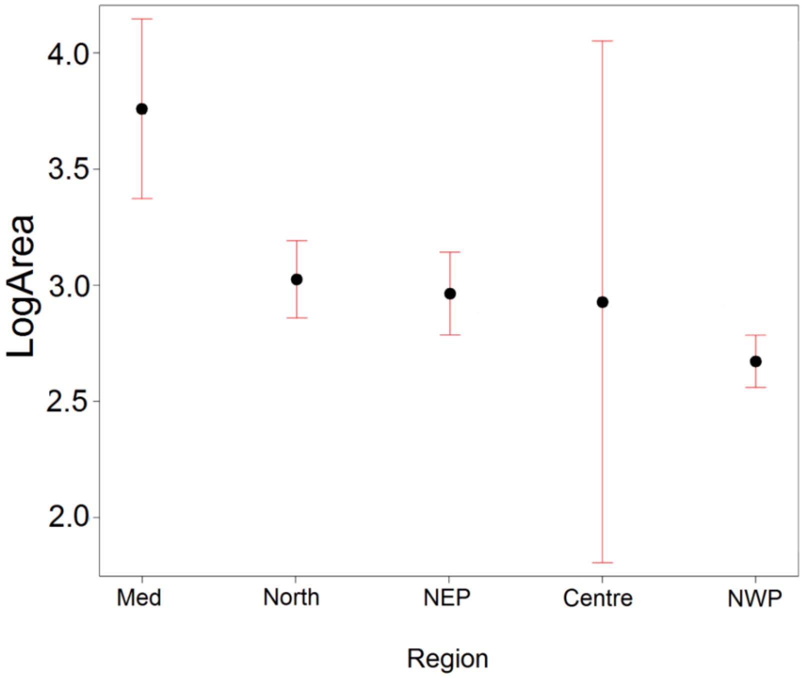

Figure 2.24. Coefficients showing the predicted logarithm of potential burned area (originally in hectares) for each of region in the model: Mediterranean (Med), northern Iberian Peninsula (North), northeastern Portugal (NEP), central Iberian Peninsula (Centre), and northwestern Portugal (NWP). Central black dots indicate the median. Whiskers account for ±1.58 IQR (Inter-Quartile Range).

The highest propagation risk is reported on summer, especially during June (Figure 2.22). Coniferous forests are the land cover with the highest potential spread, while the risk is the lowest in broadleaved forests, grasslands, heathlands and moors, and woodland-shrub transitions (Figure 2.23). The Mediterranean region shows higher risk of large wildfires than other regions (Figure 2.24).

The validation of the model proposed in Eq. (2.2) shows that 83.3% of wildfires are under the predicted maximum extent. The remaining 16.7% shows a maximum error of 40.5 ha. The validation for the complementary model defined in Eq. (2.3) results in 83.5% of accuracy and a maximum error of 44.6 ha. Using the model in Eq. (2.4), the accuracy is of 84.8%. Only one out of the 86 episodes exceeding the extent predicted in Eq. (2.4) presents a very large error (1,487 ha), while the remaining fires have a maximum error of 40.8 ha.

2.9.4. Discussion

A. Soil moisture and land surface temperature condition wildfire spreading

SMOS-derived soil moisture is found to be an important explanatory variable in evaluating fire propagation, in particular the potential extent of wildfires. Results show that wet soils strongly limit burned area in the Iberian Peninsula whereas drier soils increase the potential risk of large forest fires (Figure 2.17). This result is consistent with similar studies in other regions of the world (Bartsch et al., 2009). Also, as expected, an inverse effect is found for surface temperature (Figure 2.17).

A relationship among soil moisture, surface temperature and burned area is reported considering the largest fires in each combination of moisture-temperature conditions. Not surprisingly, a considerable percentage of fires occurred under high temperatures and dry soils, but low soil moisture and high temperatures did not directly determine fire ignition or burned area (Figure 2.17). In that sense, note that in high fire risk situations, the final burned area may not be in agreement with the extent predicted by fire risk indices (Moreno et al., 2005), as other factors such as fire extinction capacity are not considered. Indeed, wildfire ignition and spreading are strongly linked to a wide range of variables related to human, weather and biogeographical factors not included in the model (see Whelan, 1995; Padilla and Vega-García, 2011; and Sections 2.1 and 2.2). For instance, the contribution of wind is essential in most cases, and the inclusion of this variable in combination with moisture and temperature must be a next goal in this research line (see Section 6.3).

Among the studied variables, land cover explains approximately a 7% of the potential burned area. The land cover which results more vulnerable to wildfire spread is coniferous forests (see Figure 2.23). The fact that conifers are prone to fire propagation is also found in previous works, which also stress that broadleaved forests are less dangerous areas (Bajocco and Ricotta, 2008; Verdú et al., 2012), coherently with the results here obtained. In contrast, unexpectedly, wildland fires burning in sparse vegetation covers reach important sizes (see Figure 2.23). We suggest that, possibly, part of this lands might correspond to abandoned crops intermingled with other vegetation areas. In that sense, it is interesting to note that burned area in the Iberian Peninsula during the last decades (1961–2005) is increasing in non-forested areas and decreasing in forests (Moreno et al., 2005). Nevertheless, a more detailed analysis of this land cover type would be needed to understand this effect. Also, the median burned area in mixed forests and sclerophyllous vegetation is higher than in the remaining land covers. Finally, note that the described effects of land covers on fire extension can be related also to other factors affecting fire propagation. For instance, coniferous forests are partially located in areas where topography facilitates the rapid spread of fires, and limits the accessibility of fire extinction services.

The region accounting with the highest propagation risk is the Mediterranean (see Figure 2.24), and the effect of dry soils increasing burned area is evident in this region (Figure 2.20). These results are coherent with the climate-fire link in the region. Nevertheless, the effect of temperature on fire spread is unexpected in the Mediterranean. Actually, the relationship between burned area and surface temperature is negative (see Figure 2.21). This might be explained by (i) the strong influence of soil moisture on the predicted potential burned area in the Mediterranean, (ii) the importance of other factors not considered in this study (e.g., wind and orography), and (iii) the fact that the studied forest fires in the region occurred in hot conditions (>297 K). The latter point suggests that surface temperature could be a factor weakly conditioning the extent of large wildfires burning in the warmest soils. A similar conclusion could be drawn in the central Iberian Peninsula, where no relationship is found between burned area and temperature, and forest fires burned at temperatures higher than 306 K. However, this is unclear as the sample for the central region is little (n = 6), and the lack of temperature effect is also observed in northeastern Portugal, where the range of temperatures prior to fire occurrences is wider (see Figure 2.21).

In the northern Iberian Peninsula and the north of Portugal, which are the more humid regions, warm and dry soils increase the potential burned area (with the exception of the northwestern Portugal, where only the moisture effect is significant). In these regions, wet soils prevail. Consequently, fuel is largely available, but its low flammability limits the spread of wildfires. Generally, large forest fires occur in humid regions when drought and/or heat events dry the available fuel (Verdú et al., 2012). This can explain the effect of dry soils and high temperatures increasing propagation risk in these regions. A similar effect is found in dry soils of the central Iberian Peninsula (see Figure 2.20 and Figure 2.21).

Finally, dry soils increase the potential extent of fires during most months, and especially in summer time (see Figure 2.19), possibly being a trigger factor at high temperatures. Also, summer months are the ones with higher burned area. However, the increased effect on June is probably due to a limited sample (n = 7; Figure 2.22).

B. Predicting potential burned area as a risk of fire propagation

The model proposed in Eq. (2.2) explains that an important part of the variance (65%) of the potential burned area is a function of the moisture-temperature conditions, land cover, the region of occurrence, and the month when the fire burned. The validation shows 83.3% of agreement with a maximum error of 40.5 ha.

Soil moisture explains 33% of the variability of the potential burned area. This result suggests that the use of remotely sensed soil moisture at L-band could help anticipating forest fires extension in the Iberian Peninsula. In addition, the near real time availability of the SMOS dataset in the region facilitates its use in early warning systems. The applicability of land surface temperature in fire prevention services is promising, but future research is mandatory -especially in the Mediterranean region- to correctly quantify the relationship between surface temperature and fire extension. Additionally, exploring LST satellite-derived datasets to complement modelled temperature data would be desired. However, the cloud-masking of infrared data is a limitation to that objective. Possibly, observations from the Spinning Enhanced Visible and Infrared Imager (SEVIRI) sensor on board of Meteosat Second Generation satellites could contribute to partially overcome this limitation. As LST data is provided every 15 minutes by this sensor, the probability to avoid cloud masking during part of the day would increase.

Regarding land cover, region, and month, these variables are easy to obtain and apply. The simultaneous use of the three variables contributes in >10% of the prediction of the potential spread of fires.

A complementary model excluding the month of occurrence (Eq. (2.3)) has been developed for validation and future application in the months of January, May, November and December, which account with small samples. Similarly, a model excluding land cover has been defined in Eq. (2.4) and it is applicable in agricultural areas. Both equations have been validated and the results obtained are similar to those from the main model. Also, note that most studied fires burned in the northwestern Iberian Peninsula (see Figure 2.5). The use of a longer fire record would be necessary to neutralize the shifting and to extend the final model to central and southern Portugal. Then, further research including a larger sample (more years of moisture, temperature and forest fires data) is recommended in order to improve the model usefulness. In addition, a longer dataset would help enhancing the reliability of the proposed model, which is limited by the availability of SMOS-derived data (5 years when the study presented in this chapter was conducted).

Despite these limitations, the proposed methodology is the starting point for future research. An updated version of this algorithm can be developed, considering the following recommendations. Firstly, it will be necessary to extend the studied sample with SM, LST and fires data beyond 2014. Secondly, it will be required to combine surface moisture-temperature data with wind information. Thirdly, the moisture-temperature data could be able to complement soil status information within the FWI. Going further, we can stand that the proposed methodology also sets the basis for future research that integrates soil moisture-temperature with other weather-related variables, human-derived factors, orography, and vegetation information (see Section 6.3).

2.9.5. Fire risk maps and future operational implementation

Results show how the suggested methodology provides good approximation to the maximum expected fire spread. Its applicability will increase with its integration in more complex fire spread prediction tools (see Section 6.3) and, as discussed above, future research should provide improved performance for the model. Nevertheless, at this point it is feasible to build the first fire risk maps based on the developed model. In that sense, an example was presented at the European Space Agency's Living Planet Symposium (Prague, May 2016) and is reproduced here in Figure 2.25. To build the map, the predicted potential area was classified in different risk categories according to Table 2.5, in order to ease the interpretation.

Table 2.5. Predicted potential burned area and the associated fire risk categories displayed in Figure 2.25.

Predicted area (ha)	<10 ha	10-100 ha	100-1,000 ha	1,000-10,000 ha	>10,000 ha
Risk category	Low	Moderate	High	Very high	Extreme

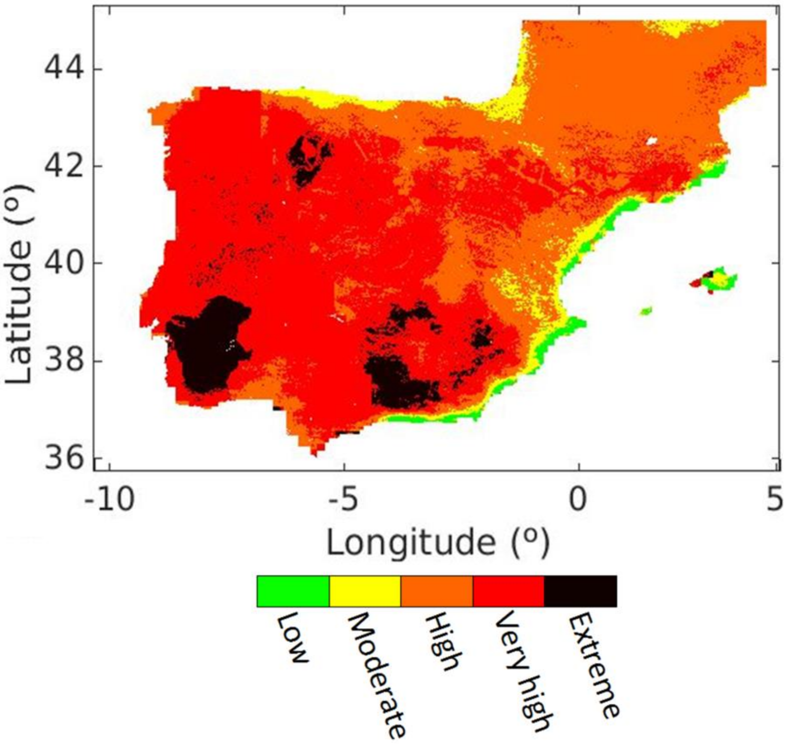

Figure 2.25. Example of a fire risk map (24th June 2010) derived from the linear model built in this chapter. The colorbar shows fire risk categories.

2.10. Conclusions

The European Union's Copernicus programme encompasses the acquisition, management, and dissemination of a wide range of variables needed in fire risk assessment frameworks. The data provided by Copernicus allows a comprehensive approach to the study of fire risk, including information on WUI areas, land covers and land use, topography, vegetation conditions, soil status and weather conditions, among others. It is remarkable that Copernicus also provides fire risk information (FWI), which is in part based on estimating dead fuel moisture conditions from meteorological models. In this work, it is suggested that this information could be complemented –or even enhanced- by soil moisture data derived from L-band microwave radiometry satellite missions. These missions offer global coverage of SM retrievals (overcoming the limited availability of meteorological stations in some regions), and provide a proxy to the water content in fuels. Recent research has demonstrated that the SMOS-derived soil moisture can replace fuel moisture information from other fire risk indices.

In this context, this chapter has studied the relationship between high resolution SMOS SM and fire risk in the Iberian Peninsula, a high fire risk region. The study has been conducted for more than 2,000 fires burning between 2010 and 2014. The SMOS SM information has been complemented with LST modelled data to obtain a better approach on the soil surface state both in normal conditions and in conditions prior to fire outbreaks. The main conclusions of this analysis can be summarized as follows:

- Moisture-temperature patterns are coherent with climates in the region, and reflect the contrast between the northwestern area –colder and wetter- and the Mediterranean area –warmer and drier-. This is consistent with the different fire patterns in these two regions.

- Dry and warm soils are frequent in the region, and this is captured by the studied variables. Fires burn usually –but not exclusively- in these conditions in summer. For this reason, yearly overall medians of moisture and temperature serve to detect the situations in which most fires (75% to 80%) occur, which are generally at SM<0.12 m^3/m^3 and LST>295 K.

- Soil moisture and temperature anomalies detect drought conditions posing risk of fires out of summer season. These variables are able to capture anomalous anticyclonic situations linked to long drought periods, which lead to important fire episodes. Anomalies of SMOS-derived SM show great potential to detect these adverse situations.

- Differences in burned area can be explained in part by moisture and temperature in soils, as the largest fires are linked to the driest and warmest conditions.

Hence, the complementary application of high resolution SMOS soil moisture and modelled LST has great potential to develop new risk assessment tools. In that sense, a preliminary risk index has been built and has been put in operational service. SM-LST thresholds have served to distinguish four risk levels with accuracy between 56% and 87%, depending on the fire risk category. The most dangerous conditions (risk of fires >3,000 ha) have been stablished for very dry soils (<0.08 m^3/m^3) at high temperatures (>306 K).

Finally, an improved model has been built to estimate the potential burned area that a fire can reach under particular SM-LST conditions. The model has considered also information on land cover, region and month of the fire outbreak. Validation resulted on 83.3% of agreement, with a maximum error of 40.5 ha. From the model construction and its results, several conclusions can be drawn:

- SMOS high-resolution data has shown high sensitivity to the potential extension of fires in the Mediterranean and in the northwestern Iberian Peninsula.

- High temperatures increase the risk of fires in some regions, but have an unexpected negative effect in the Mediterranean. It is suggested that other factors (e.g.,moisture and wind) play a major role in fire extension in the region, but also that a larger sample should be studied to confirm or dismiss this result.

- Results are generally consistent for the different land covers and regions studied.

- Future work should be directed to include wind data and remotely-sensed LST in the model, as well as to increase the sample of the model. It is concluded that SM-LST combined data is a potential candidate to include in the computation of the FWI. More details of future work are provided in Section 6.3.

In conclusion, the proposed approach is valid for estimating the risk of propagation of wildfires in the Iberian Peninsula, and has permitted to demonstrate and apply the high potentiality of L-band soil moisture data in fire risk assessment. This opens a new path for improving fire risk prediction tools in a context of changing climate conditions which could increase fire risk in some regions.

3

The role of climatic anomalies and soil moisture in the decline of drought-prone forests

Abstract

Droughts and high-temperatures have been associated to forest decline episodes in many parts of the world. These episodes are expected to become more common under climate change. Therefore, there is a need for monitoring and modelling of forest decline. In this chapter, a forest condition monitoring program (DEBOSCAT) is used to study the spatial distribution of decline events after the extraordinarily dry summer in 2012 in Catalonia (NE Spain). A logistic model to explain forest decline probability was fitted as a function of species, precipitation and temperature anomalies, SMOS soil moisture data, and solar radiation. The statistical model explained almost 40% of forest decline occurrence, wherein almost 50% of this variability was explained by species effect, with broadleaved trees being generally more sensitive to the studied factors than conifers. Climatically wetter areas and those more exposed to radiation were more likely to be affected, suggesting better adaptation of forests in dry areas. In general, more damaged forests were characterized by high-positive temperature anomalies, lower than average rainfall, and low soil moisture in summer 2012.

3.1. Introduction

Disturbances associated to severe droughts and heatwaves, together with human activities (e.g., land-use pressure) endanger the health of the forestry regions on Earth. As a consequence, forest decline episodes have been detected in many regions and are projected to expand under changing climate conditions. Nowadays, the determinants of forest decline are still uncertain, and specific research on the effects of droughts on forest conditions is required (see Section 1.2.2). The lack of programs monitoring forest dieback at regional to global scales using standardized protocols and surveying exhaustively all forested lands greatly limits the capacity to draw strong conclusions on the vulnerability of different forest types or different areas within the distribution of a given species (Allen et al., 2010; Martínez-Vilalta et al., 2012a; Trumbore et al., 2015). At regional or continental scales, the available studies tend to use the databases assembled for national forest inventories (Klos et al, 2009; Vilà-Cabrera et al., 2011; Ruiz-Benito et al., 2013; Neumann et al., 2017). However, the applicability of large-scale forest inventories to tree mortality research suffers from important limitations, including low temporal resolution (typically ~10 years) and/or low number of trees sampled per plot, which limits the capability to detect and quantify relatively random and usually infrequent events (Stokland et al., 2005).

In this chapter, one of the few existing yearly regional monitoring programs has been used. The DEBOSCAT (Forest Decline in Catalonia) program covers the forests of Catalonia (northeastern Spain) from 2010, registering areas >0.03 km^2 in which trees are affected by mortality, and/or leaf loss, and/or discoloration. In this research, the decline occurrences detected by DEBOSCAT in 2012 have been associated with meteorological datasets and with the SMOS-MODIS L4 high resolution soil moisture product in order to detect drought conditions threatening forests. The fact that water availability to plants depends critically on soil water content and on the physical properties of soil suggests that the application of a soil moisture product should increase the capacity to explain the drought impacts on vegetation health.

The study is conducted in Catalonia, which has several features that make it particularly suitable to explore the spatial determinants of forest decline: (i) droughts are common in the region and most of its forests are considered to be limited by water; (ii) its predominant Mediterranean climate determines high spatiotemporal variability in temperature and rainfall, which causes particularly severe and spatially complex drought events; (iii) the orography and climate of Catalonia are extremely variable for the size of the region (~32,000 km^2; see Section 3.2.1); and (iv) Catalonia is at the boundary between Mediterranean and Euro-Siberian biogeographic regions, which determines that several species reach their southern (and dry) distribution limit in the area. Previous studies suggested that these species may be particularly vulnerable to increasing drought stress in the study area (e.g., see Jump et al. 2006 for *Fagus sylvatica* or Galiano et al. 2010 for *Pinus sylvestris*).

The main objectives here are (i) to use the DEBOSCAT database together with GIS tools, climatic information and remote sensing soil moisture data to determine the main environmental drivers of recent forest decline in Catalonia in terms of climate, drought characteristics, and soil water availability, (ii) to establish the vulnerability to drought-induced decline of the main tree species in Catalonia, and (iii) to evaluate the applicability of SMOS soil moisture data to explain forest decline occurrence. The main hypothesis in this chapter are: (i) forest decline will affect preferentially areas with high-temperature anomalies, high drought intensity, and low soil moisture; (ii) climatically drier sites will not necessarily be more vulnerable to drought-induced forest decline, due to the greater drought resistance of the dominant vegetation in these areas; and (iii) Euro-Siberian species reaching their southern distribution limit in the Iberian Peninsula (particularly *Fagus sylvatica* and *Pinus sylvestris*) will be more vulnerable than typically Mediterranean species (i.e., *Quercus ilex*, *Quercus suber*, or *Pinus halepensis*).

3.2. Data and methods

3.2.1. Study area

The forested area of Catalonia (42° 51′N–40° 31′N, 0° 9′E–3° 19′E; Figure 3.1) has been studied. Most of the study area has a typical Mediterranean climate, with mild winters and hot dry summers, with an irregular pattern of precipitation among years. Mean annual rainfall ranges from 336 to 1,464 mm and mean annual temperature from 0 to 17.3 °C (see Figure 3.2 a and b; Ninyerola et al., 2003; SMC, 2018). Different relief units influence climate and vegetation. Colder and wetter conditions are found in the Pyrenees mountain ranges (up to 3,150 m), in the north of the region. Much drier climates occur along the coast and particularly in the central depression, where rainfall is <500 mm/year, and there is a noticeable continental influence (see Figure 3.2 a and b). Otherwise, coastal ranges (up to 1,700 m) present mild temperatures due to maritime influence, although conditions vary depending on elevation and distance to the coast.

Severe drought events are common in the study area. The most recent ones were registered in 2012 and 2016, which were preceded by the period October 2004–October 2008, the driest and longest drought event registered in the last 100 years in northeastern Spain (Altava, 2010). This chapter focuses on the drought registered in 2012 which -although not as severe as its preceding period- was also important, especially in winter, when the accumulated precipitation was 70%–100% lower than the climatic mean (e.g., less than 25 mm in the west areas of the country; SMC, 2012a). The spatial distribution of precipitation during spring was irregular with northern and central areas above the mean (+10% to +100%) and northeastern, western, and southern areas being drier (10% to 70% lower than the climatic average; SMC, 2012b). During summer, the accumulated precipitation registered values between −30% to −100% below the mean in almost all Catalonia, particularly in northeastern regions (SMC, 2012c). Temperature and rainfall anomalies (the latter measured using the SPI) for summer 2012 are given in Figures Figure 3.2d and Figure 3.3a, respectively. Mean summer temperature anomaly was +1.6 °C for 2012 and it was positive throughout the study area (Figure 3.2d).

Catalan forests occupy more than 11,400 km^2 (nearly 40% of the territory). The most widely distributed species are *Pinus halepensis* (Aleppo pine; 2,430 km^2) and *Quercus ilex* (evergreen oak; 2,004 km^2; CREAF and Generalitat de Catalunya, 2005). Both are Mediterranean species typically coexisting in coastal forests, although *Quercus ilex* has a wider altitudinal range. *Pinus sylvestris* (Scots pine; covering 1,965 km^2) and *Fagus sylvatica* (beech; 336 km^2) are Euro-Siberian species living close to its southern distribution limit (Lloret et al., 2009). *Pinus nigra* (1,070 km^2) grows mostly in the pre-Pyrenees and Catalan inlands. Deciduous oaks are also abundant, mainly *Quercus pubescens* (820 km^2) and *Quercus faginea* (325 km^2) (CREAF and Generalitat de Catalunya, 2005; Lloret et al., 2009).

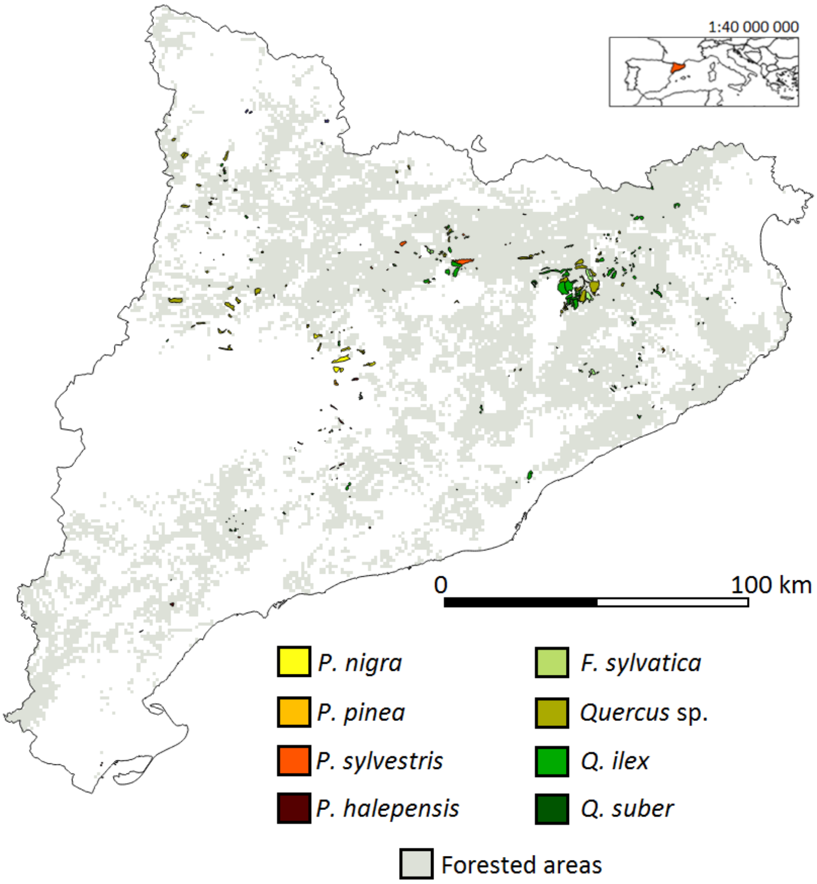

Figure 3.1. Map of Catalonia showing the location (1 km × 1 km resolution) of forests affected by 2012 decline events (colors represent the dominant species within each episode) and unaffected forested areas (grey). Top right corner map shows the location of Catalonia in southern Europe.

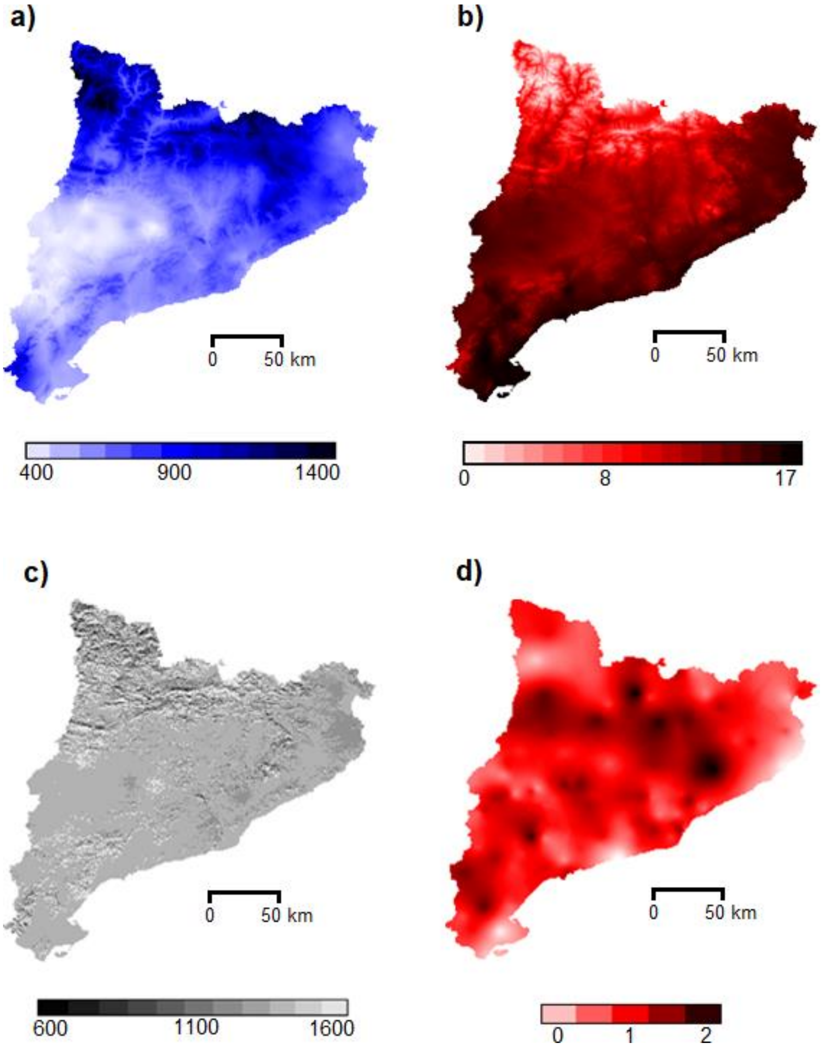

Figure 3.2. (a) Mean annual accumulated precipitation (mm) for the period 1950–1998; (b) mean annual temperature (°C) for the period 1950-1998; (c) mean daily solar radiation (10 $kJ/m^2 \cdot day$) for the period 1950-1998 and (d) summer temperature anomaly (°C) in summer 2012. Data for panels (a)–(c) were obtained from the Climatic Digital Atlas of Catalonia (Ninyerola et al., 2003). Data for panel (d) was provided by the Catalan Meteorological Service (SMC).

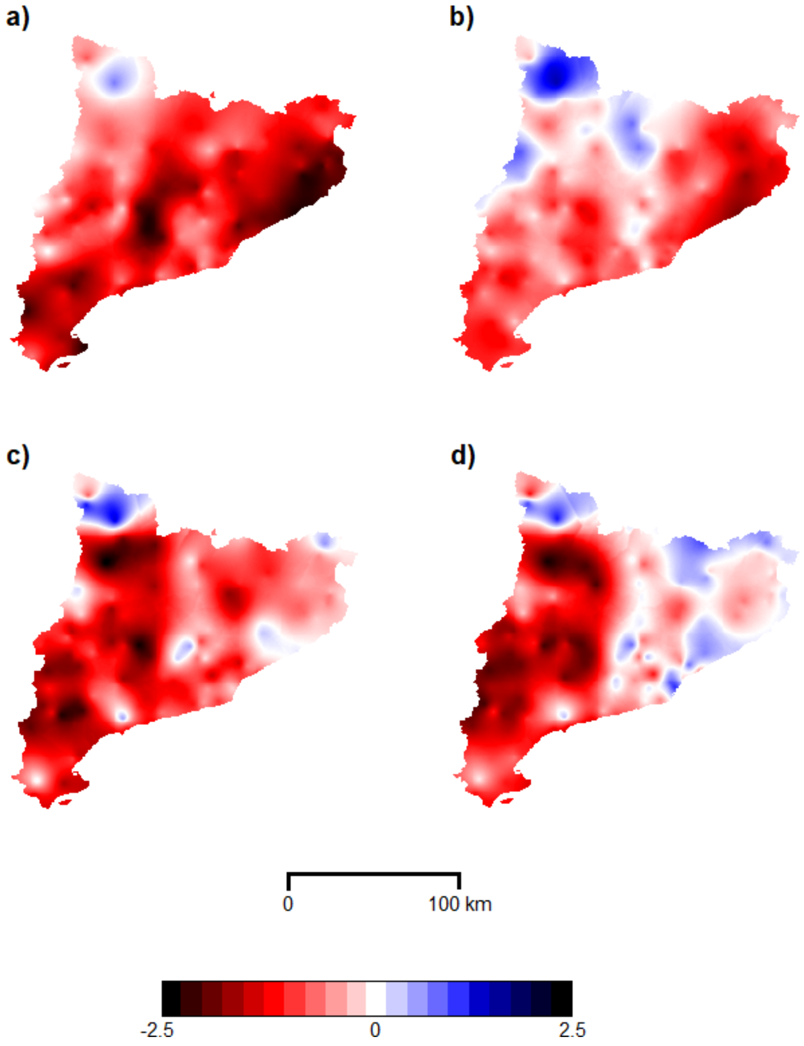

Figure 3.3. SPI (McKee et al., 1993; see Section 3.2.3) calculated for different time periods: (a) June–August 2012 (SPI3); (b) March–August 2012 (SPI6); (c) September 2011–August 2012 (SPI12) and (d) September 2010–August 2012 (SPI24). SPI is a dimensionless variable. Positive values indicate precipitation above the mean and negative values indicate precipitation below the mean. Reference period: 1961–2013. Provided by the SMC.

3.2.2. Forest condition database (DEBOSCAT)

DEBOSCAT is a monitoring program started in 2010 to assess health condition in all the forests in Catalonia. The project is coordinated by the Centre for Ecological Research and Forestry Applications (CREAF, Barcelona, Spain). All the forests in Catalonia are surveyed annually (in September) by forest rangers deployed by the Catalan Government in order to detect forest decline events after summer. Forest decline events are defined as areas >0.03 km^2 in which tree mortality is higher than 5% or the sum of leaf loss plus discoloration exceeds 50% in the canopies of at least one abundant tree species (with >15% canopy cover). Each event is identified by a unique code, and the recorded information includes: (i) exact geographical location and perimeter of the affected area, (ii) the abundance of the dominant species (in terms of canopy coverage) and (iii) the percent of crowns affected and the type of damage (mortality, discoloration and/or leaf loss) for each species. All the registered events are transferred to a GIS layout with its corresponding database (Banqué et al., 2013). Validations of the DEBOSCAT survey have been conducted by an independent team showing good agreement between different observers, as the percentage of estimated non-damaged trees [i.e., 100 – (% mortality + % discoloration + % leaf loss)] is within 10% of the initially estimated value in 81% of cases (N = 20 resampled events; M. Banqué, unpublished results).

In this study, the recent events detected in 2012 have been analysed, as the surveys from previous years (2010 and 2011) were preliminary and have been used here only to determine which events correspond to new 2012 occurrences. Additionally, events detected in 2014 have been also studied to assess forest recovery. DEBOSCAT registered more than 230 km^2 newly affected in 2012, distributed in 340 events (see Table 3.1; Banqué et al., 2013) which are shown in Figure 3.1. Each event could contain more than one affected species, but this analysis only retains combinations of events by species for which mortality was >5% or (discoloration + leaf loss) occurred in >25% of the canopies to ensure that affectation was high in all instances (note that not all species within an event fulfilled the 50% criteria stated in the previous paragraph). Only 11.8% of the combinations of events by species in the database have a percentage of discoloration + leaf loss between 25% and 50%. This work focuses on the most affected species and merges all deciduous oaks into one single category (deciduous *Quercus*, including basically *Quercus pubescens* and *Quercus faginea*) due to the high morphological and ecophyisiological similarity of the species and due to the fact that they frequently hybridize in the study area (Sánchez de Dios et al., 2006). Hence, the studied species are deciduous *Quercus*, *Quercus ilex*, *Quercus suber*, *Fagus sylvatica*, *Pinus sylvestris*, *Pinus nigra*, *Pinus halepensis*, and *Pinus pinea*. These species dominate 75% of the forests in Catalonia and represent 99% of the events detected in 2012. Once all the episodes fulfilling the mentioned criteria have been chosen, the final database contains a total of 288 out of the original 340 events (84.7%; see Table 3.1 and Figure 3.1). For deciduous species (deciduous *Quercus* and *Fagus sylvatica*), the timing of DEBOSCAT field surveys (early September) ensures that the events reported do not overlap with autumn leaf shedding (starting approximately in late October in the study region).

In order to compare affected events with unaffected areas, the Land Cover Map of Catalonia (CREAF and Generalitat de Catalunya, 2005) has been used. A 1 km × 1 km grid has been created and each cell in the grid has been linked to the modal species of the land cover map.

Grid cells have been classified as affected, if at least 10% of its surface overlapped with a polygon affected by forest decline, or unaffected, if there are no events overlapping the corresponding cell, or they cover <10% of the cell's surface. In the few cases in which an event does not cover more than 10% of the surface of any cell, the event has been assigned to the most affected cell. To assess the impact of this 10% threshold on the results, the analyses have been repeated using higher threshold levels (20%, 30%, 40%, and 50%), confirming that they do not change the main results (not shown).

Table 3.1. Decline events detected in 2012 by species in terms of number of events, affected area, percentage in relation to total affected area, total area occupied by each species, and percentage of the total area occupied that was affected. Data on decline events were obtained from the DEBOSCAT survey, and species distribution areas were obtained from the land cover map of Catalonia (CREAF and Generalitat de Catalunya, 2005).

Species	**Events**	**Affected area (km^2)**	**% affected**	**Occupied area (km^2)**	**%**
Dec. *Quercus*	219	100.10	42.39	1260.76	7.94
F. sylvatica	36	19.29	8.17	336.11	5.74
Q. ilex	205	82.02	34.74	2003.50	4.09
Q. suber	26	5.38	2.28	608.32	0.88
Broadleaved species	**486**	**206.79**	**87.58**	**4208.69**	**4.91**
P. nigra	39	9.87	4.18	1070.44	0.92
P. sylvestris	42	8.05	3.41	1965.43	0.41
P. pinea	18	0.90	0.38	332.25	0.27
P. halepensis	38	4.51	1.91	2429.54	0.19
Conifers	**137**	**23.33**	**9.88**	**5797.66**	**0.40**
Other species	66	6.00	2.54	1397.43	0.19
Total	**340***	**236.12**	**100.00**	**11403.78**	**2.04**

*Total of events is lower than the addition of events for each species because one event might contain more than one species. The study finally contained a total of 288 events (the remaining 52 were not considered because they affected species that were not included in this study or the magnitude of the reported damage did not fulfil the criteria).

3.2.3. Environmental databases

Several explanatory variables are used to model the distribution of decline events in summer 2012, including lithology, historical climate characteristics, and specific climatic conditions and soil moisture during summer 2012, which have been obtained as follows:

Lithology has been obtained from the geological map of Catalonia (ICGC, 2010) and has been reclassified in two categories: basic (calcareous) and acidic (siliceous) soils. Historical climate data have been used to characterize "long-term," average conditions, and have been obtained from the Climatic Digital Atlas of Catalonia (Ninyerola et al., 2003) for the period 1950–1998. This data include mean annual and summer (June to August) temperatures, mean accumulated annual and summer (June to August) precipitations, and mean annual solar radiation. All variables have been upscaled from 180 m × 180 m to 1 km × 1 km resolution using a bilinear interpolation method.

The SPI has been used to characterize drought intensity at different time scales. Essentially, the SPI for a given month is calculated as the difference between the mean precipitation for the previous n-months and the mean for a reference time period, divided by the standard deviation for that reference period (McKee et al., 1993). The SPI data used has been provided by the SMC for periods of 3 months (SPI3: June 2012–August 2012), 6 months (SPI6: March 2012–August 2012), 12 months (SPI12: September 2011–August 2012), and 24 months (SPI24: September 2010–August 2012) (see Figure 3.3). The reference period corresponds to years 1961–1990. Map resolution is 1 km × 1 km. Negative values indicate drier conditions than the reference (extremely drier below −2) and positive values reflect wetter conditions (extremely wetter above +2; McKee et al., 1993). The temperature anomaly in summer 2012 (ΔT_summer) has been provided by the SMC at 1 km × 1 km spatial resolution, and has been calculated as the difference between mean summer temperature in 2012 and mean summer temperature for the period 1961–1990.

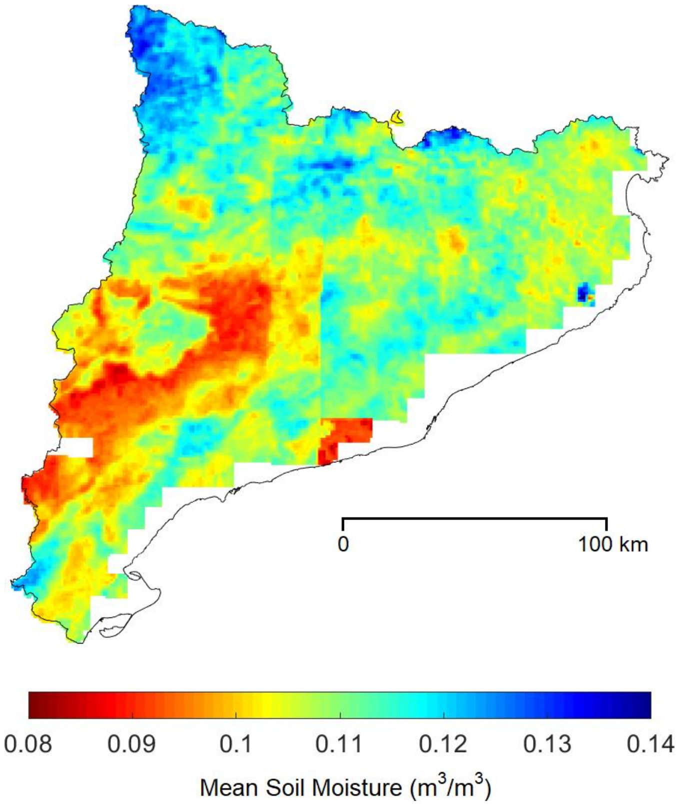

Figure 3.4. Mean soil moisture in Catalonia for the summer 2012. No data are obtained in coastal areas due to inexact transition between SMOS measures.

Daily SMOS-derived soil moisture maps at 1-km spatial resolution (SMOS-MODIS product; see Section 1.3) for summer 2012 (June 2012– August 2012) have been obtained from the BEC (BEC, 2018). For this study, the mean summer soil moisture over Catalonia has been obtained using SMOS afternoon passes (~17 h.; Figure 3.4). Mean values show the dry conditions of the soil during summer 2012, with moisture values ranging from 0.08 to 0.14 m^3/m^3. Although this range is narrow and near to 0.04 m^3/m^3 (the SMOS-derived soil moisture product expected accuracy), this is largely due to the fact that data have been averaged for a period of three months. Daily ranges of SMOS-derived soil moisture are wider than 0.04 m^3/m^3 for more than 90% of the days, and at least twice the expected accuracy for more than 60% of the days.

3.2.4. Statistical methods

Forest decline probability for each species has been modelled as a function of lithology, climate characteristics, specific climatic conditions in summer 2012, and soil moisture, using logistic regression models. Pearson's correlation coefficients (r) have been used to detect redundancy among the explanatory variables (Table 3.2). Whenever a pair of variables presents a correlation $r > 0.51$, the one resulting in a better model fit in terms of the Akaike Information Criterion (AIC) has been chosen and the other one has been rejected, to avoid multicollinearity.

Table 3.2. Correlation matrix between pairs of variables. Each cell shows Pearson's correlation coefficient (*r*).

	P_an	T_sum	P_sum	R_an	ΔT_sum	SPI3	SPI6	SPI12	SPI24	SM
T_an	-0.64	0.98	-0.75	0.15	-0.10	-0.62	-0.70	0.02	0.02	-0.50
P_an		-0.72	0.91	-0.17	0.04	0.33	0.18	0.23	0.46	0.51
T_sum			-0.78	0.17	-0.05	-0.55	-0.61	-0.10	-0.12	-0.55
P_sum				-0.14	0.11	0.49	0.37	0.04	0.33	0.45
R_an					0.07	-0.11	-0.08	-0.11	-0.10	-0.14
ΔT_sum						0.00	0.18	-0.12	-0.03	-0.05
SPI3							0.78	-0.05	-0.06	0.28
SPI6								0.08	-0.08	0.30
SPI12									0.78	0.28
SPI24										0.24

T_an: mean annual temperature (°C); P_an: accumulated annual precipitation (mm); T_sum: mean summer temperature (°C); P_sum: accumulated summer precipitation (mm); R_an: mean annual radiation (10·kJ/m^2·day); ΔT_sum: summer anomaly of temperature (°C); SPI3, SPI6, SPI12 and SPI24: Standard Precipitation Index calculated for 3, 6, 12 and 24 months, respectively; SM: soil moisture (m^3/m^3) derived from SMOS afternoon passes (~17h UTC).

The final set of explanatory variables is composed by species (Tables Table 3.1 and Table 3.3), mean annual precipitation (Figure 3.2a), mean annual radiation (Figure 3.2c), summer 2012 temperature anomaly (Figure 3.2d), SPI3 and SPI12 (Figure 3.3 a and c, respectively), and mean summer SM (Figure 3.4). All the quantitative predictors have been centred and standardized at a global level before fitting the models. As the main focus of this work is on the effects of the specific environmental conditions during 2012, the analysis also considers the interactions between species and summer 2012 temperature anomaly, SPI3, SPI12, and soil moisture. Additional models including the interactions of radiation and precipitation with species have been considered during model selection but do not improve model fit significantly and these interactions have been removed in the final analyses. Similarly, preliminary models have shown that the effect of lithology is not significant and this variable has not been included in the final models.

Table 3.3. Number of unaffected and affected cells included in the final model for each species.

	Cells	
Species	Unaffected	Affected
Quercus ilex	354	373
Fagus sylvatica	55	108
Pinus halepensis	627	40
Pinus pinea	61	10
Pinus sylvestris	483	59
Pinus nigra	247	40
Deciduous *Quercus*	164	422
Quercus suber	163	24
TOTAL	**2154**	**1076**

To avoid a highly unbalanced sample due to the higher number of unaffected entries in the dataset, only a random subset of unaffected entries corresponding to twice the number of affected ones has been used (Table 3.3). This random resampling has been done globally, and not per species, because the interest of the study is on the general capacity of the model to explain decline occurrence in the study area (with its current distribution of different forest types) and not necessarily in capturing the true decline probabilities by species. Although modelled decline probabilities do not necessarily represent the species' absolute decline probabilities, the relative probabilities across species are conserved (see Albert and Thuiller, 2008). The random selection has been repeated ten times to ensure that the main results are robust to this selection (see Table A.2 in Appendix A). The residuals of the final model have shown only moderate spatial structure at small spatial scales (below 20 km). The variance inflation factors (VIF) for the model variables have been used to quantify the severity of multicollinearity. VIF is >5 only for SPI3 (VIF = 6.48). To explore the potential effect of multicollinearity in this study, the model has been refitted without this variable. Results show that remaining model coefficients are similar to those in the original model in terms of significance, sign, and magnitude (results not shown), implying that multicollinearity does not have a major influence in this case. In the final model, predicted probabilities of being affected have been compared with the binary information from the observed dataset, and model performance has been assessed using the area under the receiver operating characteristic curve (AUC). Significance for all statistical analyses has been accepted at $p < 0.05$.

3.3. Results

3.3.1. Overview of forest decline events detected in 2012

A total of 340 new decline events were detected in September 2012, affecting 236.12 km^2 (2.1% of total forested area in Catalonia). These events impacted mostly broadleaved species, both in absolute terms (number of events and area affected) and in relative terms (in relation to the overall distribution area of each species). The percentage of the species' distribution area affected ranged from 0.9% (*Quercus suber*) to 7.9% (deciduous *Quercus*) in broadleaved species, and between 0.2% (*Pinus halepensis*) and 0.9% (*Pinus nigra*) in conifers (see Table 3.1). Deciduous *Quercus* forests accounted for 42% of all affected areas, *Quercus ilex* accounted for 35%, and *Fagus sylvatica* for 8.2%. Conifers were much less affected and, overall, accounted for only 10% of the impacted areas. In absolute terms, *Pinus pinea and Pinus pinaster* were the least affected species, whereas *Pinus halepensis* was the least affected in relative terms, as only 0.19% of its distribution area was damaged (Table 3.1).

Table 3.4. Number of episodes per species and % of episodes with standing mortality >5%, in 2012. The number of decline episodes in 2014 is also shown.

Species	Episodes		
	Number (2012)	% Mortality (2012)	Number (2014)
Quercus ilex	205	62.0	228
Fagus sylvatica	36	0	14
Pinus halepensis	38	34.1	64
Pinus pinea	18	54.5	43
Pinus sylvestris	42	86.7	136
Pinus nigra	39	56.1	84
Deciduous *Quercus*	219	8.8	172
Quercus suber	26	84	30

The percentage of events affected by mortality varied widely among species, independently of the differences in the amount of decline between broadleaves and conifers. In particular, most species showed mortality in >50% of the episodes, except for *Pinus halepensis* (34.1 %), *Quercus suber* (8.8%), and *Fagus sylvatica*, which was only affected by defoliation and/or discoloration (Table 3.4). Finally, the amount of decline events increased two years later on most species (mainly on *Pinus sylvestris*), but decreased on deciduous *Quercus* and *Fagus sylvatica* (Table 3.4).

3.3.2. Determinants of forest decline

The models explain 36% to 39% of the variance in the decline probability depending on the random selection of non-affected cells (Table A.2 in Appendix A). AUC for the final model is 0.893 (AUC > 0.8 indicates an excellent fit; Hosmer and Lemeshow, 2000). All models give very consistent results in terms of the values of the estimated coefficients and the significance of the effects (Table A.2 in Appendix A) and the following results are based on the model with lowest AIC, which is the final model (39.3% of explained deviance, Table A.3 in Appendix A). Not surprisingly, considering what has been reported in Section 3.3.1, the model identifies species identity as the most influential factor explaining forest decline (Table 3.5). The ranking of species damage predicted by the model follows closely the results reported in Section 3.3.1 (see Figure 3.5). Climatic radiation and precipitation have a positive effect on decline occurrence (Table A.3 in Appendix A).

Table 3.5. Variance explained by the model and by different variables and interactions. The column "Percentage (model)" disaggregates model deviance and the column "Percentage (total)" disaggregates the percentage of total deviance explained by the variables included in the model.

Variable/Interaction	Percentage (model)	Percentage (total)
Null		
R_an	0.20	0.08
P_an	16.50	6.48
Species	50.33	19.76
ΔT_sum	6.92	2.72
SPI3	3.11	1.22
SPI12	4.69	1.84
SM	3.81	1.50
Species x ΔT_sum	3.27	1.28
Species x SPI3	5.11	2.01
Species x SPI12	5.01	1.97
Species x SM	1.04	0.41
	100.00	**39.25**

P_an: accumulated annual precipitation (mm); R_an: mean annual radiation ($10\cdot kJ/m^2\cdot day$); ΔT_sum: summer anomaly of temperature (ºC); SPI3 and SPI12 are Standard Precipitation Index calculated for 3 and 12 months, respectively; SM: soil moisture (m^3/m^3) derived from SMOS afternoon passes (~17h UTC).

Regarding the variables characterizing the environmental conditions during year 2012, they all show significant interactions with species (Table A.3 in Appendix A). The effect of SPI3 and SPI12 on the decline probability is consistently negative, but not always significant, for all species, except for *Pinus sylvestris*. The negative effect of SPI3 on decline occurrence is significant for *Pinus halepensis*, *Pinus nigra*, and *Fagus sylvatica* (Figure 3.6), whereas SPI12 presents significant negative effects for *Pinus nigra*, *Quercus suber*, *Quercus ilex*, and *Fagus sylvatica* (Figure 3.7). Thus, lower rainfall is associated with higher decline. Summer temperature anomaly (ΔT_summer) increases decline probability in most species and has strong and significant effects on all species except *Pinus nigra*, *Pinus pinea*, and *Pinus halepensis* (Figure 3.8). Finally, low values of soil moisture increase the probability of forest decline in all species, with significant effects for deciduous *Quercus*, *Quercus ilex*, *Fagus sylvatica*, *Pinus nigra*, and *Pinus sylvestris* (Figure 3.9).

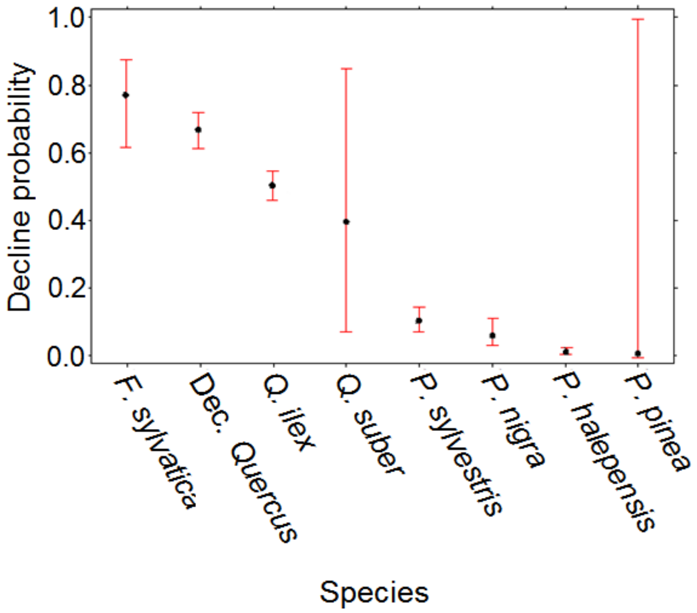

Figure 3.5. Modelled decline probability for each of the studied species in the final model of forest decline occurrence. Central black dots indicate the median probability of suffering decline per species as estimated by the logistic model. Note that these probabilities may not reflect species' absolute decline probabilities (see Section 3.2.4). Whiskers account for +/-1.58 IQR (Inter-Quartile Range).

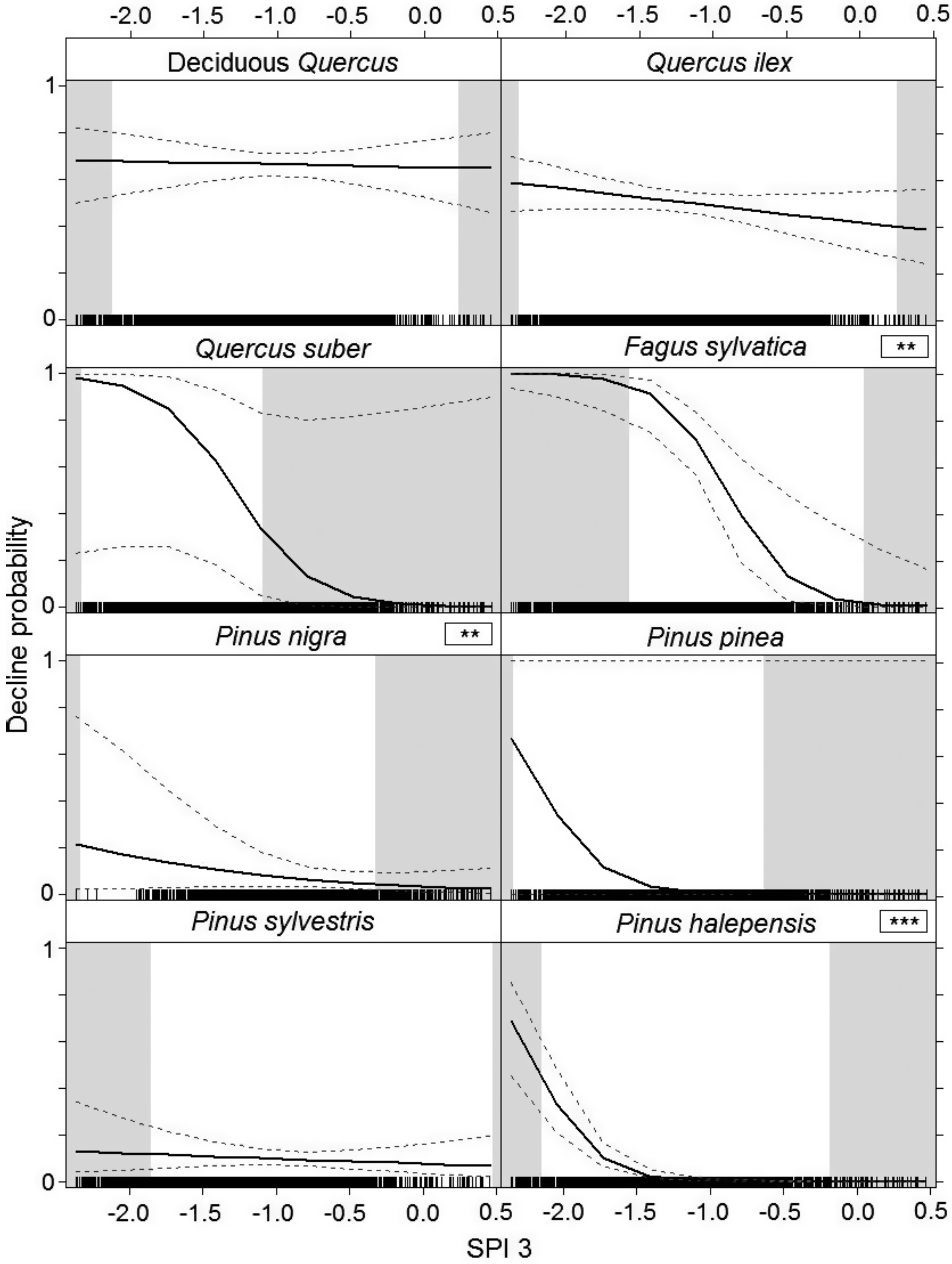

Figure 3.6. Modelled effect of the SPI3 on decline probability for each of the studied species. SPI3 is dimensionless. Values of SPI3 were back-transformed to the original scale for display purposes. Black curves show effects and dashed lines show 95% confidence intervals. Shaded rectangles show SPI3 values out of the range for each species, where effects are extrapolated. Top-right boxes show the significance of the effects for a given species, as $p<0.05$ (*), $p<0.01$ (**) and $p<0.001$ (***). A rug plot is shown giving the marginal distribution of the predictor on the horizontal axis.

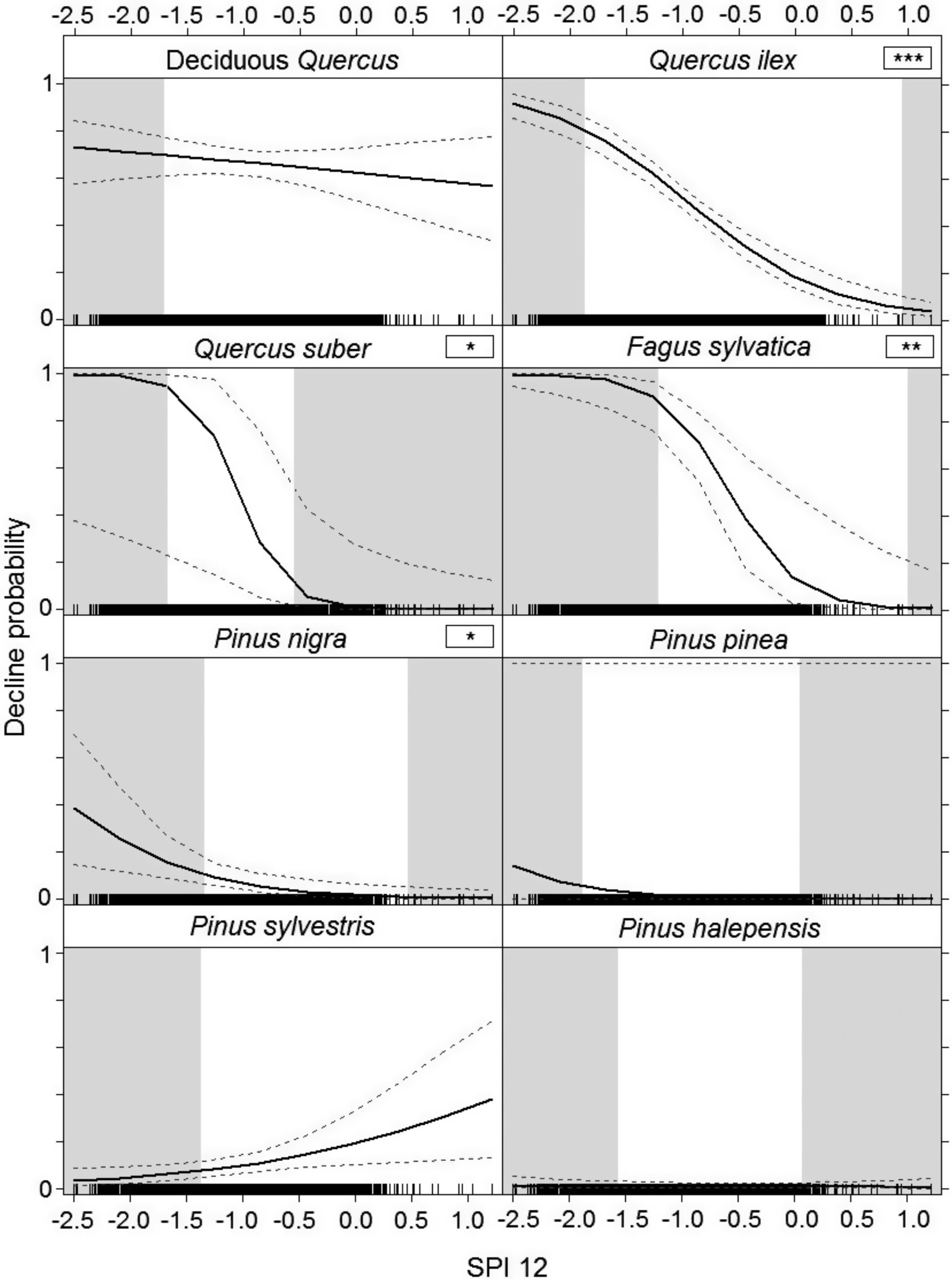

Figure 3.7. Modelled effect of the SPI12 on decline probability for each of the studied species. SPI12 is dimensionless. Values of SPI12 were back-transformed to the original scale for display purposes. Black curves show effects and dashed lines show 95% confidence intervals. Shaded rectangles show SPI12 values out of the range for each species, where effects are extrapolated. Top-right boxes show the significance of the effects for a given species, as $p<0.05$ (*), $p<0.01$ (**) and $p<0.001$ (***). A rug plot is shown giving the marginal distribution of the predictor on the horizontal axis.

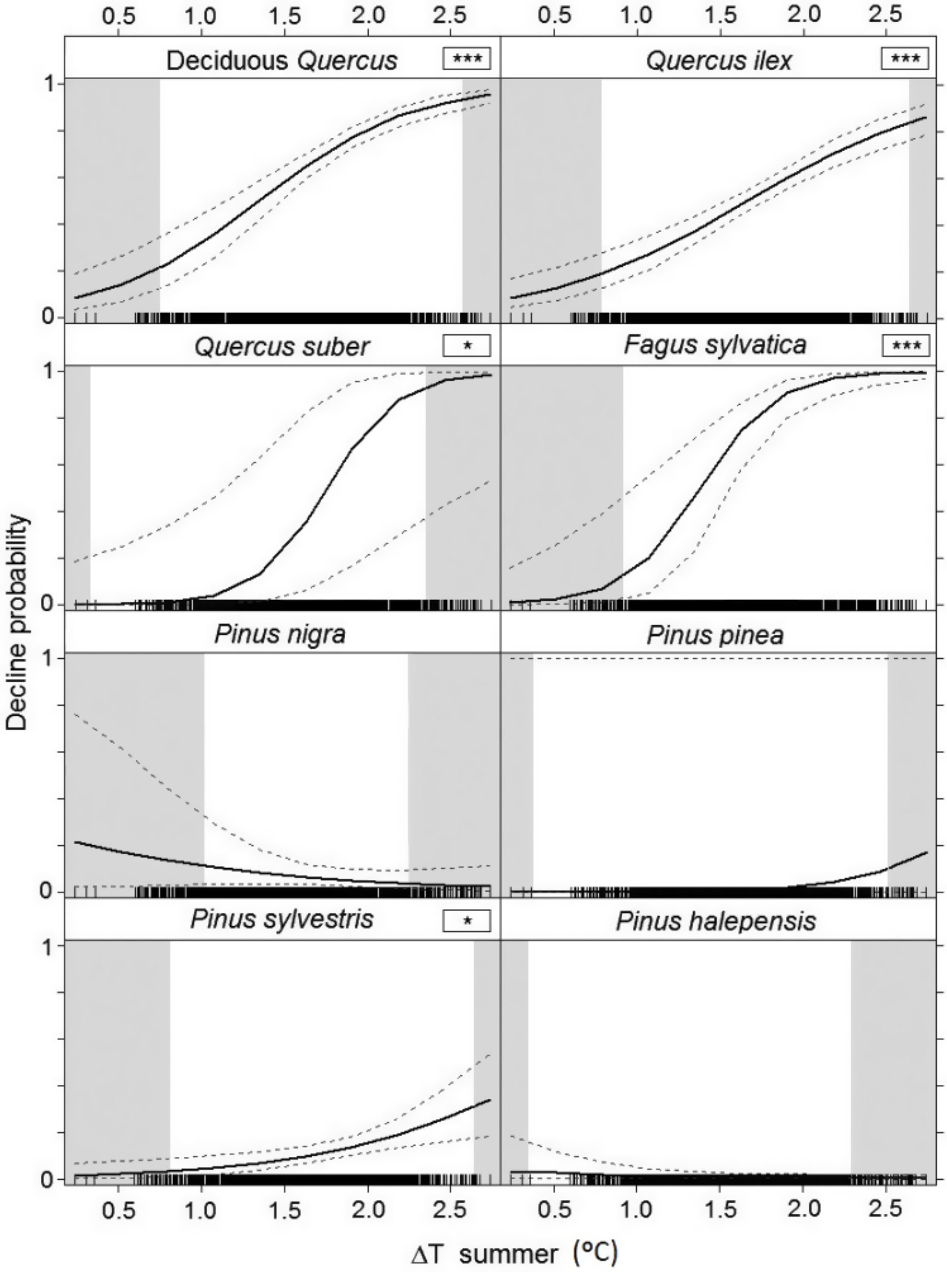

Figure 3.8. Modelled effect of the summer 2012 temperature anomaly (ΔT_summer, in ºC) on decline probability for each of the studied species. Values of ΔT_summer were back-transformed to the original scale for display purposes. Black curves show effects and dashed lines show 95% confidence intervals. Shaded rectangles show ΔT_summer values out of the range for each species, where effects are extrapolated. Top-right boxes show the effect significance as p<0.05 (*), p<0.01 (**) and p<0.001 (***). A rug plot is shown giving the marginal distribution of the predictor on the horizontal axis.

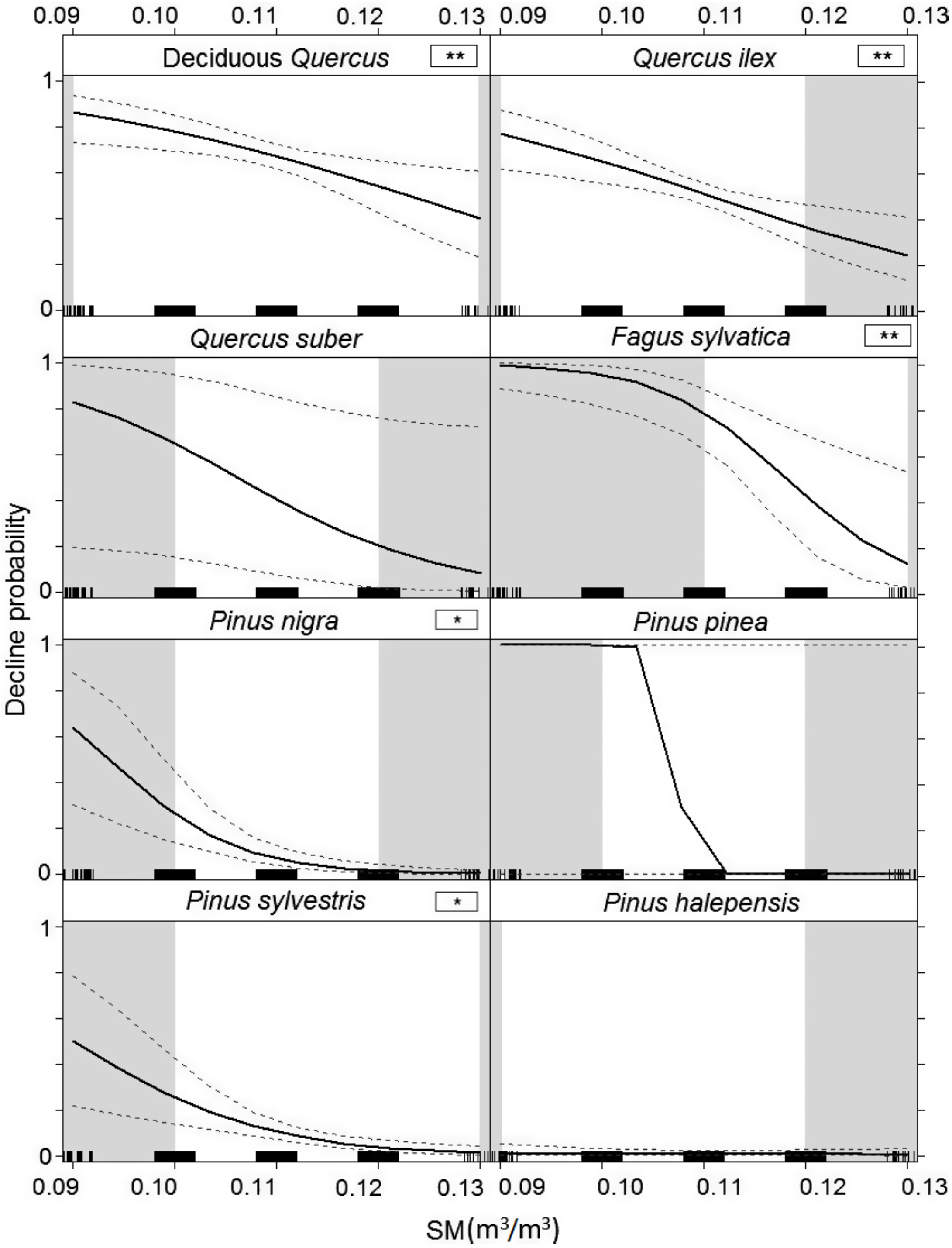

Figure 3.9. Modelled effect of soil moisture (SM, in m^3/m^3) on decline probability for each of the studied species. Values of SM were back-transformed to the original scale for display purposes. Black curves show effects and dashed lines show 95% confidence intervals. Shaded rectangles show SM values out of the range for each species, where modelled effects are extrapolated. Top-right boxes show the significance of the effects for a given species, as $p<0.05$ (*), $p<0.01$ (**) and $p<0.001$ (***). A rug plot is shown giving the marginal distribution of the predictor on the horizontal axis.

3.4. Discussion

3.4.1. Local climatic anomalies as determinants of drought effects on different forest species

Results show a remarkable coherence in the effects of the variables describing climate anomalies and soil moisture distribution. In general, an area was more likely to be affected wherever temperatures were particularly high and rainfall particularly low during summer 2012, compared to long-term averages, resulting in low water content in surface soils. Interestingly, the effects of rainfall at the summer and whole-year timescales are spatially independent from each other, suggesting that rainfall accumulated at these different timescales might need to be accounted for separately in models of drought effects on forests (Vicente-Serrano et al., 2013). The positive relationship between temperature anomaly and decline occurrence observed in the study is consistent with reports highlighting the key role of high temperatures in drought-induced forest mortality (Williams et al., 2013; McDowell et al., 2016; Neumann et al., 2017). Similarly, results are in agreement with the studies highlighting soil moisture as an important factor explaining the spatial distribution of forest decline. For instance, in Anderegg et al., 2013b it is shown that low shallow (<10 cm) soil moisture was associated to the spatial patterns of sudden aspen (*Populus tremuloides*) decline in Western USA. It should be noted, however, that the study species are likely to extract most water from deeper soil layers than those sensed by SMOS, and the relationship between L-band derived soil moisture data and soil water availability to plants requires further investigation, which should be focused on the application of root zone soil moisture products (see Section 6.3). In that sense, a recent study from Kharuk et al., 2017 shows that increased mortality of Siberian pine (*Pinus sibirica*) and fir (*Abies sibirica*) in the region of Lake Baikal (Siberia) was associated to negative anomalies of soil moisture for a depth ranging between 0 and 100 cm.

Results show that forests growing in sites under wetter mean climatic conditions and in areas more exposed to radiation were more likely to experience decline. Recent studies have shown that the vulnerability to drought may remain approximately constant across biomes (Choat et al., 2012), and that even species from very humid locations (e.g., tropical rainforests) are prone to suffer from drought (Engelbrecht et al., 2007). Similarly, populations from drier areas may be better adapted to drought, resulting in a similar or higher vulnerability in wetter areas even within the range of a given species (e.g., Martínez-Vilalta et al., 2012b).

3.4.2. Broadleaved trees were more affected by the 2012 drought than conifers

Consistently with the higher susceptibility of broadleaved species, they tended to be more sensitive to the studied drivers of drought stress than conifers. This result agrees with the fact that conifers have wider safety margins from hydraulic failure in their xylem, both in general (Choat et al., 2012) and also in particular for the set of species studied here (Table A.4 in Appendix A). However, drought resistance in plants is complex and multifaceted, and vulnerability to xylem embolism is by no means its only component, nor the only one differing between angiosperms and gymnosperms (Brodribb et al., 2012). Generally, broadleaved species tend to have deeper roots, and all the broadleaves included in this study are able to resprout, whereas the studied conifers are not. These differences might explain why the higher damage of broadleaves observed in summer 2012 was not observed in the previous DEBOSCAT surveys conducted in years 2010 and 2011 (Banqué et al., 2013). In 2013, a wet year in the study area, only 37 new decline events were recorded in the DEBOSCAT survey. Interestingly, however, the two species with higher area affected by new 2013 events were pines (*Pinus halepensis* and *Pinus sylvestris*). In addition, several decline events registered during 2012 were recovered two years later in most broadleaved species, showing that the post-drought dynamics of the studied episodes should be a matter of study. In contrast, the increased number of decline events mainly in conifers on 2014 suggests that they may be more prone to suffer lagged mortality effects (e.g., Hereş et al., 2012 for *Pinus sylvestris* in the same study region, consistently with results shown in Table 3.4 for this species). Also, these results suggest that the differential vulnerability to drought of broadleaves and conifers might depend on the temporal development of drought and can vary from year to year even within a given location, perhaps providing an effective resilience mechanism over larger spatial and temporal scales (Lloret et al., 2012).

3.4.3. Are Euro-Siberian species more vulnerable than Mediterranean species?

The hypothesis that Euro-Siberian species at the southern (and dry) limit of their distribution would be more vulnerable to drought is only partially verified. Although *Fagus sylvatica*, a typical central European species, was highly impacted by drought in 2012 and was the most sensitive species to the majority of studied variables, another northern species, such as the mostly Boreal *Pinus sylvestris*, was much less impacted (in 2012) and this impact was poorly related to the studied drivers. This result for *Pinus sylvestris* contrasts with several decline events detected for this species in the study area (Martínez-Vilalta and Piñol, 2002; Galiano et al., 2010; Hereş et al., 2012; Vilà-Cabrera et al., 2013) and with the higher damage of the species reported on the 2010, 2011, 2013, and 2014 DEBOSCAT campaigns (Banqué et al., 2013). For the 2012 effects studied here, the influence of the species' biogeographical range was clearly less important than the type of species (broadleaved compared to conifers). Some typical Mediterranean species, such as *Quercus ilex* and *Quercus suber*, were highly affected, while *Pinus halepensis* was not. The high sensitivity of *Fagus sylvatica* to the studied factors suggests that increasing temperatures and droughts could strongly affect this species in the study region (Jump et al., 2006) and elsewhere in Europe (Meier et al., 2011).

3.4.4. Towards a predictive monitoring of forest vulnerability to drought

The fact that the species distribution and the climatic anomalies during the study year explain a substantial proportion of the spatial distribution of forest decline, and that climatic effects were largely consistent across species, offers a promising avenue in terms of predicting forest decline at large spatial scales using GIS and remote sensing data. All the variables included in the study are relatively easy to calculate or readily available at different temporal and spatial resolutions for many regions of the globe (e.g., see Fick and Hijmans, 2017). At the same time, however, it must be noted that the proposed model explains ∼40% of the spatial variability in forest decline, and this percentage would be probably lower if the model is used to predict future decline events. This fact suggests that major determinants of the decline process are not accounted for in the study. The effect of previous droughts (such those occurred between 2004 and 2008 in the study area), for instance, might represent an important predisposing factor partially explaining the spatial distribution of current decline events. Although no large-scale pest effects were detected in 2012 in the study area, the impact of biotic agents is likely to be locally important (Anderegg et al., 2015). Patterns of tree death are often patchy at fine spatial scales across the synoptic drought-affected region, which suggests the need to include more detailed-scale factors in future editions of the DEBOSCAT survey. Actually, decline patterns depend on the combination of ecosite variability (e.g., soils or slope) and density-dependent processes (e.g., competition or insect outbreaks; Allen et al., 2010). Stand development and structural characteristics have been related to forest decline in many studies (e.g., Carnicer et al., 2011; Vilà-Cabrera et al., 2011). Also, the combination of drought conditions with larger basal area (implying water-mediated competition) and with functional traits has been linked to increased mortality (Young et al., 2017; Greenwood et al., 2017). Disturbance legacies, including past forest management practices, are the main determinants of current stand characteristics over most of the study region (Vilà-Cabrera et al., 2011; Ruiz-Benito et al., 2013), and may explain the clustering of decline episodes in some areas (see Figure 3.1). Finally, fine scale soil characteristics such as texture or vertical development are also obvious contributors to forest decline occurrence (Vilà-Cabrera et al., 2011), as root development is limited on shallow and/or rocky soils, obviously influencing water retention and availability independently of direct climatic effects.

High resolution soil moisture data obtained from remote sensing, such as the SMOS-derived dataset used in this study, offers a path forward for the predictive modelling of drought effects. The major limitation of SMOS downscaled data at present is the shallow soil depths at which SMOS is sensitive to, as it only captures a small fraction of the rooting zone of most tree species (Jackson et al., 1996). This drawback may explain the low explanatory power of soil moisture in this study. This issue could be improved using surface moisture models or by estimating water content in deeper layers from surface soil moisture (see Section 6.3). Concerning its spatial resolution, the downscaled product is applicable to regional studies (while the L2 product is not) but a better resolution would be desirable (see Section 6.3). Hence, satellite soil moisture data applicability and the possibility of improving its characteristics makes it a promising tool with many potential applications in forest ecology.

3.5. Conclusions

The model proposed in this work is able to explain a substantial proportion (~40%) of the spatial distribution of forest decline detected after the extremely dry summer of 2012 in Catalonia, using widely available environmental data. It has been concluded that precipitation anomaly at different time scales, anomalies of temperatures, and surface soil moisture, were important and complementary to explain forest decline patterns. These results are promising because they show that predicting forest decline is possible. At the same time, however, the substantial proportion of variance that could not be explained by our model indicates that other factors (e.g., soil properties, ecosite variability, stand structure and management history, or occurrence of previous droughts) are also likely to be important and need to be taken under consideration in future monitoring programs and decline models.

In general, climatically wetter and more exposed forests were more vulnerable than those located in drier or more shaded areas. More affected forests were characterized by high positive temperature anomalies, low rainfall accumulated for the whole summer and for the previous year, and by low soil moisture in surface layers. However, species differed in their overall affectation and in their susceptibility to the studied drivers. Overall, broadleaved species were more affected than conifers. Interestingly, species at the southern limit of their distribution were not necessarily more sensitive to the studied explanatory variables, nor necessarily more affected (e.g., *Pinus sylvestris*) than species distributed over drier areas, at least in the short term.

Finally, the applicability of satellite soil moisture data to forest decline assessment is promising, showing a coherent relationship between drier soils and larger forest affectation, especially in the more sensitive broadleaved species. Nevertheless, the capacity of this variable to explain a substantial proportion of forest decline spatial distribution is still scarce. Future work should be addressed to model and apply moisture information in deeper layers than those sensed by SMOS, in order to effectively estimate water availability in the root zone (see Section 6.3). Additionally, it is expected further development of soil moisture downscaling algorithms. This would increase the power of L-band soil moisture estimates to predict forest decline in particular, and to provide more detailed and valuable information for forest ecology applications in general.

4

Applicability of VOD to monitor carbon stocks in tropical forests

Abstract

Monitoring vegetation biomass is essential to the global carbon assessment. VOD data have been applied for biomass estimation using frequencies ranging from 1 to 30 GHz (L- to K-bands). As lower microwave frequencies have greater penetration depths through canopy, the L-band VOD (1.4 GHz) should provide the best ability to estimate carbon stocks. This chapter compares the sensitivity of VOD at L, C, and X-bands, and of the EVI index, to the above-ground carbon density (ACD) in Peru, southern Colombia and Panama. It quantifies the relative contribution of ACD and forest cover proportion (FC) to the VOD/EVI signals. Results confirm the enhanced sensitivity of L-band VOD to ACD, and show that ACD explains 34% and forest cover 30% of L-band VOD variance. These proportions gradually decrease for EVI, C-, and X-band VOD, respectively. Results are consistent regardless of altitude, carbon density, and regions and forest types studied. Results also show that C-, X-band VOD and EVI provide complementary information to L-band VOD, especially in flooded forests and in mountains, indicating that synergistic approaches could lead to improved retrievals in these regions. Results from this study support the use of new L-band VOD estimates for mapping the carbon of tropical forests.

4.1. Introduction

The quantification of carbon stocks in tropical regions is essential for global carbon assessment and is needed to support forest conservation initiatives. Intact tropical forests (i.e., not affected by human activities) are responsible for half of the carbon sequestration in woodlands across the world (Pan et al., 2011), and maintain forest resources and biodiversity (Foley et al., 2005). However, deforestation and disturbances in tropical regions (including drought, heat, and wildfires) cause tropical forests to be a net carbon source (Pan et al., 2011; Liu et al., 2015; Baccini et al., 2017; see Section 1.2.3). Despite this fact, globally terrestrial ecosystems act as carbon sinks. This has immediate consequences for the global carbon balance, and provides negative feedback to anthropogenic climate change.

Satellites are the only means to provide an efficient and cost-effective monitoring of vegetation biomass changes over large areas and over extended periods (Goetz et al., 2009). Previous research on biomass estimation from space observations has been frequently based on the combination of diverse remote sensing sources and on complementing satellite data with field plots. The most widely used technique for vegetation monitoring is based on visible-infrared (VIS/NIR) vegetation indices. These indices have been constructed to exploit the particular properties of green vegetation to strongly absorb red wavelengths and reflect in the near-infrared. Several studies have used such indices for biomass estimation. For example, data from MODIS has been applied to map carbon density in tropical regions (Baccini et al., 2008; Baccini et al., 2017) and in China (Sun et al., 2015). Spectral vegetation indices, such as the NDVI and EVI, have also been combined with field measurements to estimate forest biomass (e.g., Myneni et al., 2001; Dong et al., 2003; González-Alonso et al., 2006; Blackard et al., 2008; Yuan et al., 2016). Despite their importance on vegetation studies, VIS/NIR vegetation indices have serious limitation for monitoring carbon stocks because (i) they are masked by clouds, (ii) can only monitor the top of the vegetation canopies, (iii) saturate at moderate and high levels of vegetation densities, and (iv) are poorly related to total biomass.

Differently from –and complementarily to- the VIS/NIR datasets, optical remote sensing based on the reception of laser pulses (i.e., LiDAR) presents the unique advantage of capturing the vertical structure of vegetation. It can be used to map the forest height and architecture in detail. The application of LiDAR enhances the capacity to capture vegetation biomass at different spatial scales and, in that sense, new estimations of biomass and carbon fluxes throughout the Earth tropical regions have been obtained merging LiDAR satellite data with MODIS information and/or microwave datasets (Saatchi et al., 2011; Baccini et al., 2012 and 2017). At present, LiDAR surveys of forest biomass are limited to airborne platforms, although the Ice, Cloud, and land Elevation Satellite (ICESat) provided LiDAR measurements between 2003 and 2009. ICESat data was used for mapping forest canopy height (Simard et al., 2011), and future satellite missions like the ICESat-2 and the Global Ecosystem Dynamics Investigation mission (GEDI) will produce LiDAR retrievals of canopy structure from space. Importantly for the scope of this work, airborne LiDAR from the Carnegie Airborne Observatory (CAO) –in combination with field and modelled datasets- has been used to produce ACD maps at regional scales in Peru, southern Colombia and Panama (Asner et al., 2012, 2013 and 2014).

Microwave remote sensing, either from active or passive sensors (i.e., radars or radiometers, respectively), provides an alternative technique that has a double advantage: it is insensitive to cloud cover, and it is able to sense through the vegetation layers. Microwave sensors are responsive to soil moisture and vegetation water content (see Section 1.3). In order to derive biomass estimates, it is assumed that the vegetation water content to which microwaves are sensitive is tightly linked to the biomass of the plant. The relationship between measurements from space-borne radars and biomass in tropical forests has been widely demonstrated (Luckman et al., 1997; Kuplich et al., 2000; Hamdan et al., 2011; Morel et al., 2011; Sinha et al., 2015; Viet Nguyen et al., 2016). Radar data have been used to provide vegetation biomass estimates either in synergy with LiDAR and VIS/NIR data (Saatchi et al., 2007; Lucas et al., 2015) or as an independent data source (Thurner et al., 2014; Bouvet et al., 2018). The use of passive microwave measurements for biomass assessments relies on the estimation of the VOD. Different VOD products have been applied to study forests conditions and biomass (Liu et al., 2013; Lucas et al., 2015; van Marle et al., 2016; Brandt et al., 2017 and 2018). In particular, trends in global terrestrial biomass have been estimated using long-term retrievals of VOD at C-, X- and K-bands (>4 GHz; Liu et al., 2011 and 2015). In this regard, since the penetration depth of microwaves through the vegetation canopy is greater at lower frequencies, VOD at L-band (1 to 2 GHz) is expected to enhance the capacity to derive information on vegetation for a wide range of applications.

L-band VOD datasets have been used in vegetation research to study GPP (Teubner et al., 2018) and crop yields (Chaparro et al., 2018, and Chapter 4). L-band VOD has shown good agreement with vegetation biomass and forest height (Vittucci et al., 2016a and 2016b; Konings et al., 2017a). Brandt et al. (2018) have demonstrated its applicability to monitor carbon dynamics associated to weather trends in African drylands, and have shown reduced saturation for L-band VOD at high values of vegetation biomass as compared to higher frequency (shorter wavelength) microwaves. Vittucci et al. (2016b) have reported that on July 2015 L-band VOD showed stronger relationship with biomass and forest height than C-band VOD, in tropical forests of South America and Africa. However, they have found low relationship of L- and C-bands VOD with biomass in Indonesian forests, with similar performance for biomass estimation at both frequencies. In this context, further work is needed to quantify and compare the relationship between above-ground carbon stocks and VOD at different frequencies and for different forest types. At present it is still unclear to what extent L-band VOD shows higher sensitivity to capture carbon patterns than other frequency bands and vegetation indices.

The main goal of this chapter is to assess and compare the sensitivity of VOD (at L-, C-, and X-bands) to ACD, and benchmark it with respect to EVI. The study is conducted with a principal focus on tropical forests in Peru, southern Colombia and Panama. The chapter is structured in three parts. First, the relationship between satellite VOD and ACD derived from airborne LiDAR surveys is established and analysed. This shows the effect of vegetation density on the L-band VOD signal and compares it to the different microwave frequencies. Second, the relative contribution of ACD and FC to the VOD signal is studied. This allows understanding to what extent the VOD could depend on the changing forest cover within a region rather than on the carbon density variability *per se*. In this second part, the EVI is included to complement the study. Its dependence on ACD and FC is also presented and compared to VOD. And third, the analyses presented are reproduced specifically for the Andes Mountains and for the flooded forests found in the study area, which exhibit distinct vegetation and VOD patterns.

The comparisons among VOD frequencies and EVI will be presented at 25 km. Also, since SMAP L-band VOD is available on a 9 km grid (obtained from the enhanced brightness temperature product, but with the instrument's native ~36 km spatial resolution; see Section 4.2.2.A and Chaubell, 2016), dedicated analyses will be performed at 9 km.

4.2. Materials and methods

4.2.1. Study area

The study area (Figure 4.1) is defined based on the availability of ACD maps. It encompasses Peru (∼1.3 million km^2), Panama (∼75,000 km^2) and part of the Colombian Amazon (∼165,000 km^2). Peru and southern Colombia comprise the Amazon basin, crossed by the Amazon River and its tributaries. In western Peru, the Andes Mountains reach altitudes above 6,500 m.

The evergreen tropical rainforests in the region are the main target of this study. Near some rivers edges, and particularly in northcentral Peru, these forests are flooded forests (Figure 4.1a). The Amazonian forests constitute one of the main land carbon reservoirs on Earth. Other land covers are found in the Andes, where a transition from dense forests to shrublands, grasslands, and bare soils occurs with increasing altitudes. Also, croplands, shrublands and grasslands are present in the north of the studied area of Colombia and in western Panama (Figure 4.1a).

4.2.2. Datasets

A. Vegetation Optical Depth

The L-band (1.4 GHz) VOD is retrieved from the SMAP satellite using the Multi-Temporal Dual-Channel Algorithm, which allows estimating SM and VOD from single look-angle observations using two consecutive overpasses and no ancillary information on vegetation (Konings et al., 2016, and Section 1.4.2.B). SMAP VOD datasets retrieved using MT-DCA have shown good agreement with vegetation and land cover patterns at the global scale (Konings et al., 2017a). Here, the first year of SMAP VOD data (April 2015 - March 2016) is used. This dataset is retrieved from SMAP Backus-Gilbert enhanced brightness temperatures using the MT-DCA and is provided in the 9 km EASE 2.0 grid (NSIDC, 2017a). Figure 4.1b shows the annual average of L-band VOD at 9 km gridding. Figure 4.2 shows its aggregation at 25 km scale (obtained using bilinear interpolation), which is used for comparison with the higher frequency VOD bands at their available grid scale (see below), and with EVI.

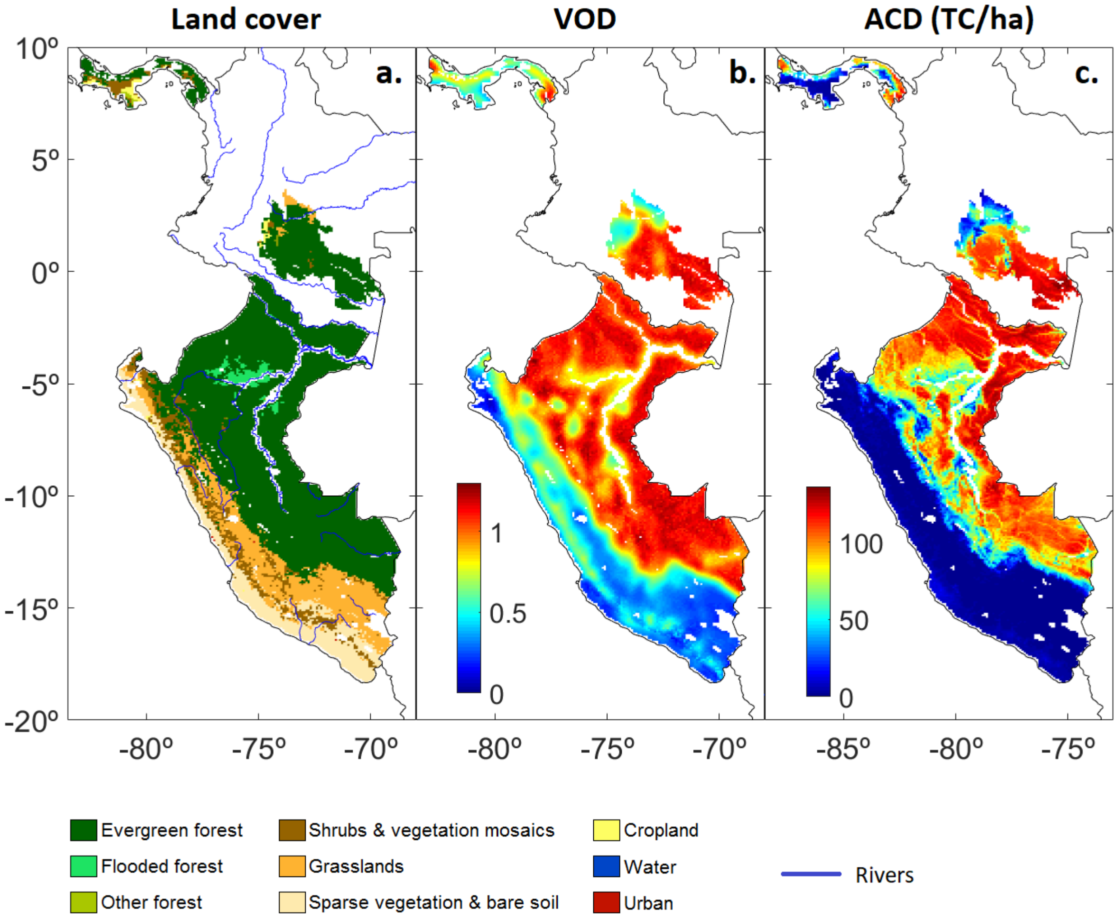

Figure 4.1. Description of the study area, which includes Panama, southern Colombia and Peru. (a) Dominant land cover constructed by selecting the modal class over 9 km grid cells from a 2015 land cover map (ESA-CCI, 2017), and major rivers (UNESCO, 2017); (b) Mean L-band SMAP 9 km VOD data (dimensionless; period April 2015-March 2016); (c) Above-ground Carbon Density (TC/ha) aggregated to 9 km (Asner et al., 2012, 2013 and 2014). Areas with insufficient VOD and/or ACD data (e.g.,rivers and coastlines) are not plotted.

The VOD at C-bands (6.9 and 7.3 GHz, hereafter named C1 and C2 respectively) and X-band (10.7 GHz) are derived from AMSR2, on board of the Japan Aerospace Exploration Agency's GCOM-W1 satellite. VOD is retrieved with the Land Parameter Retrieval Model (see Section 1.3.4). The dataset is provided on a 25 km grid (Vrije Universiteit Amsterdam and NASA GSFC, 2014), and is adapted to the EASE2 grid at the same scale using bilinear interpolation. The yearly averages are computed for each frequency band and are shown in Figure 4.2.

B. Above-ground carbon density

The above-ground carbon density maps produced by the CAO (Asner et al., 2012, 2013 and 2014) are used as a benchmark to assess the sensitivity of VOD to variability on carbon stocks.

The ACD dataset is based on intensive airborne LiDAR sampling carried out between years 2010 and 2012. LiDAR measurements are converted to top-of-canopy height information which, in turn, is transformed to ACD data (100 m resolution) using calibration against field plots and information on topography, vegetation and precipitation. ACD ranges between 0 and 140 TC/ha in the study area. The degree of uncertainty at the original ACD resolution reaches up to 28.3% in Colombia and 23% in Panama. This is computed in terms of error relative to the mean. In the case of Peru, the uncertainty in the vast majority of the tropical forest area is below 10%. It may increase in flooded regions and river areas ranging from <5% to 50% in most of these regions. Errors around 80% are found in the Andes, but this is largely due to the fact that the mean ACD values per pixel are close to zero in this area, causing large relative uncertainties with low ACD absolute errors. More details on the ACD datasets are provided in Asner et al. 2012 (Colombia), 2013 (Panama), and 2014 (Peru). In this work, the ACD datasets are aggregated to the 9 and 25 km scales to match the VOD layers, and are shown in Figure 4.1, and Figure B.1 in Appendix B, respectively.

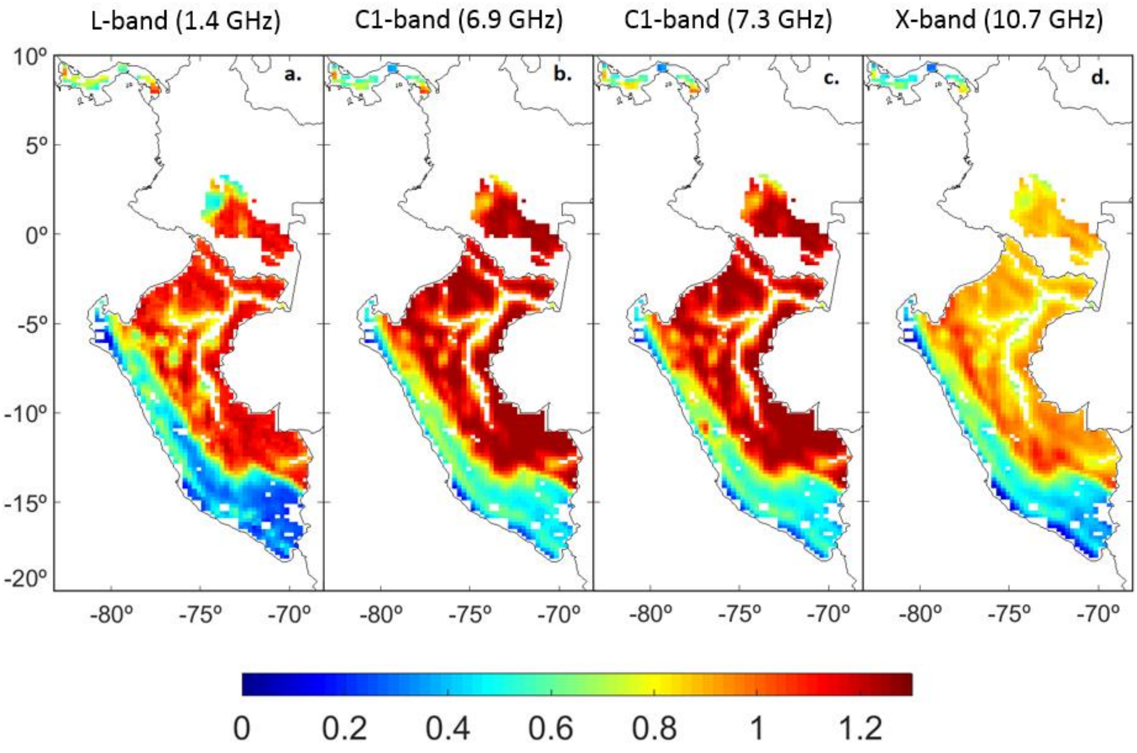

Figure 4.2. Mean VOD data (dimensionless) for the period April 2015 – March 2016, retrieved at (a) L-band (1.4 GHz); (b) C1-band (6.9 GHz); (c) C2-band (7.3 GHz) and (d) X-band (10.7 GHz). Datasets are converted to a common 25 km grid.

C. Enhanced Vegetation Index

The EVI is a VIS/NIR index used as a proxy of vegetation condition, photosynthetic activity and biomass (Huete et al., 2002). Here it is used to provide comparison with the microwave datasets when their sensitivity to ACD and FC is studied. The EVI dataset is derived from

MODIS. Original EVI data is the 16-day MODIS/Terra MOD13C1 v.6 product, on a 0.05° latitude/longitude global grid. EVI is converted to the EASE2 grids using bilinear interpolation.

D. Forest cover maps

The ESA-CCI 2015 land cover map (ESA-CCI, 2017; 300 m resolution) is used in this work to produce a binary forest mask and to obtain maps of forest cover percentages and flooded forest proportion. The land cover categories considered as forests in this research are tree covers as well as vegetation mosaics with (tree + shrub) or (tree + shrub + herbaceous) covers occupying >50% of surface. Pixels at the study scales are classified as forests when this grouped category is dominant (modal class). Also, the FC variable is computed as the fraction of forests in the pixel and its contribution to the VOD is studied. Likewise, the proportion of flooded forests is also computed.

E. Water fraction maps

Information on water bodies is needed to provide a specific analysis of VOD sensitivity to carbon stocks in pixels with varying amounts of standing water. In this study, the water occurrence product from the European Commission Joint Research Centre's Global Surface Water Explorer (Pekel et al., 2016; European Commission, 2017) is considered to be more appropriate than the land cover map. This product specifically provides information on the water bodies detected using Landsat for the period 1984-2015. The dataset shows the percentage of satellite acquisitions which detected water in each 30 m pixel (i.e., % of water occurrence) during the mentioned period (Pekel et al., 2016). Here, pixels exceeding 50% of water occurrence are considered as water pixels. The percentages of water at the study scales are computed once this reclassification has been applied.

F. Digital Elevation Model

To take into account the impact of increasing altitudes on ACD and VOD (mainly in the Andes) the ETOPO1 Global Relief Model (Amante and Eakins, 2009) is used. The ETOPO1 provides global land elevation and ocean bathymetry at 1 arc-minute resolution. It is supplied by the National Oceanic and Atmospheric Administration (NOAA, 2017). This dataset is aggregated at the studied spatial scales.

G. Data screening

Only pixels containing >95% of ACD high resolution information are considered, in order to guarantee a highly representative sample of the carbon dataset. Regions without VOD data are also excluded. The overall area studied is of ∼1.3 million km^2, containing ∼900,000 km^2 of forests. More specific details are reported in Table A.5 in Appendix A.

4.2.3. Statistical methods

A. Analysis of the VOD-ACD relationship

VOD and ACD datasets are compared and their relationship is analysed for the entire study area. The spatial cross-correlation between VOD at each band and ACD is calculated and compared using the Lee's Index, which is a bivariate spatial association method (Lee, 2001). This index is computed using the 'spdep' R package (Bivand et al., 2013; Bivand and Piras, 2015) at 25 km and for increasing distances from 25 km to 1,250 km. Also, regressions of each VOD product as functions of ACD are estimated using Generalized Additive Models (GAM; Hastie and Tibshirani, 1990). GAMs have been previously used to explore the relationships between remote sensing data and biomass (Baccini et al., 2004) and forest structural attributes (Frescino et al., 2001). The 'gam' R package (Hastie, 2018) is used to compute these regressions using cubic spline smoothing classes. GAM functions are applied both at 9 km scale (for L-band assessment) and at 25 km scale (for comparison among bands). To make the samples comparable between the finer and the coarser grids, 1,000 random replicas for the model at 9 km were made with the same sample used at 25 km (1,978 pixels).

The main focus of this work is on forests, which represent approximately 70% of the study region. Linear regressions of VOD as a function of ACD are computed for the entire forested area as:

$$VOD = \alpha + \beta \cdot ACD, \qquad (4.1)$$

where VOD and ACD stand for the vegetation optical depth at each band and the above-ground carbon density (TC/ha), respectively, and α and β are constant terms. Samples for L-band VOD regressions at 9 km gridding are also equalised to samples at 25 km gridding following the method explained above. Exponential and quadratic functions are also tested, but do not improve the fitting and are therefore discarded (results not shown). In addition, Eq. (4.1) is specifically applied in the densest forests, where the penetration capacity of microwaves through vegetation could be reduced. Two categories of dense forests are studied: ACD≥80 TC/ha and ACD≥100 TC/ha.

B. Relative contribution of carbon density and forest cover to VOD and EVI

The spatial variability of VOD may be affected not only by ACD, but also by spatial variations in FC. Furthermore, both can change markedly through different altitudes, as altitude strongly conditions vegetation characteristics. These relationships are studied for VOD, and are benchmarked to EVI in order to provide comparison between microwave and optical-infrared information.

To understand to what extent the VOD variability in the different bands could depend on forest cover changes rather than on the inherent carbon density of forests, VOD datasets are studied as a function of ACD and FC using a multiple regression:

$$VOD = \alpha + \beta \cdot ACD + \delta \cdot FC, \quad (4.2)$$

where VOD is the VOD at each band, ACD and FC stand for above-ground carbon density (TC/ha) and forest cover proportion, respectively, and α, β and γ are constant terms. Note that the equation terms will change for each band. This analysis is carried out in order to obtain the relative importance of ACD and FC on the VOD signal using the 'relaimpo' R package (Grömping, 2006), which provides the relative contribution of each variable in a linear regression. The analysis is extended also to the EVI for comparison. Additionally, this procedure is replicated separately for different areas, providing a geographical division in six regions including Panama (A), Colombia and northern Peru (B), and four latitudinal strips in Peru: north-central Peru (C), central Peru (D), south-central Peru (E) and southern Peru (F). A map with this division is shown in Figure B.2 in Appendix B.

C. VOD-ACD study over the Andes and in flooded forests

Residuals for the L-band VOD – ACD regression in Eq. (4.1), computed as predicted minus observed VOD, are mapped to assess the impact of different geographical features on the VOD-ACD relationship in forests. The map of residuals is compared to maps of flooded forest proportion, water fraction, and altitude. Also, the VOD-ACD residuals and the VOD values are plotted against altitude, water fraction, flooded forest proportion, and ACD data.

Distinct VOD-ACD relationships are found at different altitudes, as well as in flooded forests and in regions containing water bodies (see Section 4.3.3). For this reason, the analyses described in Eqs. (4.1) and (4.2) are reproduced specifically for: (i) three different altitude groups (1,000 to 2,000 m; 2,000 to 3,000 m; and >3,000 m), (ii) regions containing >3% of water fraction, and (iii) two groups of flooded forest proportion (5 to 50%; and 50 to 100%). These categories are chosen due to their geographical location (mountain or flooded forest regions), their positive or negative residuals with respect to the VOD-ACD regression model in Eq. (4.1), and their differences in terms of carbon density. T-tests are used to check that these criteria are accomplished for the different groups. In particular, T-tests are applied to study whether the proposed categories presented residuals significantly different from 0, and to compare the proposed categories with the remaining regions (i.e., altitude <1,000 m, water <3%, and flooded forest <5%) in terms of ACD. These regions contained the vast majority of pixels and are considered as reference groups. Significance for T-tests is stablished at $p<0.05$.

4.3. Results

The results section is divided in three parts following the structure explained in Section 4.1. The relationship between VOD and ACD is presented in Section 4.3.1. The study on VOD and EVI sensitivities to both ACD and FC is presented in Section 4.3.2. Finally, Section 4.3.3 describes spatial patterns of the VOD-ACD relationship, and provides specific analyses in the

Andes and in flooded forests. Note that results are displayed at the original L-band 9 km grid except for those figures which present comparison among different VOD bands, or between VOD and EVI, for which the spatial scale used is 25 km.

4.3.1. VOD-ACD relationship

VOD and ACD maps are shown in Figure 4.1, Figure **4.2**, and Figure B**.1** in Appendix B. The highest VOD and ACD values are found in the evergreen forests of Peru and Colombia, while both variables decrease in non-forested areas (especially in the Andes). At L-band, VOD is lower in the river edges and in flooded regions, partially reproducing reduced ACD in these areas. This qualitative pattern is less clear at C- and X-bands (Figure 4.2). L-band shows the highest spatial cross-correlation (Lee's index; Lee, 2001) with ACD for approximately 0 to 300 km distance. Both L- and C-bands show better spatial cross-correlation with ACD than X-band, independently of the distance analysed (Figure 4.3). Note that the decrease on the Lee's index with distance (Figure 4.3) might be also due to the uncertainty of ACD estimates, which is not accounted for here. This is further discussed in Section 4.4.3.

Scatterplots in Figures Figure **4.4** and Figure **4.5** show the VOD-ACD relationships for the studied bands. The sensitivity of VOD to ACD decreases according to the increasing frequencies studied (i.e., L-, C-, and X-band, respectively). In particular, results for GAM functions (Figure 4.4) show R^2 values between 0.80 and 0.83 for L-band, between 0.71 and 0.72 for C-bands, and 0.64 for X-band. Note that the term R^2 must not be interpreted in this case as VOD explained variance in the context of a linear regression. GAM curves change from a portion with very steep slopes (for ACD<10 TC/ha and VOD<0.5, which correspond to non-forested regions) to gradually smoother slopes (for VOD>0.5 approximately, in forest areas). This change is continuous at L-band, but irregular at the other studied frequencies (Figure 4.4).

Linear regressions in forest areas are shown in Figure 4.5. The percentages of VOD variance explained by ACD are 57% (L-band), 30 to 32% (C-band) and 1% (X-band). Results for both L-band grids are consistent, although the finer scale shows slightly lower coefficients of determination (Figures Figure B**.3** and Figure B**.4** in Appendix B). Importantly, note that the shape of the VOD-ACD scatterplots suggests that the relationship between both variables is not exactly linear (Figures Figure **4.4** and Figure **4.5**). In that sense, it must be taken into account that VOD shows decreased sensitivity to ACD changes in the densest forests (Table A.6 in Appendix A). Still, linear regression has shown similar or improved fitting in comparison to exponential and quadratic functions (see Section 4.2.3.A).

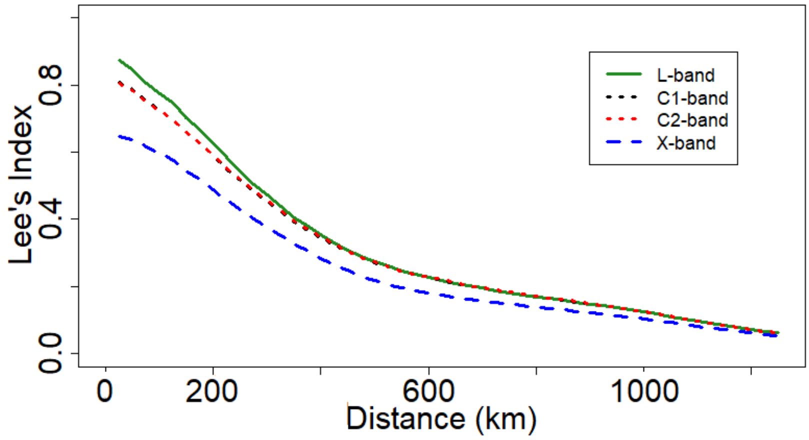

Figure 4.3. Spatial cross-correlation (Lee's Index) between ACD and each of the mean VOD datasets studied (25 km grid): L-band (green), C1-band (black), C2-band (red) and X-band (blue). Lee's Index is computed for each 25 km step from the common 25 km grid, to a maximum distance of 1,250 km.

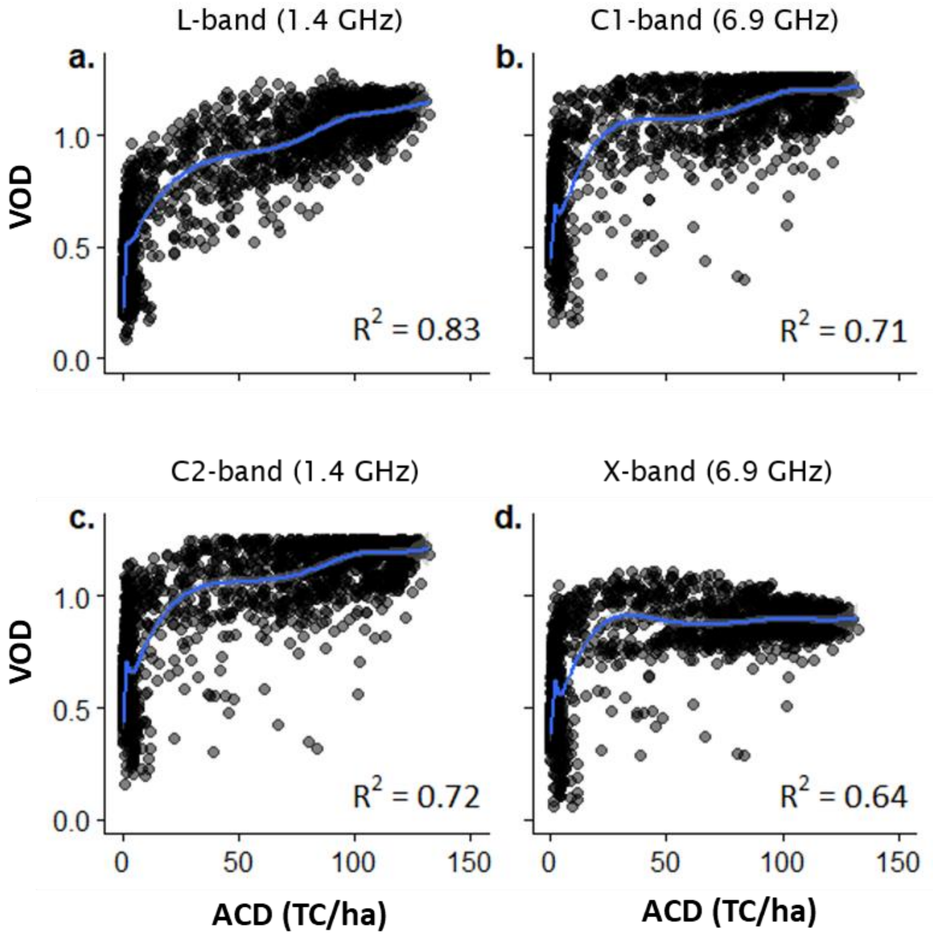

Figure 4.4. Regressions of VOD as a function of ACD using Generalized Additive Models (GAM). (a) L-band (1.4 GHz); (b) C1-band (6.9 GHz); (c) C2-band (7.3 GHz); and (d) X-band (10.7 GHz). Models are fitted on the basis of a cubic spline function. All regressions are significant ($p<0.0001$).

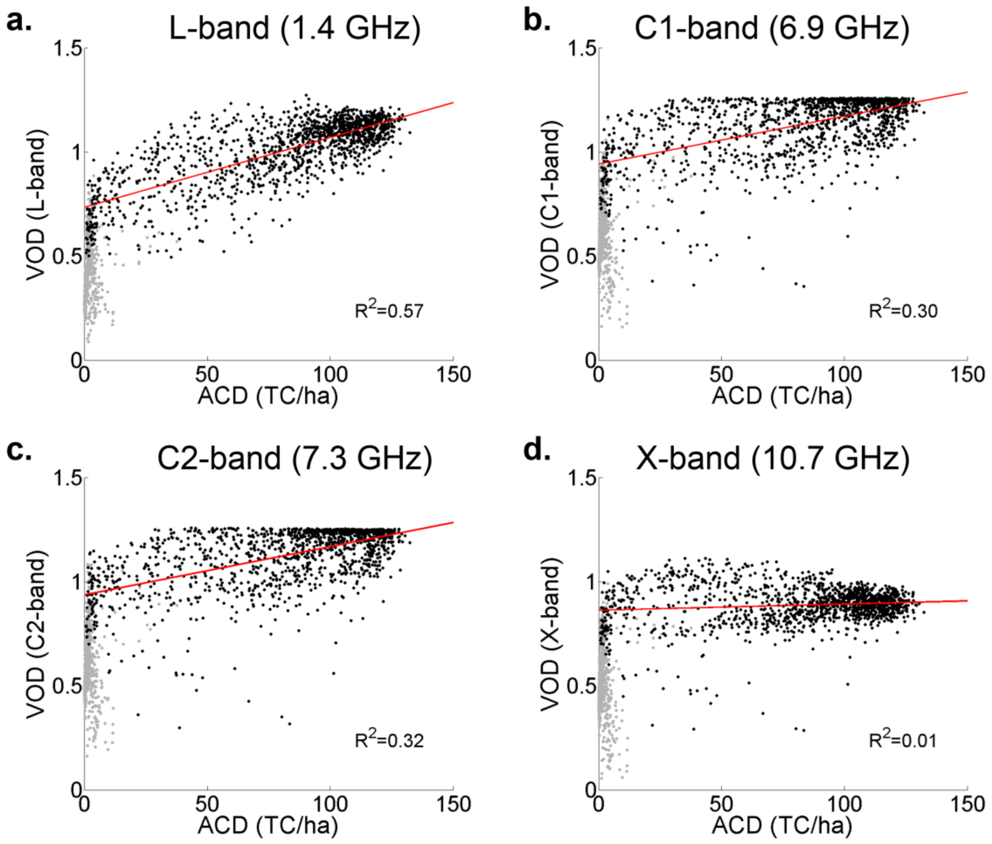

Figure 4.5. Linear regressions of VOD as a function of ACD (Eq. (4.1)) in forest areas. (a) L-band (1.4 GHz); (b) C1-band (6.9 GHz); (c) C2-band (7.3 GHz); and (d) X-band (10.7 GHz). All regressions are significant ($p<0.001$). Grey dots show pixels without forest dominant cover and are excluded from the regressions.

4.3.2. Contribution of carbon density and forest cover to VOD and EVI

Figure 4.6 shows the relationship of L-band VOD and EVI with ACD and FC, as well as the VOD-EVI and ACD-FC scatterplots. Note that the EVI is included here to provide a comparison between microwave and visible-infrared datasets in forested areas. Altitude is shown as a third variable in each subplot. In Figures Figure **4.6**a and Figure **4.6**b it is reported that L-band VOD is more sensitive to ACD (R^2 = 0.51) than EVI (R^2 = 0.37). In turn, EVI is more sensitive to ACD than VOD at C- and X-bands (Figure 4.5 and Figure **4.6**b). Also, it is shown that VOD, EVI and ACD decrease for increasing altitudes. This effect is more evident for EVI than for VOD. Figure 4.6c shows VOD ranging from 0.5 to 1.25 in completely forested pixels, while its maximum decreases to 0.8 in pixels with less than 50% of forests. In the case of EVI, it is higher at low altitudes (especially <1,000 m), and its maximum also decreases at lower forest proportions. The latter pattern is clearer for higher altitudes, where EVI can drop below 0.2 (Figure 4.6d). Figure 4.6e shows a positive association between VOD and EVI in forests above 1,000 m. Note that ACD decreases with increasing altitude and decreasing forest cover proportion (Figure 4.6f).

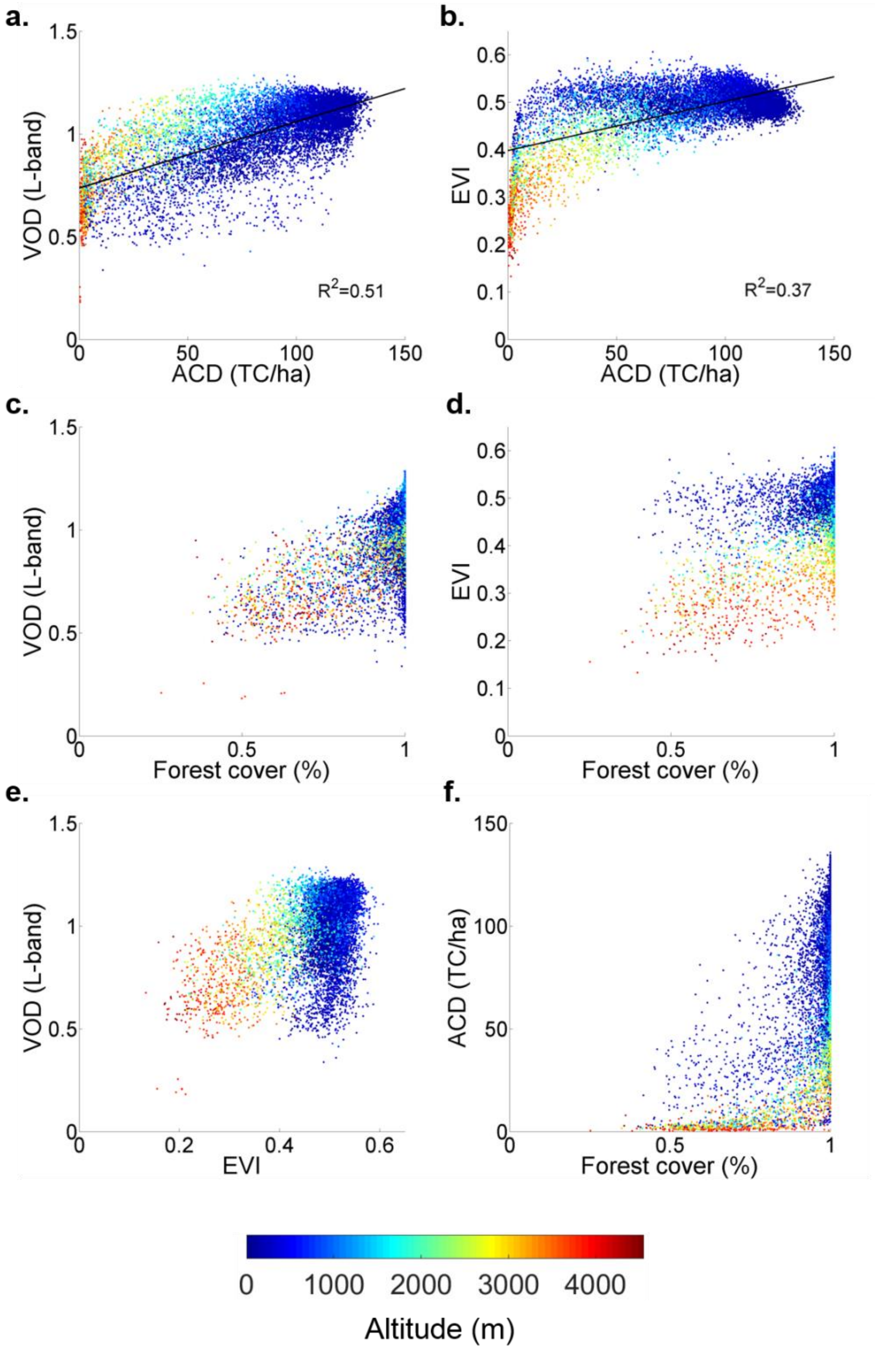

Figure 4.6. Relationships between: (a) ACD and L-band VOD (Eq. (4.1)); (b) ACD and EVI; (c) forest cover and L-band VOD; (d) forest cover and EVI; (e) EVI and L-band VOD and (f) forest cover and ACD. In (a) and (b), linear regressions are significant ($p<0.0001$). Only forest pixels are plotted. Colour shows the altitude.

The relative contribution of ACD and FC to the VOD and the EVI variances is provided in Figure 4.7. ACD explains 34.2% of L-band VOD variability, while this percentage decreases for EVI (26.9%), C-band (18% and 19.4% for C1 and C2, respectively), and X-band (negative coefficient). FC explains similar proportions of EVI (32.5%) and L-band VOD (30%). This proportion is lower at C- and X-bands (17.3% for C1, 15.9% for C2, and 9.1% for X-band). Overall, the relative contributions of ACD and FC are consistent for most of the studied regions, although the absolute percentages change (Figure B.2 in Appendix B). Additionally, in the southernmost region of Peru, EVI shows higher sensitivity to ACD and FC than any VOD band (Figure B.2 in Appendix B).

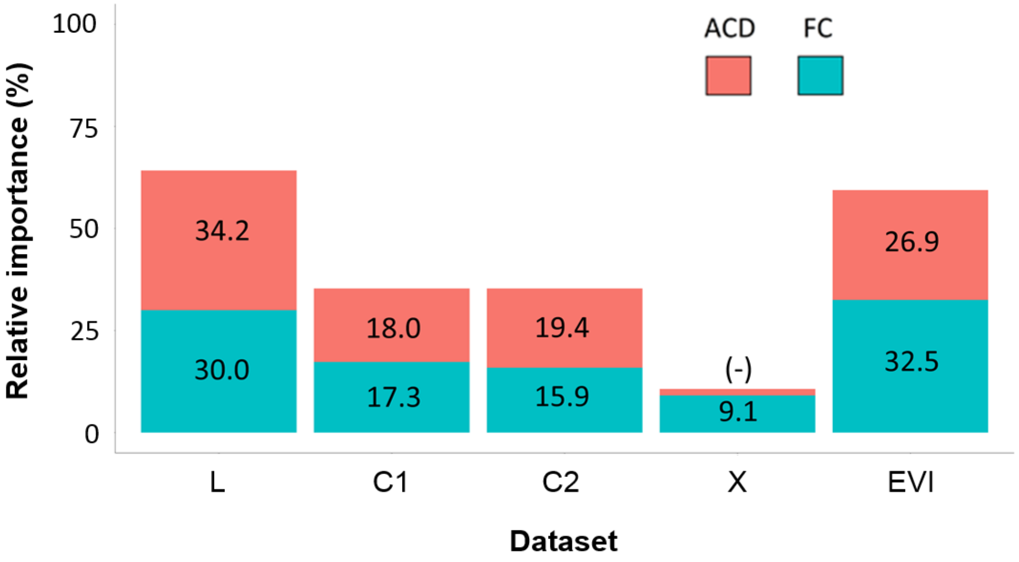

Figure 4.7. Relative importance of ACD and FC as predictors of VOD and EVI in Eq. (4.2). All effects are significant (p<0.0001). All effects are positive, except for the effect of ACD on X-band VOD which is negative (-). Numbers represent relative importance (%) of each variable. All results are significant (p<0.0001).

4.3.3. VOD residuals and VOD-ACD relationships in the Andes and in flooded regions

Positive residuals are associated with decreasing ACD and increasing altitudes in the Andes Mountains. Nevertheless, above 3,000 m residuals seem to be equally distributed around zero (Figure 4.8a, Figure 4.8d and Figure 4.9a). Negative residuals of VOD at L-band are found in river edges and in flooded forest regions, where ACD is lower for pixels with dominant flooded forest cover (Figure 4.8a, Figure 4.8b and Figure 4.9c). In addition, the relationship between water proportion, VOD residuals and ACD is unclear (Figure 4.8a, Figure 4.8c and Figure 4.9b). Importantly, the relationship between the residuals and the fitted VOD values is shown in Figure B.5 in Appendix B. The observed patterns show how, as commented in Section 4.3.2, the VOD-ACD relationship is not completely linear. The geographical patterns for VOD residuals shown in Figure 4.8a might be also influenced by this fact.

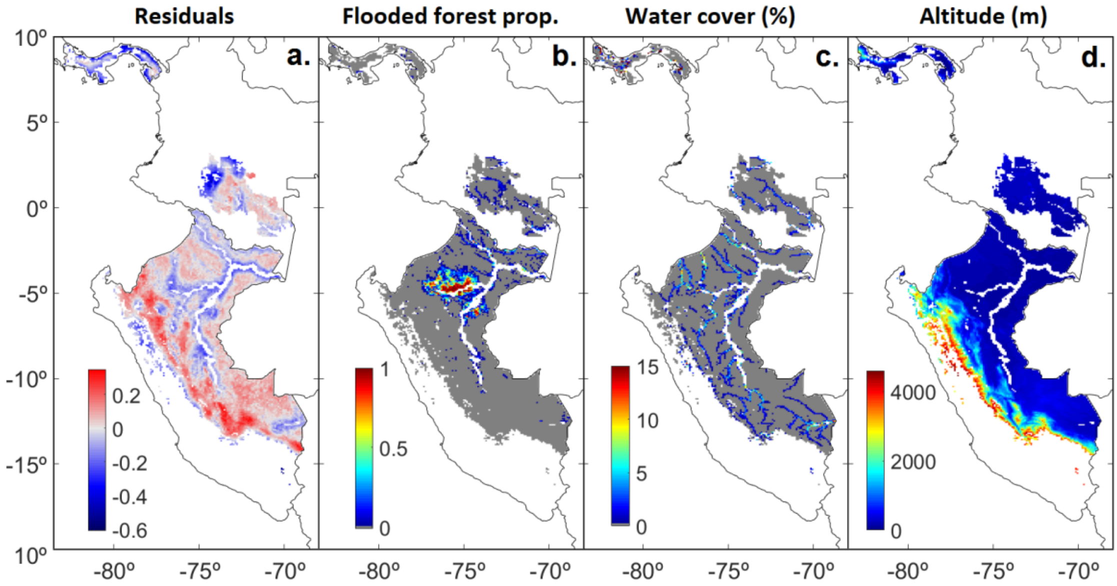

Figure 4.8. (a) Residuals for Eq. (4.1); (b) percentage of flooded forest (grey=0%); (c) percentage of water cover (grey=0%) and (d) altitude (m). Areas without dominant forest cover and areas with insufficient VOD and/or ACD data are not plotted.

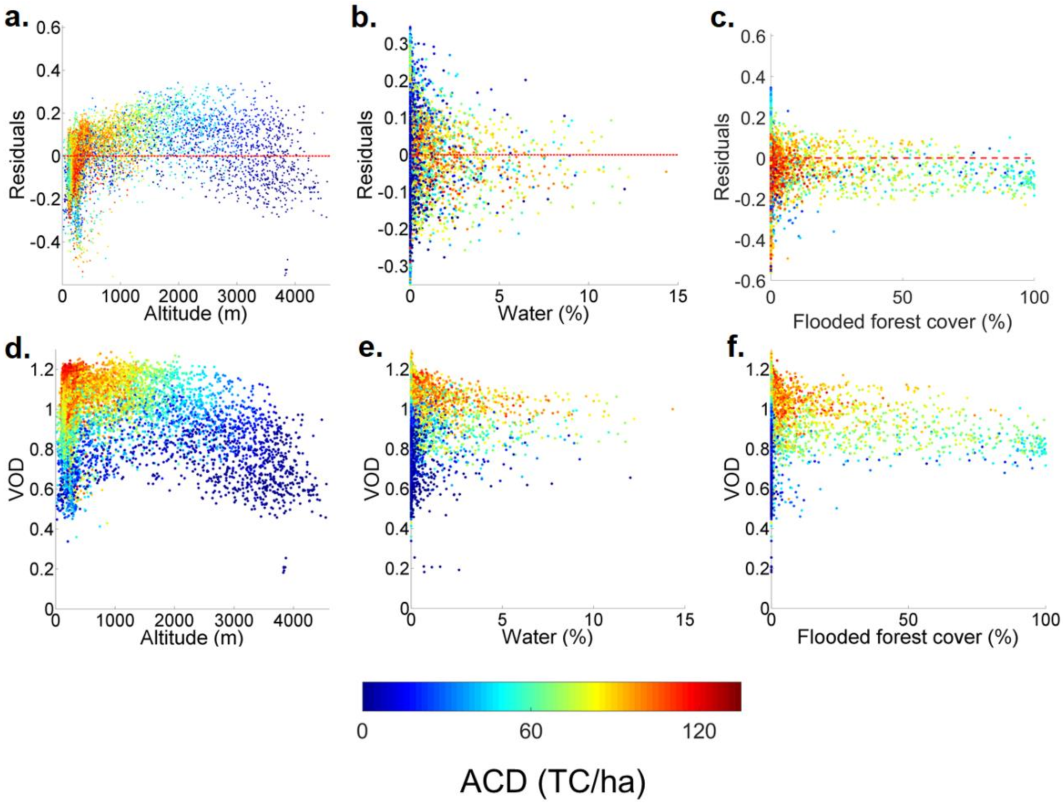

Figure 4.9. Top: relationship between residuals for Eq. (4.1) and (a) altitude, (b) percentage of water and (c) percentage of flooded forest. Dashed red lines show residuals equal to 0. Bottom row: relationship between L-band VOD and (d) altitude, (e) percentage of water and (f) percentage of flooded forest.

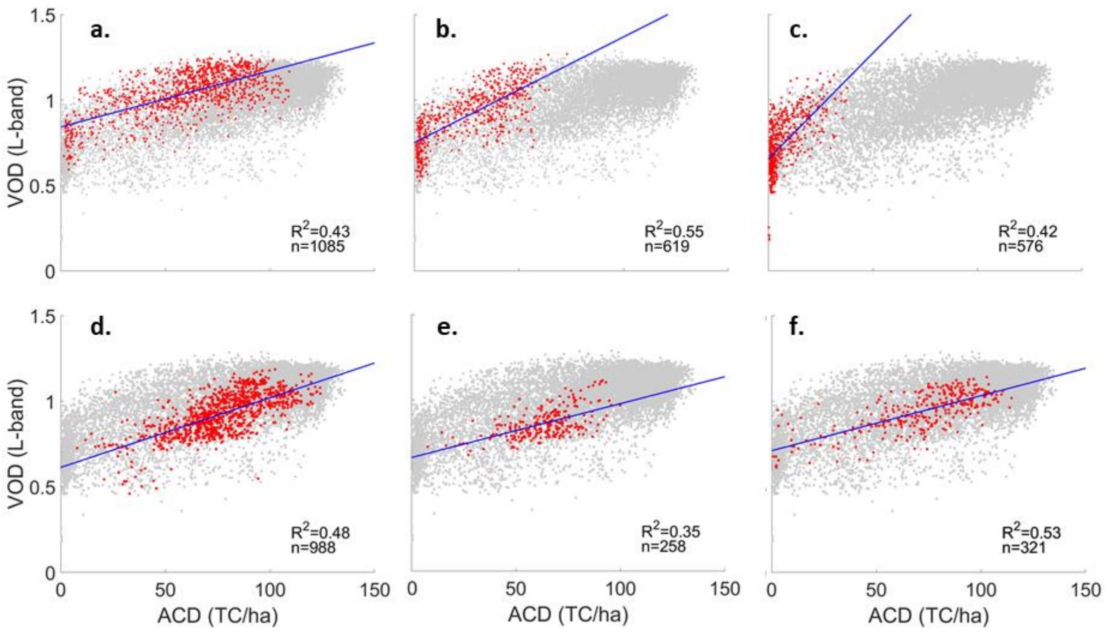

Figure 4.10. Regression of VOD as a function of ACD (Eq. (4.1); blue line) for pixels within different categories (plotted with red dots): (a) altitude between 1,000 and 2,000 m; (b) altitude between 2,000 and 3,000 m; (c) altitude above 3,000 m; (d) proportion of flooded forest between 5 and 50%; (e) proportion of flooded forest above 50%; (f) water proportion above 3%. Grey dots represent the VOD-ACD data for all the forest pixels in the region.

Following the patterns described, T-tests for the different categories of altitude, water, and flooded forest proportion (see Section 4.2.3.C) report that VOD residuals are significantly different from 0, and/or that ACD shows significant differences with reference groups, for all the studied categories (Figure B.6 in Appendix B). This confirms that providing particular analyses for the proposed categories permits to study the VOD-ACD relationship in forests of different biomass, and in regions where the VOD, as a function of ACD, is overestimated or underestimated.

Figure 4.10 a, b and c show regressions of L-band VOD as a function of ACD (Eq. (4.1)) at three altitude ranges. It can be seen that the regression slopes increase with altitude, with R^2 ranging from 0.42 to 0.55. Figure 4.11 a, b and c shows how the ACD relative importance for L-band is higher than the ACD contribution to C- and X-bands and EVI in all cases. For L-band VOD, the ACD relative importance is similar regardless of the altitude group (30.6% to 34.4%). For VOD at C1- and X-bands, the relative importance of ACD is higher above 2,000 m than at lower altitudes. In C2-band and EVI the ACD contribution is higher for the 2,000 – 3,000 m category.

Figure 4.10 d and e show regressions for flooded forest categories (5-50% cover: R^2 = 0.48; 50-100% cover: R^2 = 0.35). In Figure 4.11 d and e the sensitivity of VOD to ACD in flooded regions is higher than the sensitivity found in the overall models shown in Figure 4.7, regardless of the frequency band. The relative contribution of ACD is higher than the relative contribution of FC in these regions. L-band VOD shows the highest sensitivity to ACD (relative importance from 51% to 62.8%), followed by C-bands (39.7% to 42.9%), and by X-band (29.3% to 32.6%), in this order. In contrast, ACD and FC show low and not significant contribution to EVI in flooded forests. EVI has a very low variability in these areas (from 0.45 to 0.49). This illustrates the added value of using microwave over optical remote sensing in flooded forests. Finally, note that the category of water fraction >3% is not presented in Figure 4.11 due to a reduced sample (n<10).

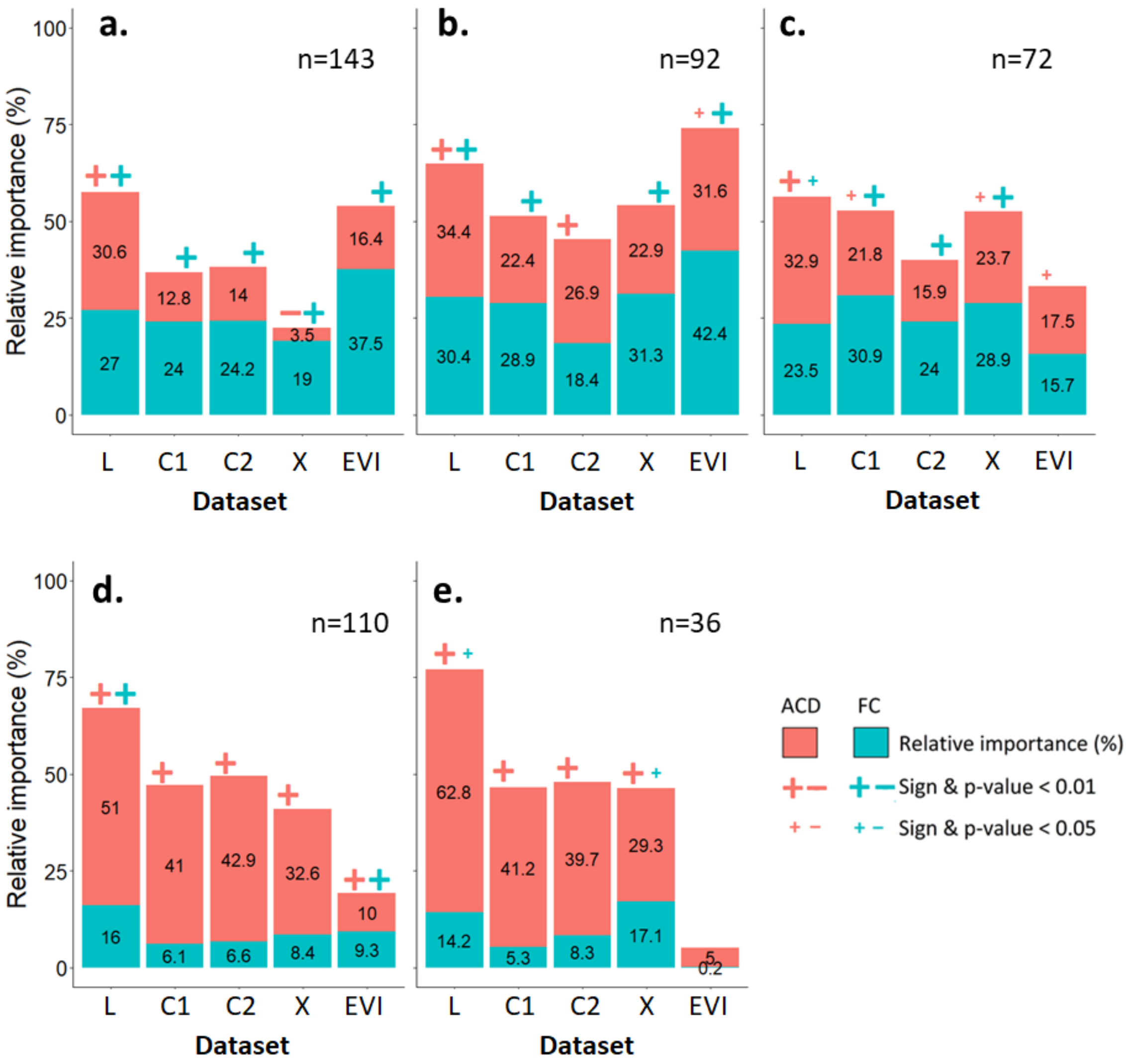

Figure 4.11. Relative importance of ACD and FC as predictors of VOD and EVI (Eq. (4.2)). Sign and significance for each variable are plotted if at least p<0.05. If no sign is plotted, this means not significance at 95% confidence level (i.e., p≥0.05). Results in top row show altitudinal ranges: (a) 1000 to 2000 m; (b) 2000 to 3000 m; (c) >3000 m. Results in the bottom row show flooded forest categories: (d) 5 to 50%; (e) 50 to 100%.

4.4. Discussion

4.4.1. L-band VOD shows enhanced sensitivity to carbon stocks

The ability of remote sensing techniques to capture vegetation carbon density largely depends on the sensitivity of the studied signal to biomass. The VOD-ACD relationship shows the existing link between wet, green and woody biomass in nature, as the ability of VOD to capture ACD depends on its sensitivity to the VWC, and on its capacity to penetrate through the canopy. Both characteristics should be a function of the microwave frequency used for the VOD retrieval. The results presented in this work confirm this fact, as VOD shows a greater sensitivity to ACD up to higher canopy densities with decreasing frequencies (L-, C- and X-bands, ordered by decreasing sensitivity). Results are also consistent with the lack of L-band VOD saturation at higher carbon densities (Figure 4.4), which has been previously reported in Brandt et al. (2018). This stresses the advantage of using L-band VOD for mapping carbon stocks at local and regional scales (up to ~300 km; Figure 4.3).

The relationship between VOD and carbon density in the study area shows contrasting patterns between the forest and the non-forest regions, with non-forested pixels clustered at low VOD and ACD values. GAM functions have captured both patterns, and the continuity on the L-band GAM curve in the transition zone suggests that this microwave frequency could be the most appropriate to capture biomass on vegetation transitions to forests (see Section 4.3.1 and Figure 4.4). The GAM functions fits (i) confirm the enhanced sensitivity of L-band VOD to ACD (R^2 between 0.80 and 0.83), (ii) show that the scarce frequency difference between C1 and C2 bands is not relevant to detect ACD changes, and (iii) confirm the lower sensitivity of the X-band to carbon variability. Nevertheless, it should be noted that GAM functions are a statistical method more appropriate for exploratory analysis than for predictive purposes (Hastie and Tibshirani, 1990; Frescino et al., 2001; Baccini et al., 2004) and therefore other statistical tools would be preferable for predicting carbon stocks from satellite data.

In forest areas, results are also in agreement with the fact that the sensitivity of VOD to carbon density increases with decreasing microwave frequencies. This is also found in the densest forests, although with reduced sensitivity of VOD to carbon changes. Hence, further work is needed to stablish a more accurate VOD-ACD relationship in these forests. In that sense, (i) applying a mutual information analysis (Konings et al., 2015) would disentangle the VOD and ACD contributions and would provide a more robust estimate of their relationship; and (ii) complementarity among VOD bands, as well as among different datasets (e.g., EVI, LiDAR, or radar data) would increase the capacity to stablish an accurate relationship (see Section 4.4.4). In addition, ACD estimates from VOD data would benefit from multi-year observations. In other studies this has allowed providing estimates of carbon trends using VOD either at L-band (Brandt et al., 2018) or at C- and X-bands (Liu et al, 2015).

The main results discussed in this section are consistent for L-band VOD at 9 and 25 km scales. ACD explains between 2% and 8% less of VOD variance using the more detailed grid, suggesting that the 9 km VOD dataset could be applicable to future carbon stock estimations in tropical regions without an important loss of the quality of these estimates. This is interesting as spatial detail is commonly regarded as the main limitation of VOD data in comparison with very high resolution optical and active microwave techniques. In this regard, the use of oversampling measurements and latest advances in optimal interpolation techniques for image reconstruction are particularly promising for microwave radiometry (Chaubell, 2016; González-Gambau et al., 2016).

4.4.2. Carbon density and forest cover contributions to VOD and EVI

VOD changes can be explained by a combined effect of carbon stocks and forest cover (the latter limits the variability of VOD and ACD; Figure 4.6). Interestingly, the VOD variance explained by ACD in Eq. (4.2) is also decreasing with increasing microwave frequencies (Figure 4.7, and Figure B.2 in Appendix B). This is consistent with the discussion provided in Section 4.4.1. Furthermore, ACD and FC show similar contribution to the VOD variability at the studied bands (Figure 4.7), and the addition of the FC variable (see Eq. (4.2)) to the VOD-ACD regression shown in Eq. (4.1) does not result in an important increase of the explained VOD variance (only between 3% and 8% depending on the VOD frequency). Consequently, approximately half of the VOD variance initially explained by ACD (see Section 4.3.1) is due to the spatial variability in forest cover. Nevertheless, the relative importance of the ACD and FC variables changes among regions (Figure B.2 in Appendix B), possibly due to different variability of ACD or to different vegetation patterns (e.g., evergreen forest in Peru contrasts with vegetation mosaics in Panama; Figure 4.1a).

To explore the complementarity and differences between VOD and VIS/NIR indices, MODIS-derived EVI has been included in the study. Results show that the sensitivity of EVI to ACD is lower than the sensitivity of VOD at L-band, and larger than the sensitivity of VOD at C- and X-bands (Figure 4.5, Figure **4.6** and Figure **4.7**). In particular, ACD and FC explain 59% of EVI and 64% of L-band VOD variances. Nevertheless, forest cover has greater relative importance than ACD on the EVI signal, which is coherent to the low canopy penetration of VIS/NIR indices. In addition, it should be noted that (i) EVI shows no association with L-band VOD in forests below 1,000 m, and (ii) EVI equals or enhances the sensitivity to ACD in regions D and F with respect to L-band VOD (Figure B.2 in Appendix B). In general, the results presented are in agreement with other studies reporting poor correlation between L-band VOD and VIS/NIR indices at the global scale, suggesting that these two metrics can complement each other (Grant et al., 2016).

4.4.3. Effect of different vegetation types on the VOD/EVI sensitivity to carbon stocks

Different patterns are found throughout the studied region analysing the residuals of the VOD-ACD relationship. These patterns are linked to decreasing carbon density in mountain areas (which should be related to vegetation transitions through altitude), flooded forests, river edges, and vegetation mosaics.

Possible reasons for positive L-band VOD residuals found in the Andes Mountains include (i) a different response to other vegetation types in the mountains, (ii) uncertainties on the VOD retrievals in regions with sharp topography and/or sparse vegetation, and (iii) uncertainties in the carbon density map (Asner et al., 2012). Results show that the higher sensitivity of L-band VOD to ACD is consistent and similar across different altitude classes (i.e., among groups with different ACD; Figure 4.11, and Figure B.6 in Appendix B). To maintain this coherence, modelling carbon stocks in the Andean forests would need calibration considering different elevations (or different vegetation types linked to elevation), as slopes for the VOD-ACD regression increase with decreasing ACD at different heights (Figure 4.10).

In the studied altitude groups, the joint ACD + FC contribution to the VOD at C- and X-bands and to the EVI signal (Figure 4.11) is higher than the observed in the entire study area (Figure 4.7). This effect is not consistently increasing with altitude, nor significant in some cases, but in general it is consistent to the fact that higher VOD frequencies and EVI have a greater sensitivity to changes in canopy and biomass in less dense forests. Dividing altitude into three separate groups enables a more detailed analysis, but it also limits the ranges of the studied variables and thus reduces their resulting relative importance. This can explain why only the 2,000 – 3,000 m category reports a high weight of ACD on EVI (Figure 4.11b), when positive EVI-ACD and EVI-VOD trends are found above 1,000 m (Figure 4.6 b and **Figure 4.6**e). These trends are in agreement with the results in Todd et al. (1998), which show that NDVI can be considered an accurate proxy of biomass in areas of low vegetation density.

Flooded forests and river edges present negative residuals in the VOD-ACD regression. The higher proportion of water in these areas, which can be flooded up to ten months in a year (WWF, 2018), partially masks the soil emissions ultimately reducing VOD. Although the vegetation covers are very different, this effect has been found previously for rice fields in Thailand: VOD remains low while fields are inundated, but EVI increases following the vegetation growth (Piles et al., 2017). Consistently with previous results, in flooded forests the VOD at L-band shows higher sensitivity to ACD than the VOD at higher frequencies. Nevertheless, the high ACD contribution to VOD at L-band (>60%) in the category containing >50% of flooded forests is not coherent with results obtained at the finer grid (Figure 4.10e). This should be further explored using a larger sample.

Interestingly, ACD in flooded forests explains an important proportion of VOD also at C- and X-bands (Figure 4.11). Flooded forests are complex ecosystems which include several vegetation stages (grasses, shrubs, and early and late successional forests; Daly and Mitchell, 2000; WWF, 2018). This causes a complex structure in terms of vegetation distribution, height, and biomass, as well as lower ACD, which can explain the better response of VOD to carbon. In contrast, EVI has reached saturation and therefore shows very low variability in this area, and forest cover contribution to the studied variables is marginal, as the forest proportion is high and homogenous (95% of flooded forest pixels present >90% of forest proportion). Hence, VOD could potentially contribute to the study of carbon balance in flooded forests, which remains poorly known and hard to investigate with classical spectral indexes (Davidson et al., 2012). This analysis should be extended to river edges of the Amazon and its tributaries, which are flooded seasonally (and present accordingly negative residuals). The fact that the water occurrence product used has not detected water bodies in these regions is possibly due to the limitation of the product to detect water bodies under dense vegetation covers (Pekel et al., 2016). In this study the maximum water proportion is only of 15% (main rivers are not included in the analysis due to lack of ACD data), and therefore further analysis of the water occurrence product is unfeasible.

Additionally, it should be noted that vegetation mosaics (southern Panama and northern of the Colombian study region) show negative residuals because the VOD-ACD regression is dominated by evergreen forests. These present larger ACD and VOD values if compared to those from vegetation mosaics. Further work is needed to provide specific analyses in these regions.

Finally, note that the VOD residuals may respond partially to other factors which should also be mentioned. Firstly, the distribution of the residuals values shows that the VOD-ACD relationship is not completely linear (Figure B.5 in Appendix B). This may lead to overestimations and underestimations of VOD. Nevertheless, other fitting functions studied did not report different results (see Section 4.2.3.A; results not shown). Secondly, the uncertainty of ACD estimates may be a source of spatial variability which must be considered to calibrate carbon stock models. The main sources of uncertainty are the validity of the relationship between the LiDAR tree height measures and the ACD values, and the extrapolation of LiDAR ACD estimates to regional scales (Asner et al., 2012).

4.4.4. Synergy of L-band VOD with multiple remote sensing sources to enhance carbon estimates

The SMAP-derived L-band VOD information is sensitive to carbon density through most of the study area, and could improve the capability of EVI and VOD at higher frequencies to estimate carbon stocks. Nevertheless, the sensitivity of VOD is decreased at high vegetation densities (≥80 TC/ha). This represents approximately 60% of forests in the studied region. In this regard, future missions operating at lower frequency bands and therefore with greater penetration capacity through vegetation would probably be beneficial complementing current VOD estimates. This is the case of the BIOMASS mission (expected in 2020; Le Toan et al., 2011; ESA, 2018b), specifically designed to measure forests and their biomass with a P-band (435 MHz) synthetic aperture radar (SAR). The combined use of L- and P-band sensors should provide improved assessments of carbon density in very dense vegetation.

Remote sensing sources can be blended for more accurate carbon estimates, as the synergy among different remote sensing techniques can overcome the limitations from each data source (Goetz et al., 2009). In this study, it has been shown how EVI information could complement L-band VOD, especially in southern Peru and in montane forests. The L-band VOD-EVI joint application for mapping carbon stocks should be a matter of future work (Section 6.3). The synergetic use of VOD at different frequencies (at least L-, C- and X-bands) and EVI would be particularly appropriate for biomass studies in vegetation transitions of the tropical montane forests. In the case of flooded forests, VOD data at different bands could have great potential for biomass estimation if used in a synergistic fashion. In this forest type, the combined application of VOD and LiDAR should also be investigated, as flooded forests are complex in terms of vegetation height variability, and LiDAR presents the unique capacity of capturing the vertical structure of vegetation. In that sense, the upcoming GEDI mission is expected to provide high resolution information of the forest canopy. Additionally, EVI has shown limited sensitivity to carbon changes in flooded forests, and SAR leads to biomass overestimation in flooded areas (Lucas et al., 2015).

It is worth saying that recent research has provided carbon trend estimates at continental and global scales using VOD data at L-band (Brandt et al., 2018) and at C- and X-bands (Liu et al., 2015). Importantly, the application of C- and X-bands VOD, LiDAR, and VIS/NIR indices, has led to new global biomass datasets (Liu et al., 2011; Saatchi et al., 2011; Avitabile et al., 2016; Baccini et al., 2017). Hence, the synergy between L-band VOD and other remote sensing sources can contribute to enhance carbon mapping and reduce its uncertainties.

4.5. Conclusions

This chapter provides a comparison of SMAP-derived L-band VOD with other VOD products from higher frequencies (from AMSR2 C- and X-bands) and with MODIS-EVI, in terms of their sensitivity to vegetation carbon stocks in Peru, Panama and southern Colombia. To this purpose, the remote sensing variables have been analysed as a function of ACD data obtained by airborne LiDAR. L-band VOD has a higher sensitivity to carbon up to higher densities, and this sensitivity decreases progressively at C- and X-bands, consistently with their increasing frequencies. Therefore, results confirm a fundamental physical phenomenon: lower frequency bands allow capturing the attenuation of soil emissivity as it passes through the whole vegetation canopy. A spatial cross-correlation analysis has shown that the capacity to reproduce carbon spatial patterns at local and regional scales decreases following increasing frequencies. Generalized additive models and linear regressions of VOD as a function of ACD have confirmed the enhanced sensitivity of L-band VOD to carbon variability. The combined effect of the ACD and the FC on the VOD and the EVI signals has been disentangled and quantified analysing the relative importance of each variable in bilinear regressions. At L-band, ACD and FC explain 34% and 30% of VOD variance in tropical forests of the region, respectively.

The study has been stratified by altitude and regions, and a particular analysis has been conducted in flooded forests. Results confirm that L-band VOD presents the strongest relationship to ACD regardless of altitude, vegetation covers and carbon density. These results are also consistent in the studied regions, except in southern Peru, where EVI shows higher sensitivity to ACD than L-band VOD. Also, it has to be noted that (i) ACD and FC partially represent an important contribution to EVI and VOD at C- and X-bands when lower density forests are studied in the Andes, (ii) VOD at all bands shows significant, positive stronger relationship with ACD and FC in flooded forests, and (iii) an important proportion of evergreen forests in the region (those with higher carbon densities) should be further analysed to stablish a more accurate VOD-ACD relationship. Hence, it is suggested that the complementary use of

L-band VOD with VOD at higher frequencies and with different remote sensing sources would be needed. In particular, (i) the future BIOMASS mission, with a P-band SAR on board (Le Toan et al., 2011; ESA, 2018b), would have higher penetration to canopy layers and therefore would improve or complement the present VOD estimates on dense evergreen forests; (ii) the combined application of L-band VOD and the future GEDI LiDAR measurements could provide accurate ACD estimates in flooded forests; and (iii) the synergetic application of VIS/NIR indices and L-band VOD could enhance biomass estimates in forests with lower carbon density, such as montane ones. This chapter presents evidence that L-band VOD is a promising ecological indicator that could help enhancing present global biomass estimates, thus providing a new step forward on understanding the Earth carbon budget.

5

Vegetation optical depth seasonal metrics for crop yield assessment

Abstract

VOD could be a valuable source of information on agroecosystems, especially at lower frequencies for which greater portion of the vegetation canopy contributes to the observed brightness temperature. This chapter proposes a series of L-band VOD metrics for crop yield assessment using the first annual cycle of SMAP data (April 2015 to March 2016) over north-central United States. The yield-VOD relationship is explored using principal components regressions. Results show that 66% of yield variance is explained over the whole region by the first principal component (PC1). In corn-soy crops, PC1 explains 78% of yield amount, and maximum, standard deviation, and range of VOD capture the yield spatial patterns. Mixture of crops and scene heterogeneity weaken these relationships. Hence, in wheat and mixed crops, PC1 explains 42% of yield variance. Results suggest that complementary information on maximum biomass, growth rate, and VOD amplitude can provide robust yield estimates, and that the uncertainty of these estimates depends on crop heterogeneity. This study provides evidence that L-band VOD metrics can potentially be used to enhance crop yield forecasts.

5.1. Introduction

Agriculture represents the most common human land use in the world, occupying ~38% of continental land. During the last fifty years, concurrently to the doubling of human population, the global crop production has increased substantially (Foley et al., 2011). In particular, most main grains have tripled (e.g., wheat and rice) or quadrupled (e.g., corn) their stocks (Godfray et al., 2010; FAO 2017). Nevertheless, total consumption can exceed production when adverse weather conditions occur (Becker-Reshef et al., 2010a). The possible increase of adverse weather for crop production due to climate change may result in decline of most grain yields (Deryng et al., 2014; Asseng et al., 2015; Zhao et al., 2017; see also Section 1.1). Furthermore, the population is growing, and there is a need for increased food supply in the coming decades, at least until the middle of this century. Additionally, agriculture has important environmental impacts: the loss of biodiversity, the increase of deforestation, or the land and water degradation (Foley et al., 2005). In this context, agriculture faces a remarkable challenge: to fulfil the raising food demands improving food security, while reducing the environmental impacts. Present and future EO missions are key to help achieving this goal, and close the so-called ‘yield gaps’ (i.e., reduce the difference between the potential and the real yield on croplands; Godfray et al., 2010; Foley et al., 2011; Tilman et al., 2011).

Agricultural monitoring and yield forecasts are essential to mitigate the impacts of shortages in crop production. Information on crop status and yield are needed to be updated timely and regularly during the crop season. Satellite remote sensing can provide this information worldwide with reasonable costs. The complementarity between remote sensing tools and high quality survey data eases the development and calibration of remote sensing based crop yield models (e.g., Becker-Reshef et al., 2010a). Satellite data is the only means to obtain this information for developing countries were ground-based surveys are most needed but least available (Atzberger, 2013).

Studies on crop phenology and crop yield forecasting from satellite information have been focused mainly on vegetation indices from the visible and the near-infrared spectral regions. These indices measure the amount of photosynthetic active vegetation, which depends on the biotic and abiotic conditions that affect crop status and, ultimately, determine final yield. In particular, the NDVI is the most widely used index for crop yield forecast (Rembold et al., 2013; Alemu and Henebry, 2013). The EVI, in turn, has also been shown useful for this purpose, with the advantage of being less sensitive than NDVI to atmosphere and soil effects (Huete et al., 2002). A variety of yield modelling studies covering different crop types and regions have used these two indices (e.g., Quarmby et al., 1993; Maselli et al., 1993; Doraiswamy and Cook, 1995; Mika et al., 2002; Weissteiner and Kühbauch, 2005; Wall et al., 2008; Becker-Reshef et al., 2010a; Son et al., 2014; Mosleh et al., 2016). Also, they are the basis for global operational agricultural monitoring systems such as the Global Agricultural Monitoring project (Becker-Reshef et al., 2010b) or the European Commission’s Monitoring Agricultural Resources (European Commission, 2017).

Despite the common use of visible-infrared indices, they present several limitations: (i) clouds and aerosols as well as seasonal decreases in solar light in high latitudes limit the global coverage and the accuracy of the indices; (ii) these indices saturate for dense crops with high

Leaf Area Index values; (iii) they are limited to monitor the top of the crops canopy; and (iv) the photosynthetic activity is not always the main factor conditioning the final yield (Liu et al., 2011 and 2013; Jones et al., 2012). Alternatively, microwave remote sensors can be used to overcome the above-mentioned limitations (Ulaby et al., 1981, pp. 1-5). In active systems, radar backscattering allows obtaining microwave vegetation indices, which provide information on vegetation status and characteristics (see recent reviews of Vereecken et al., 2012 and McNairn and Shang, 2016). In passive systems, the VOD is directly proportional to the VWC (see Section 1.2; Ulaby et al., 1986, pp. 1551-1596; Jackson and Schmugge, 1991), and is linked to the amount of living biomass as well as to the water stress experienced by the vegetation (Momen et al., 2017). VOD from passive microwave sensors at C- and X-bands has been applied to study biomass, carbon balance (Liu et al., 2011, 2013 and 2015), and isohydricity on forests (Konings and Gentine, 2017), to analyse vegetation phenology (Jones et al., 2011 and 2012; Guan et al., 2014), and vegetation dynamics in drylands (Andela et al., 2013; Tian et al., 2016). Related to agriculture monitoring, VOD at C- and X-bands retrieved from AMSR-E has been studied as a predictor of yield in the United States, showing highest correlation for summer months, when the peak of season occurs. Still, this VOD dataset has shown less predictive capacity for yield than EVI and NDVI (Mladenova et al., 2017; Guan et al., 2017). Interestingly, Guan et al. (2017) have found that VOD at X-band in the United States Corn Belt is linked not only to biomass, but also to environmental stresses driving yield in the region, providing essential information to improve crop yield predictability.

Hence, VOD is a promising tool in crop phenology monitoring and in yield assessment. Nevertheless, three main limitations must be stressed in the latter sense. Firstly, VOD coarse (9 to 36 km) resolution ideally requires relatively homogenous cropland regions to avoid the impact of fragmented landscapes in the VOD signal. Even so, major crop areas in the world with a crucial role in food supply are prone to be target regions for crop studies using VOD (e.g., the US Corn Belt, the Sahel region, central Eurasia, or India, among others). Secondly, the presence of standing water or bare land in agricultural fields (e.g., due to irrigation or crop rotation) may have an important impact on the VOD signal and subsequent crop analysis. The most significant case is rice fields when flooded, where standing water leads to a sharp decrease in VOD that impedes tracking the rice phenology (Piles et al., 2017). Thirdly, VOD allows infering the crop biomass, but its linkage to crop grain yields may depend on weather conditions (e.g., high temperatures during corn pollination may decrease final yield without affecting the total plant biomass and therefore the measured VOD).

The sensitivity of VOD to vegetation water content and its relationship with biomass is higher at L-band than at higher frequency bands (see Chapter 4 for a study case in forests). In this regard, there is an increasing interest in recent SMOS and SMAP VOD retrievals, and in the continuity of L-band passive microwave observations, since they can contribute to quantify the dynamics of carbon stocks over forests and complement optical data in global vegetation monitoring.

The SMOS retrieval algorithm is based on a multi-angular and dual-polarization approach obtaining simultaneous information of soil moisture and VOD (Kerr et al., 2012 and Section 1.3.4). The performance of SMOS-derived VOD in the field of agriculture research has been assessed in previous studies showing that, despite of the presence of instrumental noise limits detecting short-term changes, long-term and seasonal trends on SMOS VOD can be used to provide crop phenology and crop yield information. In that sense, Lawrence et al. (2014) found that SMOS VOD followed the increase of vegetation indices during the growing season, and their decrease during the crop senescence. The peak of VOD lagged the peaks of visible-infrared vegetation indices, which can be explained by the fact that maximum greenness precedes maximum biomass. Similarly, Hornbuckle et al. (2016) found that the SMOS VOD followed the corn development in the region, and that the VOD peak corresponded to a specific development stage of this crop (i.e., the milk stage, when the maximum water content is reached). Furthermore, the relationship between the SMOS VOD and yield in Iowa was investigated by Patton and Hornbuckle (2013). They found that the increase of VOD during the crop season explained ~60% of yield variability in the region. Additionally, a new SMOS VOD product -the SMOS-IC- is now available. It has shown improved correlation with NDVI than the standard L3 SMOS VOD, and its applications to vegetation studies are promising (Fernández-Morán et al., 2017).

The SMAP radiometer measures terrestrial emission and provides brightness temperatures (TB) at ∼40 km resolution (Entekhabi et al., 2010). The SMAP MT-DCA algorithm is proposed for the retrieval of soil moisture, VOD and effective scattering albedo from SMAP (Konings et al., 2016, and Section 1.3.4). The resulting SMAP MT-DCA VOD product has already showed potential for monitoring agro-ecosystems' phenology in Iowa (USA), Nigeria, Argentina, and Thailand (Piles et al., 2017). The present study explores the relationship between the first year of SMAP MT-DCA VOD information and in situ crop yield data. It is hypothesized that: (i) L-band VOD will reproduce temporal and spatial patterns of crop phenology and crop yield, respectively; and (ii) the capacity of VOD data to assess crop yields will depend on main crop types in the region. In order to infer end-of-season crop yields from the dynamics of VOD, a number of metrics of VOD need to be defined. This study introduces metrics that reliably predict yields for various crops using SMAP VOD and ground-based survey data from croplands in the north-central United States.

5.2. Materials and methods

5.2.1. Study area

This study is focused on the extensive croplands of North Dakota (ND), South Dakota (SD), Nebraska (NE), Minnesota (MN), Iowa (IA), Illinois (IL), Indiana (IN), and Ohio (OH) (Figure 5.1). The center and southeastern areas of the study region are located within the US Corn Belt, which contributes to ~50% of corn and ~40% of soy production in the world (Guan et al., 2017). In the USA, 73% of corn and 70% of soy production are obtained in this region. In contrast, other crops are planted in the northernmost regions of the study area, with predominance of spring wheat. In particular, 68% of spring wheat production in the United States is harvested in North Dakota, South Dakota, and Minnesota (USDA, 2015; data for the period 2010-2014). In the entire study area, the US Department of Agriculture routinely collects valuable and detailed crop cultivation and crop stages information based on surveys.

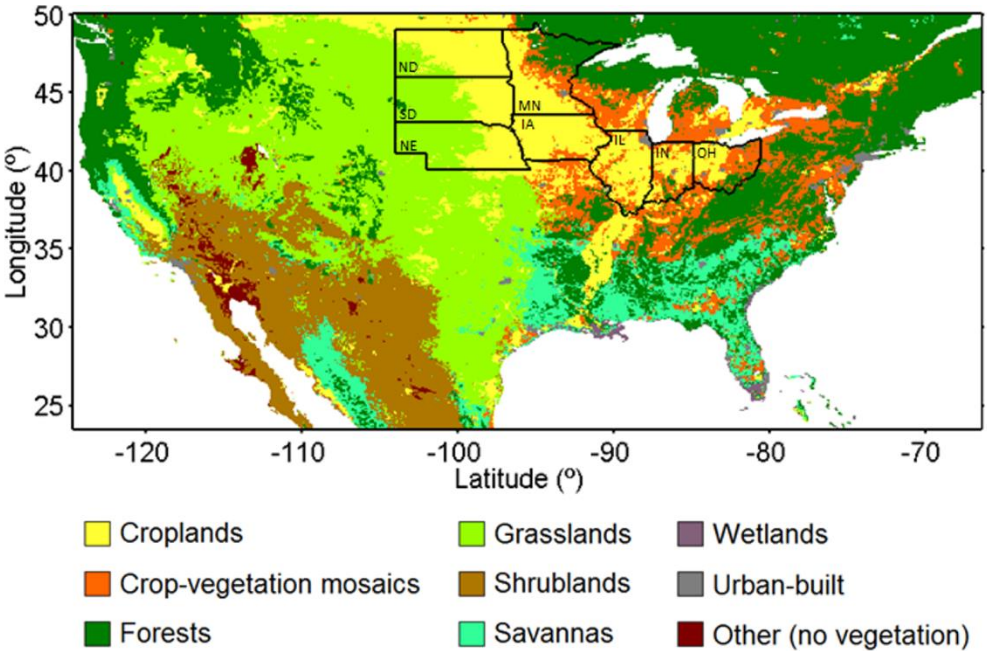

Figure 5.1. Land use in the United States according to IGBP (reclassified from 16 to 10 categories). The study area includes croplands in North Dakota (ND), South Dakota (SD), Nebraska (NE), Minnesota (MN), Iowa (IA), Illinois (IL), Indiana (IN), and Ohio (OH).

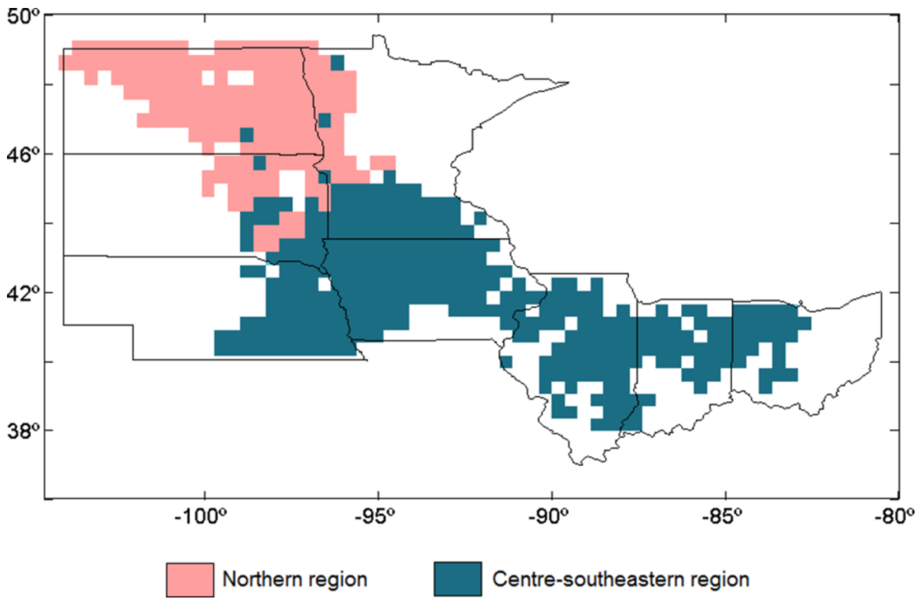

Figure 5.2. Clusters in the study area. In the center-southeastern region, (soy + corn) proportion is ≥95%. In the northern region the sum of both crops proportions is <95%. See Section 5.2.3.

Concerning the coexistence of different crops in the study region, note that yields for various crop types are dependent on the phenology of the plant as well as on environmental conditions such as available moisture and degree-days for growth. Within each crop, seed varieties can also influence the phenology. Therefore, the patterns of cultivation (crop and variety choices) and mixture of crops affect the metrics of plant growth based on optical and microwave remote sensing. To provide an accurate assessment of yield, the study area is analysed as a whole as well as divided in two clusters: a corn-soy region in the central-southeastern area, and a wheat and mixed crops region in the north (Figure 5.2). These divisions are coherent with respect to the dominant cultivations (see Section 5.2.3).

5.2.2. Datasets

A. VOD data from SMAP

The MT-DCA algorithm (Konings et al., 2016) provides estimates of soil moisture, VOD, and effective scattering albedo (time-invariant) from single look-angle observations using a number of consecutive overpasses (depending on the measurements mutual information; Konings et al., 2015). When applied to SMAP brightness temperatures, two consecutive observations can be used to retrieve two soil moisture estimates, one VOD estimate, and a single value of albedo for the entire study period (Konings et al., 2017a). SMAP VOD datasets retrieved using MT-DCA have shown mean values comparable in magnitude to those from SMOS data - although with a larger dynamic range-, and good agreement with global vegetation and land cover patterns (Konings et al., 2016 and 2017a).

In this study, the first year of SMAP-based VOD (from 1st April 2015 to 31st March 2016) was used. This dataset was provided in the EASE2 grid (NSIDC, 2017a) at 9 km posting. The following processing steps were applied in this study: (i) pixels with frozen soils were detected by SMAP radiometer-derived freeze/thaw flags and modelled surface temperature (NSIDC, 2017b), and were screened out; (ii) a 7-day average moving window was applied to VOD in order to reduce high-frequency noise and focus on seasonal phenology; and (iii) missing data were interpolated using a linear fit (this only affected 1.3% of the studied pixels). Longer 15 and 21-day average moving windows were also explored, but they were found to over-smooth the data such that the seasonal cycle was underestimated (results not shown). Note that the 7-day smoothing window applied actually reduces the frequency observation of VOD measurements, which becomes comparable to the one obtained from optical-near infrared indices when affected by short periods of clouds. Still, it is important to stress that VOD and optical data explain different phenological traits on plants (see Section 5.4.1).

A representative example of a resulting VOD time series is shown in Figure 5.3. Within the crop season, increasing and decreasing VOD correspond to growing and senescence of crops, respectively. Out of the crop season, a certain increase of VOD values is also found. This is discussed in Section 5.4.1. Considering the whole study region, the lag between minimum and maximum VOD (i.e., the period when vegetation grows) ranges between 1 and 118 days. To avoid inconsistency with plant phenology patterns, pixels with less than 19 days growth period were not considered (0.9% of the studied pixels). The threshold of 19 days corresponds to the first percentile.

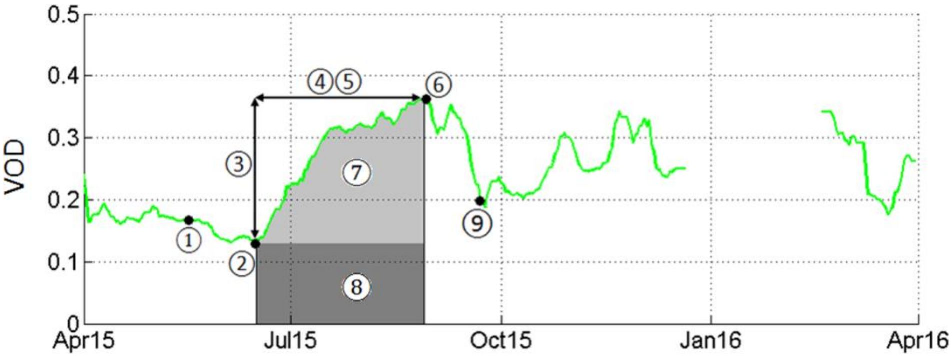

Figure 5.3. Example of a VOD time series and VOD metrics for a pixel sited in northern Iowa. Crop season spans between beginning of season (SOS; ①) and end of season (EOS; ⑨). VOD metrics are computed between minimum (②) and maximum (⑥) VOD dates. VOD metrics are: ③ range, ④ average, ⑤ standard deviation, ⑥ maximum, ⑦ small integral, and ⑦ + ⑧ large integral.

B. Land cover

The land cover classification data used by the SMAP Project (Kim, 2013) was also used here to identify croplands in the region. This dataset applies the International Geosphere-Biosphere Program (IGBP) land cover type classification. The land cover map was projected to the EASE2 grid (NSIDC, 2017b) at 3 km resolution, and is shown in Figure 5.1. Only pixels classified as croplands (yellow areas in Figure 5.1) were considered in this study.

C. Crops databases

Information on area planted, yield, and phenology of crops was obtained from the United States Department of Agriculture – National Agriculture Statistics Service (USDA-NASS). It represents an exhaustive database containing crop information and crop production estimates based on hundreds of yearly sample surveys (USDA-NASS, 2017). This database has been applied in previous studies (e.g., Patton and Hornbuckle, 2013; Hornbuckle et al., 2016; Guan et al., 2017). The information used in this paper corresponds to the 2015 season and includes all the cultivated fields in the region: barley, beans, canola, corn, flaxseed, lentils, oats, peas, sorghum, soybeans, and wheat.

Area planted and yield data from the USDA-NASS database are available for each crop type at a county scale (mean area of counties = 1,905 km^2). This information was transferred to a georeferenced raster by assigning to each VOD pixel at 9 km resolution the information from the county where it was contained. The centre of the pixel was used in case of pixels covering more than one county.

Yield values for each crop type are shown in Figure B.7 in Appendix B. The original units (bushels/acre or lb/acre, depending on the crop) were converted to kg/m^2 according to Table A.7 in Appendix A. To obtain a single yield datum for each pixel, a weighted value was calculated as a function of yield and area planted for each crop. Figure B.7 in Appendix B shows that corn is the most productive crop (median grain yield of ~1.06 kg/m^2), with soy and wheat having a median grain yield of ~0.35 kg/m^2.

The USDA-NASS database provides weekly information on crop phenology progress. In particular, the percentage of area planted of each crop type that has reached each crop stage is available. These stages include planting, emergence, vegetative phase, reproductive phase, senescence, maturity, and harvest. This information is available at a state level.

5.2.3. Crops distribution and heterogeneity

Percentages of area cultivated per each crop type are displayed in Figure 5.4a. Corn and soybeans are the major crops in the central and southeastern areas, with corn dominating over soy (except Ohio, where soy occupies ∼60% of croplands). In contrast, wheat predominates across North Dakota and northwestern Minnesota counties, where other species (referred to as mixed crops) are present in a lower proportion. The heterogeneity or mixture of crops was measured using the Gini-Simpson Index (GSI; Simpson, 1949). This index has been successfully used to measure heterogeneity of land cover conditions in previous studies (Piles et al., 2015; Konings et al, 2016). In this paper, the GSI is calculated as follows:

$$GSI = 1 - \sum p_i^2, \tag{5.1}$$

where p_i is the proportion of area planted of each crop. The heterogeneity of crops for the study region as measured by GSI is shown in Figure 5.4b. Note that values of GSI near 1 show high heterogeneity and values near 0 show high homogeneity. As expected, Figure 5.4b confirms that the highest heterogeneity (GSI>0.6) is found in the northernmost region, while values near 0.5 are found in the central and southeastern areas due to the presence of corn and soy in similar proportions. Based on this crops distribution, two clusters were selected in the study area: (i) a central-southeastern region where (corn + soy) proportion sums ≥95%, and (ii) a northern region where this sum is <95% (Figure 5.2). This clustering is coherent with the GSI, showing higher heterogeneity in the north (median GSI = 0.59; maximum GSI = 0.74), than in the central-southeastern region (median GSI = 0.49; maximum GSI = 0.54). In addition, for each cluster, a linear regression was performed between corn proportion and yield. This aimed to provide information on the effect of the most productive crop on yield.

In order to provide a complementary analysis on the yield for specific crops, pixels where corn, soy or wheat exceeded 50% of area planted were chosen. As the VOD signal is dominated by corn, pixels with >50% of area planted with soy or wheat were considered only if the corn proportion was <20%. This led to a selection of 281 corn pixels, 19 soy pixels and 9 wheat pixels. Note that specific analyses for other crops were impossible due to lack of sample.

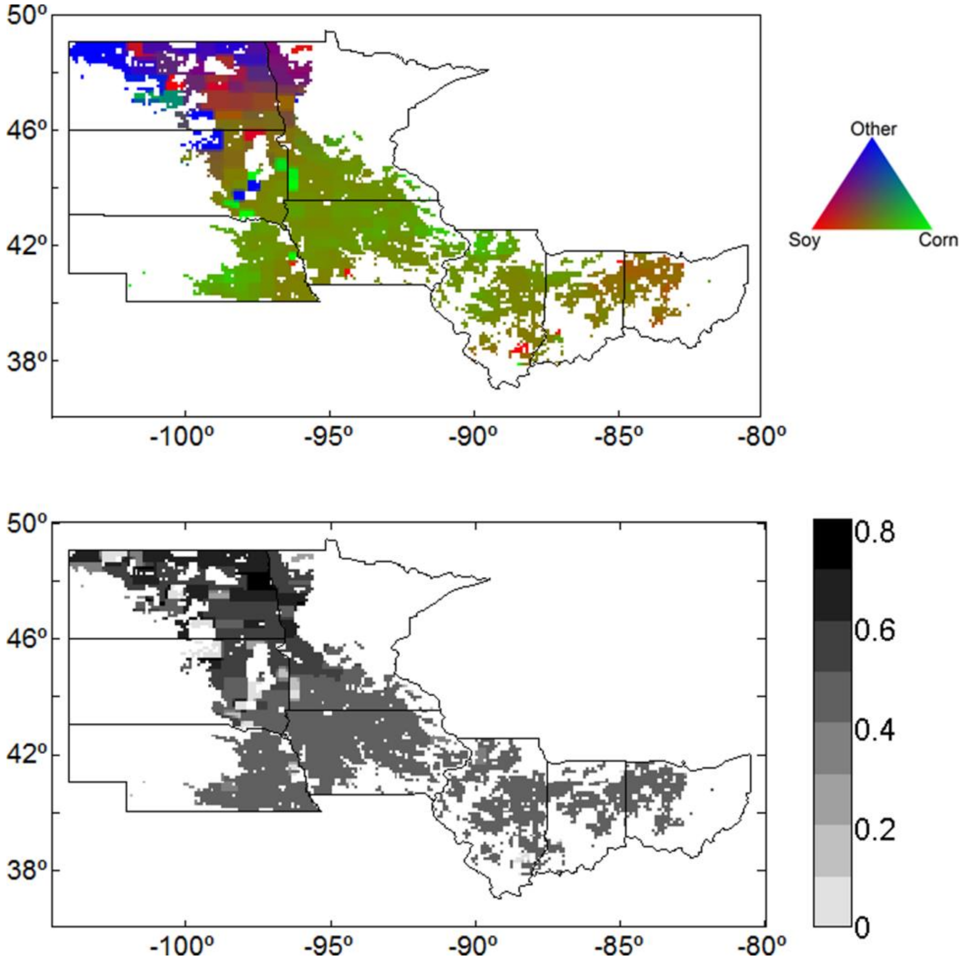

Figure 5.4. (a) Percentage of area planted for corn, soy, and other crops (mainly wheat). Each vertex in the triangle corresponds to 100%; (b) GSI of crop types showing high homogeneity for values near 0, and high heterogeneity for values near 1. Scale: 9 km.

5.2.4. Crop season definition

Daily percentages of crop phenology stages were calculated from the USDA-NASS weekly information using linear interpolation. Information on crop progress stages was used to calculate the beginning and the end of each crop season. The start of season (SOS) and end of season (EOS) were established as the dates when 50% of crop had emerged and had reached maturity, respectively, as suggested in Hornbuckle et al. (2016). Table A.8 in Appendix A reports the SOS and EOS obtained for the most common crops.

Since a variety of crops coexist in the same state, SOS and EOS from the dominant crop were assigned only when that crop exceeded 50% of area planted. In cases where there was not a clear dominant crop, SOS and EOS from the two most extensive crops were compared, and the latest SOS and the earliest EOS were selected. The latter criterion was needed to discard the increasing VOD values that are found in some particular pixels out of the crop season (this is discussed in Section 5.4.1). Since information on the date of maturity for wheat, oats, and barley in Minnesota was missing, the date when 90% of leaves had reached senescence was used instead, consistently with the phenology of these crops in other states. An example of a crop season within a VOD time series is provided in Figure 5.3.

5.2.5. VOD during crop senescence and after harvest

Although the present study is focused on the crop growth period, it is necessary to fully understand the behaviour of the VOD signal during other periods. For this reason, the crops senescence has been investigated computing the difference of VOD between the maximum VOD during the crop season and the EOS date. Additionally, the spatial patterns of VOD after the crop season have been studied computing the maximum VOD after the EOS date. Using the Pearson's correlation coefficient, these patterns have been related to (i) the proportion of winter wheat in the region, which has a different phenological cycle than the studied crops, and (ii) the proportion of corn and the final yield in the region, as crop residues left in the soil after harvest may affect the VOD signal. It is assumed that larger corn proportion and yield lead to a larger amount of crop residues.

5.2.6. Data filtering and aggregation

To ensure that this study is based on mostly homogeneous cropland regions, the SMAP (9 km resolution) pixels were considered only when they were totally classified as croplands, following the IGBP 3 km map. Also, note that yield data was obtained originally at county scale, and should be compared to VOD metrics at a similar scale in order to avoid oversampling. To that purpose, crop and VOD datasets were averaged to 36 km to approximately match the county scale as well as the SMAP native instrument resolution. The resulting pixels were excluded when the sample for averaging was <5 finer (9 km) resolution pixels. Finally, 495 pixels at 36 km resolution remained and form the basis for this study. The area covered is ~640,000 km^2.

5.2.7. VOD metrics

In this study, the following VOD metrics are proposed: maximum, average, range, standard deviation, small integral (i.e., integration of ranges), and large integral (i.e. integration of absolute values; see Figure 5.1). All metrics were calculated between the minimum and maximum VOD reached within the crop season (Table A.9 in Appendix A).

Differences in crop and seed varieties result in different temporal patterns of phenology. Also, different crops and varieties respond differently to environmental stresses such as soil moisture deficit or abnormally high or low temperatures at different stages of growth. Therefore, different statistical metrics were defined as each should capture different characteristics in the VOD dynamics. Range and standard deviation capture the rate of growth.

Integrals of VOD in time capture accumulations. Maximum and average capture the level during growth and when growth ends.

Principal component regressions (PCR) were used to optimally combine the metrics, taking profit of their ability to capture the VOD dynamics and its different traits. The different VOD metrics above were used to derive the principal components, using crop yield as the response variable. Regression models were tested for an increasing number of components, and they resulted in similar coefficients of determination. Only the dominant first principal component (PC1) was chosen. In order to facilitate the comparison between yield and VOD metrics, both were scaled between 0 (equivalent to minimum value) and 1 (equivalent to maximum value). For the entire region, the spatial patterns of yield and VOD metrics were compared, and the Pearson coefficient of correlation (r) between them was computed.

PCR is expected to capture the maximum variability explained by the VOD metrics. Hence, regressions of yield as a function of $PC1$ were fitted for each cluster, as well as for the corn, soy and wheat subsets. Linear and exponential fittings were tested, and the latter provided the best agreement with yield variability. The equation used was:

$$Yield = \alpha + \beta \cdot (1 - e^{-\delta \cdot PC1}), \tag{5.2}$$

where α, β, and δ are constant terms. Complementarily, the same regression was computed for each VOD metrics separately. For these regressions the Levenberg–Marquardt algorithm was used, and outliers were filtered applying bi-square weights. Results for regressions in each cluster are plotted, and the coefficient of determination is computed to provide the proportion of yield variability which is explained by VOD.

5.3. Results

5.3.1. Relationship of VOD with yield and crop composition

Maximum, minimum and mean values for yield and for the proposed VOD metrics are provided in Table 5.1. Yield ranges from 0.13 to 1.08 kg/m^2. VOD maximum reaches 0.48, and mean values range between 0.09 and 0.36 (Table 5.1). Corn leads to the largest yields (with median = 1.06 kg/m^2), while wheat and soy are less productive (median ∼0.36 kg/m^2; Figure B.7 in Appendix B). Results for VOD during crop senescence and beyond the end of the crop season are shown in Figure B.8 in Appendix B.

Figure 5.5 shows the spatial patterns for the VOD metrics and yield. It also shows Pearson correlation coefficients (r) between yield and VOD metrics, which range between 0.56 and 0.81. Best results are obtained for PC1 (r = 0.81), and for maximum, both integrals, and average (r>0.7). Generally, highest yield values are found in the central-southeastern region, with a decreasing trend towards east. Most VOD metrics reproduce the high yields in the centre of the study area and, in particular, PC1, maximum, standard deviation and range of VOD show the best agreement with yield in this area. Also, the decrease of yield in the easternmost states matches with the distribution of PC1, maximum, and average. The lowest yield found in the northern region is best reproduced by the small integral, although all the VOD metrics consistently display low values in this region.

Figure 5.6 shows the relationship between yield and PC1, as well as its dependence on crop proportions (Figure 5.6a) and on heterogeneity (Figure 5.6b). Higher values of PC1 are associated with higher yields. Nevertheless, this relationship is weaker when high yield saturates in corn-dominated pixels (approximately at PC1 values > 0.7). Also, the plots show how corn proportion and crops diversity strongly conditions yield: pixels where soy and heterogeneous crops are planted show lower yield and lower VOD than corn-dominated pixels (Figure 5.6, and Figure B.9 in Appendix B).

Table 5.1. Statistical scores (minimum, mean, and maximum) for reported yield, and the SMAP VOD metrics over the entire study region: first principal component (PC1), maximum (Max), average (Avg), large integral (LInt), small integral (SInt), range (∆VOD), and standard deviation (Std).

	Yield (kg/m^2)	VOD metrics						
		PC1	Max	Avg	LInt	SInt	∆VOD	Std
Minimum	0.13	-5.55	0.14	0.09	1.98	0.39	0.04	0.01
Mean	0.66	0	0.32	0.23	15.17	7.07	0.19	0.05
Maximum	1.08	4.65	0.48	0.36	27.60	16.25	0.37	0.12

5.3.2. VOD metrics for yield estimation

The first principal component (PC1) derived from PCR has the highest correlation with yield through the entire study area (r = 0.81), explaining 66% of yield variability. PC1 results from a linear combination of VOD metrics. Table A.10 in Appendix A details the coefficients used for the PC1 computation. Maximum and small integral have the highest weights, although in general terms coefficients are similar for all the metrics. Regressions of yield as an exponential function of PC1 are provided in Figure 5.7 for the central-southeastern region, and in Figure 5.8 for the northern region. In the central-southeastern area, PC1 explains 78% of yield amount, while in the northern region it explains 42% of its variance. Intercepts (term α in Eq. (5.2)) are not significantly different than zero ($p>0.05$) in these regressions. Terms β and δ in Eq. (5.2) are positive and significant in the central-south-eastern region, but they are not significantly different than zero in the northern region (i.e. their values are near to zero and consequently the shape is almost linear, as shown in Figure 5.8). Table 5.2 provides the coefficients of determination for the yield-VOD metrics regressions.

Specific results for corn, soy and wheat are provided in Figure B.10 in Appendix B. PC1 explains 68% and 47% of corn and soy yield variance, respectively. For wheat, the yield variance explained is 50% for linear regression, and 75% for the model in (4.2). These differences might be due to the small sample (n=9).

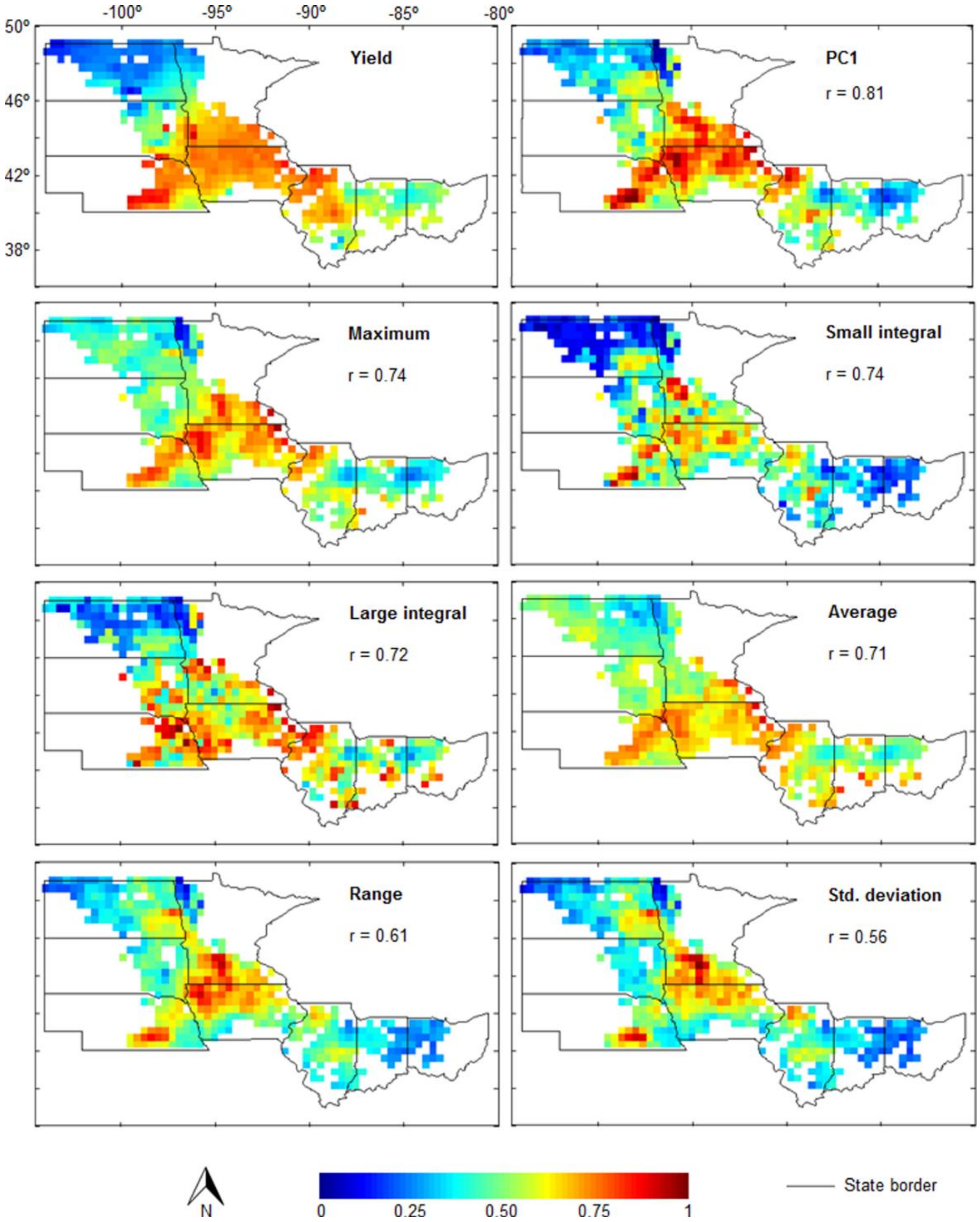

Figure 5.5. Maps of yield and the proposed VOD-derived metrics (scaled). Pearson's correlation coefficient between yield and each VOD metric (r) is shown for each map. Resolution: 36 km.

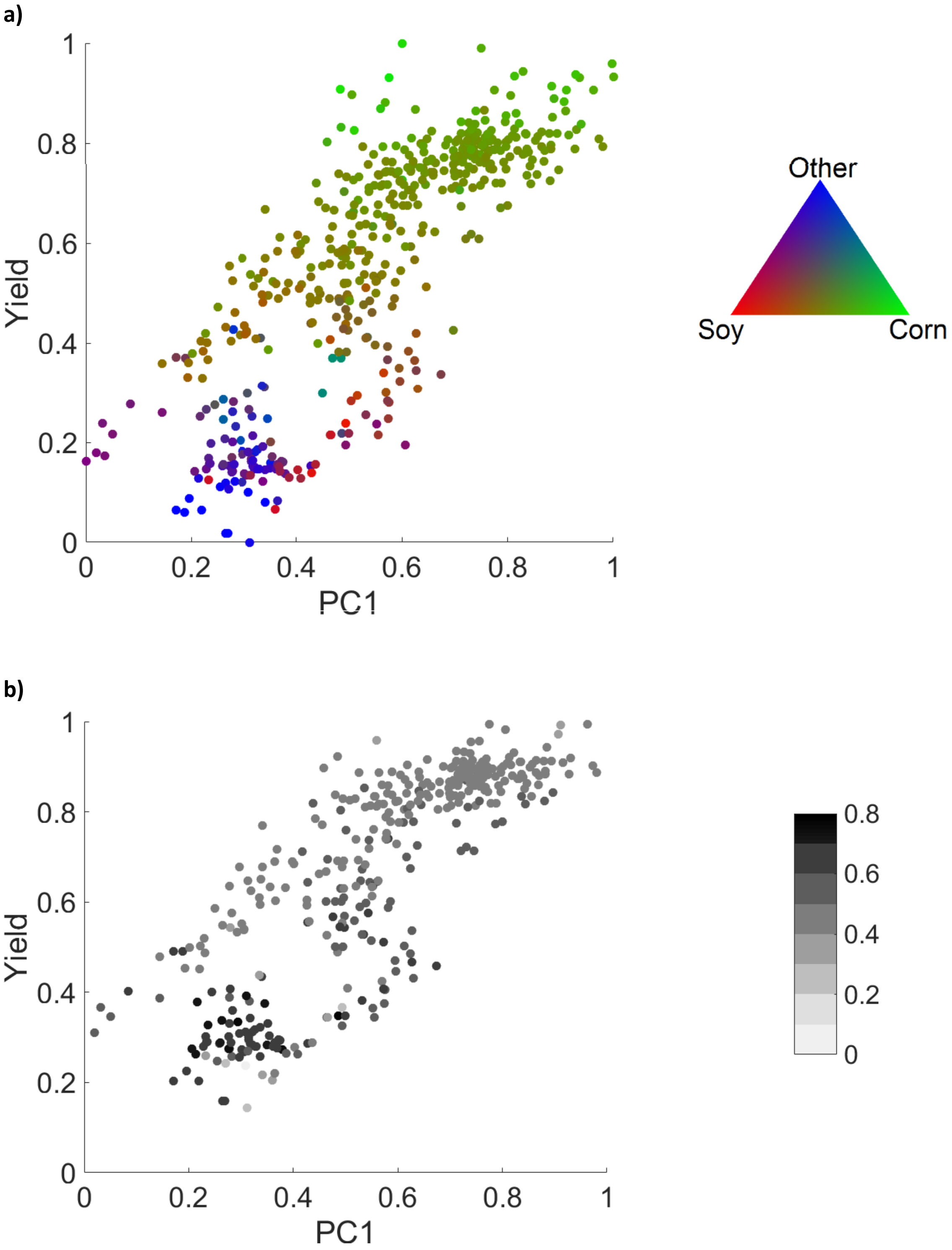

Figure 5.6. (a) Scatter plot showing the relationship between PC1 and yield, and its dependence on crop proportion. Both variables are scaled. Percentages of corn, soy, and other crops (mainly wheat) are represented using the triangle, where each vertex corresponds to 100%; (b) Scatter plot showing the relationship between PC1 and yield, and its dependence on GSI of crop types showing high homogeneity for values near 0, and high heterogeneity for values near 1.

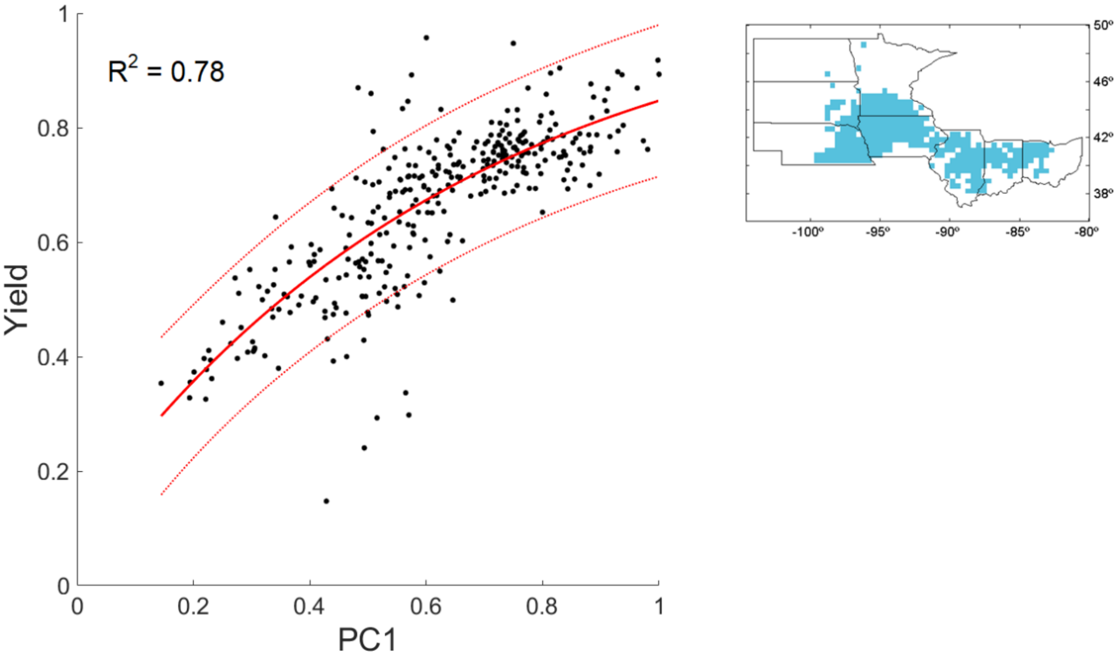

Figure 5.7. Fitting of yield as a function of PC1 for the center-southeastern region. Both variables are scaled. Red dotted lines represent 95% confidence intervals. The inset panel shows the cluster map.

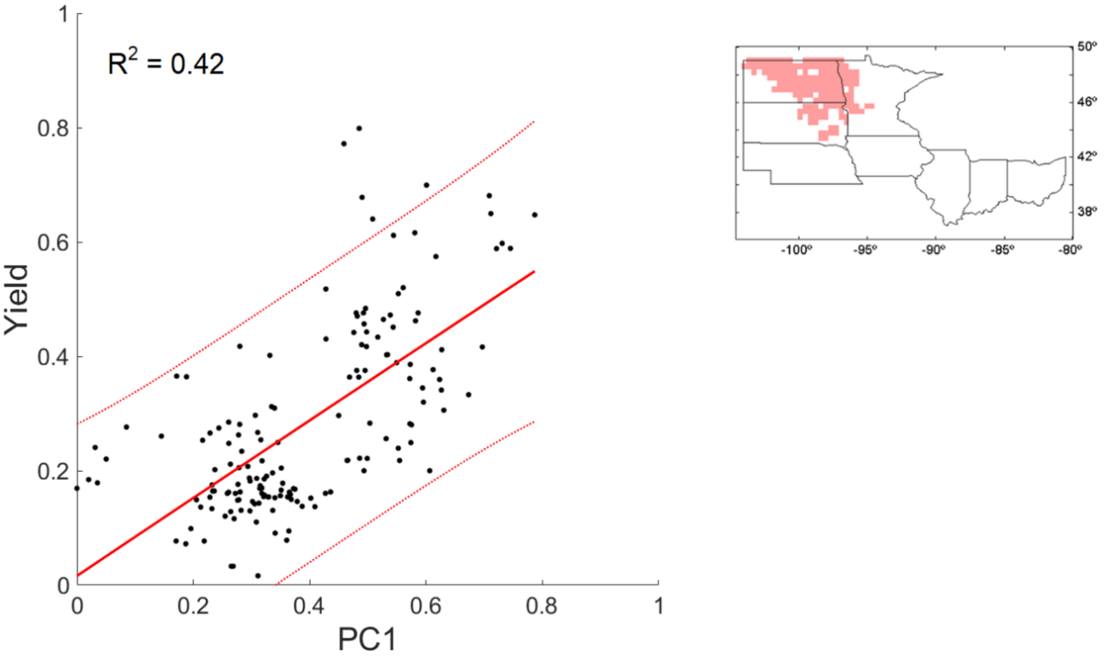

Figure 5.8. Yield as a function of PC1 for the northern region. Both variables are scaled. Red dotted lines represent 95% confidence intervals. The inset panel shows the cluster map.

Table 5.2. Coefficients of determination for the yield-VOD metrics regressions for each cluster.

VOD metrics	Cluster	
	Center-southeastern	Northern
Maximum	0.74	0.18
Small integral	0.63	0.49
Large integral	0.23	0.44
Standard deviation	0.70	0.17
Range	0.69	0.22
Average	0.44	0.15

5.4. Discussion

5.4.1. VOD time series match crop season phenology

VOD-derived vegetation phenology has been previously used to capture biomass changes in annual vegetation, both in natural landscapes (e.g., Tian et al., 2016) and in croplands (e.g., Patton and Hornbuckle, 2013). Here, the VOD dataset applied is shown to reproduce biomass and water content variability. In particular, VOD times series show that (i) minimum VOD values occur in June during crop emergence (SOS) and in October when crops are mature and dry (EOS); (ii) maximum VOD values occur in August, when the plant reaches the highest water content (Figure 5.3); (iii) VOD increases during the vegetative and reproductive phases of crops, when plants grow and water content rises; and (iv) VOD decreases during senescence and maturity, when crops dry. These patterns, as well as the SOS and EOS dates used for crop season delimitation, are very consistent with previous studies (Patton and Hornbuckle, 2013; Lawrence, 2014; Hornbuckle et al., 2016; Guan et al., 2017). Concerning to the maximum VOD, it is delayed by one month with respect to maximum greenness in the region (in July), as maximum biomass takes some weeks to grow after the greenness peak (Guan et al., 2017; Piles et al., 2017). Additionally, note that the decrease on VOD during senescence is consistent with previous research showing good correlation between this period and the VOD reduction ($0.5 < r < 0.7$; Piles et al., 2017). Here, this VOD reduction is lower (in absolute terms) than the VOD increase during crop growth (see Figure 5.5, and Figure B.8a in Appendix B). This possibly occurs because the VOD signal at the end of crop season responds not only to harvest, but also to VOD patterns after the EOS.

There are some unexpected VOD peaks out of the crop season, (i.e., before emergence and after harvest; Figure 5.3). These peaks do not affect the present study, which is limited to the crop season (see Section 5.2.4). Similar peaks are reported in previous studies (e.g., Patton and Hornbuckle, 2013; Lawrence et al., 2014; Hornbuckle et al., 2016; Guan et al., 2017).

Hornbuckle et al. (2016) attribute these anomalies to changes in soil roughness produced by tilling practices. However, tilling practices are decreasing in the region: in 2012, 60% of farmers used no tillage or reduced tillage in Iowa, and this proportion had risen in 2015 (Arbuckle, 2016). Also, a sensitivity analysis on the effect of soil roughness in MT-DCA VOD retrievals showed that the impact of roughness on VOD was minor (Konings et al., 2016). Other plausible explanation to the changes on VOD occurring out of the crop season is the impact of changes on the scattering albedo and the fractional vegetation cover, which are not accounted for. In this regard, it is important to stress that a constant albedo value is retrieved per pixel for the entire study period. This value is relatively high (>0.15) in the US Corn Belt croplands (see Figure 5 in Konings et al., 2017a), and unrealistic when the crops are harvested. Future work should be directed to assess the impact of constant albedo and roughness on VOD retrievals, and to evaluate the possibility of dynamic estimations of albedo in croplands (Jagdhuber et al., 2017). Finally, changes on VOD after crop harvest could be also due to: (i) crop residues left in the soil to maintain its ecological and agricultural functions; (ii) an incomplete filtering of frozen ground, due to errors in the SMAP frozen/thaw flags; and (iii) the growth of winter wheat in part of the study area. Considering crop residues, the moderate correlation between the maximum VOD after harvest and the crop yield and corn proportion datasets (Figure B.8a in Appendix B) suggests that larger crop yields could lead to higher amount of crop residues, which could be one of the factors explaining the VOD peaks found after the crop season. Regarding winter wheat, when all crops had reached EOS in the study region, only between 0 and 25% of winter wheat had emerged. Hence, it had little effect on VOD measurements during the crop season. Although it could lead to VOD changes after harvest in particular pixels, there is no relationship between maximum VOD peaks after crop harvest and the winter wheat proportion.

5.4.2. VOD metrics as suitable tools for crop yield assessment

The relationship between VOD variables and yield shows moderate to high correlation ($0.56 \leq r \leq 0.81$) with remarkable spatial coherence and agreement between yield and VOD-derived variables. Most VOD metrics capture the high yield values in the relatively homogeneous central region –with PC1, standard deviation, and range showing the best agreement-. Seasonal integrals show better spatial agreement with lower crop production and higher heterogeneity in the north. This suggests that the metrics are complementary and that their composite is the most versatile and applicable predictor. Consequently, information on VOD maximum and mean values, amplitude (i.e., range), and growth rate (i.e., standard deviation and integrals), are all needed to obtain reliable yield estimates at a regional scale. This is confirmed by the fact that PC1 provides the best regional proxy of crop biomass (r=0.81), explaining a substantial proportion of final yield variability (66%), and capturing yield spatial patterns through the entire study region (see Figure 5.5). The fact that different crop types present diverse growth cycles explains why different VOD metrics are needed to capture yield variability throughout the region.

Interestingly, previous research conducted by Guan et al. (2017) concluded that the VOD captured environmental stresses affecting final yield. Actually, ~40% of inter-annual yield changes on corn, soy, and wheat in the United States depend on climate variability among different years (Ray et al., 2015). This indicates that using an L-band VOD record spanning through several years may result in a second principal component related to climate information. This should be a matter of future studies.

The proposed VOD metrics capture the distribution of crop types as well as the crop proportion variability within the study region. This is not surprising, as VOD, yield, heterogeneity, and corn percentages are linked. As higher yields are found for corn-soy mixed crops, clustering has been based on the addition of corn and soy proportions. Note that under this criterion four pure soy pixels have been classified within the "high yield" region (i.e., the central-southeastern region) despite their low yield values (see Figure 5.6a). Still, some tests were conducted to ensure that their effect in the computed yield-PC1 regression is minor (results not shown).

In the central-southeastern region, PC1 explains a substantial proportion (78%) of the overall yield variability. For corn and soy, 68% and 47% of the variances are explained, respectively. This shows that the complementary application of different VOD metrics can provide very reliable estimations of yields for the entire region and for corn crops in particular. Actually, the results in this region outperform those reviewed in research literature for mixed corn-soy croplands (Table A.11 in Appendix A). In this study area, it is also interesting to note that the maximum VOD captures the high productivity of corn crops in the central area better than seasonal integrals do (Figure 5.5 and Table 5.2). In contrast, the use of seasonal maximum from most common optical-infrared vegetation indices (e.g., NDVI) is usually limited by saturation and, in these cases, integrals are needed to improve fitting with vegetation patterns (Olsson et al., 2005; Tian et al., 2016). Here, maximum VOD overcomes the saturation effects, making it a promising index for vegetation and agriculture research. In this corn-soy dominated region, results also show that the seasonal amplitude of VOD and the crop growth rate are relevant for yield estimation in corn-soy crops, as range and standard deviation have good agreement with yield in the area (Figure 5.5 and Table 5.2). This is consistent with results reported by Patton and Hornbuckle (2013) and Chaparro et al. (2017) in Iowa, where the range of VOD explained more than half of yield variability. Additionally, in the central-southeastern region it is also remarkable that yield shows partial saturation for PC1 > 0.7. This saturation could be explained by a high density of the plant canopy cover when optimum yield is reached. This high density is explained by an excess of plant population, which limits the individual grain production due to competition. Hence, an increase on the number of plant individuals –and therefore a larger aboveground biomass- does not lead to a higher yield (Dobermann et al., 2002; Overman and Scholtz, 2011), but can lead to higher VOD values. This is also consistent with the resulting shape of the regression in this cluster.

In the northern region, PC1 can only explain 42% of yield variability. Although the specific analysis for wheat shows higher coefficients of determination (Figure B.10 in Appendix B), a larger sample should be studied to confirm this result. Both integrals and yield are correlated in the region and, actually, they provide better fitting than PC1 (Table 5.2) probably because other metrics reduce goodness of fit in the PC1 computation. This suggests that the length of the crop season and the VOD amplitude are important factors for crop yield estimation in this area, and that VOD metrics could be species-specific for yield forecasting purposes (integrals for wheat crops, in this case). In addition, the heterogeneity of crops in the region possibly diminishes the capability of VOD-related information to report better yield estimations. This is in contrast to the more homogenous central-southeastern cluster. Interestingly, Lawrence et al. (2014) found lower correlation of SMOS VOD with NDVI and EVI in wheat and hay crops, than in corn-soy areas. Additionally, the goodness of fit reported in this region is lower than (considering the whole region) or similar to (considering only wheat) the one found in other research studies using visible and near infrared vegetation indices (Table A.11 in Appendix A, and Figure B.10c in Appendix B). These indices do not saturate for crops with low final production, such as cereals, and have shown good capacity to predict their yields (Rembold et al., 2013, and Table A.11 in Appendix A). Hence, the capacity of VOD to complement or outperform the yield estimates obtained with traditional vegetation indices seems to depend also on crop types.

Finally, part of yield variability has not been explained by the proposed VOD metrics. This could be largely due to the fact that VOD is linked to plant biomass, but its relationship with crop grain yield is indirect or –even in some cases- it could be inexistent. This may occur when unfavourable weather conditions impact grain yield without affecting the final biomass of plants (e.g., when high temperatures difficult pollination in corn kernels). Also, part of the unexplained VOD variability could be due to the fact that grains are still filling when maximum biomass and VOD have been reached (note that VOD metrics are computed here until the maximum VOD is reached; see Figure 5.3).

5.4.3. Contributions of microwave remote sensing to yield forecasts

SMAP-based L-band VOD estimates provide highly valuable information for crop yield estimation mainly in corn, soy, and wheat crops, in the north-central United States. Similarly, previous studies (Patton and Hornbuckle, 2013) report good predictive capability with SMOS-based L-band VOD for corn yield assessment in Iowa. Here, we show this extends across the US Corn Belt and for VOD from SMAP. Previous research using passive microwave measurements at higher frequencies (C- and X-bands) that do not sense as much of the vegetation canopy have reported slightly lower correlations between yield and VOD (Mladenova et al., 2017; Guan et al., 2017). Nevertheless, the dependence (if any) of yield prediction quality on the frequency band used still requires more quantitative assessments. Furthermore, the combined application of L-band data with C- and X-bands VOD may hold some potential to account for inter-annual climate variability and for information from different layers in the crop canopy as well as the soil.

VOD is also complementary to other microwave remote sensing products, as well as to other satellite and modelled datasets. Information on vegetation conditions and biomass can also be derived from a large number of active and passive microwave systems. Microwave radars have also been used to monitor crop phenology (e.g., Vereecken et al., 2012; McNairn and Shang, 2016). Interestingly, Guan et al. (2017) found good relationship between Ku-band radar backscatter and yield-derived net primary production ($0.62 \leq r \leq 0.66$). The authors also reported that the combination of remote sensing and modelled information (VOD, radar backscatter, fluorescence, evapotranspiration, EVI, and temperature, among others) allowed a comprehensive approach to study yield variability and its causes.

In addition to VOD, passive microwave remote sensing at L-band can provide soil moisture information, which is crucial in agro-ecosystems and yield studies. Mladenova et al. (2017) presented a complete analysis on the correlation between yield and different satellite and modelled soil moisture and evapotranspiration products. Also, El Sharif et al. (2015) assimilated SMAP simulated soil moisture data in an agricultural model to improve yield predictions. The combined application of soil moisture and VOD products from passive microwave sensors should be addressed in future studies.

5.5. Conclusions

This study addresses the relationship between SMAP-based L-band VOD retrievals and crop yields in the north-central United States. The VOD time series follow crop progress and their phenological phases. VOD seasonal metrics have been proposed for the crop growth period, and have been compared to in situ yield information, showing good agreement with yield and crop proportion spatial patterns in the study region. Different metrics capture various aspects of the time-series dynamics. Different crop types result in various features in the dynamics. The metrics are each designed to capture these features.

A principal components regression combining the different VOD metrics explained a substantial proportion (66%) of crop yield variability over the entire study area. The complementary application of maximum, integrals, range, standard deviation, and average of VOD are used for crop yield analysis. The maximum and the small integral of VOD are the metrics with the highest correlations with yield across crop types.

Two clusters are defined in the study area: a homogeneous corn-soy region in the central-southeastern study area and a mixed crops region with wheat predominance in the north. Regressions of yield as a function of the proposed VOD principal component are calculated for each cluster. For the corn-soy dominated cluster, 78% of yield variance is explained with principal components regression. In this area, maximum and seasonal variability in biomass show high spatial agreement with crop yields. This is coherent with previous studies (Patton and Hornbuckle, 2013). For wheat and mixed croplands characterized by high heterogeneity, the principal components regression explains 42% of yield variability. VOD integrals show the best agreement with yield in this cluster. The predictive capacity of VOD metrics improves with crop homogeneity allowing the development of crop-specific relationship between yield and VOD metrics.

L-band microwave information on vegetation biomass and phenology has potential synergy with other remote sensing products. They can complement one another resulting in potential for the development of still improved yield forecast methods. This study with focus on L-band VOD metrics is a step forward to achieve this goal.

6

Conclusions and future work

Abstract

This PhD Thesis has investigated the added-value of using satellite-based L-band SM and VOD data to assess environmental risks and to monitor vegetation state. This is of the outmost importance, since present environmental changing conditions involve drying and warming trends, forest degradation, or natural hazards, among other factors, which may threaten vegetation health and endanger livelihood conditions for humans. This chapter details the main conclusions and applications of this PhD Thesis, which has explored specifically: (i) the capability of combined SM-LST information to predict fire risk situations (Chapter 2); (ii) the ability of SMOS SM information to detect dry soils threatening vegetation health (Chapter 3); (iii) a sensitivity analysis of VOD to carbon stocks in tropical regions (Chapter 4); and (iv) the ability of VOD seasonal metrics to model crop yields (Chapter 5). In this chapter, the original contributions of this work and future research lines arising from this PhD Thesis are also detailed.

6.1. Main conclusions

Microwave radiometers on board the SMOS and SMAP missions measure the electromagnetic radiation emitted by the soil at low frequency microwaves (L-band). This emission is mainly a function of the soil water content, and its attenuation through the overlying vegetation depends on the vegetation water content and on the canopy density. In comparison to higher microwave frequencies, L-band has greater penetration capacity through soils and vegetation. Therefore, satellite L-band measurements provide a new and unique means to monitor the hydric conditions of soils and vegetation, and to infer information on the vegetation biomass at the global scale. This is of great importance to assess and prevent the impacts on vegetation caused by a changing environment.

In this context, this PhD Thesis has investigated the use of L-band SM and VOD data as new remotely sensed ecological indicators for: (i) preventing and understanding specific drought impacts such as forest fires and forest decline episodes; (ii) quantifying the sensitivity of microwave and optical sensors to the above-ground carbon density in tropical regions; and (iii) providing crop yield assessment. The main conclusions and contributions of this Thesis are described hereafter.

Chapter 2 studies the relationship between SMOS SM data at enhanced resolution (1 km) and fire risk in the Iberian Peninsula for the period 2010-2014. Importantly, rather than using SM information alone, SM is complemented with LST data to allow a more complete characterization on the soil surface state before fire occurrences. Results are summarized as follows:

- Absolute SM-LST values detect the dry and warm conditions preceding ~80% of the registered fires. These conditions mainly occur in summer, with SM below and LST above their annual median. In particular, the occurrence of very large fires (>3,000 ha) has been associated to very dry soils (<0.08 m^3/m^3) and high temperature (>306 K) conditions.

- SM-LST anomalies explain droughts and anticyclonic situations out of the summer season, which lead to an important number of fire episodes in the northwestern Iberian Peninsula.

- Dry soil conditions are linked to the potential extension of wildfires both in the Mediterranean region and in the northwestern Iberian Peninsula. High temperatures, in turn, increase the expected burned area of fires in some regions, but have a negative effect in the Mediterranean. The latter should be assessed using a larger sample.

Based on the above-mentioned studies, a fire risk model for the Iberian Peninsula built on SM-LST data was developed. To do so, a preliminary version was first built based on empirical thresholds. Fire risk maps at near real time produced with this first approach were provided to the DiBA for their 2015 and 2016 summer (i.e., mid-June to mid-September) fire risk prevention campaigns. An improved fire risk model has been proposed based on a regression which also incorporates SM, LST, and ancillary information on land cover, ecoregions, and date of fire occurrence. This model estimates the potential burned area that a fire can reach applying a linear regression model. Results show high accuracy, with 83.3% of fires not exceeding the expected fire size, and with a maximum error of 40.5 ha.

In **Chapter 3** the forest decline occurrences associated to the severe 2012 summer drought in Catalonia are modelled as a function of climate variables and SMOS high-resolution SM. The model explains ~40% of the spatial distribution of forest decline, suggesting that this phenomenon is also dependent on specific ecosystem and soil characteristics which should be further studied. The main conclusions of this study are:

- Forests impacted by high temperature anomalies, low rainfall, and dry soils during summer are the most affected by forest decline. Also, forests in climatically wetter regions and those more exposed to solar radiation are more vulnerable.

- In the studied case, the vulnerability to forest decline is very dependent on the studied species. Broadleaved trees have resulted more affected than conifers. The most vulnerable species is *Fagus sylvatica*, a Euro-Siberian species, contrasting with *Pinus halepensis*, a typically Mediterranean species, which shows low sensitivity to drought.

- Soil moisture data derived from SMOS shows a coherent pattern with increasing forest affectation when soils get drier, especially for broadleaved species. Nevertheless, SM has explained a little proportion of the modelled forest decline variance (<5%). Probably, root-zone soil moisture data would be very valuable to improve this result (see Section 6.3), as trees uptake water from deeper soil layers than those sensed by SMOS.

Differently from –and complementarily to- soil moisture information, VOD data allows monitoring vegetation phenology, water content, and biomass. Research in Chapter 4 has investigated the applicability of L-band VOD to estimate carbon stocks on tropical forests. The work in Chapter 5 has explored the temporal signature of L-band VOD over agro-ecosystems and has proposed seasonal metrics for crop yield assessment.

Chapter 4 compares the sensitivity of microwave VOD products (retrieved using L-, C- and X-bands) and the optical-infrared index EVI to the ACD of vegetation in tropical regions. L-band VOD shows the best sensitivity to carbon changes and the lowest saturation at high biomass values. The sensitivity decreases with increasing microwave frequencies, confirming that low frequencies capture well the attenuation of soil emissivity through the canopy layer. The obtained results are consistent for the different regions, vegetation types, carbon densities and altitudes studied. Also, Chapter 4 quantifies the relative contribution of carbon density and forest cover proportion to the VOD and EVI signals, showing that 34% of L-band VOD variance is explained by carbon variability and that 30% of this variance is due to changes on the forest cover proportion. These percentages are lower for EVI, C-band VOD and X-band VOD, in decreasing order. Nevertheless, the capacity of EVI to monitor carbon changes in mountain forests (less dense forests) is higher than in tropical evergreen forests, suggesting that EVI should complement L-band VOD measurements for low density vegetation. Also, VOD at C- and X-bands have higher sensitivity to carbon changes in flooded forests than in other regions, and should complement L-band data in flooded areas.

In **Chapter 5**, six SMAP VOD metrics obtained during the crop growth season are studied in order to model crop yields in the United States Corn Belt. These metrics have good qualitative agreement with the spatial variability of crop yield in the region and with the distribution of the different crop types. The complementary application of these metrics using a principal components regression is able to explain 66% of crop yield variance through the study region. This percentage decreases (42%) for heterogeneous wheat-dominated crops, and increases (78%) in a more homogenous region with corn and soy crops. Results indicate that the predictive capacity of VOD metrics should improve with crop homogeneity, and that it can be applied to derive specific crop yield assessment for the major crops within the study area. The approach presented in Chapter 5 opens a promising path forward for the enhancement of present global crop yield assessment approaches, which are mainly based on optical satellite imagery. This would be especially important for developing countries, where crop insecure situations are frequent and may increase during this century.

Importantly, in Chapters 4 and 5 of this Thesis it is stressed that the synergetic application of L-band VOD with other remote sensing products (e.g., different VOD frequencies, LiDAR data, VIS/NIR indices, fluorescence, or radar backscatter) could enhance our capacity to monitor vegetation biomass and phenology, both for tropical forests (Chapter 4) and for croplands (Chapter 5). The complementarity among VOD and SM data for the applications reported in this work is also an interesting research that should be subject of future studies (see Section 6.3).

As a final conclusion, it is worth saying that this PhD Thesis opens a path to new L-band remote sensing applications over land. Measuring soil and vegetation conditions from SMOS and SMAP has demonstrated highly applicable to assess and forecast increasing environmental risks over vegetation and human livelihood conditions, and to further explore present challenges concerning the need of monitoring forest carbon sinks and of improving crop security. Therefore, L-band missions have been shown in this PhD Thesis as potentially helpful tools to deal with present and future impacts derived from environmental changes.

6.2. Original contributions

The original contributions of this PhD Thesis are:

- A new approach for fire risk assessment over the Iberian Peninsula based on the complementary application of satellite L-band soil moisture data and land surface temperature information. It assigns a fire risk category based on the modelled potential extension of wildfires.

- Development of the first fire risk maps based on SMOS-derived soil moisture information. The preliminary version of this product (see Chaparro et al. 2016b and Section 2.9.1) was operationally used by the DiBA during the 2015 summer fire risk prevention campaign. The final version is described in Chaparro et al. (2016a) and in Section 2.9.2, and will be available through the BEC website (BEC, 2018) in a near future.

- New assessment of forest decline causes taking profit of climate information and of SMOS-derived soil moisture data. SM shows great potentiality to detect drought conditions threatening forest health.

- A sensitivity analysis of different VOD products and EVI to carbon stocks of tropical vegetation, based on a quantitative assessment of the ACD contribution to VOD and EVI signals, and on specific analyses in the Andes region and in flooded forests.

- L-band VOD seasonal metrics for crop yield assessment have been proposed using the first year of SMAP VOD data over the US Corn Belt and survey data from USDA-NASS. The metrics proposed explain an important proportion of crop yield variability and could be studied for crop yield prediction purposes.

6.3. Future research lines

The future research lines opened by the work presented on this PhD Thesis are:

- Expand the fire risk assessment approach presented in this PhD Thesis using other meteorological variables (mainly wind), as well as considering human factors, orography, and vegetation conditions. The application of VOD and EVI data to complement the presented risk index would be interesting in order to include the hydric conditions of life fuels.

- Study the applicability of the SM-LST data in the FWI, which is used as the basis for the EFFIS fire risk assessment tool of the European Commission.

- Use estimates of root-zone soil moisture obtained from SMOS/SMAP surface soil moisture data in fire risk assessment tools, forest decline modelling, and crop yield estimates. Study the benefit of using soil moisture vertical profiles with respect to the use of either surface or root-zone soil moisture.

- Analyse the impact of using longer L-band satellite and *in-situ*/survey data records in the proposed applications. In that sense, expanding the study period in the fire risk analysis (e.g., to 2010-2018) would provide a larger sample, which is needed to strengthen the results obtained. Also, applying multi-year VOD records would allow accounting for interannual variability in crop yield assessment, and would permit to analyse carbon gains or losses in forests.

- Develop a modelling framework for the prediction of forest decline based on climate data and SM and VOD estimates to anticipate drought impacts on forests.

- Develop crop yield prediction models using satellite VOD together with optical data (e.g., EVI) and other supporting information available (e.g., yield from previous years, or climatic information).

- Explore synergies among different remote sensing products to enhance the applications and research here presented. In particular, study the complementarity between SM and VOD information for an accurate assessment of soil and vegetation hydric conditions in global biomes.

- The applications presented in this PhD Thesis would benefit from future improvements in the SM and VOD products applied. This should include:
    - Enhance the spatial resolution of SM to the order of meters.
    - Explore the possibility of enhancing the spatial resolution of SMOS and SMAP VOD datasets.
    - Assess the impact of using a fixed global soil roughness parameter and a static vegetation scattering albedo in SMAP MT-DCA VOD estimates.

Appendix A
Supplementary tables

A.1. Supplementary tables for Chapter 2

Table A.1. Summary of the model proposed in Equation (2.2) of potential extension of wildfires as a function of soil moisture, land surface temperature, month, region, and land cover. The significance of all effects is referred to the northern Iberian Peninsula (North), in broadleaved forests (ForB), on February (intercept). Estimates in shaded areas are additive to the intercept. Estimates in white areas correspond to slopes (SM and LST) or modify SM and LST slopes additively (interactions). Significance is given as p<0.1 (.), p<0.05 (*), p<0.01 (**) and p<0.001 (***). Further insight in similar models can be found in Fox (2003) if the reader is not familiar with this model output.

Variable	Estimate	t value	P-value	Significance
(Intercept) February, North, ForB	-15.32 ± 3.66	-4.189	5.1E-05	***
Soil Moisture	-4.03 ± 4.71	-0.855	0.394	
Land Surface Temperature	0.06 ± 0.01	5.074	1.3E-06	***
March	-0.19 ± 0.64	-0.291	0.772	
April	-0.51 ± 0.64	-0.805	0.422	
June	2.39 ± 0.78	3.083	0.002	**
July	0.86 ± 0.66	1.309	0.193	
August	-0.06 ± 0.55	-0.104	0.918	
September	-0.63 ± 0.56	-1.114	0.267	
October	0.08 ± 0.60	0.135	0.893	
Central Peninsula	34.39 ± 35.06	0.981	0.329	
Mediterranean	67.09 ± 9.04	7.419	1.3E-11	***
NE Portugal	3.11 ± 5.58	0.558	0.578	
NW Portugal	19.44 ± 4.31	4.514	1.4E-05	***
Coniferous forest	0.49 ± 0.18	2.744	0.007	**
Mixed forest	0.15 ± 0.17	0.874	0.384	
Natural grasslands	-0.04 ± 0.14	-0.309	0.758	
Heathlands-moors	-0.05 ± 0.13	0.392	0.696	
Sclerophyllous vegetation	0.11 ± 0.17	0.679	0.498	
Woodland-shrub	-0.04 ± 0.12	-0.318	0.751	
Sparse vegetation	0.28 ± 0.14	1.988	0.049	*

Soil Moisture x March	1.04	±	5.07	0.204	0.839	
Soil Moisture x April	3.09	±	5.18	0.598	0.551	
Soil Moisture x June	-18.09	±	6.31	-2.866	0.004	**
Soil Moisture x July	-8.39	±	5.60	-1.497	0.137	
Soil Moisture x August	2.23	±	4.62	0.483	0.630	
Soil Moisture x September	6.41	±	4.69	1.368	0.174	
Soil Moisture x October	-2.19	±	5.28	-0.414	0.680	
Soil Moisture x Central Peninsula	-15.84	±	10.59	-1.495	0.137	
Soil Moisture x Mediterranean	-21.67	±	4.28	-5.059	1.4E-06	***
Soil Moisture x NE Portugal	4.64	±	3.30	1.404	0.163	
Soil Moisture x NW Portugal	-6.77	±	2.40	-2.816	0.006	**
LST x Central Peninsula	-0.109	±	0.112	-0.970	0.334	
LST x Mediterranean	-0.213	±	0.029	-7.326	2.1E-11	***
LST x NE Portugal	-0.012	±	0.018	-0.652	0.516	
LST x NW Portugal	-0.063	±	0.014	-4.505	1.5E-05	***

A.2. Supplementary tables for Chapter 3

Table A.2. Summary of the final model of forest decline occurrence and ten similar models with different random selections for unaffected entries. Forest decline probability is modelled as a function of species, historic climate variables, and summer 2012 climatic conditions and soil moisture. For each effect and each model, + refers to positive effects and – to negative ones, referred to the reference species (Deciduous *Quercus*). Significance is represented as follows: $p<0.1$ (.), $p<0.05$ (*), $p<0.01$ (**), $p<0.001$(***). Rad_an: mean annual radiation (10kJ/m^2·day); Prec_an: accumulated annual precipitation (mm); ΔT_sum: summer anomaly of temperature; SPI3 and SPI12: Standard Precipitation Index calculated for 3 and 12 months, respectively; SM: soil moisture (m^3/m^3).

Effects	FINAL	1	2	3	4	5	6	7	8	9	10
(Intercept) *Q.*deciduous	+ ***	+ ***	+ ***	+ ***	+ ***	+ ***	+ ***	+ ***	+ ***	+ ***	+ ***
Rad_an	+ *	n.s.	+ .	+ **	+ **	+ **	+ **	+ *	+ ***	+ *	+ .
Prec_an	+ ***	+ ***	+ ***	+ ***	+ ***	+ ***	+ ***	+ ***	+ ***	+ ***	+ ***
ΔT_sum	+ ***	+ ***	+ ***	+ ***	+ ***	+ ***	+ ***	+ ***	+ ***	+ ***	+ ***
SPI3	n.s.	n.s.	n.s.	n.s.	n.s.	n.s.	n.s.	n.s.	n.s.	n.s.	n.s.
SPI12	n.s.	n.s.	- **	- *	n.s.	n.s.	- *	n.s.	- *	n.s.	- .
SM	- **	- **	n.s.	n.s.	- *	- .	- **	- *	- .	n.s.	- ***
F. sylvatica	n.s.	n.s.	n.s.	n.s.	n.s.	n.s.	+ *	n.s.	n.s.	+ *	n.s.
P. halepensis	- ***	- ***	- ***	- ***	- ***	- ***	- ***	- ***	- ***	- ***	- ***
P. nigra	- ***	- ***	- ***	- ***	- ***	- ***	- ***	- ***	- ***	- ***	- ***
P. pinea	n.s.	- .	- .	- .	- .	- *	n.s.	- *	- .	- .	- .
P. sylvestris	- ***	- ***	- ***	- ***	- ***	- ***	- ***	- ***	- ***	- ***	- ***
Q. ilex	- ***	- ***	- ***	- ***	- ***	- ***	- ***	- ***	- ***	- ***	- ***
Q. suber	n.s.	n.s.	n.s.	n.s.	n.s.	n.s.	n.s.	n.s.	n.s.	n.s.	n.s.
F. sylvatica x ΔT_sum	+ .	+ **	+ *	+ *	+ *	+ *	n.s.	+ *	n.s.	n.s.	+ .
P. halepensis x ΔT_sum	- ***	- ***	- ***	- ***	- ***	- ***	- ***	- ***	- ***	- ***	- ***
P. nigra x ΔT_sum	- ***	- ***	- ***	- ***	- ***	- ***	- ***	- ***	- ***	- ***	- ***
P. pinea x ΔT_sum	n.s.	n.s.	n.s.	n.s.	n.s.	n.s.	n.s.	n.s.	n.s.	n.s.	n.s.
P. sylvestris x ΔT_sum	n.s.	n.s.	n.s.	n.s.	n.s.	n.s.	- .	- .	- *	- .	n.s.
Q. ilex x ΔT_sum	n.s.	n.s.	n.s.	- *	n.s.	n.s.	- *	- .	- ***	n.s.	n.s.
Q. suber x ΔT_sum	n.s.	n.s.	n.s.	n.s.	n.s.	n.s.	n.s.	n.s.	n.s.	n.s.	n.s.

F. sylvatica x SPI3	- **	n.s.	n.s.	- *	- **	- .	- **	n.s.	- .	- *	- *
P. halepensis x SPI3	- ***	- ***	- ***	- ***	- ***	- ***	- ***	- ***	- ***	- ***	- ***
P. nigra x SPI3	- ***	- ***	- **	- **	- **	- **	- ***	- ***	- **	- ***	- ***
P. pinea x SPI3	n.s.	n.s.	n.s.	n.s.	n.s.	n.s.	n.s.	n.s.	n.s.	n.s.	n.s.
P. sylvestris x SPI3	n.s.	n.s.	n.s.	n.s.	n.s.	n.s.	n.s.	n.s.	n.s.	n.s.	n.s.
Q. ilex x SPI3	n.s.	- *	n.s.	n.s.	n.s.	n.s.	- *	- .	n.s.	n.s.	n.s.
Q. suber x SPI3	n.s.	n.s.	n.s.	n.s.	n.s.	n.s.	- .	- .	n.s.	n.s.	n.s.
F. sylvatica x SPI12	- **	- ***	- **	- ***	- ***	- **	- **	- **	- **	- *	- **
P. halepensis x SPI12	n.s.	n.s.	n.s.	n.s.	n.s.	n.s.	n.s.	n.s.	n.s.	n.s.	n.s.
P. nigra x SPI12	- *	- **	n.s.	n.s.	- *	n.s.	- .	- *	n.s.	- *	- .
P. pinea x SPI12	n.s.	- *	n.s.	- .	n.s.	n.s.	- .	- *	n.s.	n.s.	n.s.
P. sylvestris x SPI12	+ *	+ *	+ ***	+ ***	+ *	+ **	+ **	+ *	+ **	+ *	+ **
Q. ilex x SPI12	- ***	- ***	- *	- **	- ***	- **	- **	- ***	- **	- ***	- **
Q. suber x SPI12	- *	- *	- *	- .	- .	- *	- *	- *	- .	n.s.	- .
F. sylvatica x SM	- .	- *	- **	- *	n.s.	- *	n.s.	- ***	- *	- *	n.s.
P. halepensis x SM	n.s.	n.s.	n.s.	n.s.	n.s.	n.s.	n.s.	n.s.	n.s.	n.s.	n.s.
P. nigra x SM	- *	- **	- ***	- **	- **	- **	- **	- **	- ***	- **	- *
P. pinea x SM	n.s.	n.s.	n.s.	n.s.	n.s.	n.s.	n.s.	n.s.	n.s.	n.s.	n.s.
P. sylvestris x SM	n.s.	- .	- *	- **	- .	- .	n.s.	- *	- .	- *	n.s.
Q. ilex x SM	n.s.	n.s.	- *	n.s.	- .	n.s.	n.s.	n.s.	- *	- .	n.s.
Q. suber x SM	n.s.	- .	n.s.	n.s.	n.s.	n.s.	n.s.	n.s.	n.s.	n.s.	n.s.
Explained deviance (%)	39.3	37.3	38.6	36.2	36.3	37.9	38.8	36.0	38.6	36.4	38.2

Table A.3. Summary of the final model of forest decline probability as a function of species, climate variables, and summer 2012 climatic conditions and soil moisture. The significance of all effects is referred to the reference species (deciduous *Quercus*). Sig.: significance, refers to: p<0.1 (.), p<0.05 (*), p<0.01 (**), p<0.001 (***). Rad_an: mean annual radiation (10kJ/m^2·day); Prec_an: accumulated annual precipitation (mm); ΔT_sum: summer anomaly of temperature; SPI3 and SPI12: Standard Precipitation Index calculated for 3 and 12 months, respectively; SM: soil moisture (m^3/m^3).

Effects	Estimate			z value	Pr(>|z|)	Sig.
(Intercept)	0.6194	±	0.12829	4.828	1.38E-06	***
Rad_an	0.13086	±	0.05138	2.547	0.010872	*
Prec_an	0.40513	±	0.07582	5.343	9.13E-08	***
ΔT_sum	0.85522	±	0.12204	7.008	2.42E-12	***
SPI3	-0.02726	±	0.13426	-0.203	0.839111	
SPI12	-0.10558	±	0.11875	-0.889	0.373919	
SMOS	-0.3398	±	0.12248	-2.774	0.005532	**
F. sylvatica	0.54126	±	0.40847	1.325	0.185145	
P. halepensis	-5.30047	±	0.55687	-9.518	< 2e-16	***
P. nigra	-3.30238	±	0.36827	-8.967	< 2e-16	***
P. pinea	-5.12607	±	11.35899	-0.451	0.651789	
P. sylvestris	-2.83399	±	0.25001	-11.336	< 2e-16	***
Q. ilex	-0.69489	±	0.14962	-4.644	3.41E-06	***
Q. suber	-1.16642	±	1.06172	-1.099	0.271936	
F. sylvatica x ΔT_sum	0.8688	±	0.47195	1.841	0.065642	.
P. halepensis x ΔT_sum	-1.25798	±	0.28848	-4.361	1.30E-05	***
P. nigra x ΔT_sum	-1.24169	±	0.34004	-3.652	0.000261	***
P. pinea x ΔT_sum	0.20836	±	0.99255	0.21	0.833726	
P. sylvestris x ΔT_sum	-0.30563	±	0.21836	-1.4	0.161613	
Q. ilex x ΔT_sum	-0.20358	±	0.15692	-1.297	0.194517	
Q. suber x ΔT_sum	0.9674	±	0.73375	1.318	0.187358	
F. sylvatica x SPI3	-2.24794	±	0.76877	-2.924	0.003455	**
P. halepensis x SPI3	-2.34412	±	0.40978	-5.72	1.06E-08	***
P. nigra x SPI3	-0.87807	±	0.24422	-3.595	0.000324	***
P. pinea x SPI3	-2.17412	±	2.44851	-0.888	0.374574	
P. sylvestris x SPI3	-0.1012	±	0.24923	-0.406	0.68472	
Q. ilex x SPI3	-0.11847	±	0.17051	-0.695	0.487172	
Q. suber x SPI3	-1.91838	±	1.25367	-1.53	0.125964	
F. sylvatica x SPI12	-1.68399	±	0.58131	-2.897	0.003769	**
P. halepensis x SPI12	0.02756	±	0.25002	0.11	0.912237	
P. nigra x SPI12	-0.67192	±	0.29731	-2.26	0.02382	*
P. pinea x SPI12	-0.83032	±	0.90313	-0.919	0.357895	
P. sylvestris x SPI12	0.52329	±	0.20522	2.55	0.010776	*

Q. ilex x SPI12	-0.74201	±	0.16143	-4.596	4.30E-06	***
Q. suber x SPI12	-2.41591	±	1.14511	-2.11	0.034879	*
F. sylvatica x SM	-0.65057	±	0.35447	-1.835	0.066458	.
P. halepensis x SM	0.23788	±	0.23502	1.012	0.311452	
P. nigra x SM	-0.63648	±	0.25448	-2.501	0.012382	*
P. pinea x SM	-7.91707	±	145.8026	-0.054	0.956696	
P. sylvestris x SM	-0.3111	±	0.2155	-1.444	0.148839	
Q. ilex x SM	-0.01756	±	0.16331	-0.108	0.914372	
Q. suber x SM	-0.26403	±	0.38244	-0.69	0.489949	

Deg. of freedom: 3040 AIC: 2493 AUC: 0.893 Explained deviance: 0.393

Table A.4. Stem vulnerability to xylem embolism (ψ_{50}), minimum midday leaf water potential (ψ_{min}) and hydraulic safety margin (ψ_{50} SF) for the studied species. ψ_{50} SF is calculated as ψ_{min} - ψ_{50}, where: ψ_{50} (MPa) is the xylem water potential at which 50% of hydraulic conductivity is lost, and ψ_{min} is the minimum leaf water potential measured in natural conditions. Adapted from Choat et al. (2012) and references therein.

Group	Specie	ψ_{50} (MPa)	ψ_{min} (MPa)	ψ_{50} SF (MPa)
Angiosperms	*Quercus pubescens*[1]	-2.50	-4.60	-2.10
Angiosperms	*Quercus ilex*	-3.19	-3.82	-0.63
Angiosperms	*Quercus suber*	-5.20		
Angiosperms	*Fagus sylvatica*	-3.08	-2.21	0.87
Gymnosperms	*Pinus nigra*	-3.27	-2.40	0.87
Gymnosperms	*Pinus sylvestris*	-3.19	-1.99	1.20
Gymnosperms	*Pinus halepensis*	-4.46	-2.95	1.51
Gymnosperms	*Pinus pinea*	-4.00	-2.40	1.60

[1] This species is representative of deciduous *Quercus.*

A.3. Supplementary tables for Chapter 4

Table A.5. Number of pixels studied for each country and scale.

	9 km scale				25 km scale			
	Peru	Colombia	Panama	**Total**	Peru	Colombia	Panama	**Total**
All	14,488	1,768	552	**16,808**	1,730	209	39	**1,978**
Forests	9,500	1,619	436	**11,555**	1,152	198	36	**1,386**

Table A.6. Results (R^2 and significance) for the VOD-ACD regression in Eq. (4.1), applied to dense forests. Significance is shown as follows: $p<0.001$ (***), $p<0.01$ (**), $p<0.05$ (*), $p\geq0.05$ (n.s.).

Band	**ACD category**	
	≥80 TC/ha	≥100 TC/ha
L (1.4 GHz)	0.12 (***)	0.05 (***)
C1 (6.9 GHz)	0.04 (***)	n.s.
C2 (7.3 GHz)	0.05 (***)	n.s.
X (10.7 GHz)	n.s.	n.s.

A.4. Supplementary tables for Chapter 5

Table A.7. Yield conversions, from bu/acre and lb/acre to kg/m^2.

Crop	**Kg per bushel***
Barley	21.77
Corn, flaxseed, sorghum	25.40
Oats	15.42
Soybeans, wheat	27.22
Other conversions	
1 lb** = 0.45 kg	
1 acre = 4046,86 m^2	

*Source for conversions: USDA, 1992.

**Pounds have been converted to kg for beans, canola, lentils and peas.

Table A.8. Main crops' phenology. Dark grey shows emergence dates (50% of crop has emerged) through all the study area. Light grey shows maturity dates (50% of crop has reached maturity) through all the study area. Abbreviations show the states with the highest proportion of each crop, and the dates of emergence and maturity in those particular states. Abbreviations: Iowa (IA), Nebraska (NE), North Dakota (ND), and Ohio (OH).

	CROP PHENOLOGY																									
	apr-15				may-15					June 15				July 15				August 15					September 15			
CROP	5	12	19	26	3	10	**17**	24	31	7	14	21	28	5	12	19	26	2	9	16	23	30	6	13	**20**	27
Corn						▓	▓ **IA,NE**	▓	▓															░	░ **IA,NE**	░
Soybeans								▓ **OH**	▓	▓														░	░ **OH**	░
Spring wheat				▓	▓	▓	▓ **ND**											░	░ **ND**							

Table A.9. Dates for minimum VOD after SOS, and dates for maximum VOD within crop season. Note that these dates mark the limits for the computation of the VOD metrics per pixel.

	Earliest	Percentile 5	Median	Percentile 95	Latest
Date of minimum VOD	12th May	29th May	12th June	26th June	11th July
Date of maximum VOD	15th June	28th July	17th August	8th September	19th September

Table A.10. Coefficients for the first principal component (PC1).

Metrics	Coefficients
Maximum	0.450
Small integral	0.440
Range	0.417
Standard deviation	0.393
Large integral	0.373
Average	0.369

Table A.11. Review on some of the previous studies modelling crop yield as a function of remotely sensed data and complementary information.

Reference	Site	Crops	Data	Mean R^2	Scale	N
Patton & Hornbuckle, 2013	Iowa (US)	Corn, soybeans	VOD (L-band)	0.58	County	99
Guan et al., 2017	US Cornbelt	Corn, soybeans	VOD (X-band) EVI Multiple observations(1)	0.18 0.42 0.62	County	~300
Chaparro et al., 2017	US Cornbelt	Corn, soybeans Wheat, soybeans	VOD (L-band)	0.65 0.21	SMAP pixels	100 50
Mika et al., 2002	Hungary	Corn Wheat	NDVI NDVI	0.62 0.51	District District	18
Weissteiner & Kühbauch, 2005	SW Germany	Barley	NDVI, GDD	0.65	District	4
Wall et al., 2008	S Canada	Wheat	NDVI, soil type, moisture index	0.57	District	40
Boken & Shaykewich, 2002	Saskatchewan (Canada)	Wheat	NDVI, moisture index	0.78	District	5
Manjunath et al., 2002	Rajasthan (India)	Wheat	NDVI, precipitation	0.71 0.41	District State	15 1
Labus et al., 2002	Montana (US)	Wheat	NDVI	0.70	State	1
Becker-Reshef et al., 2010a	Kansas (US) Ukraine	Wheat	NDVI	0.77 0.55	Years(2) Years(2)	8 8
Diouf et al., 2016	Senegal	Mixed herbaceous	FAPAR, agrometeorological data	0.69	Field plots	90

(1) X-band VOD, EVI, Ku-band radar backscatter and evapotranspiration.

(2) One state or country aggregated value per year.

A.4. Supplementary tables for Chapter 5

Appendix B
Supplementary figures

B.1. Supplementary figures for Chapter 4

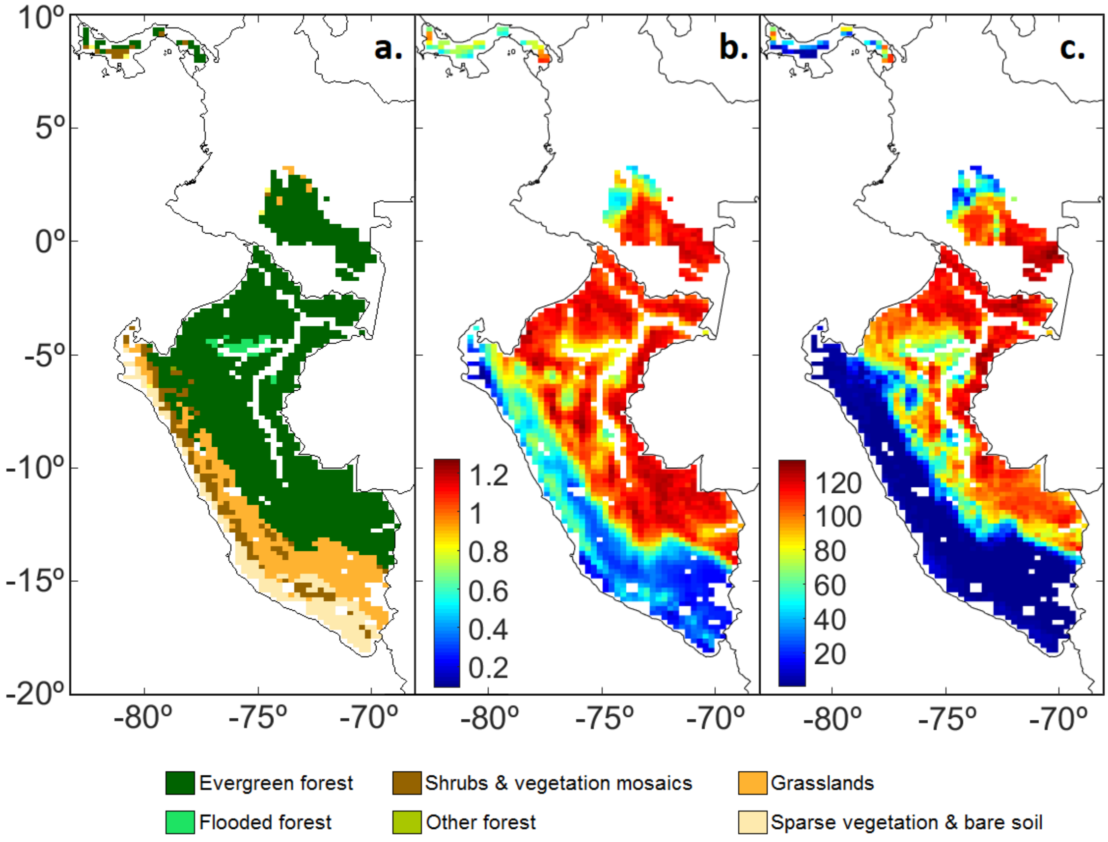

Figure B.1. The study area includes Panama, southern Colombia, and Peru. (a) Land cover mode for the year 2015 (ESA-CCI, 2017); (b) mean VOD data retrieved at L-band (dimensionless; period April 2015-March 2016) and (c) ACD (TC/ha). All subfigures are plotted using the 25 km grid. Areas with insufficient VOD and/or ACD data (e.g., rivers edges and coastlines) are not plotted.

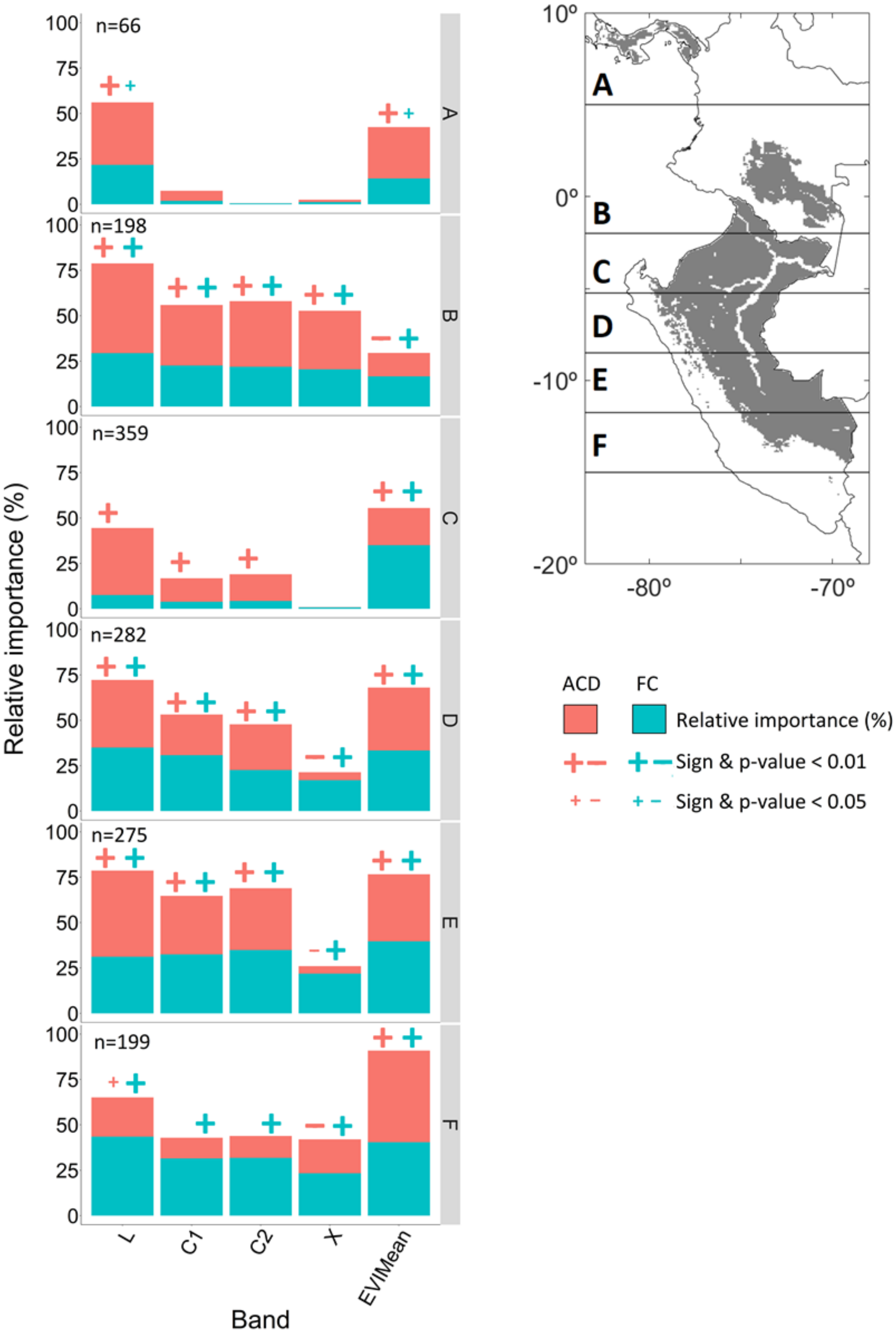

Figure B.2. Relative importance of ACD and FC as predictors of VOD and EVI (Eq. (4.2)). Sign and significance for each variable are plotted if at least p<0.05. Results are reported for regions (A) Panama, (B) Colombia and northern Peru, (C) north-central Peru, (D) central Peru, (E) south-central Peru and (F) southern Peru.

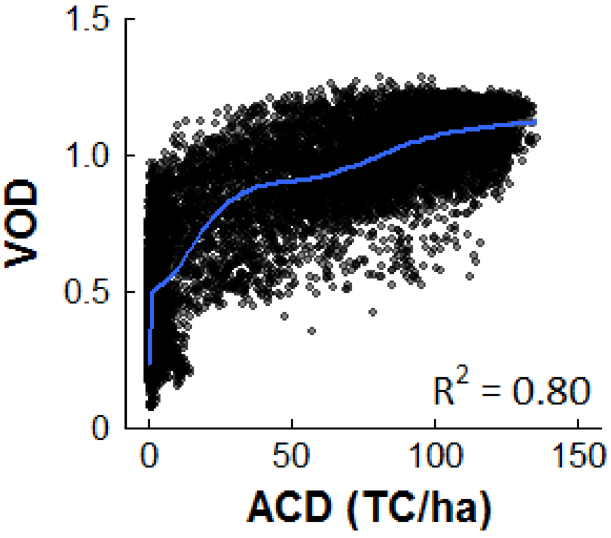

Figure B.3. Regression of L-band VOD as a function of ACD using a generalized additive model. The model is fitted on the basis of a cubic spline function. The regression is significant ($p<0.0001$).

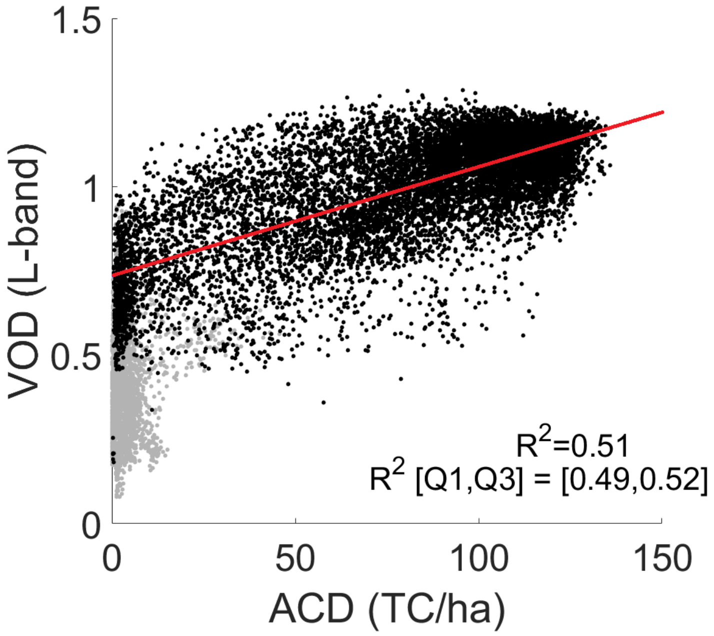

Figure B.4. Linear regression of L-band VOD as a function of ACD in forested areas. The regression is significant ($p<0.0001$). Grey dots show pixels without forest dominant cover and are excluded from the regressions.

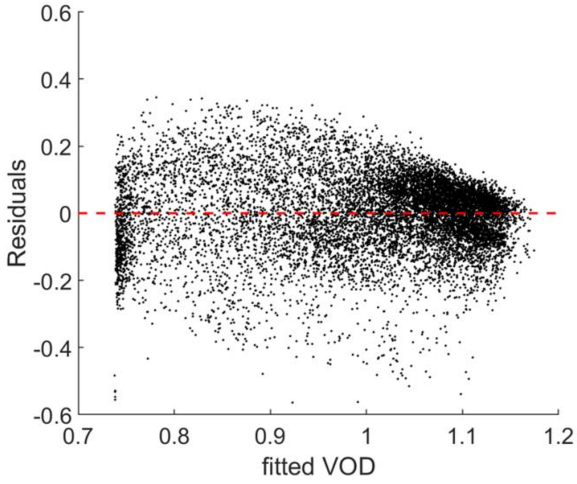

Figure B.5. Fitted VOD values and residuals of VOD for the VOD-ACD linear regression.

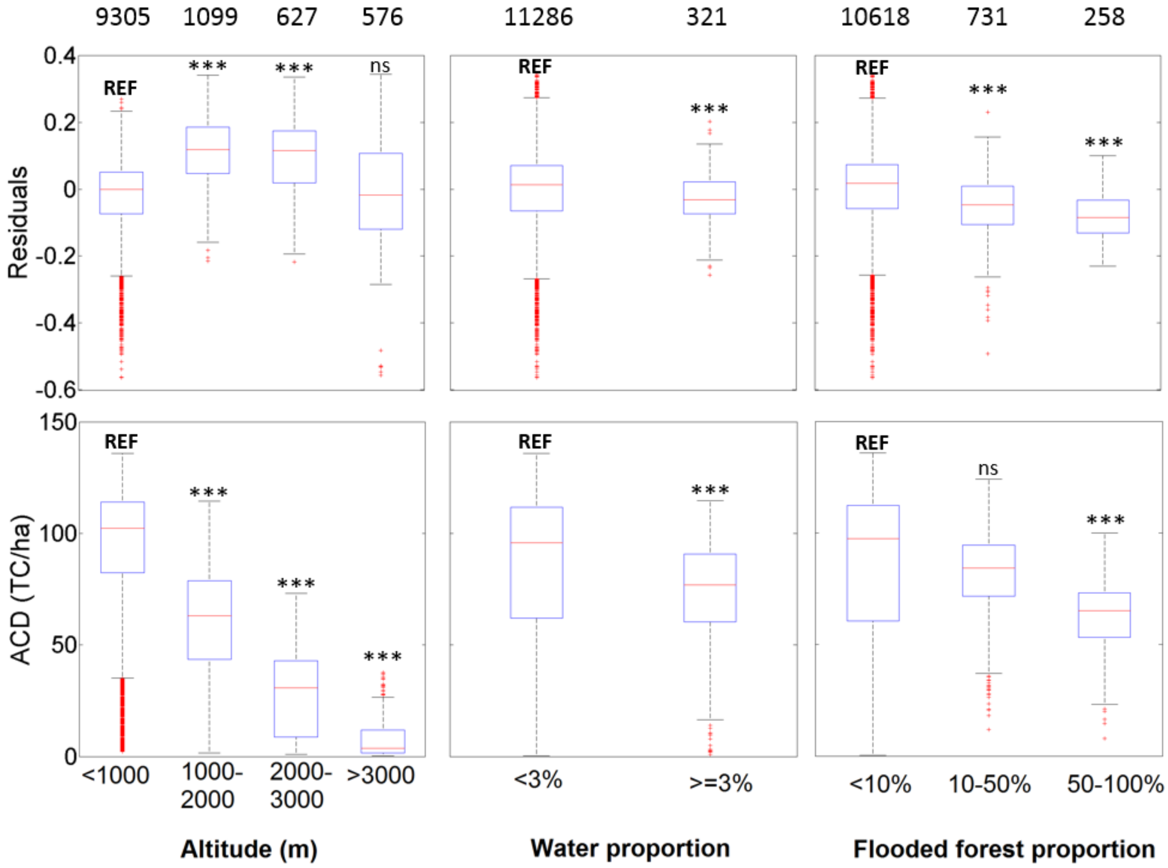

Figure B.6. Residuals for the model in Eq. (4.1) (using VOD at L-band, 9 km grid; top row), and ACD (bottom row), for different categories of altitude (left), water proportion (centre) and flooded forest proportion (right). It is tested if residuals are different from zero (top row), and if ACD for each group is different from the reference group (REF). Significance: REF (reference; not evaluated), ns ($p>0.05$), * ($p<0.05$), ** ($p<0.01$), *** ($p<0.001$). Numbers above the graph show the sample for each group.

B.2. Supplementary figures for Chapter 5

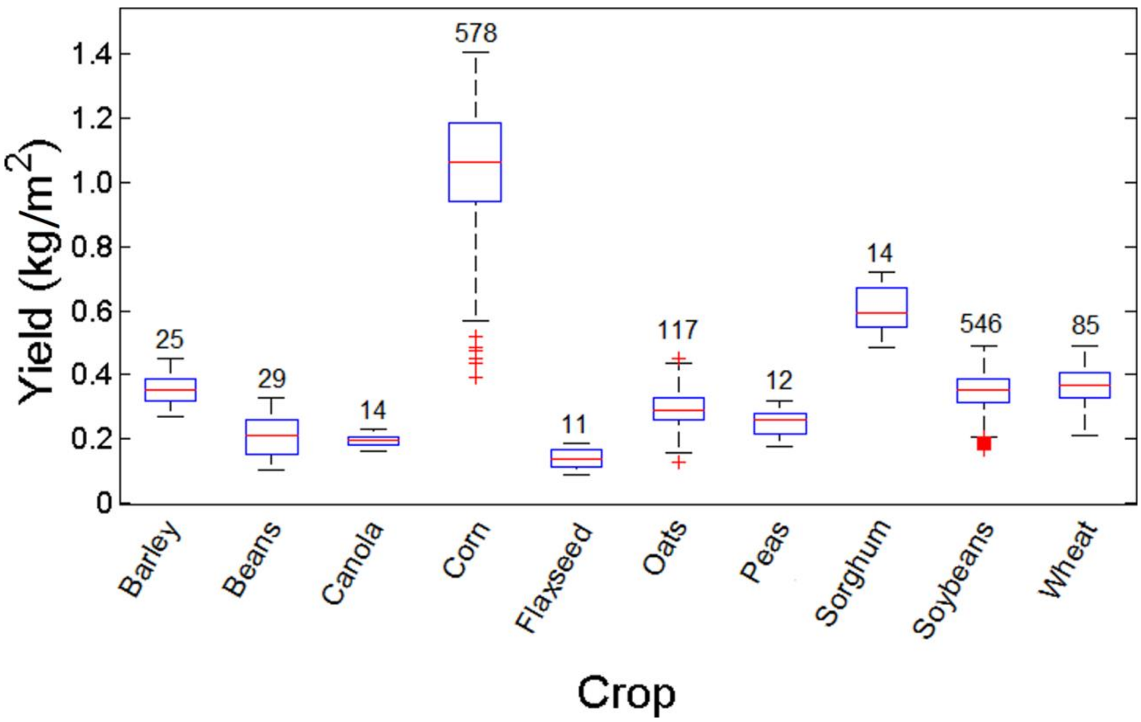

Figure B.7. Yield for each crop type in the entire study area. Boxes represent yield quartiles including all the counties where each crop is planted. Whiskers represent percentiles 5 and 95. The number of counties where each crop is planted in the study region is shown for each box.

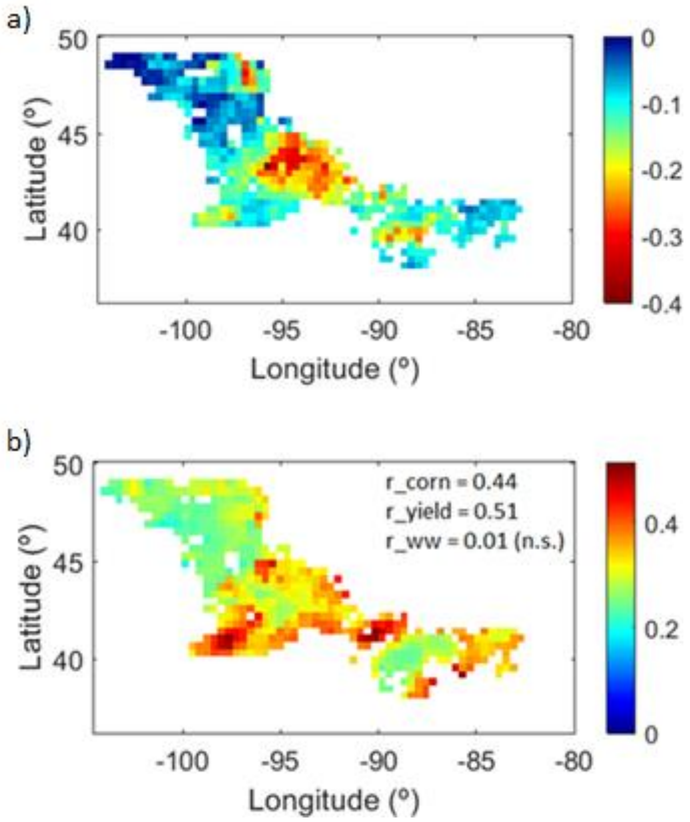

Figure B.8. (a) Difference between the maximum VOD and the VOD at EOS data (crops senescence) and (b) maximum VOD after crop season (colorbar). The Pearson's correlation coefficient with corn proportion (r_corn; $p<0.0001$), yield (r_yield; $p<0.0001$) and winter wheat proportion (r_ww; $p=0.67$) are shown.

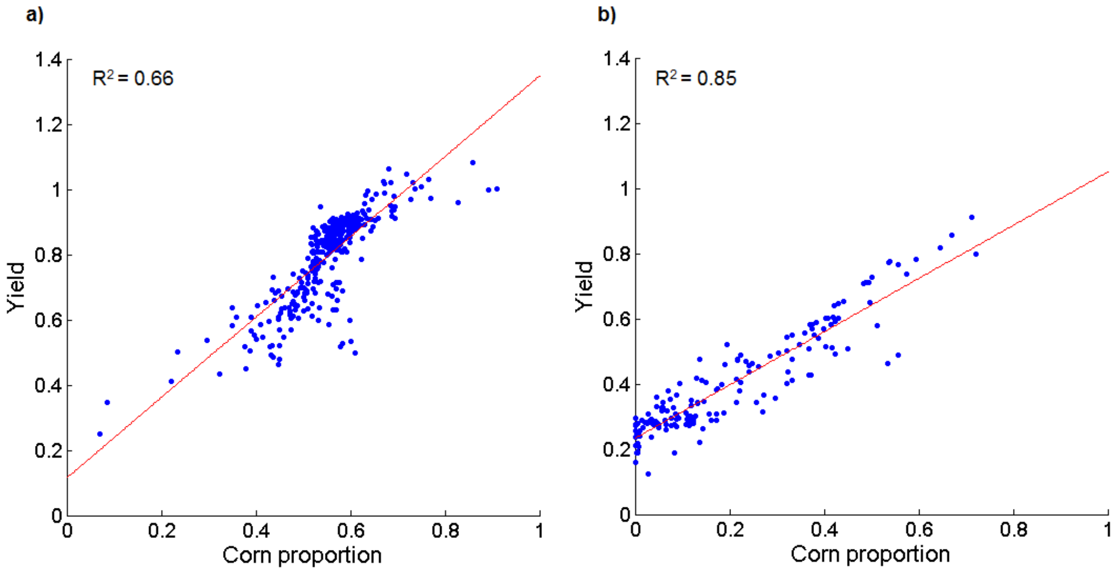

Figure B.9. Relationship between corn proportion and yield in: (a) the center-southeastern region and (b) the northern region. The coefficient of determination is shown (R^2).

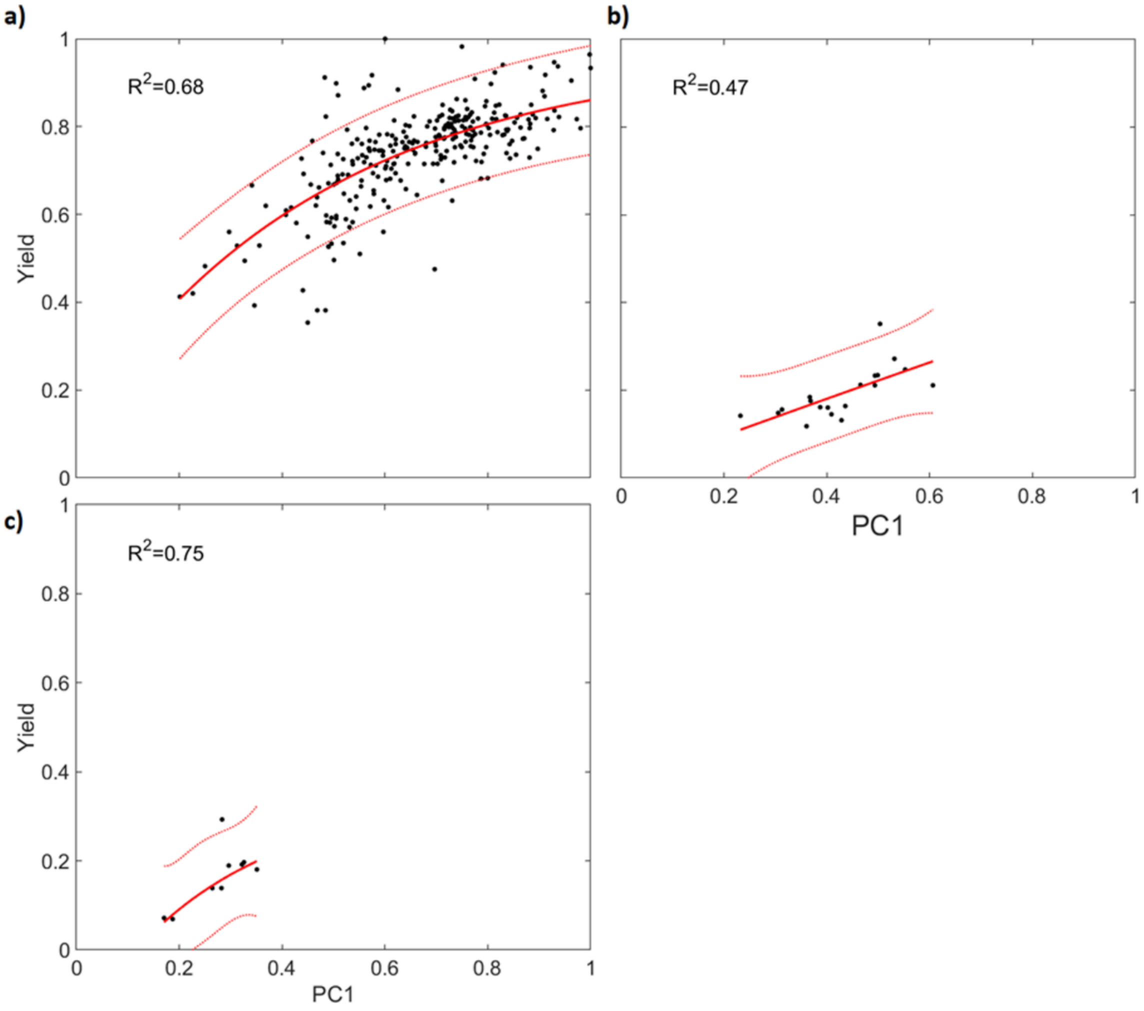

Figure B.10. Yield as a function of PC1 for (a) corn-dominated pixels; (b) soy-dominated pixels and (c) wheat-dominated pixels. Both variables are scaled. Red dotted lines represent 95% confidence intervals. Linear regressions were also tested: corn (R^2 = 0.48; $p<0.0001$), soy (R^2 = 0.47; $p<0.01$) and wheat (R^2 = 0.50; $p=0.03$).

Appendix C
List of publications

This list reports the publications in journals, books, conferences and workshops which have beeen published (or are submited for publication) during this PhD. Some publications are linked to chapters of this PhD thesis, and this is highlighted at the end of each reference.

Journal papers

1. **Chaparro, D.**, Duveiller, G., Piles, M., Cescatti, A., Vall-llossera, M., Camps, A., Entekhabi, D. Mapping carbon stocks of Central and South American tropical forests with L-band passive microwaves. Manuscript submitted for publication in *Remote Sensing of Environment* (May 2018). ***Chapter 4.***

2. **Chaparro, D.**, Piles, M., Vall-llossera, M., Camps, A., Konings, A. G., & Entekhabi, D. (2018). L-band vegetation optical depth seasonal metrics for crop yield assessment. *Remote Sensing of Environment, 212*, 249-259. doi: 10.1016/j.rse.2018.04.049. ***Chapter 5.***

3. Portal, G., Vall-llossera, M., Piles, M., Camps, A., **Chaparro, D.**, Pablos, M., & Rossato, L. (2018). A spatially consistent downscaling approach for SMOS using an adaptive moving window. *IEEE Journal of Selected Topics in Applied Earth Observations and Remote Sensing*. doi: 10.1109/JSTARS.2018.2832447

4. **Chaparro, D.**, Vayreda, J., Vall-llossera, M., Banqué, M., Piles, M., Camps, A., Martínez-Vilalta, J. (2017). The role of climatic anomalies and soil moisture in the decline of drought-prone forests. *IEEE Journal of Selected Topics in Applied Earth Observations and Remote Sensing, 10*(2):503-514. doi: 10.1109/JSTARS.2016.2585505. ***Chapter 3.***

5. **Chaparro, D.**, Vall-llossera, M., Piles, M., Camps, A., Rüdiger, C., Riera-Tatché, R. (2016). Predicting the extent of wildfires using remotely sensed soil moisture and temperature trends. *IEEE Journal of Selected Topics in Applied Earth Observations and Remote Sensing, 9*(6):2818 – 2829. doi: 10.1109/JSTARS.2016.2571838. ***Chapter 2.***

6. **Chaparro, D.**, Piles, M., Vall-llossera, M., Camps, A. (2016). Surface moisture and temperature trends anticipate drought conditions linked to wildfire activity in the Iberian Peninsula. *European Journal of Remote Sensing, 49,* 955-971. doi: 10.5721/EuJRS20164950. ***Chapter 2.***

Book chapters

1. **Chaparro, D.**, Vall-llossera, M., Piles, M. (2018). A review on European remote sensing activities in wildland fires prevention. In: Petropoulos, G.P., Islam, T. (Eds.). Remote sensing of hydrometeorological hazards (pp. 237-260). CRC Press. Taylor & Francis Group. ***Chapter 2.***

2. **Chaparro, D.**, Piles, M., Vall-llossera, M. (2016). Remotely sensed soil moisture as a key variable in wildfires prevention services: towards new prediction tools using SMOS and SMAP data. In: Srvastava, P., Petropoulos, G., & Kerr, Y.H. (Eds.) Satellite soil moisture retrieval: techniques and applications (pp. 379-400). Elsevier. ***Chapter 2.***

Conference proceedings

1. **Chaparro, D.,** Piles, M., Martínez-Vilalta, J., Vall-llossera, M., Vayreda, J., Banqué-Casanovas, M., Camps, A. (2018). Modelling forest decline using soil moisture and vegetation optical depth. *Proceedings of the 2018 IEEE International Geoscience and Remote Sensing Symposium (IGARSS).* Valencia, Spain: Institute of Electrical and Electronics Engineers (IEEE).

2. **Chaparro, D.**, Piles, M., Vall-llossera, M., Camps, A., Konings, A.G., Entekhabi, D., Jagdhuber, T. (2018). L-band vegetation optical depth for crop phenology monitoring and crop yield assessment. *Proceedings of the 2018 IEEE International Geoscience and Remote Sensing Symposium (IGARSS).* Valencia, Spain: Institute of Electrical and Electronics Engineers (IEEE). ***Chapter 5.***

3. Portal, G., Vall-llossera, M., Piles, M., Camps, A., **Chaparro, D.**, Pablos, M., Rossato, L., Abouch, K. (2018). Microwave and optical data fusion for global mapping of soil moisture at high resolution. *Proceedings of the 2018 IEEE International Geoscience and Remote Sensing Symposium (IGARSS).* Valencia, Spain: Institute of Electrical and Electronics Engineers (IEEE).

4. **Chaparro, D.**, Piles, M., Vall-llossera, M., Camps, A., Konings, A.G., Entekhabi, D. (2017). SMAP multi-temporal Vegetation Optical Depth retrieval as an indicator of crop yield trends and crop composition. *Proceedings of the 2017 IEEE International Geoscience and Remote Sensing Symposium (IGARSS)* (pp. 4362-4365). Fort Worth, Texas, USA: Institute of Electrical and Electronics Engineers (IEEE). ***Chapter 5.***

5. Piles, M., **Chaparro, D.**, Entekhabi, D., Konings, A.G., Jagdhuber, T., Camps-Valls, G. (2017). Remote sensing of vegetation dynamics in agro-ecosystems using SMAP Vegetation Optical Depth and optical vegetation indices. *Proceedings of the 2017 IEEE*

International Geoscience and Remote Sensing Symposium (IGARSS) (pp. 4346-4349). Fort Worth, Texas, USA: Institute of Electrical and Electronics Engineers (IEEE).

6. Portal, G., Vall-llossera, M., Piles, M., Camps, A., **Chaparro, D.**, Pablos, M., Rossato, L. (2017). A spatially consistent downscaling approach for SMOS using an adaptive moving window. *Proceedings of the 2017 IEEE International Geoscience and Remote Sensing Symposium (IGARSS)* (pp. 4151-4153). Fort Worth, Texas, USA: Institute of Electrical and Electronics Engineers (IEEE).

7. **Chaparro, D.**, Vall-llossera, M., Piles, M., Camps, A., Rüdiger, C. (2015). Low soil moisture and high temperatures as indicators for forest fires occurrence and extent across the Iberian Peninsula. *Proceedings of the 2015 IEEE International Geoscience and Remote Sensing Symposium (IGARSS)* (pp. 3325-3328). Milan, Italy: Institute of Electrical and Electronics Engineers (IEEE). ***Chapter 2.***

8. **Chaparro, D.**, Vayreda, J., Martínez-Vilalta, J., Vall-llossera, M., Banqué, M., Camps, A., Piles, M. (2014). SMOS and climate data applicability for analyzing forest decline and forest fires. *Proceedings of the 2014 IEEE International Geoscience and Remote Sensing Symposium (IGARSS)* (pp. 1069-1072). Quebec, Canada: Institute of Electrical and Electronics Engineers (IEEE). ***Chapters 2 and 3.***

Workshops

1. **Chaparro, D.**, Duveiller, G., Cescatti, A., Piles, M., Vall-llossera, M., Camps, A. (2018). Biomass estimation in tropical forests using L, C, and X-band vegetation optical depth. *Geophysical Research Abstracts, 20. EGU General Assembly 2018.* Vienna, Austria: European Geosciences Union. Retrieved from: https://meetingorganizer.copernicus.org/EGU2018/EGU2018-7043.pdf. ***Chapter 4.***

2. **Chaparro, D.**, Piles, M., Vall-llossera, M., Camps, A. (2016). Predicting potential forest fires spread risk using SMOS-derived soil moisture and surface temperature trends. Poster presentation. *ESA Living Planet Symposium*. Prague, Czech Republic: European Space Agency. Retrieved from: http://lps16.esa.int/page_session187.php#2324p. ***Chapter 2.***

3. Piles, M., Entekhabi, D., Konings, A.G., Akbar, R., Jagdhuber, T., **Chaparro, D.**, Das, N.N. (2016). Monitoring the phenology of global agroecosystems using SMAP multi-temporal vegetation optical depth retrievals. *Fall General Assemblt 2016 of the Americal Geophysical Union*. San Francisco, United States: American Geophysical Union. Retrieved from: http://adsabs.harvard.edu/abs/2016AGUFM.H23N..07P

4. **Chaparro, D.**, Vall-llossera, M., Piles, M., Portal, G., Camps, A., Pou, X. (2015). Remotely sensed soil moisture is related to forest decline occurrence. *2nd SMOS*

Science Conference. Madrid, Spain: European Space Agency. Retrieved from: https://www.dropbox.com/s/luatxg0vsgpcosk/Abstract%20Book.pdf?dl=0. ***Chapter 3.***

5. **Chaparro, D.**, Vall-llossera, M., Piles, M., Camps, A., Vayreda, J., Martínez-Vilalta, J., Banqué, M., Rüdiger, C. (2015). Remotely-sensed soil moisture predicting forest risks. *IEEE Young Professionals Conference on Remote Sensing*. Barcelona, Spain: Institute of Electrical and Electronics Engineers (IEEE). ***Chapters 2 and 3.***

6. **Chaparro, D.**, Vall-llossera, M., Piles, M., Camps, A., Rüdiger, C. (2015). Predicting the maximum fire spread using SMOS-derived soil moisture and temperature reanalysis. *Fuegored International Meeting*. Málaga, Spain: FuegoRed. ***Chapter 2.***

7. Portal, G., Vall-llossera, M., **Chaparro, D.**, Piles, M., Camps, A., Pou, X., Sánchez, N., Martínez-Fernández, J. (2015). SMOS and ECV long term soil moisture comparison: study over the Iberian Peninsula. *2nd SMOS Science Conference.* Madrid, Spain: European Space Agency. Retrieved from: https://www.dropbox.com/s/luatxg0vsgpcosk/Abstract%20Book.pdf?dl=0

Appendix D

List of symbols

Latin symbols

a_n, a_{ni}	Regression coefficients for high-resolution SM estimation. Subindex n refers to the number of the coefficient. Subindex i refers to the angle observed.
b	Empirical parameter for the estimation of vegetation optical depth
$B(\theta,\phi)$	Brightness or radiance [W·sr^{-1}·m^{-2}]
B_{bb}	Total brightness of a blackbody [W·sr^{-1}·m^{-2}]
B_f	Spectral brightness: brightness per unit bandwidth [W·sr^{-1}·m^{-2}·Hz]
$B_i(\theta,\phi)$	Total brightness incident over an antenna [W·sr^{-1}·m^{-2}]
c	Speed of light: c = 3·10^8 [m/s]
$e(\theta,\phi)$	Emissivity
f	Frequency [Hz]
k_B	Boltzmann's constant: k_B = 1.38·10^{-23} [J/K]
L_a	Atmospheric attenuation
LC	Land cover type
$LogArea$	Logarithm of the potential burned area
LST_N	Normalized LST
M	Month of the year when a fire burned
$NDVI_N$	Normalized NDVI
p_i	Proportion of area planted for each crop
r	Pearson's correlation coefficient
R	Region where a fire burned
SM_{HR}	High-resolution soil moisture [m^3·m^{-3}]
T	Physical temperature [K]

$T_{AP}(\theta,\phi)$	Apparent brightness temperature [K]
$T_B(\theta,\phi)$	Brightness temperature [K]
T_{UP}	Atmospheric upward radiation [K]
T_S	Effective soil temperature [K]
T_V	Effective vegetation temperature [K]
T_{SC}	Downward atmospheric radiation scattered by the Earth’s surface [K]

Greek symbols

α, β, δ	Regression coefficients
γ	Transmissivity of the vegetation
Δ_f	Bandwith [Hz]
ε_S	Complex dielectric constant of soils $\varepsilon_S = \varepsilon'_S + j\varepsilon''_S$
ε'_S	Effective permittivity (real part of ε_S)
θ	Incidence angle referred to nadir [°]
λ	Wavelength $\lambda = c/f$ [m]
τ	Vegetation opacity or vegetation optical depth [Np]
ϕ	Azimuth angle referred to nadir [°]
ψ_{min}	Minimum water potential [MPa]
ψ_{50}	Xylem water potential at which 50% of hydraulic conductivity is lost [MPa]
ψ_{50} SF	Hydraulic safety margin [MPa]
ω	Vegetation single scattering albedo

Appendix E
List of acronyms

AAFC	Agriculture and Agri-Food Canada
ACD	Above-ground Carbon Density
AIC	Akaike Information Criterion
AMSR2	Advanced Microwave Scanning Radiometer 2
AMSR-E	Advanced Microwave Scanning Radiometer for Earth observation
ASCAT	Advanced SCATterometer
AUC	Area Under the Curve
BEC	Barcelona Expert Centre
BUI	Build Up Index
CAO	Carnegie Airborne Observatory
CREAF	Centre de Rercerca Ecològica i Aplicacions Forestals (Centre for Ecological Research and Forestry Applications)
CSIC	Consejo Superior de Investigaciones Científicas (Spanish National Research Council)
DC	Drought Code
DEBOSCAT	Decaïment dels Boscos a Catalunya (Forest Decline in Catalonia)
DEM	Digital Elevation Model
DF	Drought Factor
DiBa	Diputació de Barcelona (Provincial Government of Barcelona)
DMC	Duff Moisture Code
DMSP	Defense Meteorological Satellite Program
DOI	Degrees Of Information
EASE	Equal-Area Scalable Earth grid
ECV	Essential Climate Variable
ECMWF	European Centre for Medium-range Weather Forecasts
EFAS	European Flood Awareness System
EFFIS	European Forest Fires Information System
EO	Earth Obervation
EOS	End Of Season
ESA	European Space Agency
ESA-CCI	ESA Climate Change Initiative
ET	Evapotranspiration
EU-DEM	European DEM
FAPAR	Fraction of Absorbed Photosynthetically Active Radiation
FC	Forest Cover fraction
FFDI	Forest Fire Danger Index
FFMC	Fine Fuel Moisture Content
FMC	Fuel Moisture Content

FWI	Fire Weather Index
GAM	Generalized Additive Models
GCOM-W1	Global Change Observation Mission 1st – Water
GEDI	Global Ecosystem Dynamics Investigation mission
GEO	Group of Earth Observations
GSI	Gini-Simpson Index
GPP	Gross Primary Productivity
GWIS	Global Wildfire Information System
ICESat	Ice, Cloud and land Elevation Satellite
IGBP	International Geosphere-Biosphere Program
ISI	Initial Spread Index
LiDAR	Light Detection and Ranging
LPRM	Land Parameter Retrieval Model
LST	Land Surface Temperature
MPDI	Microwave Polarization Difference Index
MIRAS	Microwave Imaging Radiometer using Aperture Synthesis
MODIS	Moderate Resolution Imaging Spectroradiometer
MT-DCA	MultiTemporal-Dual Channel Algorithm
NASA	National Aeronautics and Space Administration
NDVI	Normalized Difference Vegetation Index
NWP	Numerical Weather Prediction
PC1	First Principal Component
PCR	Principal Components Regression
RZSM	Root-Zone Soil Moisture
SAR	Synthetic Aperture Radar
SM	Soil moisture [m3/m3]
SMAP	Soil Moisture Active Passive
SMC	Servei Meteorològic de Catalunya (Catalan Meteorological Service)
SMD	Soil Moisture Deficit
SMOS	Soil Moisture and Ocean Salinity
SOS	Start Of Season
SPI	Standard Precipitation Index
SPEI	Standard Precipitation Evaptranspiration Index
SSS	Sea Surface Salinity
SWDI	Soil Water Deficit Index
SWI	Soil Water Index
TMI	TRMM Microwave Imager
TRMM	Tropical Rainfall Measuring Mission
UPC	Universitat Politècnica de Catalunya (Polytechnic University of Catalonia)
USDA-NASS	United States Department of Agriculture-National Agriculture Statistics Service
VIF	Variance Inflation Factor
VIS/NIR	Visible/Near Infrared
VOD	Vegetation Optical Depth
VWC	Vegetation Water Content
WUI	Woodland-Urban Interface

Appendix F
Resum (summary in Catalan)

Actualment, les condicions ambientals estan canviant i això amenaça els ecosistemes i, més concretament, la vegetació. Aquests canvis són induïts principalment per l'activitat humana, ja sigui directament o indirecta. En són exemples l'escalfament global causat per l'increment en la concentració atmosfèrica de gasos d'efecte hivernacle, la desforestació i els canvis en les cobertes del sòl provocats per l'expansió de l'agricultura, o els canvis en les propietats de les superfícies de la terra, dels oceans i del gel que alteren l'albedo de la superfície del planeta. A més a més, la freqüència i la intensitat de riscos mediambientals com les sequeres o els incendis forestals poden augmentar en algunes regions degut als canvis en el clima.

En aquest context, els satèl·lits per a l'observació de la Terra són necessaris per a estudiar el medi ambient, mesurant la vegetació i els recursos hídrics, així com el carboni emmagatzemat en la vegetació. En concret, els sensors passius de microones permeten obtenir, de manera regular, mapes globals de la humitat del sòl i de l'atenuació de les microones (emeses pel sòl) quan travessen la coberta vegetal. Aquesta atenuació s'expressa com la profunditat òptica de la vegetació, o VOD per les seves sigles en anglès. El VOD està relacionat amb el contingut d'aigua de la vegetació, i també amb la densitat de carboni de la fracció aèria de les plantes. Les microones de baixa freqüència (banda L) són més sensibles per a mesurar les cobertes vegetals més denses i la humitat del sòl, i en canvi les microones de freqüències més altes ho són menys (per exemple les bandes C o X). Les primeres missions espacials que porten radiòmetres en banda L a bord per a mesurar la humitat del sòl s'han llençat en els darrers deu anys. Són la Soil Moisture and Ocean Salinity (SMOS; la missió per a l'estudi de la humitat del sòl i la salinitat dels oceans llençada per l'Agència Espacial Europea l'any 2009), i la Soil Moisture Active Passive (SMAP; la missió per a l'estudi de la humitat del sòl de forma activa i passiva, llançada per la NASA, l'agència espacial dels Estats Units, l'any 2015).

L'objectiu principal d'aquesta Tesi Doctoral és valorar l'aplicabilitat de les dades d'humitat i VOD en banda L per a estudiar la vegetació. La primera part d'aquesta Tesi aplica informació d'humitat del sòl –complementàriament amb altres fonts de dades- per a analitzar i prevenir impactes de les sequeres en la vegetació de la Península Ibèrica:

- S'apliquen dades d'humitat i de temperatura de la superfície del sòl per a estudiar l'estat dels sòls prèviament a la ignició dels incendis a la regió. Es desenvolupa un índex de risc d'incendis per a predir l'extensió que els focs poden arribar a tenir, sota determinades condicions d'humitat i temperatura. Els resultats mostren com la humitat explica més d'un 30% de l'àrea potencial dels incendis.

- Es realitza un model per a explicar el decaïment forestal a Catalunya després d'una important sequera que va tenir lloc l'estiu de 2012. El decaïment s'estudia en funció de les espècies, de la humitat del sòl, i de variables climàtiques. L’efecte de la humitat en el decaïment dels boscos és coherent amb l’efecte que mostren les altres variables estudiades, i explica aproximadament un 5% de la variància.

La segona part d’aquesta Tesi Doctoral analitza la capacitat per a inferir les condicions de la vegetació i la densitat de carboni amb dos estudis específics:

- Es compara la sensibilitat a la densitat de carboni del VOD de la banda L amb la de freqüències més altes i amb la d’índexs de vegetació en l’òptic i l’infraroig. El VOD en banda L mostra major sensibilitat en la majoria de regions, independentment de l’altitud i dels tipus de vegetació. L’ús complementari de VOD a diferents freqüències i d’índexs de vegetació en l’òptic-infraroig pot millorar les estimacions de carboni.

- Es proposen mètriques estacionals de VOD per a avaluar el rendiment dels cultius. Els resultats en la regió del “US Corn Belt” (nord dels Estats Units) mostren com el VOD explica un 78% de la variància del rendiment, i que el VOD és una eina amb potencial per a millorar les prediccions en el rendiment dels cultius.

Els resultats que es presenten en aquesta Tesi Doctoral contribueixen a millorar la capacitat de predir els incendis, el decaïment forestal, i el rendiment dels cultius, així com a millorar el monitoratge de la densitat de carboni als boscos, utilitzant nova informació a escala global provinent de sensors d’observació de la Terra que mesuren en banda L. La contribució de la humitat del sòl i del VOD en banda L pot ser una eina molt valuosa per a prevenir la degradació d’ecosistemes i les situacions de risc alimentari, i per a millorar les estimacions del contingut de carboni a la Terra.

Appendix G
Resumen (summary in Spanish)

Actualmente, las condiciones ambientales están cambiando y esto amenaza los ecosistemas y, más concretamente, la vegetación. Estos cambios están inducidos principalmente por la actividad humana, ya sea directa o indirectamente. Son ejemplos de estos cambios el calentamiento global causado por el aumento de la concentración atmosférica de los gases de efecto invernadero, la deforestación y los cambios en las cubiertas del suelo provocados por la expansión de la agricultura, o los cambios en las propiedades de las superficies de la tierra, de los océanos y del hielo que alteran el albedo de la superficie del planeta. Además, la frecuencia y la intensidad de los riesgos medioambientales como las sequías o los incendios forestales pueden aumentar en algunas regiones debido a los cambios en el clima.

En este contexto, los satélites para la observación de la Tierra son necesarios para estudiar el medio ambiente, midiendo la vegetación y los recursos hídricos, así como el carbono almacenado en la vegetación. En concreto, los sensores pasivos de microondas permiten obtener, de forma regular, mapas globales de la humedad del suelo y de la atenuación de las microondas (emitidas por el suelo) cuando atraviesan la cubierta vegetal. Esta atenuación se expresa como la profundidad óptica de la vegetación, o VOD por sus siglas en inglés. El VOD está relacionado con el contenido de agua de la vegetación, y también con la densidad de carbono de la fracción aérea de las plantas. Las microondas de baja frecuencia (banda L) son más sensibles para medir las cubiertas vegetales más densas y la humedad del suelo, y en cambio las microondas de frecuencias más altas lo son menos (por ejemplo las bandas C o X). Las primeras misiones espaciales que llevan radiómetros en banda L a bordo para medir la humedad del suelo se han lanzado en los últimos diez años. Son la Soil Moisture and Ocean Salinity (SMOS; la misión para el estudio de la humedad del suelo y la salinidad de los océanos lanzada por la Agencia Espacial Europea en el año 2009), y la Soil Moisture Active Passive (SMAP; la misión para el estudio de la humedad del suelo de forma activa y pasiva, lanzada por la NASA, la agencia espacial de los Estados Unidos, en el año 2015).

El objetivo principal de esta Tesis Doctoral es valorar la aplicabilidad de los datos de humedad y VOD en banda L para estudiar la vegetación. La primera parte de esta Tesis aplica información de humedad del suelo –complementariamente con otras fuentes de datos- para analizar y prevenir impactos de las sequías en la vegetación de la Península Ibérica:

- Se aplican datos de humedad y temperatura de la superficie del suelo para estudiar el estado de los suelos previamente a la ignición de los incendios en la región. Se desarrolla un índice de riesgo de incendios para predecir la extensión que los fuegos

pueden llegar a tener, bajo determinadas condiciones de humedad y temperatura. Los resultados muestran como la humedad explica más de un 30% del área potencial de los incendios.

- Se realiza un modelo para explicar el decaimiento forestal en Cataluña después de una importante sequía que tuvo lugar en verano de 2012. El decaimiento se estudia en función de las especies, la humedad del suelo, y de variables climáticas. El efecto de la humedad en el decaimiento de los bosques es coherente con el efecto que muestran las otras variables estudiadas, y explica aproximadamente un 5% de la variancia.

La segunda parte de esta Tesis Doctoral analiza la capacidad para inferir las condiciones de la vegetación y la densidad de carbono con dos estudios específicos:

- Se compara la sensibilidad a la densidad de carbono del VOD de la banda L con la de frecuencias más altas y con la de índices de vegetación del óptico y del infrarrojo. El VOD en banda L muestra mayor sensibilidad en la mayoría de regiones, independientemente de la altitud y del tipo de vegetación. El uso complementario de VOD a diferentes frecuencias y de índices de vegetación en el óptico-infrarrojo puede mejorar las estimaciones de carbono.

- Se proponen métricas estacionales de VOD para valorar el rendimiento de los cultivos. Los resultados en la región del “US Corn Belt” (norte de Estados Unidos) muestran como el VOD explica un 78% de la variancia del rendimiento, y que el VOD es una herramienta con potencial para mejorar las predicciones en el rendimiento de los cultivos.

Los resultados que se presentan en esta Tesis Doctoral contribuyen a mejorar la capacidad de predecir los incendios, el decaimiento forestal, y el rendimiento de los cultivos, así como a mejorar el monitoreo de la densidad de carbono en los bosques, utilizando nueva información a escala global proveniente de sensores de observación de la Tierra que miden en banda L. La humedad del suelo y el VOD en banda L pueden ser herramientas muy valiosas para prevenir la degradación de ecosistemas y las situaciones de riesgo alimentario, y para mejorar las estimaciones del contenido de carbono en la Tierra.

References

AAFC. Agriculture and Agri-Food Canada. (2016). About satellite soil moisture maps. Retrieved from: http://www.agr.gc.ca/eng/programs-and-services/drought-watch/satellite-soil-moisture/about-satellite-soil-moisture-maps/?id=1471963812568

AEMET. Agencia Estatal de Meteorología. (2012). *Resumen anual climatológico 2011*. Agencia Estatal de Meteorología, Ministerio de Agricultura, Alimentación y Medio Ambiente.

AEMET. Agencia Estatal de Meteorología. (2013). *Resumen anual climatológico 2012*. Agencia Estatal de Meteorología, Ministerio de Agricultura, Alimentación y Medio Ambiente.

AEMET. Agencia Estatal de Meteorología. (2015). *Resumen anual climatológico 2014*. Agencia Estatal de Meteorología, Ministerio de Agricultura, Alimentación y Medio Ambiente.

Aguiar, C., Mesquita, S., & Honrado, J. (2008). Introdução à carta biogeográfica de Portugal (Costa et al. 1998). In Costa et al., *Atlas das Aves Nidificantes em Portugal*, (pp. 47-50). Lisboa, Portugal: Instituto da Conservação da Natureza e da Biodiversidade, Assírio & Alvim.

Al Bitar, A., Mialon, A., Kerr, Y. H., Cabot, F., Richaume, P., Jacquette, E., ... & Al-Yaari, A. (2017). The global SMOS Level 3 daily soil moisture and brightness temperature maps. *Earth System Science Data, 9*(1), 293. doi: 10.5194/essd-9-293-2017

Albergel, C., Rüdiger, C., Pellarin, T., Calvet, J. C., Fritz, N., Froissard, F., ... & Martin, E. (2008). From near-surface to root-zone soil moisture using an exponential filter: an assessment of the method based on in-situ observations and model simulations. *Hydrology and Earth System Sciences Discussions, 12*, 1323-1337. doi: 10.5194/hess-12-1323-2008

Albergel, C., De Rosnay, P., Gruhier, C., Muñoz-Sabater, J., Hasenauer, S., Isaksen, L., ... & Wagner, W. (2012). Evaluation of remotely sensed and modelled soil moisture products using global ground-based in situ observations. *Remote Sensing of Environment, 118*, 215-226. doi: 10.1016/j.rse.2011.11.017

Albert, C. H., & Thuiller, W. (2008). Favourability functions versus probability of presence: advantages and misuses. *Ecography*, *31*, 417–422. doi:10.1111/j.0906-7590.2008.05221.x

Alemu, W. G., & Henebry, G. M. (2013). Land surface phenologies and seasonalities using cool earthlight in mid-latitude croplands. Environmental Research Letters, 8(4), 045002. doi:10.1088/1748-9326/8/4/045002

Allen, C.D., Macalady, A.K., Chenchouni, H., Bachelet, D., McDowell, N., Vennetier, M., ..., & Cobb, N. (2010). A global overview of drought and heat-induced tree mortality reveals emerging climate change risks for forests. *Forest Ecology and Management, 259*(4)*,* 660–684. doi: 10.1016/j.foreco.2009.09.001

Altava, V. (2010). *Caracterització i monitoratge de les sequeres a Catalunya i al nord del País Valencià. Càlcul d'escenaris climàtics per al segle XXI.* Universitat de Barcelona, Barcelona, Spain.

Amante, C., & Eakins, B.W. (2009). ETOPO1 1 Arc-Minute Global Relief Model: Procedures, Data Sources and Analysis. NOAA Technical Memorandum NESDIS NGDC-24. National Geophysical Data Center, NOAA. doi:10.7289/V5C8276M

Amraoui, M., Pereira, M.G., Da Camara, C.C., & Calado, T.J. (2014). Severe fire activity and associated atmospheric patterns over Iberia and North Africa. In X. Viegas (Ed.), *Advances in forest fire research*. Coimbra: Coimbra University Press. doi: 10.14195/978-989-26-0884-6_102

Andela, N., Liu, Y. Y., Van Dijk, A. I. J. M., De Jeu, R. A. M., & McVicar, T. R. (2013). Global changes in dryland vegetation dynamics (1988-2008) assessed by satellite remote sensing: comparing a new passive microwave vegetation density record with reflective greenness data. *Biogeosciences, 10*(10), 6657. doi: 10.5194/bg-10-6657-2013

Andela, N., Morton, D. C., Giglio, L., Chen, Y., van der Werf, G. R., Kasibhatla, P. S., ... & Bachelet, D. (2017). A human-driven decline in global burned area. *Science, 356*(6345), 1356-1362. doi: 10.1126/science.aal4108.

Anderegg, W.R.L., Kane, J.M., & Anderegg, L.D.L. (2013a). Consequences of widespread tree mortality triggered by drought and temperature stress. *Nature Climate Change, 3*, 30–36. doi: 10.1038/nclimate1635

Anderegg, L.D.L., Anderegg, W.R.L., Abatzoglou, J., Hausladen, A.M., Berry, J.A. (2013b). Drought characteristics' role in widespread aspen forest mortality across Colorado, USA. *Global Change Biology, 19*(5), 1526-1537. doi: 10.1111/gcB.72146

Anderegg, W.R.L., Hicke, J.A., Fisher, R.A., Allen, C.D., Aukema, J., Bentz, B., ..., & Zeppel, M. (2015). Tree mortality from drought, insects, and their interactions in a changing climate. *New phytologist, 208*(3), 674-683. doi: 10.1111/nph.13477

Arbuckle, J. G. (2016). Iowa Farm and Rural Life Poll: 2015 Summary Report.

Asner, G. P., Clark, J. K., Mascaro, J., García, G. G., Chadwick, K. D., Encinales, D. N., ... & Balaji, A. (2012). High-resolution mapping of forest carbon stocks in the Colombian Amazon. *Biogeosciences, 9*(7), 2683. doi:10.5194/bg-9-2683-2012.

Asner, G. P., Mascaro, J., Anderson, C., Knapp, D. E., Martin, R. E., Kennedy-Bowdoin, T., ... & Potvin, C. (2013). High-fidelity national carbon mapping for resource management and REDD+. *Carbon Balance and Management, 8*(1), 7. doi: 10.1186/1750-0680-8-7.

Asner, G. P., Knapp, D. E., Martin, R. E., Tupayachi, R., Anderson, C. B., Mascaro, J., ... & Llactayo, W. (2014). Targeted carbon conservation at national scales with high-resolution monitoring. *Proceedings of the National Academy of Sciences, 111*(47), E5016-E5022. doi: 10.1073/pnas.1419550111.

Asseng, S., Ewert, F., Martre, P., Rötter, R. P., Lobell, D. B., Cammarano, D., ... & Reynolds, M. P. (2015). Rising temperatures reduce global wheat production. *Nature Climate Change, 5*(2), 143. doi: 10.1038/nclimate2470

Atzberger, C. (2013). Advances in remote sensing of agriculture: Context description, existing operational monitoring systems and major information needs. *Remote Sensing, 5*(2), 949-981. doi: 10.3390/rs5020949

Aubrecht, C., Elvidge, C.D., Baugh, K.E., & Hahn, S. (2012). Identification of wildfire precursor conditions: linking satellite based fire and soil moisture data. In J.M.R.S. Tavares & R.M.N. Jorge (Eds.), *Computational Vision and Medical Image Processing: VipIMAGE 2011*. London: Taylor & Francis Group.

Avitabile, V., Herold, M., Heuvelink, G. B. M., Lewis, S. L., Phillips, O. L., Asner, G. P., … & Willcock, S. (2016). An integrated pan-tropical biomass map using multiple reference datasets. *Global Change Biology, 22*(4), 1406–1420. doi:10.1111/gcb.73139

Baccini, A., Friedl, M. A., Woodcock, C. E., & Warbington, R. (2004). Forest biomass estimation over regional scales using multisource data. *Geophysical Research Letters, 31*(10). doi: 10.1029/2004GL019782

Baccini, A., Laporte, N., Goetz, S. J., Sun, M., & Dong, H. (2008). A first map of tropical Africa's above-ground biomass derived from satellite imagery. *Environmental Research Letters, 3*(4), 045011. doi:10.1088/1748-9326/3/4/045011.

Baccini, A. G. S. J., Goetz, S. J., Walker, W. S., Laporte, N. T., Sun, M., Sulla-Menashe, D., ... & Samanta, S. (2012). Estimated carbon dioxide emissions from tropical deforestation improved by carbon-density maps. *Nature Climate Change, 2*(3), 182. doi: 10.1038/nclimate1354.

Baccini, A., Walker, W., Carvalho, L., Farina, M., Sulla-Menashe, D., & Houghton, R. A. (2017). Tropical forests are a net carbon source based on aboveground measurements of gain and loss. *Science, 358*(6360), 230-234. doi: 10.1126/science.aam5962.

Bajocco, S. & Ricotta, C. (2008). Evidence of selective burning in Sardinia (Italy): Which land-cover classes do wildfires prefer? *Landscape Ecology 23*(2), 241–48. doi: 10.1007/s10980-007-9176-5

Banqué, M., Vayreda, J., Martínez-Vilalta, J. (2013). *Monitoreo del decaimiento de bosques de Cataluñna: Proyecto DEBOSCAT.* 6° Congreso Forestal Español. Vitoria-Gasteiz, 10-14 junio 2013. Retrieved from: https://www.congresoforestal.es/actas/doc/6CFE/6CFE01-438.pdf

Barriopedro, D., Fischer, E. M., Luterbacher, J., Trigo, R. M., & García-Herrera, R. (2011). The hot summer of 2010: redrawing the temperature record map of Europe. Science, 332(6026), 220-224. doi: 10.1126/science.1201224

Bartsch, A., Balzter, H., & George, C. (2009). The influence of regional surface soil moisture anomalies on forest fires in Siberia observed from satellites. *Environmental Research Letters, 4*(4), 045021. doi: 10.1088/1748-9326/4/4/045021

BEC (Barcelona Expert Centre). (2018). *Land Variables.* Retrieved from: http://bec.icm.csic.es/land-datasets. Last accessed: 12th January 2018.

Becker-Reshef, I., Vermote, E., Lindeman, M., & Justice, C. (2010a). A generalized regression-based model for forecasting winter wheat yields in Kansas and Ukraine using MODIS data. *Remote Sensing of Environment, 114*(6), 1312-1323. doi: 10.1016/j.rse.2010.01.010

Becker-Reshef, I., Justice, C., Sullivan, M., Vermote, E., Tucker, C., Anyamba, A., ... & Hansen, M. (2010b). Monitoring global croplands with coarse resolution earth observations: The Global Agriculture Monitoring (GLAM) project. *Remote Sensing, 2*(6), 1589-1609. doi:10.3390/rs2061589.

Bennett, A.C., McDowell, N.G., Allen, C.D., & Anderson-Teixeira, K.J. (2015). Larger trees suffer most during drought in forests worldwide. *Nature Plants*, *1*, 15139. doi: 10.1038/nplants.2015.139

Bircher, S., Skou, N., Jensen, K. H., Walker, J. P., & Rasmussen, L. (2012). A soil moisture and temperature network for SMOS validation in Western Denmark. *Hydrology and Earth System Sciences, 16*(5), 1445-1463. doi:10.5194/hess-16-1445-2012

Bircher, S., Skou, N., & Kerr, Y. H. (2013). Validation of SMOS L1C and L2 products and important parameters of the retrieval algorithm in the Skjern River Catchment, Western Denmark. *IEEE Transactions on Geoscience and Remote Sensing, 51*(5), 2969-2985. doi: 10.1109/TGRS.2012.2215041

Bivand, R., Hauke, J., & Kossowski, T. (2013). Computing the Jacobian in Gaussian spatial autoregressive models: an illustrated comparison of available methods. *Geographical Analysis, 45*(2), 150-179. doi: 10.1111/gean.12008

Bivand, R., & Piras, G. (2015). Comparing implementations of estimation methods for spatial econometrics. *Journal of Statistical Software, 63*(18). doi: 10.18637/jss.v063.i18

Blackard, J. A., Finco, M. V., Helmer, E. H., Holden, G. R., Hoppus, M. L., Jacobs, D. M., ... & Tymcio, R.P. (2008). Mapping US forest biomass using nationwide forest inventory data and moderate resolution information. *Remote Sensing of Environment, 112*(4), 1658-1677. doi: 10.1016/j.rse.2007.08.021.

Boken, V. K., & Shaykewich, C. F. (2002). Improving an operational wheat yield model using phenological phase-based Normalized Difference Vegetation Index. *International Journal of Remote Sensing, 23*(20), 4155-4168. doi: 10.1080/014311602320567955

Bonan, G.B. (2008). Forests and climate change: forcings, feedbacks and the climate benefits of forests. *Science, 320*(5882), 1444–1449. doi: 10.1126/science.1155121

Bouvet, A., Mermoz, S., Le Toan, T., Villard, L., Mathieu, R., Naidoo, L., & Asner, G. P. (2018). An above-ground biomass map of African savannahs and woodlands at 25m resolution derived from ALOS PALSAR. *Remote Sensing of Environment, 206*, 156-173. doi: 10.1016/j.rse.2017.12.030.

Brandt, M., Rasmussen, K., Peñuelas, J., Tian, F., Schurgers, G., Verger, A., ... & Fensholt, R. (2017). Human population growth offsets climate-driven increase in woody vegetation in sub-Saharan Africa. *Nature Ecology & Evolution, 1*(4), 0081. doi: 10.1038/s41559-017-0081

Brandt, M., Wigneron, J. P., Chave, J., Tagesson, T., Penuelas, J., Ciais, P., ... & Rodriguez-Fernandez, N. (2018). Satellite passive microwaves reveal recent climate-induced carbon losses in African drylands. *Nature Ecology & Evolution, 2*, 827-835. doi: 10.1038/s41559-018-0530-6.

Brocca, L., Ponziani, F., Moramarco, T., Melone, F., Berni, N., & Wagner, W. (2012). Improving landslide forecasting using ASCAT-derived soil moisture data: A case study of the Torgiovannetto landslide in central Italy. *Remote Sensing, 4*(5), 1232-1244. doi: 10.3390/rs4051232

Brocca, L., Pellarin, T., Crow, W. T., Ciabatta, L., Massari, C., Ryu, D., ... & Kerr, Y. (2016). Rainfall estimation by inverting SMOS soil moisture estimates: A comparison of different methods over Australia. *Journal of Geophysical Research: Atmospheres, 121*(20). doi: 10.1002/2016JD025382

Brodribb, T.J., Pittermann, J., & Coomes, D.A. (2012). Elegance versus speed: examining competition between conifer and angiosperm trees. *International Journal of Plant Sciences, 173*(6), 673–694. doi: 10.1086/666005

Brown, M. E., Escobar, V., Moran, S., Entekhabi, D., O'Neill, P. E., Njoku, E. G., ... & Entin, J. K. (2013). NASA's soil moisture active passive (SMAP) mission and opportunities for applications users. *Bulletin of the American Meteorological Society, 94*(8), 1125-1128. doi: 10.1175/BAMS-D-11-00049.1

Camps, A., Vall-llossera, M., Duffo, N., Torres, F., & Corbella, I. (2005). Performance of sea surface salinity and soil moisture retrieval algorithms with different auxiliary datasets in 2-D L-band aperture synthesis interferometric radiometers. *IEEE Transactions on Geoscience and Remote Sensing, 43*(5), 1189-1200. doi: 10.1109/TGRS.2004.842096

Carnicer, J., Coll. M., Ninyerola, M., Pons, X., Sánchez, G., & Peñuelas, J. (2011). Widespread crown condition decline, food web disruption, and amplified tree mortality with increased climate change-type drought. *Proceedings of the National Academy of Sciences, 108*(4), 1474-1478. doi: 10.1073/pnas.1010070108

Ceballos, A., Scipal, K., Wagner, W., & Martínez-Fernández, J. (2005). Validation of ERS scatterometer-derived soil moisture data in the central part of the Duero Basin, Spain. *Hydrological processes, 19*(8), 1549-1566. doi: 10.1002/hyp.5585

Chakrabarti, S., Bongiovanni, T., Judge, J., Zotarelli, L., & Bayer, C. (2014). Assimilation of SMOS soil moisture for quantifying drought impacts on crop yield in agricultural regions. *IEEE Journal of Selected Topics in Applied Earth Observations and Remote Sensing, 7*(9), 3867-3879. doi: 10.1109/JSTARS.2014.2315999

Champagne, C., Davidson, A., Cherneski, P., L'Heureux, J., & Hadwen, T. (2015). Monitoring agricultural risk in Canada using L-band passive microwave soil moisture from SMOS. *Journal of Hydrometeorology, 16*(1), 5-18. doi: 10.1175/JHM-D-14-0039.1

Chan, S., Hunt, R., Bindlish, R., Njoku, E., Kimball, J., & Jackson, T. (2013). Ancillary Data Report for Vegetation Water Content. SMAP Project Document.

Chaparro, D., Vayreda, J., Martínez-Vilalta, J., Vall-llossera, M., Banqué, M., Camps, A., & Piles, M. (2014). SMOS and climate data applicability for analyzing forest decline and forest fires. *Geoscience and Remote Sensing Symposium (IGARSS), 2014 IEEE International*, 13–18 July 2014, pp. 1069–1072.

Chaparro, D., Vall-llossera, M., Piles, M., Camps, A., Rüdiger, C., & Riera-Tatché, R. (2016a). Predicting the extent of wildfires using remotely sensed soil moisture and temperature trends. *IEEE Journal of Selected Topics in Applied Earth Observations and Remote Sensing, 9*(6), 2818-2829. doi: 10.1109/JSTARS.2016.2571838

Chaparro, D., Piles, M., Vall-llossera, M. (2016b). Remotely sensed soil moisture as a key variable in wildfires prevention services: towards new prediction tools using SMOS and SMAP data. In: Srvastava, P., Petropoulos, G., & Kerr, Y.H. (Eds.) *Satellite soil moisture retrieval: techniques and applications* (pp. 379-400). Elsevier. doi: 10.1016/C2014-0-03396-5

Chaparro, D., Vall-llossera, M., Camps, A., Piles, M., Konings, A. G., & Entekhabi, D. (2017). SMAP Multi-Temporal vegetation optical depth retrieval as an indicator of crop yield trends and crop composition. *Geoscience and Remote Sensing Symposium (IGARSS), 2017 IEEE International* (pp. 4362-4365). IEEE. doi: 10.1109/IGARSS.2017.8127967

Chaparro, D., Piles, M., Vall-llossera, M., Camps, A., Konings, A. G., & Entekhabi, D. (2018). L-band vegetation optical depth seasonal metrics for crop yield assessment. *Remote Sensing of Environment, 212*, 249-259. doi: 10.1016/j.rse.2018.04.049

Chaparro, D., Duveiller, G., Piles, M., Cescatti, A., Vall-llossera, M., Camps, A., Entekhabi, D. Mapping carbon stocks of Central and South American tropical forests with L-band passive microwaves. *Manuscript submitted for publication*.

Chaubell, J. (2016). Algorithm theoretical basis document. SMAP L1B enhancement radiometer brightness temperature data product. Jet Propulsion Laboratory, California Institute of Technology.

Choat, B., Jansen, S., Brodribb, T.J., Cochard, H., Delzon, S., Bhaskar, R., ..., & Zanne, A.E. (2012). Global convergence in the vulnerability of forests to drought. *Nature, 491*, 752-755. doi: 10.1038/nature11688

Chuvieco, E., Deshayes, M., Stach, N., Cocero, D., & Riaño, D. (1999). Short-term fire risk: foliage moisture content estimation from satellite data. In E. Chuvieco (Ed.), *Remote sensing of large wildfires in the European Mediterranean Basin*. Berlin: Springer-Verlag.

Chuvieco, E., Cocero, D., Riaño, D., Martin, P., Martínez-Vega, J., de la Riva, J., & Pérez, F. (2004). Combining NDVI and surface temperature for the estimation of live fuel moisture content in forest fire danger rating. *Remote Sensing of Environment, 92*(3), pp. 322–331. doi: 10.1016/j.rse.2004.01.019

Chuvieco, E., Aguado, I., Jurdao, S., Pettinari, M.L., Yebra, M., Salas, F.J., ..., Martínez-Vega, F.J. (2014). Integrating geospatial information into fire risk assessment. *International Journal of Wildland Fire, 23*(5), 606–619. doi: 10.1071/WF12052

Ciais, P., Reichstein, M., Viovy, N., Granier, A., Ogée, J., Allard, V., ... & Chevallier, F. (2005). Europe-wide reduction in primary productivity caused by the heat and drought in 2003. Nature, 437(7058), 529. doi: 10.1038/nature03972

Cohen, J. D. (2008). The wildland-urban interface fire problem: a consequence of the fire exclusion paradigm. *Forest History Today, Fall*, 20–26.

Cohen, W.B., Yang, Z., Stehman, S.V., Schroeder, T.A., Bell, D.M., Masek, J.G., …, & Meigs, G.W. (2016). Forest disturbance across the conterminous United States from 1985-2012: the emerging dominance of forest decline. *Forest Ecology and Management, 360*, 242-252. doi: 10.1016/j.foreco.2015.10.042

Copernicus. (2018a). *Copernicus land monitoring services*. Retrieved from: http://land.copernicus.eu.

Copernicus. (2018b). *Copernicus in brief*. Retrieved from http://www.copernicus.eu/main/copernicus-brief.

Costa, J.C., Aguiar, C., Capelo, J., Lousã, M., & Neto, C. (1998). Biogeografia de Portugal Continental. *Quercetea*, *1*, 5–56.

Cramer, W., Yohe, G.W., Auffhammer, M., Huggel, C., Molau, U., da Silva Dias, M.A.F., ... & Tibig, L. (2014). Detection and attribution of observed impacts. In: Field, C.B., Barros, V.R., Dokken, D.J., Mach, K.J., Mastrandrea, M.D., Bilir, T.E., Chatterjee, M., Ebi, K.L., Estrada, Y.O., Genova, R.C., Girma, B., Kissel, E.S., Levy, A.N., MacCracken, S., Mastrandrea, P.R., & White, L.L. (Eds.) *Climate Change 2014: Impacts, Adaptation, and Vulnerability. Part A: Global and Sectoral Aspects. Contribution of the Working Group II to the 5th Assessment Report of the IPCC* (pp. 979-1037). Cambridge, United Kingdom and NY, New York, USA: Cambridge University Press.

CREAF & Generalitat de Catalunya. (2005). *Mapa de cobertes del sòl de Catalunya 3a edició*. Retrieved from: http://www.creaf.uab.es/mcsc/usa/index.htm

Daly, D. C. & J. D. Mitchell. (2000). Lowland vegetation of tropical South America – an overview. Pages 391-454. In: D. Lentz, (Ed.). *Imperfect Balance: Landscape Transformations in the pre-Colombian Americas.* Colombia University Press, New York.

Das, N. N., Entekhabi, D., & Njoku, E. G. (2011). An algorithm for merging SMAP radiometer and radar data for high-resolution soil-moisture retrieval. *IEEE Transactions on Geoscience and Remote Sensing, 49*(5), 1504-1512. doi: 10.1109/TGRS.2010.2089526

Das, N. N., Entekhabi, D., Njoku, E. G., Shi, J. J., Johnson, J. T., & Colliander, A. (2014). Tests of the SMAP combined radar and radiometer algorithm using airborne field campaign observations and simulated data. *IEEE Transactions on Geoscience and Remote Sensing, 52*(4), 2018-2028. doi: 10.1109/TGRS.2013.2257605

Davidson, E. A., de Araújo, A. C., Artaxo, P., Balch, J. K., Brown, I. F., Bustamante, M. M., ... & Munger, J. W. (2012). The Amazon basin in transition. *Nature, 481*(7381), 321-328. doi: 10.1038/nature10717

Deeming, J.E., Burgan, R.E., & Cohen, J.D. (1977). The national fire-danger rating system–1978. USDA Forest Service, rocky mountain forest and range experiment station, General Technical Report INT-39. Odgen, UT: USDA Forest Service.

Del Frate, F., Ferrazzoli, P., & Schiavon, G. (2003). Retrieving soil moisture and agricultural variables by microwave radiometry using neural networks. Remote Sensing of Environment, 84(2), 174-183. doi: 10.1016/S0034-4257(02)00105-0

Dente, L., Su, Z., & Wen, J. (2012). Validation of SMOS soil moisture products over the Maqu and Twente regions. *Sensors, 12*(8), 9965-9986. doi: 10.3390/s120809965

Deryng, D., Conway, D., Ramankutty, N., Price, J., & Warren, R. (2014). Global crop yield response to extreme heat stress under multiple climate change futures. *Environmental Research Letters, 9*(3), 034011. doi:10.1088/1748-9326/9/3/034011

Diouf, A. A., Hiernaux, P., Brandt, M., Faye, G., Djaby, B., Diop, M. B., ... & Tychon, B. (2016). Do agrometeorological data improve optical satellite-based estimations of the herbaceous yield in Sahelian semi-arid ecosystems?. *Remote Sensing, 8*(8), 668. doi: 10.3390/rs8080668

Dobermann, A.R., Arkebauer, T.J., Cassman, K.G., Lindquist, J., Specht, J.E. (2002). Understanding and managing corn yield potential. Agronomy & Horticulture – Faculty Publications. Agronomy and Horticulture Department, University of Nebraska – Lincoln.

Dong, J., Kaufmann, R. K., Myneni, R. B., Tucker, C. J., Kauppi, P. E., Liski, J., ... & Hughes, M. K. (2003). Remote sensing estimates of boreal and temperate forest woody biomass: carbon pools, sources, and sinks. *Remote Sensing of Environment, 84*(3), 393-410.

Doraiswamy, P. C., & Cook, P. W. (1995). Spring wheat yield assessment using NOAA AVHRR data. *Canadian Journal of Remote Sensing, 21*(1), 43-51.

Dorigo, W. A., Gruber, A., De Jeu, R. A. M., Wagner, W., Stacke, T., Loew, A., ... & Kidd, R. (2015). Evaluation of the ESA CCI soil moisture product using ground-based observations. *Remote Sensing of Environment, 162*, 380-395. doi: 10.1016/j.rse.2014.07.023

Dorigo, W., Wagner, W., Albergel, C., Albrecht, F., Balsamo, G., Brocca, L., ... & Haas, E. (2017). ESA CCI Soil Moisture for improved Earth system understanding: state-of-the art and future directions. *Remote Sensing of Environment, 203*, 185-215. doi: 10.1016/j.rse.2017.07.001

Drusch, M. (2007). Initializing numerical weather prediction models with satellite-derived surface soil moisture: Data assimilation experiments with ECMWF's Integrated Forecast

System and the TMI soil moisture data set. *Journal of Geophysical Research: Atmospheres, 112(D3)*. doi: 10.1029/2006JD007478

ECMWF. European Centre for Medium-Range Weather Forecasts. (2018). *Public datasets.* Retrieved from: http://apps.ecmwf.int/datasets. Last accessed: 12th January 2018.

EEA (European Environment Agency) (2008). *Impacts of Europe's Changing Climate—2008 Indicator-Based Assessment, European Environment Agency Summary*. *Report No. 4/2008.* Copenhagen, Denmark: European Environment Agency.

El Sharif, H., Wang, J., & Georgakakos, A. P. (2015). Modeling regional crop yield and irrigation demand using SMAP type of soil moisture data. *Journal of Hydrometeorology, 16*(2), 904-916. doi: 10.1175/JHM-D-14-0034.1

Engelbrecht, B.M.J., Comita, L.S., Condit, R., Kursar, T.A., Tyree, M.T., Turner, B.L., ..., Hubbell, S.P. (2007). Drought sensitivity shapes species distribution patterns in tropical forests. *Nature, 447*, 80-82. doi: 10.1038/nature05747

Entekhabi, D., Njoku, E. G., O'Neill, P. E., Kellogg, K. H., Crow, W. T., Edelstein, W. N., ... & Kimball, J. (2010). The soil moisture active passive (SMAP) mission. *Proceedings of the IEEE, 98*(5), 704-716. doi: 10.1109/JPROC.2010.2043918

ESA. European Space Agency. (2009). *Space in images. SMOS in orbit.* Retrieved from: https://www.esa.int/spaceinimages/Images/2009/09/SMOS_in_orbit

ESA. European Space Agency. (2016). *Land Cover CCI. Product user guide, version 2*. Retrieved from: http://maps.elie.ucl.ac.be/CCI/viewer/download/ESACCI-LC-PUG-v2.5.pdf.

ESA. European Space Agency. (2018a). *Earth Online. What is ERS?* Retrieved from: https://earth.esa.int/web/guest/missions/esa-operational-eo-missions/ers

ESA. European Space Agency. (2018b). Future missions. BIOMASS. Retrieved from: https://m.esa.int/Our_Activities/Observing_the_Earth/The_Living_Planet_Programme/Earth_Explorers/Future_missions/Biomass

ESA-CCI. European Space Agency – Climate Change Initiative. (2017). The European Space Agency – Climate Change Initiative (ESA-CCI) 2015 Land Cover map. Retrieved from: https://www.esa-landcover-cci.org/

Escorihuela, M. J., Merlin, O., Stefan, V., Moyano, G., Eweys, O. A., Zribi, M., ... & Ghaout, S. (2018). SMOS based high resolution soil moisture estimates for desert locust preventive management. *Remote Sensing Applications: Society and Environment, 11*, 140-150. doi: 10.1016/j.rsase.2018.06.002

European Commission. (2017). *Monitoring Agricultural ResourceS (MARS).* Retrieved from: https://ec.europa.eu/jrc/en/mars. Last accessed: 7th August 2017.

FAO (Food and Agriculture Organization of the United Nations). (2007). *Fire management-global assessment 2006. A Thematic Study Prepared in the Framework of the Global Forest Resources Assessment 2005.* Rome, Italy: Food and Agriculture Organization.

FAO (Food and Agriculture Organization of the United Nations). (2017). *FAOSTAT. Crops.* Retrieved from: http://faostat.fao.org/site/567/default.aspx#ancor.

Fernandez-Moran, R., Al-Yaari, A., Mialon, A., Mahmoodi, A., Al Bitar, A., De Lannoy, G., ... & Wigneron, J. P. (2017). SMOS-IC: An alternative SMOS soil moisture and vegetation optical depth product. *Remote Sensing, 9*(5), 457. doi: 10.3390/rs9050457

FEWS-NET. Famine Early Warning System – Network. (2018). Retrieved from: http://www.fews.net

Fick, S.E., & Hijmans, R.J. (2017). WorldClim 2: new 1-km spatial resolution climate surfaces for global land areas. *International Journal of Climatology, 37*(12), 4302-4315. doi: 10.1002/joc.5086

Foley, J.A., DeFries, R., Asner, G.P., Barford, C., Bonan, G., Carpenter, S.R., ..., & Snyder, P.K. (2005). Global consequences of land use. *Science, 309*, 570-574. doi: 10.1126/science.1111772.

Foley, J. A., Ramankutty, N., Brauman, K. A., Cassidy, E. S., Gerber, J. S., Johnston, M., ... & Balzer, C. (2011). Solutions for a cultivated planet. *Nature, 478*(7369), 337. doi: 10.1038/nature10452

Forkel, M., Thonicke, K., Beer, C., Cramer, W., Bartalev, S., & Schmullius, C. (2012). Extreme fire events are related to previous-year surface moisture conditions in permafrost-underlain larch forests of Siberia. *Environmental Research Letters, 7*(4), 044021. doi: 10.1088/1748-9326/7/4/044021

Forkel, M., Dorigo, W., Lasslop, G., Teubner, I., Chuvieco, E., & Thonicke, K. (2017). A data-driven approach to identify controls on global fire activity from satellite and climate observations (SOFIA V1). *Geoscientific Model Development, 10*(12), 4443. doi: 10.5194/gmd-10-4443-2017

Forster, P., Ramaswamy, V., Artaxo, P., Berntsen, T., Betts, R., Fahey, D. W., ... & Nganga, J. (2007). Changes in atmospheric constituents and in radiative forcing. In: Solomon, S., D. Qin, M. Manning, Z. Chen, M. Marquis, K.B. Averyt, M. Tignor and H.L. Miller (Eds.), *Climate Change 2007. The Physical Science Basis. Contribution of the Working Group I to the IPCC 4th Assessment Report* (pp. 129-234). Cambridge, United Kingdom and NY, New York, USA: Cambridge University Press.

Fox, J. (2003). Effect displays in R for generalized linear models. *Journal of Statistical Software, 8*(15), 1-27.

Frescino, T. S., Edwards, T. C., & Moisen, G. G. (2001). Modeling spatially explicit forest structural attributes using generalized additive models. *Journal of Vegetation Science, 12*(1), 15-26. doi: 10.1111/j.1654-1103.2001.tb02613.x

Galiano, L., Martínez-Vilalta, J., & Lloret, F. (2010). Drought-induced multifactor decline of Scots pine in the Pyrenees and potential vegetation change by the expansion of co-occurring oak species. *Ecosystems, 13*(7), 978-991. doi: 10.1007/s10021-010-9368-8

GCOS (Global Climate Observing System). (2010). *Implementation Plan for the Global Observing System for Climate in support of the UNFCCC, GCOS-138 (GOOS-184, GTOS-76, WMO-TD/No. 1523).* Technical report.

GEO (Group on Earth Observations). (2018). *Group on Earth Observations*. Retrieved from: https://www.earthobservations.org.

Godfray, H. C. J., Beddington, J. R., Crute, I. R., Haddad, L., Lawrence, D., Muir, J. F., ... & Toulmin, C. (2010). Food security: the challenge of feeding 9 billion people. *Science, 327*(5967), 812-818. doi: 10.1126/science.1185383

Goetz, S. J., Baccini, A., Laporte, N. T., Johns, T., Walker, W., Kellndorfer, J., ... & Sun, M. (2009). Mapping and monitoring carbon stocks with satellite observations: a comparison of methods. *Carbon Balance and Management, 4*(1), 2. doi:10.1186/1750-0680-4-2.

Gómez, D., Casanova, C., Salvador, P., Sanz, J., Piles, M., Vall-llossera, M., Garcia, M. (2017). Soil moisture influence in desert locust development. In: Dorigo, W., & Wagner, W. (Eds.). *Abstract booklet of the 4th Satellite Soil Moisture Validation and Application Workshop and the CCI Soil Moisture User Workshop*. Vienna, Austria: Technische Universität Wien. Retrieved from: http://smw.geo.tuwien.ac.at/fileadmin/editors/SMworkshop/CCI_SM_Abstract_Booklet.pdf

González-Alonso, F., Merino-De-Miguel, S., Roldán-Zamarrón, A., García-Gigorro, S., & Cuevas, J. M. (2006). Forest biomass estimation through NDVI composites. The role of remotely sensed data to assess Spanish forests as carbon sinks. *International Journal of Remote Sensing, 27*(24), 5409-5415. doi: 10.1080/01431160600830748

González-Gambau, V., Olmedo, E., Turiel, A., Martínez, J., Ballabrera-Poy, J., Portabella, M., & Piles, M. (2016). Enhancing SMOS brightness temperatures over the ocean using the nodal sampling image reconstruction technique. *Remote Sensing of Environment, 180*, 205-220. doi: 10.1016/j.rse.2015.12.032

González-Zamora, Á., Sánchez, N., Martínez-Fernández, J., Gumuzzio, Á., Piles, M., & Olmedo, E. (2015). Long-term SMOS soil moisture products: a comprehensive evaluation across scales and methods in the Duero Basin (Spain). *Physics and Chemistry of the Earth, Parts A/B/C, 83*, 123-136. doi: 10.1016/j.pce.2015.05.009

Government of Canada. (2016). *Canadian Wildland Fire Information System*. Retrieved from http://cwfis.cfs.nrcan.gc.ca/background/summary/fwi

Grant, J. P., Wigneron, J. P., De Jeu, R. A. M., Lawrence, H., Mialon, A., Richaume, P., ... & Kerr, Y. (2016). Comparison of SMOS and AMSR-E vegetation optical depth to four MODIS-based vegetation indices. *Remote Sensing of Environment, 172*, 87-100. doi: 10.1016/j.rse.2015.10.021

Greenwood, S., Ruiz-Benito, P., Martínez-Vilalta, J., Lloret, F., Kitzbeger, T., Allen, C.D., …, & Jump, A.S. (2017). Tree mortality across biomes is promoted by drought intensity, lower wood density and higher specific leaf area. *Ecology Letters, 20*, 539-553. doi: 10.1111/ele.12748

Grömping, U. (2006). Relative importance for linear regression in R: the package relaimpo. *Journal of Statistical Software, 17*(1), 1-27.

Guan, K., Wood, E. F., Medvigy, D., Kimball, J., Pan, M., Caylor, K. K., ... & Jones, M. O. (2014). Terrestrial hydrological controls on land surface phenology of African savannas and woodlands. *Journal of Geophysical Research: Biogeosciences, 119*(8), 1652-1669. doi: 10.1002/2013JG002572

Guan, K., Wu, J., Kimball, J. S., Anderson, M. C., Frolking, S., Li, B., ... & Lobell, D. B. (2017). The shared and unique values of optical, fluorescence, thermal and microwave satellite data for estimating large-scale crop yields. *Remote Sensing of Environment, 199*, 333-349. doi: 10.1016/j.rse.2017.06.043

Hamdan, O., Aziz, H. K., & Rahman, K. A. (2011). Remotely sensed L-Band SAR data for tropical forest biomass estimation. *Journal of Tropical Forest Science, 23*(3), 318-327.

Hardy, C. C., & Burgan, R.E. (1999). Evaluation of NDVI for monitoring live moisture in three vegetation types of the Western U.S. *Photogrammetric Engineering and Remote Sensing, 65,* 603–610.

Hartmann, D.L., Klein Tank, A.M.G., Rusticucci, M., Alexander, L.V., Brönnimann, S., Charabi, Y., ..., & Zhai, P.M. (2013). Observations: Atmosphere and Surface. In: Stocker, T.F., Qin, D., Plattner, G.-K., Tignor, M., Allen, S.K., Boschung, J., Nauels, A., Xia, Y., Bex, V. & Midgley, P.M. (Eds.). *Climate Change 2013: The Physical Science Basis. Contribution of the Working Group I to the 5th Assessment Report of the IPCCC* (pp. 159-254). Cambridge, United Kingdom and NY, New York, USA: Cambridge University Press.

Hastie, T. J., and Tibshirani, R.J. (1990). Generalized Additive Models. Chapman and Hall, New York.

Hastie, T. (2018). GAM: Generalized Additive Models. R package version 1.15. Retrieved from: https://CRAN.R-project.org/package=gam

Hereş, A.M., Martínez-Vilalta, J., & Claramunt López, B. (2012). Growth patterns in relation to drought-induced mortality at two Scots pine (*Pinus sylvestris* L.) sites in NE Iberian Peninsula. *Trees, 26*, 621. doi: 10.1007/s00468-011-0628-9

Holgate, C.M., van Dijk, A.I.J.M., Cary, G.J., & Yebra, M. (2017). Using alternative soil moisture estimates in the McArthur Forest Fire Danger Index. *International Journal of Wildland Fire, 26*, 806-819. doi: 10.1071/WF16217

Hornbuckle, B. K., Patton, J. C., VanLoocke, A., Suyker, A. E., Roby, M. C., Walker, V. A., ... & Endacott, E. A. (2016). SMOS optical thickness changes in response to the growth and development of crops, crop management, and weather. *Remote Sensing of Environment, 180*, 320-333. doi: 10.1016/j.rse.2016.02.043

Hosmer, D.W., & Lemeshow, S. (2000). *Applied Logistic Regression* (2nd ed.) New York, NY, USA: Wiley.

Huete, A., Didan, K., Miura, T., Rodriguez, E. P., Gao, X., & Ferreira, L. G. (2002). Overview of the radiometric and biophysical performance of the MODIS vegetation indices. *Remote Sensing of Environment, 83*(1-2), 195-213. doi: 10.1016/S0034-4257(02)00096-2

ICGC (Institut Cartogràfic i Geològic de Catalunya). (2010). *Mapa geològic comarcal de Catalunya* 1:50000. Retrieved from: http://www.icgc.cat/Administracio-i-empresa/Descarregues/Cartografia-geologica-i-geotematica/Cartografia-geologica/Mapa-geologic-comarcal-de-Catalunya-1-50.000/Mapa-geologic-comarcal-de-Catalunya-1-50.000.

Ines, A. V., Das, N. N., Hansen, J. W., & Njoku, E. G. (2013). Assimilation of remotely sensed soil moisture and vegetation with a crop simulation model for maize yield prediction. *Remote Sensing of Environment, 138*, 149-164. doi: 10.1016/j.rse.2013.07.018

IPCC (Intergovernmental Panel on Climate Change). (2012). Managing the risks of extreme events and disasters to advance climate change adaptation. A special report of orking Groups I and II of the Intergovernmental Panel on Climate Change [Field, C.B., Barros, V., Stocker, T.F., Qin, D., Dokken, D.J., Ebi, K.L., Mastrandrea, M.D., Mach, K.J., Plattner, G.-K., Allen, S.K., Tignor, M., & Midgley, P.M. (eds.)]. Cambridge University Press, Cambridge, UK, and New York, NY, USA, 582 pp.

IPCC (Intergovernmental Panel on Climate Change). (2013). Annex I: Atlas of global and regional climate projections. In: van Oldenborgh, G.J., Collins, M., Arblaster, J., Christensen, J.H., Marotzke, J., Power, S.B., Rummukainen, M. & Zhou, T. (Eds.) *Climate Change 2013: The Physical Science Basis. Contribution of the Working Group I to the 5th Assessment Report of the IPCC* (pp. 1311-1393). Cambridge University Press, Cambridge, United Kingdom and New York, NY, USA.

Jackson, T. J., & O'Neill, P. E. (1987). Salinity effects on the microwave emission of soils. *IEEE Transactions on Geoscience and Remote Sensing*, *GE-25*(2), 214-220. doi: 10.1109/TGRS.1987.289820

Jackson, T. J., & Schmugge, T. J. (1991). Vegetation effects on the microwave emission of soils. *Remote Sensing of Environment, 36*(3), 203-212. doi: 10.1016/0034-4257(91)90057-D

Jackson, R.B., Canadell, J., Ehleringer, J.R., Mooney, H.A., Sala, O.E., & Schulze, E.D. (1996). A global analysis of root distributions for terrestrial biomes. *Oecologia, 108*(3), 389–411.

Jacome, A., Bernier, M., Chokmani, K., Gauthier, Y., Poulin, J., & De Sève, D. (2013). Monitoring volumetric surface soil moisture content at the La Grande basin boreal wetland by radar multi-polarization data. *Remote Sensing, 5*, 4919–4941. doi: 10.3390/rs5104919.

Jagdhuber, T., Baur, M., Link, M., Piles, M., Entekhabi, D., Montzka, C., ... & Löw, A. (2017). Physics-based retrieval of scattering albedo and vegetation optical depth using multi-sensor data integration. *Geoscience and Remote Sensing Symposium (IGARSS), 2017 IEEE International* (pp. 4322-4325). IEEE. doi: 10.1109/IGARSS.2017.8127958

Jolly, W. M., Cochrane, M.A., Freeborn, P.H., Holden, Z.A., Brown, T.J., Williamson, G.J., & Bowman, D.M.J.S. (2015). Climate-induced variations in global wildfire danger from 1979 to 2013. *Nature Communications*, *6,* 7537. doi: 10.1038/ncomms8537

Jones, M. O., Jones, L. A., Kimball, J. S., & McDonald, K. C. (2011). Satellite passive microwave remote sensing for monitoring global land surface phenology. *Remote Sensing of Environment, 115*(4), 1102-1114. doi: 10.1016/j.rse.2010.12.015

Jones, M. O., Kimball, J. S., Jones, L. A., & McDonald, K. C. (2012). Satellite passive microwave detection of North America start of season. *Remote Sensing of Environment, 123*, 324-333. doi: 10.1016/j.rse.2012.03.025

JPL (Jet Propulsion Laboratory). (2018a). *SMAP. Soil Moisture Active Passive. Data products.* Retrieved from: https://smap.jpl.nasa.gov/data

JPL (Jet Propulsion Laboratory). (2018b). *ASTER. Advanced Spaceborne Thermal Emission and Reflection Radiometer.* Retrieved from: https://asterweb.jpl.nasa.gov/gdem.asp.

Jump, A. S., Hunt, J. M., & Peñuelas, J. (2006). Rapid climate change-related growth decline at the southern range edge of *Fagus sylvatica*. *Global Change Biology, 12*, 2163–2174. doi: j.1365-2486.2006.01250.x

Jung, M., Reichstein, M., Ciais, P., Seneviratne, S.I., Sheffield, J., Goulden, M.L., ..., & Zhang, K. (2010). Recent decline in the global land evapotranspiration trend due to limited moisture supply. *Nature, 467*(7318), 951–954. doi: 10.1038/nature09396.

Kerr, Y. H., Waldteufel, P., Wigneron, J. P., Delwart, S., Cabot, F., Boutin, J., ... & Juglea, S. E. (2010). The SMOS mission: new tool for monitoring key elements ofthe global water cycle. *Proceedings of the IEEE, 98*(5), 666-687. doi: 10.1109/JPROC.2010.2043032

Kerr, Y. H., Waldteufel, P., Richaume, P., Wigneron, J. P., Ferrazzoli, P., Mahmoodi, A., ... & Leroux, D. (2012). The SMOS soil moisture retrieval algorithm. *IEEE Transactions on Geoscience and Remote Sensing, 50*(5), 1384-1403. doi: 10.1109/TGRS.2012.2184548

Kerr, Y. (2014, November 30). Towards a Flood risk alert system with SMOS? [Blog post]. Retrieved from: http://www.cesbio.ups-tlse.fr/SMOS_blog/?tag=floods

Kharuk, V.I., Im, S.T., Petrov, I.A., Golyukov, A.S., Ranson, K.J., Yagunov, M.N. (2017). Climate-induced mortality of Siberian pine and fir in the Lake Baikal Watershed, Siberia. *Forest Ecology and Management*, *384*, 191–199. doi: 10.1016/j.foreco.2016.10.050

Kim, S. (2013). *SMAP ancillary data report on landcover classification. Jet Propulsion Lab., California Inst. Technol., Pasadena, CA, USA, JPL D-53057.*

Kim, S., Liu, Y.Y., Johnson, F.M., Parinussa, R.M., & Sharma, A. (2015). A global comparison of alternate AMSR2 soil moisture products: why do they differ*? Remote Sensing of Environment, 161*, 43–62. doi: 10.1016/j.rse.2015.02.002

Klos, R.J., Wang, G.G., Bauerle, W.L., & Rieck, J.R. (2009). Drought impact on forest growth and mortality in the southeast USA: an analysis using forest health and monitoring data. *Ecological Applications, 19*(4), 699–708. doi: 10.1890/08-0330.1

Knorr, W., Pytharoulis, I., Petropoulos, G.P., & Gobron, N. (2011). Combined use of weather forecasting and satellite remote sensing information for fire risk, fire and fire impact monitoring. *Computational Ecology and Software, 1*, 112–20.

Konings, A. G., McColl, K. A., Piles, M., & Entekhabi, D. (2015). How many parameters can be maximally estimated from a set of measurements?. *IEEE Geoscience and Remote Sensing Letters, 12*(5), 1081-1085. doi: 10.1109/LGRS.2014.2381641

Konings, A. G., Piles, M., Rötzer, K., McColl, K. A., Chan, S. K., & Entekhabi, D. (2016). Vegetation optical depth and scattering albedo retrieval using time series of dual-polarized L-band radiometer observations. *Remote Sensing of Environment, 172*, 178-189. doi: 10.1016/j.rse.2015.11.009

Konings, A.G., Williams, A.P., & Gentine, P. (2017a). Sensitivity of grassland productivity to aridity controlled by stomatal and xylem regulation. *Nature Geosciences, 10,* 284–288. doi: 10.1038/ngeo2903

Konings, A. G., Piles, M., Das, N., & Entekhabi, D. (2017b). L-band vegetation optical depth and effective scattering albedo estimation from SMAP. *Remote Sensing of Environment, 198*, 460-470. doi: 10.1016/j.rse.2017.06.037

Konings, A. G., & Gentine, P. (2017). Global variations in ecosystem-scale isohydricity. *Global Change Biology, 23*(2), 891-905. doi: 10.1111/gcB.73389

Kuplich, T. M., Salvatori, V., & Curran, P. J. (2000). JERS-1/SAR backscatter and its relationship with biomass of regenerating forests. *International Journal of Remote Sensing, 21*(12), 2513-2518. doi: 10.1080/01431160050030600

Labus, M. P., Nielsen, G. A., Lawrence, R. L., Engel, R., & Long, D. S. (2002). Wheat yield estimates using multi-temporal NDVI satellite imagery. *International Journal of Remote Sensing, 23*(20), 4169-4180.

Lawrence, H., Wigneron, J. P., Richaume, P., Novello, N., Grant, J., Mialon, A., ... & Bircher, S. (2014). Comparison between SMOS Vegetation Optical Depth products and MODIS vegetation indices over crop zones of the USA. Remote sensing of environment, 140, 396-406. doi: 10.1016/j.rse.2013.07.021

Lee, S. I. (2001). Developing a bivariate spatial association measure: an integration of Pearson's r and Moran's I. *Journal of Geographical Systems, 3*(4), 369-385. doi: 10.1007/s101090100064

Le Quéré, C.L., Raupach, M. R., Canadell, J. G., Marland, G., Bopp, L., Ciais, P., ... & Friedlingstein, P. (2009). Trends in the sources and sinks of carbon dioxide. *Nature Geoscience, 2*(12), 831. doi: 10.1038/ngeo689

Le Quéré, C. L., Andrew, R. M., Canadell, J. G., Sitch, S., Korsbakken, J. I., Peters, G. P., ... & Keeling, R. F. (2016). Global carbon budget 2016. *Earth System Science Data, 8*(2), 605-649. doi: 10.5194/essd-8-605-2016

Le Toan, T., Quegan, S., Davidson, M. W. J., Balzter, H., Paillou, P., Papathanassiou, K., ... & Ulander, L. (2011). The BIOMASS mission: Mapping global forest biomass to better understand the terrestrial carbon cycle. *Remote Sensing of Environment, 115*(11), 2850-2860. doi: 10.1016/j.rse.2011.03.020

Le Vine, D. M., Lagerloef, G. S., & Torrusio, S. E. (2010). Aquarius and remote sensing of sea surface salinity from space. *Proceedings of the IEEE, 98*(5), 688-703. 10.1109/JPROC.2010.2040550

Li, X., Song, W., Lanorte, A., & Lasaponara, R. (2016). Remote sensing fire danger prediction models applied to Northern China. In O. Gervasi, B. Murgante, S. Misra, A.M.A.C. Rocha, M.C. Torre, D. Taniar, B.O. Apduhan, E. Stankova, S. Wang (Eds). *Computational Science and Its Applications – ICCSA 2016*, *16th International Conference, Beijing, China, July 4-7, 2016, Proceedings, Part V* (pp. 624-633). *Lecture Notes in Computer Science, 9790*. Springer, Cham. doi: 10.1007/978-3-319-42092-9

Linares, J.C., Camarero, J.J., & Carreira, J.A. (2010). Competition modulates the adaptation capacity of forests to climatic stress: insights from recent growth decline and death in relict stands of the Mediterranean fir *Abies pinsapo*. *Journal of Ecology, 98*, 592–603. doi: 10.1111/j.1365-2745.2010.01645.x

Litaor, M. I., Williams, M., & Seastedt, T. R. (2008). Topographic controls on snow distribution, soil moisture, and species diversity of herbaceous alpine vegetation, Niwot Ridge, Colorado. *Journal of Geophysical Research: Biogeosciences, 113(G2)*. doi: 10.1029/2007JG000419

Liu, Y. Y., de Jeu, R. A., McCabe, M. F., Evans, J. P., & van Dijk, A. I. (2011). Global long-term passive microwave satellite-based retrievals of vegetation optical depth. *Geophysical Research Letters, 38*(18). doi:10.1029/2011GL048684

Liu, Y. Y., Dijk, A. I., McCabe, M. F., Evans, J. P., & Jeu, R. A. (2013). Global vegetation biomass change (1988–2008) and attribution to environmental and human drivers. *Global Ecology and Biogeography, 22*(6), 692-705. doi: 10.1111/geB.72024

Liu, Y. Y., Van Dijk, A. I., De Jeu, R. A., Canadell, J. G., McCabe, M. F., Evans, J. P., & Wang, G. (2015). Recent reversal in loss of global terrestrial biomass. *Nature Climate Change, 5*(5), 470. doi: 10.1038/nclimate2581

Liu, D., Mishra, A. K., Yu, Z., Yang, C., Konapala, G., & Vu, T. (2017). Performance of SMAP, AMSR-E and LAI for weekly agricultural drought forecasting over continental United States. *Journal of Hydrology, 553*, 88-104. doi: 10.1016/j.jhydrol.2017.07.049

Lloret, F., Solé, A., Vayreda, J., & Terradas, J. (2009). *Atles de les plantes llenyoses dels boscos de Catalunya*. Retrieved from: http://oslo.geodata.es/ftp/llenyoses

Lloret, F., Escudero, A., Iriondo, J.M., Martínez-Vilalta, J., & Valladares, F. (2012). Extreme climatic events and vegetation: the role of stabilizing processes. *Global Change Biology, 18*, 797–805. doi: 10.1111/j.1365-2486.2011.02624.x

Lucas, R. M., Mitchell, A. L., & Armston, J. (2015). Measurement of forest above-ground biomass using active and passive remote sensing at large (subnational to global) scales. Current Forestry Reports, 1(3), 162-177. doi: 10.1007/s40725-015-0021-9.

Luckman, A., Baker, J., Kuplich, T. M., Yanasse, C. D. C. F., & Frery, A. C. (1997). A study of the relationship between radar backscatter and regenerating tropical forest biomass for spaceborne SAR instruments. *Remote Sensing of Environment, 60*(1), 1-13. doi: 10.1016/S0034-4257(96)00121-6.

Manjunath, K. R., Potdar, M. B., & Purohit, N. L. (2002). Large area operational wheat yield model development and validation based on spectral and meteorological data. *International Journal of Remote Sensing, 23*(15), 3023-3038. doi: 10.1080/01431160110104692

Martens, B., Miralles, D., Lievens, H., Fernández-Prieto, D., & Verhoest, N. E. (2016). Improving terrestrial evaporation estimates over continental Australia through assimilation of SMOS soil moisture. *International Journal of Applied Earth Observation and Geoinformation, 48*, 146-162. doi: 10.1016/j.jag.2015.09.012

Martens, B., Miralles, D. G., Lievens, H., van der Schalie, R., de Jeu, R. A., Fernández-Prieto, D., ... & Verhoest, N. E. (2017). GLEAM v3: satellite-based land evaporation and root-zone soil moisture. Geoscientific Model Development, 10(5), 1903. doi: 10.5194/gmd-10-1903-2017

Martínez-Fernández, J., González-Zamora, A., Sánchez, N., & Gumuzzio, A. (2015). A soil water based index as a suitable agricultural drought indicator. *Journal of Hydrology, 522*, 265-273. doi: 10.1016/j.jhydrol.2014.12.051

Martínez-Fernández, J., González-Zamora, A., Sánchez, N., Gumuzzio, A., & Herrero-Jiménez, C. M. (2016). Satellite soil moisture for agricultural drought monitoring: assessment of the SMOS derived Soil Water Deficit Index. *Remote Sensing of Environment, 177*, 277-286. doi: 10.1016/j.rse.2016.02.064

Martínez-Vilalta, J., & Piñol, J. (2002). Drought-induced mortality and hydraulic architecture in pine populations of the NE Iberian Peninsula. *Forest Ecology and Management, 161*, 247–256. doi: 10.1016/S0378-1127(01)00495-9

Martínez-Vilalta, J., Lloret, F., Breshears, D.D. (2012a). Drought-induced forest decline: causes, scope and implications. *Biology Letters, 8*(5), 689–691. doi: 10.1098/rsbl.2011.1059

Martínez-Vilalta, J., Aguadé, D., Banqué, M., Barba, J., Curiel Yuste, J., Galiano, L., ..., & Vilà-Cabrera, A. (2012b). Las poblaciones ibéricas de pino albar ante el cambio climático: con la muerte en los talones. *Ecosistemas, 21*(3), 15-21. doi: 10.7818/ECOS.2012.21-3.03

Maselli, F., Conese, C., Petkov, L., & Gilabert, M. A. (1993). Environmental monitoring and crop forecasting in the Sahel through the use of NOAA NDVI data. A case study: Niger 1986–89.

International Journal of Remote Sensing, 14(18), 3471-3487. doi: 10.1080/01431169308904458

McArthur, A. G. (1967). Fire behavior in eucalypt forests. Australia Forestry and Timber Bureau Leaflet 107. Canberra, Australia: Australia Forestry and Timber Bureau.

McDowell, N.G., Beerling, D.J., Breshears, D.D., Fisher, R.A., Raffa, K.F., & Stitt, M. (2011). The interdependence of mechanisms underlying climatedriven vegetation mortality. *Trends in Ecoloy & Evolution, 26*(10), 523–532. doi: 10.1016/j.tree.2011.06.003

McDowell N.G., Williams A.P., Xu C., Pockman W.T., Dickman L.T., Sevanto S., …, & Koven, C. (2016). Multi-scale predictions of massive conifer mortality due to chronic temperature rise. *Nature Climate Change, 6*, 295-300. doi: 10.1038/nclimate2873

McKee, T.B., Doesken, N.J., & Kleist, J. (1993). The relationship of drought frequency and duration to time scales. 8th Conference on applied climatology, Anaheim, CA, United States of America, 1993.

McNairn, H., & Shang, J. (2016). A review of multitemporal synthetic aperture radar (SAR) for crop monitoring. In Ban, Y. (Ed.) *Multitemporal Remote Sensing. Methods and applications* (pp. 317-340). Springer, Cham.

Meesters, A. G., De Jeu, R. A., & Owe, M. (2005). Analytical derivation of the vegetation optical depth from the microwave polarization difference index. *IEEE Geoscience and Remote Sensing Letters, 2*(2), 121-123. doi: 10.1109/LGRS.2005.843983

Meier, E.S., Edwards Jr., T.C., Kienast, F., Dobbertn, M., & Zimmermann, N.E. (2011). Co-occurrence patterns of trees along macro-climatic gradients and their potential influence on the present and future distribution of *Fagus sylvatica* L. *Journal of Biogeography, 28*, 371–382. doi: 10.1111/j.1365-2699.2010.02405.x

Merlin, O., Chehbouni, A. G., Kerr, Y. H., Njoku, E. G., & Entekhabi, D. (2005). A combined modeling and multispectral/multiresolution remote sensing approach for disaggregation of surface soil moisture: application to SMOS configuration. *IEEE Transactions on Geoscience and Remote Sensing, 43*(9), 2036-2050. doi: 10.1109/TGRS.2005.853192

Merlin, O., Walker, J. P., Chehbouni, A., & Kerr, Y. (2008). Towards deterministic downscaling of SMOS soil moisture using MODIS derived soil evaporative efficiency. *Remote Sensing of Environment, 112*(10), 3935-3946. doi: 10.1016/j.rse.2008.06.012

Merlin, O., Al Bitar, A., Walker, J. P., & Kerr, Y. (2010). An improved algorithm for disaggregating microwave-derived soil moisture based on red, near-infrared and thermal-infrared data. *Remote Sensing of Environment, 114*(10), 2305-2316. doi: 10.1016/j.rse.2010.05.007

Merlin, O., Escorihuela, M. J., Mayoral, M. A., Hagolle, O., Al Bitar, A., & Kerr, Y. (2013). Self-calibrated evaporation-based disaggregation of SMOS soil moisture: an evaluation study at 3 km and 100 m resolution in Catalunya, Spain. *Remote Sensing of Environment, 130*, 25-38. doi: 10.1016/j.rse.2012.11.008

MET Norway & CIMR Expert Team. (2018). *CIMR. The Passive Microwave Satellite Mission for EU Copernicus.* Retrieved from: https://cimr.eu.

Mika, J., Kerényi, J., Rimóczi-Paál, A., Merza, Á., Szinell, C., & Csiszár, I. (2002). On correlation of maize and wheat yield with NDVI: Example of Hungary (1985–1998). *Advances in Space Research, 30*(11), 2399-2404. doi: 10.1016/S0273-1177(02)80288-5

Mishra, A., Vu, T., Veettil, A. V., & Entekhabi, D. (2017). Drought monitoring with soil moisture active passive (SMAP) measurements. *Journal of Hydrology, 552*, 620-632. doi: 10.1016/j.jhydrol.2017.07.033

Mitsopoulos, I., Mallinis, G., & Arianoutsou, M. (2015). Wildfire risk assessment in a typical Mediterranean wildland-urban interface of Greece. *Environmental Management, 55*(4), 900–915. doi: 10.1007/s00267-014-0432-6

Mladenova, I. E., Bolten, J. D., Crow, W. T., Anderson, M. C., Hain, C. R., Johnson, D. M., & Mueller, R. (2017). Intercomparison of soil moisture, evaporative stress, and vegetation indices for estimating corn and soybean yields over the US. IEEE Journal of Selected Topics in Applied Earth Observations and Remote Sensing, 10(4), 1328-1343. doi: 10.1109/JSTARS.2016.2639338

Momen, M., Wood, J. D., Novick, K. A., Pangle, R., Pockman, W. T., McDowell, N. G., & Konings, A. G. (2017). Interacting effects of leaf water potential and biomass on vegetation optical depth. *Journal of Geophysical Research: Biogeosciences, 122*(11), 3031-3046. doi: 10.1002/2017JG004145

Moran, M.S., Clarke, T.R., Inoue, Y., & Vidal, A. (1994). Estimating crop water deficit using the relation between surface-air temperature and spectral vegetation index. *Remote Sensing of Environment, 49*(3), 246–263. doi: 10.1016/0034-4257(94)90020-5

Morel, A. C., Saatchi, S. S., Malhi, Y., Berry, N. J., Banin, L., Burslem, D., ... & Ong, R. C. (2011). Estimating aboveground biomass in forest and oil palm plantation in Sabah, Malaysian Borneo using ALOS PALSAR data. *Forest Ecology and Management, 262*(9), 1786-1798. doi: 10.1016/j.foreco.2011.07.008.

Moreno, J.M., Chuvieco, E., Cruz, A., García, E., de Luis, E., Pérez, B., …, & Zavala, G. (2005). Impacto sobre los riesgos naturales de origen climático. Riesgo de incendios forestales. In J.M. Moreno, *Evaluación preliminar de los impactos en España por efecto del cambio climático – Proyecto ECCE, Informe final* (pp. 581-616). Centro de Publicaciones, Secretaría General Técnica, Ministerio de Medio Ambiente.

Moriondo, M., Good, P., Durao, R., Bindi, M., Giannakopoulos, C., & Corte-Real, J. (2006). Potential impact of climate change on fire risk in the Mediterranean area. *Climate Research, 31*, 85–95. doi: 10.3354/cr031085.

Mosleh, M. K., Hassan, Q. K., & Chowdhury, E. H. (2016). Development of a remote sensing-based rice yield forecasting model. *Spanish Journal of Agricultural Research, 14*(3), 0907.

Myneni, R. B., Dong, J., Tucker, C. J., Kaufmann, R. K., Kauppi, P. E., Liski, J., ... & Hughes, M. K. (2001). A large carbon sink in the woody biomass of Northern forests. *Proceedings of the National Academy of Sciences, 98*(26), 14784-14789. doi: 10.1073/pnas.261555198.

Naeimi, V., Scipal, K., Bartalis, Z., Hasenauer, S., & Wagner, W. (2009). An improved soil moisture retrieval algorithm for ERS and METOP scatterometer observations. *IEEE Transactions on Geoscience and Remote Sensing, 47*(7), 1999–2013. doi: 10.1109/TGRS.2008.2011617

NASA. National Aeronautics and Space Administration. (2014). *SMAP. Mission overview.* Retrieved from: https://www.nasa.gov/smap/overview

NASA. National Aeronautics and Space Administration. (2018). *MODIS. Moderate Resolution Imaging Spectroradiometer.* Retrieved from: https://modis.gsfc.nasa.gov

National Research Council. (2007). Earth science and applications from space: national imperatives for the next decade and beyond. Technical report. Space Studies Board, National Academies Press. Available at: http://www.nap.edu

Neumann, M., Mues, V., Moreno, A., Hasenauer, H., Seidl, R. (2017). Climate variability drives recent tree mortality in Europe. *Global Change Biology, 23*, 4788-4797. doi: 10.1111/gcB.73724

Ninyerola, M., Pons, X., Roure, J.M., Martín-Vide, J., Raso-Nadal, J.M., & Clavero, P. (2003). Atles climàtics de Catalunya [1 CD-ROM], Servei Meteorològic de Catalunya, Barcelona, Spain.

Ninyerola, M., Pons, X., & Roure, J.M. (2005). Atlas Climático Digital de la Península ibérica. Metodología y aplicaciones en bioclimatología y geobotánica. Universitat Autònoma de Barcelona. Bellaterra, 44 pp. (ISBN:932860-8-7).

NOAA. National Oceanic and Atmospheric Administration. (2017). ETOPO1 global relief model. Retrieved from: https://www.ngdc.noaa.gov/mgg/global/global.html

NSIDC (National Snow & Ice Data Center). (2017a). *NASA Distributed Active Archive Center (DAAC) at NSIDC. EASE-Grid Data*. Retrieved from: http://nsidc.org/data/ease/ease_grid2.html

NSIDC (National Snow & Ice Data Center). (2017b). *SMAP Enhanced L2 Radiometer Half-Orbit 9 km EASE-Grid Soil Moisture, Version 1.* Retrieved from: https://nsidc.org/data/spl2smp_e

Olsson, L., Eklundh, L., & Ardö, J. (2005). A recent greening of the Sahel—trends, patterns and potential causes. *Journal of Arid Environments, 63*(3), 556-566. doi: 10.1016/j.jaridenv.2005.03.008

Oppenheimer, M., Campos, M., Warren, W., Birkmann, J., Luber, G., O'Neill, B., & Takahashi, K. (2014). Emergent risks and key vulnerabilities. In T. F. Stocker, D. Qin, G.-K. Plattner, M. Tignor, S.K. Allen, J. Boschung, A. Nauels, Y. Xia, V. Bex, & P.M. Midgley (Eds.), *Climate Change 2014: Impacts, Adaptation, and Vulnerability. Contribution of the Working Group II to the IPCC 5th Assessment Report* (pp. 1039-1099). Cambridge, United Kingdom and NY, New York, USA: Cambridge University Press.

Overman, A. R., & Scholtz III, R. V. (2011). Model of yield response of corn to plant population and absorption of solar energy. *PloS One, 6*(1), e16117. doi: 10.1371/journal.pone.0016117

Owe, M., & Van de Griend, A.A. (2001). On the relationship between thermodynamic surface temperature and high frequency (37 GHz) vertical polarization brightness temperature under semi-arid conditions. *International Journal of Remote Sensing, 22*, 3521-3532.

Owe, M., de Jeu, R., Holmes, T. (2008). Multisensor historical climatology of satellite-derived global land surface moisture. *Journal of Geophysical Research, 113(F1)*. doi: 10.1029/2007JF000769

Pablos, M., González-Zamora, A., Sánchez, N., Martínez-Fernández, J. (2018). Assessment of root-zone soil moisture estimations from SMAP, SMOS and MODIS observations. *Remote Sensing, 10*(7):981. doi: 10.3390/rs10070981

Padilla, M. & Vega-García, C. (2011). On the comparative importance of fire danger rating indices and their integration with spatial and temporal variables for predicting daily human-caused fire occurrences in Spain. *International Journal of Wildland Fire 20*(1), 46–58. doi: 10.1071/WF09139

Paes do Amaral, J.M. (2000). Zonas fitogeográficas predominantes. Ministerio do Ambiente e do Ordenamento do Território, Direção-Geral do Ambiente. Lisboa.

Pan, Y., Birdsey, R. A., Fang, J., Houghton, R., Kauppi, P. E., Kurz, W. A., ..., & Ciais, P. (2011). A large and persistent carbon sink in the world’s forests. *Science, 333*(6045), 988-993. doi: 10.1126/science.1201609

Paredes-Trejo, F., & Barbosa, H. (2017). Evaluation of the SMOS-Derived Soil Water Deficit Index as Agricultural Drought Index in Northeast of Brazil. *Water, 9*(6), 377. doi: 10.3390/w9060377

Patton, J., & Hornbuckle, B. (2013). Initial validation of SMOS vegetation optical thickness in Iowa. *IEEE Geoscience and Remote Sensing Letters, 10*(4), 647-651. doi: 10.1109/LGRS.2012.2216498

Pausas, J.G. (2004). Changes in fire and climate in the eastern Iberian Peninsula (Mediterranean basin). *Climatic Change*, *63*, 337–350. doi: 10.1023/B:CLIM.0000018508.94901.9c

Pekel, J. F., Cottam, A., Gorelick, N., & Belward, A. S. (2016). High-resolution mapping of global surface water and its long-term changes. *Nature, 540*(7633), 418-422. doi:10.1038/nature20584

Peng, J., Loew, A., Merlin, O., & Verhoest, N. E. (2017). A review of spatial downscaling of satellite remotely sensed soil moisture. *Reviews of Geophysics, 55*(2), 341-366. doi: 10.1002/2016RG000543

Pereira, M.G., Trigo, R.M., da Camara, C.C., Pereira, J.M.C., & Leite, S.M. (2005). Synoptic patterns associated with large summer forest fires in Portugal. *Agricultural and Forest Meteorology, 129*, 11-25. doi: 10.1016/j.agrformet.2004.12.007

Petropoulos, G. P., Ireland, G., Srivastava, P. K., & Ioannou-Katidis, P. (2014). An appraisal of the accuracy of operational soil moisture estimates from SMOS MIRAS using validated in situ observations acquired in a Mediterranean environment. *International Journal of Remote Sensing, 35*(13), 5239-5250. doi: 10.1080/2150704X.2014.933277

Petropoulos, G. P., Srivastava, P. K., Piles, M., & Pearson, S. (2018). Earth Observation-based operational estimation of soil moisture and evapotranspiration for agricultural crops in support of sustainable water management. *Sustainability, 10*(1), 181-200.

Piles, M., Camps, A., Vall-Llossera, M., Corbella, I., Panciera, R., Rudiger, C., ... & Walker, J. (2011a). Downscaling SMOS-derived soil moisture using MODIS visible/infrared data. *IEEE Transactions on Geoscience and Remote Sensing, 49*(9), 3156-3166. doi: 10.1109/TGRS.2011.2120615

Piles, M., Camps, A., Vall-llossera, M., Marín, A., & Martínez, J. (2011b). SMOS derived soil moisture at 1 km spatial resolution and first results of its application in identifying fire outbreaks. Oral contribution to the 1st SMOS Science Conference, Arles, France. 27-29th Semptember 2011.

Piles, M., Vall-Llossera, M., Camps, A., Sanchez, N., Martínez-Fernández, J., Martinez, J., ... & Riera, R. (2013). On the synergy of SMOS and Terra/Aqua MODIS: high resolution soil moisture maps in near real-time. *Geoscience and Remote Sensing Symposium (IGARSS), 2013 IEEE International* (pp. 3423-3426).

Piles, M., Sánchez, N., Vall-llossera, M., Camps, A., Martínez-Fernández, J., Martínez, J., & González-Gambau, V. (2014). A downscaling approach for SMOS land observations: Evaluation of high-resolution soil moisture maps over the Iberian Peninsula. *IEEE Journal of Selected Topics in Applied Earth Observations and Remote Sensing, 7*(9), 3845-3857. doi: 10.1109/JSTARS.2014.2325398

Piles, M., McColl, K. A., Entekhabi, D., Das, N., & Pablos, M. (2015). Sensitivity of Aquarius active and passive measurements temporal covariability to land surface characteristics. *IEEE Transactions on Geoscience and Remote Sensing, 53*(8), 4700-4711. doi: 10.1109/TGRS.2015.2407611

Piles, M., Petropoulos, G. P., Sánchez, N., González-Zamora, Á., & Ireland, G. (2016). Towards improved spatio-temporal resolution soil moisture retrievals from the synergy of SMOS and MSG SEVIRI spaceborne observations. *Remote Sensing of Environment, 180*, 403-417. doi: 10.1016/j.rse.2016.02.048

Piles, M., Camps-Valls, G., Chaparro, D., Entekhabi, D., Konings, A. G., & Jagdhuber, T. (2017). Remote sensing of vegetation dynamics in agro-ecosystems using SMAP vegetation optical depth and optical vegetation indices. *Geoscience and Remote Sensing Symposium (IGARSS), 2017 IEEE International* (pp. 4346-4349). IEEE.

Polcher, J., Piles, M., Gelati, E., Barella-Ortiz, A., & Tello, M. (2016). Comparing surface soil moisture from the SMOS mission and the ORCHIDEE land-surface model over the Iberian Peninsula. *Remote Sensing of Environment, 174*, 69-81. doi: 10.1016/j.rse.2015.12.004

Portal, G., Vall-llossera, M., Piles, M., Camps, A., Chaparro, D., Pablos, M., & Rossato, L. (2018). A spatially consistent downscaling approach for SMOS using an adaptive moving window. *IEEE Journal of Selected Topics in Applied Earth Observations and Remote Sensing.* doi: 10.1109/JSTARS.2018.2832447

Qiu, J., Gao, Q., Wang, S., & Su, Z. (2016). Comparison of temporal trends from multiple soil moisture data sets and precipitation: the implication of irrigation on regional soil moisture trend. *International Journal of Applied Earth Observation and Geoinformation, 48*, 17-27. doi: 10.1016/j.jag.2015.11.012

Quarmby, N. A., Milnes, M., Hindle, T. L., & Silleos, N. (1993). The use of multi-temporal NDVI measurements from AVHRR data for crop yield estimation and prediction. *International Journal of Remote Sensing*, 14(2), 199-210. doi: 10.1080/01431169308904332

Rahmoune, R., Ferrazzoli, P., Singh, Y. K., Kerr, Y. H., Richaume, P., & Al Bitar, A. (2014). SMOS retrieval results over forests: comparisons with independent measurements. *IEEE Journal of Selected Topics in Applied Earth Observations and Remote Sensing, 7*(9), 3858-3866. doi: 10.1109/JSTARS.2014.2321027

Ray, D. K., Gerber, J. S., MacDonald, G. K., & West, P. C. (2015). Climate variation explains a third of global crop yield variability. *Nature Communications, 6*, 5989. doi: 10.1038/ncomms6989

Reichstein, M., Bahn, M., Ciais, P., Frank, D., Mahecha, M. D., Seneviratne, S. I., ... & Papale, D. (2013). Climate extremes and the carbon cycle. *Nature, 500*(7462), 287-295. doi: 10.1038/nature12350

Rembold, F., Atzberger, C., Savin, I., & Rojas, O. (2013). Using low resolution satellite imagery for yield prediction and yield anomaly detection. *Remote Sensing, 5*(4), 1704-1733.

Renzullo, L. J., Van Dijk, A. I. J. M., Perraud, J. M., Collins, D., Henderson, B., Jin, H., ... & McJannet, D. L. (2014). Continental satellite soil moisture data assimilation improves root-zone moisture analysis for water resources assessment. *Journal of Hydrology, 519*, 2747-2762. doi: 10.1016/j.jhydrol.2014.08.008

Rüdiger, C., Su, C. H., Ryu, D., & Wagner, W. (2016). Disaggregation of low-resolution L-band radiometry using C-band radar data. *IEEE Geoscience and Remote Sensing Letters, 13*(10), 1425-1429. doi: 10.1109/LGRS.2016.2583433

Ruiz-Benito, P., Lines, E.R., Gómez-Aparicio, L., Zavala, M.A., & Coomes, D.A. (2013). Patterns and drivers of tree mortality in Iberian Forests: climatic effects are modified by competition. *PLoS ONE, 8*(2), e56843. doi: 10.1371/journal.pone.0056843

Saatchi, S. S., Houghton, R. A., Dos Santos Alvala, R. C., Soares, J. V., & Yu, Y. (2007). Distribution of aboveground live biomass in the Amazon basin. *Global Change Biology, 13*(4), 816-837. doi: 10.1111/j.1365-2486.2007.01323.x

Saatchi, S. S., Harris, N. L., Brown, S., Lefsky, M., Mitchard, E. T., Salas, W., ... & Petrova, S. (2011). Benchmark map of forest carbon stocks in tropical regions across three continents. *Proceedings of the National Academy of Sciences, 108*(24), 9899-9904. doi: 10.1073/pnas.1019576108

Saatchi, S., Asefi-Najafabady, S., Malhi, Y., Aragão, L. E., Anderson, L. O., Myneni, R. B., & Nemani, R. (2013). Persistent effects of a severe drought on Amazonian forest canopy. *Proceedings of the National Academy of Sciences, 110*(2), 565-570. doi: 10.1073/pnas.1204651110

Sánchez, N., Martínez-Fernández, J., Scaini, A., & Perez-Gutierrez, C. (2012). Validation of the SMOS L2 soil moisture data in the REMEDHUS network (Spain). *IEEE Transactions on Geoscience and Remote Sensing, 50*(5), 1602-1611. doi: 10.1109/TGRS.2012.2186971

Sánchez, N., González-Zamora, Á., Piles, M., & Martínez-Fernández, J. (2016). A new Soil Moisture Agricultural Drought Index (SMADI) Integrating MODIS and SMOS Products: a case of study over the iberian Peninsula. *Remote Sensing, 8*(4), 287. doi: 10.3390/rs8040287

Sánchez, N., González-Zamora, Á., Martínez-Fernández, J., Piles, M., & Pablos, M. (2018). Integrated remote sensing approach to global agricultural drought monitoring. *Agricultural and Forest Meteorology, 259*, 141-153. doi: 10.1016/j.agrformet.2018.04.022.

Sánchez de Dios, R., Benito-Garzón, M., & Sainz-Ollero, H. (2006). Hybrid zones between two European oaks: a plantcommunity approach. *Plant Ecology, 187*(1), 109-125. doi: 10.1007/s11258-006-9136-1

Sánchez-Ruiz, S., Piles, M., Sánchez, N., Martínez-Fernández, J., Vall-llossera, M., & Camps, A. (2014). Combining SMOS with visible and near/shortwave/thermal infrared satellite data for high resolution soil moisture estimates. *Journal of Hydrology, 516*, 273-283. doi: 10.1016/j.jhydrol.2013.12.047

Sanchez-Ruiz, S., Moreno, A., Piles, M., Maselli, F., Carrara, A., Running, S., & Gilabert, M. A. (2017). Quantifying water stress effect on daily light use efficiency in Mediterranean ecosystems using satellite data. *International Journal of Digital Earth*, *10*(6), 623-638. doi: 10.1080/17538947.2016.1247301

Sandholt, I., Rasmussen, K., & Andersen, J. (2002). A simple interpretation of the surface temperature/vegetation index space for assessment of surface moisture status. *Remote Sensing of Environment, 79*(2-3), 213–224. doi: 10.1016/S0034-4257(01)00274-7

San-Miguel-Ayanz, J., Schulte, E., Schmuck, G., Camia, A., Strobl, P., Liberta, G., ..., & Amatulli, G. (2012). Comprehensive monitoring of wildfires in Europe: the European Forest Fire Information System (EFFIS). In J. Tiefenbacher (Ed.) *Approaches to Managing Disaster–Assessing Hazards, Emergencies and Disaster Impacts*, pp. 87-105. Rijeka, Croatia: InTech.

San-Miguel-Ayanz, J., Schulte, E., Schmuck, G., & Camia, A. (2013). The European Forest Fires Information System in the context of environmental policies of the European Union. *Forest Policy and Economics, 29*, 19–25. doi: 10.1016/j.forpol.2011.08.012

San-Miguel-Ayanz, J., Durrant, T., Boca, R., Libertà, G., Branco, A., de Rigo, D., ... & Loffler, P. (2017). Forest Fires in Europe, Middle East and North Africa 2016. EUR 28707 EN, Publications Office, Luxembourg, 2017, ISBN 978-92-79-71292-0.

Sass, G.Z., Wheatley, M., Aldred, D.A., Gould, A.J., & Creed, I.F. (2012). Defining protected area boundaries based on vascular-plant species richness using hydrological information derived from archived satellite imagery. *Biological Conservation, 147*(1), 143-152. doi: 10.1016/j.biocon.2011.12.025

Scaini, A., Sánchez, N., Vicente-Serrano, S. M., & Martínez-Fernández, J. (2015). SMOS-derived soil moisture anomalies and drought indices: a comparative analysis using in situ measurements. *Hydrological processes, 29*(3), 373-383. doi: 10.1002/hyp.10150

Schmugge, T., O'Neill, P., & Wang, J. (1986). Passive microwave soil moisture research. *IEEE Transactions on Geosciences and Remote Sensing, 24,* 12-22. doi: 10.1109/TGRS.1986.289584

Schnur, M. T., Xie, H., & Wang, X. (2010). Estimating root zone soil moisture at distant sites using MODIS NDVI and EVI in a semi-arid region of southwestern USA. *Ecological Informatics, 5*(5), 400-409. doi: 10.1016/j.ecoinf.2010.05.001

Scholze, M., Kaminski, T., Knorr, W., Blessing, S., Vossbeck, M., Grant, J. P., & Scipal, K. (2016). Simultaneous assimilation of SMOS soil moisture and atmospheric CO2 in-situ observations to constrain the global terrestrial carbon cycle. *Remote Sensing of Environment, 180*, 334-345. doi: 10.1016/j.rse.2016.02.058

Seidl, R., Thom, D., Kautz, M., Martin-Benito, D., Peltoniemi, M., Vacchiano, G., ... & Lexer, M. J. (2017). Forest disturbances under climate change. *Nature Climate Change, 7*(6), 395-402. doi: 10.1038/nclimate3303

Settele, J., Scholes, R., Betts, R., Bunn, S., Leadley, P., Nepstad, D., ... & Taboada, M.A. (2014). Terrestrial and inland water systems. In: Field, C.B., Barros, V.R., Dokken, D.J., Mach, K.J., Mastrandrea, M.D., Bilir, T.E., Chatterjee, M., Ebi, K.L., Estrada, Y.O., Genova, R.C., Girma, B., Kissel, E.S., Levy, A.N., MacCracken, S., Mastrandrea, P.R., White, L.L. (Eds.) *Climate Change 2014: Impacts, Adaptation, and Vulnerability. Part A: Global and Sectoral Aspects. Contribution of the Working Group II to the 5th Assessment Report of the IPCC* (pp. 271-359). Cambridge, United Kingdom and NY, New York, USA: Cambridge University Press.

Shvetsov, E. (2013). Fire danger estimation in Siberia using SMOS data. *Geophysical research abstracts, 15*. EGU General Assembly 2013.

Simard, M., Pinto, N., Fisher, J. B., & Baccini, A. (2011). Mapping forest canopy height globally with spaceborne lidar. *Journal of Geophysical Research: Biogeosciences, 116(G4)*. doi:10.1029/2011JG001708.

Simpson, E. H. (1949). Measurement of diversity. *Nature, 163*(4148), 688. doi: 10.1038/163688a0

Singh, D., Gupta, P. K., Pradhan, R., Dubey, A. K., & Singh, R. P. (2016). Discerning shifting irrigation practices from passive microwave radiometry over Punjab and Haryana. *Journal of Water and Climate Change, 8*(2), 303-319. doi: 10.2166/wcc.2016.122

Sinha, S., Jeganathan, C., Sharma, L. K., & Nathawat, M. S. (2015). A review of radar remote sensing for biomass estimation. *International Journal of Environmental Science and Technology, 12*(5), 1779-1792. doi: 10.1007/s13762-015-0750-0

Sippel, S., Reichstein, M., Ma, X., Mahecha, M. D., Lange, H., Flach, M., & Frank, D. (2018). Drought, Heat, and the Carbon Cycle: a Review. *Current Climate Change Reports*, 1-21. doi: 10.1007/s40641-018-0103-4

SMC (Catalan Meteorological Service). (2012a). *Butlletí climàtic estacional. Hivern del 2011-2012*. Retrieved from: http://static-m.meteo.cat/wordpressweb/wp-content/uploads/2014/11/18075101/Butlleti_hivern_2011_2012.pdf

SMC (Catalan Meteorological Service). (2012b). *Butlletí climàtic estacional. Primavera del 2012*. Retrieved from: http://static-m.meteo.cat/wordpressweb/wp-content/uploads/2014/11/18075101/Butlleti_primavera_2012.pdf.

SMC (Catalan Meteorological Service). (2012c). *Butlletí climàtic estacional. Estiu del 2012*. Retrieved from: http://static-m.meteo.cat/wordpressweb/wp-content/uploads/2014/11/18075101/Butlleti_estiu_2012.pdf.

SMC (Catalan Meteorological Service). (2018). *Atles climàtics*. Retrieved from: http://www.meteo.cat/climatologia/atles_climatic.

SMOS Algorithm Theoretical Basis Document (ATBD). (2007). Technical report, European Space Agency.

Son, N. T., Chen, C. F., Chen, C. R., Minh, V. Q., & Trung, N. H. (2014). A comparative analysis of multitemporal MODIS EVI and NDVI data for large-scale rice yield estimation. *Agricultural and Forest Meteorology, 197*, 52-64. doi: 10.1016/j.agrformet.2014.06.007

Srivastava, P. K., Han, D., Rico-Ramirez, M. A., Al-Shrafany, D., & Islam, T. (2013). Data fusion techniques for improving soil moisture deficit using SMOS satellite and WRF-NOAH land surface model. *Water Resources Management, 27*(15), 5069-5087. doi: 10.1007/s11269-013-0452-7

Stokland, J.N., Tomter, S.M., & Soderberg, U. (2005). Development of dead wood indicators for biodiversity monitoring: experiences from Scandinavia. In M. Marchetti (Ed.) *Monitoring and indicators of forest biodiversity in Europe—from ideas to operationality.* EFI Proceedings, 51, pp. 207–226. Finland: European Forest Institute.

Sun, Z., Peng, S., Li, X., Guo, Z., & Piao, S. (2015). Changes in forest biomass over China during the 2000s and implications for management. *Forest Ecology and Management, 357*, 76-83. doi: 10.1016/j.foreco.2015.08.013.

Syphard, A. D., Radeloff, V.C., Keuler, N.S., Taylor, R.S., Hawbaker, T.J., Stewart, S.I., & Clayton, M.K. (2008). Predicting spatial patterns of fire on a southern California landscape. *International Journal of Wildland Fire*, *17*, 602–613. doi: 10.1071/WF07087

Tebbs, E., Gerard, F., Petrie, A., & De Witte, E. (2016). Emerging and potential future applications of satellite-based soil moisture products. In: Srivastava, P., Petropoulos, G., & Kerr, Y.H. (Eds.) *Satellite soil moisture retrieval: techniques and applications* (pp. 379-400). Elsevier. doi: 10.1016/C2014-0-03396-5

Teubner, I. E., Forkel, M., Jung, M., Liu, Y. Y., Miralles, D. G., Parinussa, R., ... & Camps-Valls, G. (2018). Assessing the relationship between microwave vegetation optical depth and gross primary production. *International Journal of Applied Earth Observation and Geoinformation, 65*, 79-91. doi: 10.1016/j.jag.2017.10.006.

Thurner, M., Beer, C., Santoro, M., Carvalhais, N., Wutzler, T., Schepaschenko, D., ... & Schmullius, C. (2014). Carbon stock and density of northern boreal and temperate forests. *Global Ecology and Biogeography, 23*(3), 297-310. doi: 10.1111/geB.72125.

Tian, F., Brandt, M., Liu, Y. Y., Verger, A., Tagesson, T., Diouf, A. A., ... & Fensholt, R. (2016). Remote sensing of vegetation dynamics in drylands: Evaluating vegetation optical depth (VOD) using AVHRR NDVI and in situ green biomass data over West African Sahel. *Remote Sensing of Environment, 177*, 265-276. doi: 10.1016/j.rse.2016.02.056

Tilman, D., Balzer, C., Hill, J., & Befort, B. L. (2011). Global food demand and the sustainable intensification of agriculture. *Proceedings of the National Academy of Sciences, 108*(50), 20260-20264. doi: 10.1073/pnas.1116437108

Todd, S. W., Hoffer, R. M., & Milchunas, D. G. (1998). Biomass estimation on grazed and ungrazed rangelands using spectral indices. *International Journal of Remote Sensing, 19*(3), 427-438

Tomlinson, C. J., Chapman, L., Thornes, J.E., & Baker, C. (2011). Remote sensing land surface temperature for meteorology and climatology: a review. *Meteorological Applications, 18*(3), 296–306. doi: 10.1002/met.287

Trumbore, S., Brando, P., & Hartman, H. (2015). Forest health and global change. *Science, 349*(6250), 814-818. doi: 10.1126/science.aac6759

Ulaby, F. T., Moore, R. K., & Fung, A. K. (1981). *Microwave Remote Sensing Active and Passive-Volume I: Microwave Remote Sensing Fundamentals and Radiometry*. Reading, MA (USA): Addison-Wesley Publishing Company.

Ulaby, F. T., Moore, R. K., & Fung, A. K. (1986). *Microwave Remote Sensing Active and Passive-Volume III: From Theory To Applications*. Norwood, MA (USA): Artech House.

Ulaby, F.T., & Long, D.F. (2014). *Microwave Radar and Radiometric Remote Sensing*. 839 Greene Street Ann Arbor, MI 48104–3209, United States of America: University of Michigan Press.

UNESCO. United Nations Educational, Scientific and Cultural Organization. (2017). World rivers. Retrieved from: http://ihp-wins.unesco.org/layers/geonode:world_rivers

USDA. United States Department of Agriculture. (1992). Weights, measures, and conversion factors for agricultural commodities and their products. *Agricultural Handbook, 697*. Washington, D.C.: USDA Economic Research Service.

USDA. United States Department of Agriculture. (2015). *Office of the Chief Economist. Major World Crop Areas and Climate Profiles (MWCACP). North America.* Retrieved from: https://www.usda.gov/oce/weather/pubs/Other/MWCACP/namerica.htm.

USDA-NASS. United States Department of Agriculture – National Agricultural Statistics Service. (2017). *Quick Stats*. Retrieved from: https://quickstats.nass.usda.gov.

Van Marle, M. J. E., Van Der Werf, G. R., de Jeu, R. A. M., & Liu, Y. Y. (2016). Annual South American forest loss estimates based on passive microwave remote sensing (1990-2010). *Biogeosciences, 13*(2), 609-624. doi:10.5194/bg-13-609-2016.

Van Wagner, C. E. (1987). Development and structure of the Canadian forest fire weather index system. Forest technical report 35. Ottawa, Canada: Government of Canada, Canadian Forestry Service.

Vecín-Arias, D., Castedo-Dorado, F., Ordóñez, C., & Rodríguez-Pérez, J.R. (2016). Biophysical and lightning characteristics drive lightning-induced fire occurrence in the central plateau of the Iberian Peninsula. *Agricultural and Forest Meteorology, 225*, 36-47. doi: 10.1016/j.agrformet.2016.05.003

Verdú, F., Salas, J., & Vega-García, C. (2012). A multivariate analysis of biophysical factors and forest fires in Spain, 1991–2005. *International Journal of Wildland Fire*, *21*(5), 498–509. doi: 10.1071/WF11100

Vereecken, H., Weihermüller, L., Jonard, F., & Montzka, C. (2012). Characterization of crop canopies and water stress related phenomena using microwave remote sensing methods: A review. *Vadose Zone Journal, 11*(2). doi:10.2136/vzj2011.0138ra

Vicente-Serrano, S.M., Gouveia, C., Camarero, J.J., Beguería, S., Trigo, R., López-Moreno, J.I., ..., & Sanchez-Lorenzo, A. (2013). *Response of vegetation to drought time-scales across global land biomes*. *Proceeding of the National Academy of Sciences, 110*(1), 52-57. doi: 10.1073/pnas.1207068110

Viet Nguyen, L., Tateishi, R., Kondoh, A., Sharma, R. C., Thanh Nguyen, H., Trong To, T., & Ho Tong Minh, D. (2016). Mapping tropical forest biomass by combining ALOS-2, Landsat 8, and field plots data. *Land, 5*(4), 31. doi:10.3390/land5040031

Vilà-Cabrera, A., Martínez-Vilalta, J., Vayreda, J., & Retana, J. (2011). Structural and climatic determinants of demographic rates of Scots pine forests across the Iberian Peninsula. *Ecological Applications, 21*, 1162–1172. doi: 10.1890/10-0647.1

Vilà-Cabrera, A., Martínez-Vilalta, J., Galiano, L., & Retana, J. (2013). Patterns of forest decline and regeneration across Scots pine populations. *Ecosystems, 16*, 323–335. doi: 10.1007/s10021-012-9615-2

Vittucci, C., Ferrazzoli, P., Kerr, Y., Richaume, P., Guerriero, L., Rahmoune, R., & Laurin, G. V. (2016a). SMOS retrieval over forests: Exploitation of optical depth and tests of soil moisture estimates. *Remote Sensing of Environment, 180*, 115-127. doi: 10.1016/j.rse.2016.03.004

Vittucci, C., Ferrazzoli, P., Kerr, Y., Richaume, P., Guerriero, L., & Laurin, G. V. (2016b). SMOS forest optical depth intercomparisons over pan-tropical biomes. *Geoscience and Remote Sensing Symposium (IGARSS), 2016 IEEE International*, 5311-5314. IEEE. doi: 10.1109/IGARSS.2016.7730383

Vrije Universiteit Amsterdam (Richard de Jeu) & NASA GSFC (Manfred Owe). (2014). AMSR2/GCOM-W1 surface soil moisture (LPRM) L3 1 day 25 km x 25 km ascending V001. Retrieved from: https://disc.gsfc.nasa.gov/datacollection/LPRM_AMSR2_A_SOILM3_001.html. doi: 10.5067/M5DTR2QUYLS2.

Wagner, W., Hahn, S., Kidd, R., Melzer, T., Bartalis, Z., Hasenauer, S., ... & Komma, J. (2013). The ASCAT soil moisture product: a review of its specifications, validation results, and emerging applications. *Meteorologische Zeitschrift, 22*(1), 5-33. doi: 10.1127/0941-2948/2013/0399

Wall, L., Larocque, D., & Léger, P. M. (2008). The early explanatory power of NDVI in crop yield modelling. *International Journal of Remote Sensing, 29*(8), 2211-2225.

Wanders, N., Karssenberg, D., Roo, A. D., De Jong, S. M., & Bierkens, M. F. P. (2014). The suitability of remotely sensed soil moisture for improving operational flood forecasting. *Hydrology and Earth System Sciences, 18*(6), 2343-2357. doi: 10.5194/hess-18-2343-2014

Wang, L., Zhou, Y., Zhou, W., & Wang, S. (2013). Fire danger assessment with remote sensing: A case study in Northern China. *Natural Hazards, 65*, 819–834. doi: 10.1007/s11069-012-0391-2

Weissteiner, C. J., & Kühbauch, W. (2005). Regional yield forecasts of malting barley (hordeum vulgare L.) by NOAA-AVHRR remote sensing data and ancillary data. *Journal of Agronomy and Crop Science*, *191*(4), 308-320. doi: 10.1111/j.1439-037X.2005.00154.x

Whelan. R. J. (1995). The Ecology of Fire. Cambridge, United Kingdom: Cambridge University Press.

Wigneron, J. P., Calvet, J. C., Pellarin, T., Van de Griend, A. A., Berger, M., & Ferrazzoli, P. (2003). Retrieving near-surface soil moisture from microwave radiometric observations: current status and future plans. *Remote Sensing of Environment, 85*(4), 489-506. doi: 10.1016/S0034-4257(03)00051-8

Wigneron, J. P., Kerr, Y., Waldteufel, P., Saleh, K., Escorihuela, M. J., Richaume, P., ... & Grant, J. P. (2007). L-band microwave emission of the biosphere (L-MEB) model: description and calibration against experimental data sets over crop fields. *Remote Sensing of Environment, 107*(4), 639-655.

Williams, A.P., Allen, C.D., Macalady, A.K., Griffin, D., Woodhouse, C.A., Meko, D.M., ..., & McDowell, N.G. (2013). Temperature as a potent driver of regional forest drought stress and tree mortality. *Nature Climate Change*, *3*, 292–297. doi:10.1038/nclimate1693

WWF. World Wildlife Fund. (2018). Seasonally flooded river basins of Brazil, Peru and Bolivia. Retrieved from: https://www.worldwildlife.org/ecoregions/nt0128.

Young, D.J.N, Stevens, J.T., Earles, J.M., Moore, J., Ellis, A., Jirka, A.L., & Latimer, A.M. (2017). Long-term climate and competition explain forest mortality patterns under extreme drought. *Ecology Letters, 20*, 78-86. doi: 10.1111/ele.12711

Yuan, X., Li, L., Tian, X., Luo, G., & Chen, X. (2016). Estimation of above-ground biomass using MODIS satellite imagery of multiple land-cover types in China. *Remote Sensing Letters, 7*(12), 1141-1149. doi: 10.1080/2150704X.2016.1219458.

Zhao, C., Liu, B., Piao, S., Wang, X., Lobell, D. B., Huang, Y., ... & Durand, J. L. (2017). Temperature increase reduces global yields of major crops in four independent estimates. Proceedings of the National Academy of Sciences, 114(35), 9326-9331. doi: 10.1073/pnas.1701762114

Acknowledgements

Working on this PhD Thesis has been possible with the invaluable support, advice and collaboration of many people, to whom I wish to express my sincere gratitude.

First, very special thanks to my Thesis advisors, Drs. Maria Piles and Mercè Vall-llossera, as well as to Dr. Adriano Camps, who has widely contributed to this work. I am very grateful to Maria Piles, who has enthusiastically passed me on her huge motivation for doing science: this has been vital for me. She has thoroughly provided her deep insight and detailed contributions, which have been crucial for the research performed and for the works published, including this document. I equally thank very much Mercè Vall-llossera, who has provided enormous support, patience and dedication to me and to this research. Mercè's advices and her contributions to this Thesis have been essential. Her great kindness and encouragement have made the work possible and pleasant. I also wish to express many especial thanks to Adriano Camps, who has provided brilliant ideas and discussions, detailed contributions and amendments, and a lot of dedication. He has also taught me how good sense of humour and efficiency (even for scientists!) go hand in hand.

Importantly, I wish to thank very much Drs. Grégory Duveiller and Alessandro Cescatti, who hosted me during my stay at the JRC in Italy. Their warm welcome and their advice were essential during this great professional and personal experience. Their contributions and help allowed developing an important part of the work. Many thanks also to Drs. Jordi Martínez-Vilalta, Jordi Vayreda, and Mireia Banqué, at CREAF, who worked consciously and contributed a lot to an important part of the research. I hope we will continue working on forest decline soon. Likewise, I wish to express my gratitude to Drs. Nilda Sánchez and Cristina Vega-García for accepting to be reviewers of this PhD Thesis. Also, I wish to specially thank all people who have been involved in this Thesis contributing to the research and co-authoring the publications.

Further, I would like to thank very much all people who has worked or works currently with me. To Gerard Portal for his help on improving my MATLAB knowledge, and to Miriam Pablos for her support –I hope we will be working together again now-. Also, to all the colleagues, especially to Israel Durán for his friendship and support, and for very fun times and shared breakfasts, and also importantly to Roselena, Santi, Julio, Luciana, Marc and Joan, as well as to people providing important technical and administrative support: Ferran and Aynie. Also, many thanks to Manu and Yeray, and to all people in Ispra: it was a great time with all of you.

Very specially, I want to express my huge gratitude to my people. To my parents, Beatriz and Joan Anton and to my sister Marina, for all their love and support. To my grandparents, for their huge love: "Pepe y Tita", I hope you will be proud of having a new doctor in the family; "Avis", I miss you a lot, and I know you would be happy to see this work finished. Also, thanks a lot to all my family, and to my friends from Cerdanyola, who have also encouraged me.

Finally, I want to write these most important closing lines for you, Blanca: many, many special thanks for your unconditional love, support, and patience during all these years, and especially during my stay in Italy. This PhD Thesis is also yours.

This PhD Thesis has been founded by the Spanish government through: the pre-doctoral grant Ayudas para contratos predoctorales para la Formación de Doctores, with reference BES-2013-066240; the grant EEBB-I-17-12200; the projects ESP2015-67549-C3-1-R and ESP2017-89463-C3-2-R; and the award "Unidad de Excelencia Maria de Maeztu" MDM-2016-0600, financed by the "Agencia Estatal de Investigación" (Spain). The work has been supported also by the European Regional Development Fund (ERDF).

Fires data have been provided by the European Forest Fire Information System – EFFIS (http://effisjrc.ec.europa.eu) of the European Commission Joint Research Centre. DEBOSCAT data have been provided by the Centre for Ecological Research and Forestry Applications (CREAF). The Carnegie Airborne Observatory has made the ACD maps available.